THERMAL REMOTE SENSING OF URBAN SURFACE TEMPERATURES

By

James Adrian Voogt

B. Sc., Queen's University, 1986

M. Sc., University of British Columbia, 1989

A THESIS SUBMITTED IN PARTIAL FULFILLMENT OF

THE REQUIREMENTS FOR THE DEGREE OF

DOCTOR OF PHILOSOPHY

in

THE FACULTY OF GRADUATE STUDIES

DEPARTMENT OF GEOGRAPHY

We accept this thesis as conforming

to the required standard

THE UNIVERSITY OF BRITISH COLUMBIA

1995

© James Adrian Voogt, 1995

In presenting this thesis in partial fulfilment of the requirements for an advanced degree at the University of British Columbia, I agree that the Library shall make it freely available for reference and study. I further agree that permission for extensive copying of this thesis for scholarly purposes may be granted by the head of my department or by his or her representatives. It is understood that copying or publication of this thesis for financial gain shall not be allowed without my written permission.

(Signature)

Department of Geography

The University of British Columbia
Vancouver, Canada

Date Sept. 18, 1995

DE-6 (2/88)

Abstract

Thermal remote sensors have been used extensively to examine urban surface temperature patterns but without explicit consideration of the complex form of the urban surface. This research investigates the extent of possible biases which may be present due to the unique structure of the urban surface and is an attempt to address some of the issues raised by Roth *et al.* (1989).

The research approach is primarily observational. An extensive measurement programme integrating ground and airborne remote sensor platforms as well as fixed monitoring sites was designed and implemented to obtain information from three of the most common urban surface types: downtown office/commercial, residential and light industrial. Both nadir and off-nadir high resolution thermal imagery was collected to obtain information on component surface temperatures, and to determine the extent of anisotropy in urban surface emissions at the land use scale.

Vertical facet temperatures are shown to exhibit large diurnal temperature ranges which strongly control the anisotropic longwave emission of the urban surface. Airborne observations reveal strong anisotropy of surface longwave emissions over each of the sites at times of maximum temperature contrast between opposing canyon facets. The magnitude of the anisotropy is sufficient to demand consideration whenever daytime thermal remote measurements are made over urban surfaces.

Mixed distribution modelling has been explored as a technique to recover component surface temperatures from composite temperature frequency distributions. A low number of component distributions can be used to successfully model the composite distribution, however, the successful extraction of individual component temperatures is more difficult

and depends upon the nature of the surface, and the temperature contrasts present.

Estimates of the complete urban surface temperature have been made for the first time by combining remote and surface-based estimates of horizontal and vertical facet temperatures. The complete surface temperature is cooler than nadir or off-nadir remote measurements and is shown to be best approximated by off-nadir measurements in the direction of the most shaded vertical facet.

A simple two-dimensional geometric urban surface model (a slightly modified version of that orignally presented by Sobrino and Caselles (1989) and extended by Caselles *et al.* (1992)) is used to investigate the nature of anisotropy over the study areas. Urban surface temperature components are specified from observed data but a modified version of the Myrup (1969) surface energy balance model is shown to be adequate for estimating surface temperatures in canyon environments for the extension of geometrical surface modelling to other times and locations. Results indicate that the two-dimensional representation of the urban surface is generally inadequate. The development of a three-dimensional surface geometrical model is recommended to better reperesent the structure of the urban surface.

Table of Contents

Abstract ii

Table of Contents iv

List of Tables xi

List of Figures xiv

List of Symbols and Abbreviations xxv

Acknowledgements xxxiii

1 INTRODUCTION 1

1.1 Thermal Infra-red Remote Sensing of Urban Areas 1

1.2 Limitations of TIR remote sensing 6

1.3 The Urban Surface 6

1.4 TIR Remote Sensing of the Urban Surface 9

1.5 TIR Remote Sensing of Agricultural and Forest Surfaces 10

1.6 Modelling of Thermal Emissions over Plant Canopies 11

1.7 Objectives 14

1.8 Methodology 15

1.9 Study Sites 16

1.9.1 Industrial (False Creek South) 18

1.9.2 Downtown 18

1.9.3 Residential (Sunset) 20

1.10 Prevailing Climate 23

2 AUTOMOBILE TEMPERATURE TRAVERSES 28
2.1 Introduction 28
2.2 Method 29
2.2.1 Sensor Configurations 29
2.2.2 Sampling Methodology 30
2.2.3 Projected FOV 32
2.2.4 Processing 34
2.3 Surface Emissivity 34
2.4 Everest - AGEMA Scanner Comparisons 39
2.5 Temperature Distributions 41
2.5.1 Traverse Configuration 1 41
2.5.2 Traverse Configuration 2. 46
2.5.3 Modelled Temperature Distributions 46
2.6 Summary 57

3 AVERAGE TEMPERATURES OF CANYON FACETS 59
3.1 Distribution Truncation 59
3.1.1 Surface/air Temperature Relations in the Study Areas 61
3.1.1.1 Industrial Area 61
3.1.1.2 Downtown 65
3.1.1.3 Residential 66
3.1.2 Results 68
3.1.2.1 Industrial Study Area 68
3.1.2.2 Downtown 70
3.1.2.3 Residential Area 75
3.2 Mixed Distribution Modelling 75

3.2.1 Road Surface Temperature 79
3.2.2 Wall Surface Temperatures 85
3.2.3 A Single Model for Canyon Facets 95
3.3 Summary 95

4 AIRBORNE TIR OF SELECTED LAND-USE AREAS 98

4.1 Introduction 98
4.2 Methods 99
4.2.1 Thermal Imaging System 99
4.2.2 Helicopter-AGEMA Installation 100
4.2.3 Remote Sensing Flights 101
4.3 Atmospheric Corrections 104
4.4 Surface Temperature Analysis 104
4.4.1 Industrial Area 104
4.4.2 Residential 116
4.4.3 Downtown 126
4.4.4 Summary 129
4.5 Modelling the Distribution of Surface Temperature 131
4.5.1 Introduction 131
4.5.2 Modelling a Simple Case 132
4.5.3 Modelling Road Surface Temperatures 132
4.5.4 Modelling the Study Area Distributions 138
4.5.4.1 Temperature Frequency Distributions 138
4.5.4.2 Frequency Distribution Differences 143
4.5.4.3 Summary 149
4.6 Surface Temperature Anisotropy 150

4.6.1 Observational Results 150
4.6.2 Comparison with Other Surfaces 158
4.6.3 Scale of Anisotropy 161
4.6.4 Anisotropy Relative to Other Influences Upon Remotely Sensed Surface Temperature 163

5 THE COMPLETE URBAN SURFACE TEMPERATURE 167

5.1 Definition of the Complete Urban Surface 167
5.1.1 Estimating the Complete Surface Area 168
5.1.1.1 Buildings 168
5.1.1.2 Trees 169
5.1.1.3 Horizontal 172
5.1.1.4 Top-of-Canopy Plan Area 173
5.1.1.5 Complete Surface Area 173
5.1.2 Complete Surface Areas of the Study Sites 173
5.1.2.1 Industrial 173
5.1.2.2 Downtown 175
5.1.2.3 Residential 176
5.2 A Complete Urban Surface Temperature 184
5.2.1 Definitions 184
5.2.2 Estimating the Complete Surface Temperature 185
5.2.2.1 Nadir Airborne and Traverse Temperature Distributions 185
5.2.2.2 Nadir and Off-nadir airborne 187
5.3 Comparison of Complete and Incomplete Surface Temperatures 189
5.3.1 Industrial Area 189
5.3.2 Downtown Area 193

5.3.3 Residential Area 199
5.4 Surface and Air Temperature Relations 203
5.5 Summary 208

6 MODELLING URBAN SURFACE THERMAL EMISSIONS 209

6.1 Introduction 209
6.2 Geometric Models to Estimate Longwave Surface Anisotropy 209
6.2.1 Extension to Urban Surfaces 210
6.3 Model Description 210
6.4 An Energy Balance Model to Estimate Surface Temperatures 216
6.4.1 Urban Surface Temperature Models 216
6.4.2 The Myrup 1-D Surface Energy Balance Model 217
6.4.3 Modifications to the Myrup Model 220
6.5 Model Tests Against Observations 223
6.5.1 Road surface temperatures 224
6.5.1.1 Sensitivity Analysis 224
6.5.1.2 Industrial 228
6.5.1.3 Residential 230
6.5.1.4 Downtown 230
6.5.2 Roof Temperatures 232
6.5.3 Grass Surfaces 234
6.5.4 Facet Temperatures 236
6.5.4.1 An Individual Building 236
6.5.4.2 Canyon Facets in the Study Areas 238
6.6 Summary 245
6.7 Application of the SC Model 246

6.7.1 Application to the Study Areas: Overflight Days 246
6.7.1.1 Downtown 247
6.7.1.2 Industrial 250
6.7.1.3 Residential 255
6.7.2 Summary 259

7 CONCLUSIONS **260**
7.1 Summary of Conclusions 260
7.2 Suggestions for Future Work 264

References **267**

A AGEMA 880 LWB INFRARED SCANNER **280**
A.1 Instrument Description 280
A.2 Instrument Theory 282
A.3 Instrument Calibration 285
A.4 Radiance-Photon-Temperature Relations 288
A.5 Spectral Response Considerations 290
A.5.1 Introduction 290
A.5.2 LOWTRAN 7 Parameters 290
A.5.3 Results 293
A.6 Conclusions 294

B ATMOSPHERIC CORRECTIONS OF THERMAL IMAGERY **295**
B.1 Introduction 295
B.2 Methodology 296
B.3 LOWTRAN 7 Atmospheric Radiation Model 297
B.4 Composite Atmospheric Profiles 298

B.4.1 Local Radiosonde Profiles 298
B.4.2 Climatological Radiosonde Profiles 300
B.4.3 Climatological Data 305
B.5 Airborne Imagery vs. Surface-Based Measurements 306
B.5.1 Discussion 313
B.5.1.1 Sea Surface Temperatures 320
B.5.1.2 Grass Temperatures 323

C EVEREST INTERSCIENCE MODEL 4000A IRT 325
C.1 Instrument Description. 325
C.2 Instrument Operation 325
C.3 Instrument Calibration 328

D TIR REMOTE SENSING COVERAGE OF THE STUDY AREAS 331

List of Tables

1.1 Summary of past urban TIR remote sensing studies. 2

1.2 Examples of observed longwave anisotropy over agricultural and forest surfaces. 12

2.1 Sampling intervals per urban surface structural unit. 32

2.2 Surface emissivities for surface materials in urban areas. 35

2.3 View factors for the mid-point on the floor of a canyon and a point low on the canyon wall for canyon H/W representative of the three study areas. 36

2.4 Facet temperatures (estimated from traverse data for the Industrial study area) with calculated apparent temperature for wall 2 using canyons with H:W = 1:1 and 1:2. 37

2.5 Difference between true and apparent wall temperatures at select times for a H:W = 1:4 canyon. 38

2.6 Model parameters used in EIRT distribution modelling. 53

2.7 Model parameters for EIRT distribution modelling. 55

3.1 Description of symbols used in Figures 3.2, 3.3 and 3.4. 62

3.2 Temperature distributions assigned to a simple model of EIRT response, and results from mixed distribution modelling on the EIRT model output. 94

4.1 Flights conducted to acquire airborne thermal imagery. 103

4.2 Comparison of component temperature distributions for an image of a simple scale model. 134

4.3 Percentage of the FOV occupied by component surfaces of a N-S transect in the Industrial area. 144
4.4 Temperature differences between means for pairs of view directions. . . . 156
4.5 Magnitude of temperature differences produced by processes affecting remote thermal measurement of an urban surface. 164
4.6 Satellite parameters for satellites commonly used in thermal analysis of urban areas. 166

5.1 Definition of area component symbols. 168
5.2 Major surface component areas and percentages of the complete surface area for the Industrial area. 174
5.3 Major surface component areas and percentages of the complete surface area for the Downtown area. 176
5.4 Building types in the Residential study area. 179
5.5 Statistical summary of estimated tree structural parameters. 183
5.6 Major surface component areas and percentages of the complete surface area for the Residential area. 183

6.1 User input required for the SC model. 214
6.2 Myrup model input requirements. 218
6.3 Myrup model output. 219
6.4 Base input parameters: asphalt sensitivity tests. 226
6.5 Reference values of asphalt thermal properties used in the Myrup model. 228
6.6 Model input: Summer Equipment building facets. 236
6.7 Model input: Industrial, Downtown and Residential Sites. 238
6.8 SC model surface parameters for the Study areas. 246

A.1 Technical specifications: AGEMA 880 LWB TIR system. 282
A.2 Scanner constants: AGEMA THV880 LWB (AGEMA, 1991) 284
A.3 LOWTRAN 7 input parameter summary. 292
A.4 Sensor normalized photon emissions calculated from LOWTRAN 7 radiance estimates. 293

B.1 Local radiosonde (Airsonde) launch times and maximum altitude. *est.* indicates maximum altitude was estimated based upon assumed ascent rate and comparison of temperature and humidity profiles with other flights. 299
B.2 Summary of radiosonde data collected. 306
B.3 Summary of reporting differences for radiosonde measurements. 308
B.4 Ground calibration sites and surface types sampled 309
B.5 Surface emissivities for ground calibration surfaces. 318
B.6 Reported values of ϵ for surface types tested. 319
B.7 Solar position and AGEMA scanner and Everest azimuth angle direction: Flights 1–5. 322

C.1 Everest Interscience Model 4000A Infrared Transducer Specifications. . . 325
C.2 EIRT calibration results. 329

List of Figures

1.1 Various definitions of the urban surface. 8

1.2 Length scales used to simplify and generalize the three-dimensional urban surface. 9

1.3 Location of the three study areas within the city of Vancouver, B.C. . . . 17

1.4 The Industrial area. 19

1.5 The Downtown study area. 21

1.6 The Residential study area. 22

1.7 Pacific Weather Centre surface analysis for August 15, 1992. 24

1.8 Pacific Weather Centre surface analysis for August 16, 1992. 25

1.9 Pacific Weather Centre surface analysis for August 17, 1992. 26

1.10 General weather conditions on the three study days: August 15 - 17, 1992. 27

2.1 Traverse configurations used to sample surface temperatures. 29

2.2 The traverse vehicle outfitted in traverse configuration 2. 31

2.3 Projected EIRT FOV dimensions and overlaps. 33

2.4 Vertical transect of T_r up the face of a north-facing wall of a glass-clad office building. 39

2.5 Surface temperature time series using EIRT and AGEMA scanner. 40

2.6 Apparent surface temperature distributions for the AGEMA scanner and EIRT obtained from the traverse tests. 42

2.7 Frequency distributions of T_r obtained during a mid-morning traverse of the Industrial study area. 44

2.8 North and south facet temperature distributions in alleys and streets in the Industrial area. 45
2.9 Facet temperature distributions for streets and alleys in the Residential area. Note variation in frequency scales. 47
2.10 Frequency distributions of T_r from the right-facing EIRT obtained during a mid-morning traverse of the Downtown study area. 48
2.11 Frequency distributions of T_r from the left-facing EIRT obtained during a mid-morning traverse of the Downtown study area. 49
2.12 Cumulative frequency distribution of building heights for Downtown (traversed northeast facets only) and Industrial (north street and alley facets). 50
2.13 Modelled and measured EIRT temperature distributions for north facets during a mid-morning traverse in the Industrial study area. 51
2.14 Modelled and observed EIRT temperature distributions for a mid-morning traverse in the Downtown study area (Southwest facets only). 52
2.15 Modelled and observed 10° left-facing EIRT temperature distributions for a mid-morning traverse in the Industrial study area. 56

3.1 Temporal variation of canyon floor surface temperatures in an E/W street canyon compared with 0.5 m air temperature. 60
3.2 North-facing alley facet temperatures and air temperatures in the Industrial study area. 63
3.3 Subset of northeast-facing facet and air temperatures in the Downtown study area. 65
3.4 Subset of north-facing facet and air temperatures in the Residential study area. 67

3.5 Mean facet temperatures and standard deviations following distribution truncation in the Industrial study area. 69
3.6 Mean facet temperatures of each street in the Industrial study area. . . . 71
3.7 Mean facet temperatures and standard deviations following distribution truncation in the Downtown study area. 72
3.8 Mean facet temperatures of blocks or block sequences in the Downtown study area. 73
3.9 Mean facet temperatures of blocks or block sequences in the Downtown study area for each EIRT. 74
3.10 Mean facet temperatures and standard deviations following distribution truncation in the Residential study area. 76
3.11 Mean facet temperatures of each street in the Residential study area. . . 77
3.12 Temperature distribution from a satellite image. 78
3.13 Distribution of T_{road} in the Industrial study area. 81
3.14 T_{road} statistics for the component populations derived from mixed distribution modelling for the Industrial area. 82
3.15 T_{road} statistics derived from mixed distribution modelling for the Downtown study area. 83
3.16 T_{road} statistics derived from mixed distribution modelling for the Residential study area. 84
3.17 Morning east-facing facet temperature distribution with component populations from the Industrial study area. 86
3.18 Late-afternoon, west-facing facet temperature distribution and component populations from the Industrial study area. 87
3.19 Morning southeast-facing facet temperature distribution from the Downtown study area. 88

3.20 Facet surface temperature statistics derived from mixed distribution modelling for the Industrial study area. 89
3.21 Facet surface temperature statistics derived from mixed distribution modelling for the Downtown study area. 90
3.22 Facet surface temperature statistics derived from mixed distribution modelling for the Residential study area. 92

4.1 AGEMA 880 system components. 99
4.2 Thermal imaging system installed in the helicopter. 100
4.3 Scanner mounting arrangement. 102
4.4 Thermal image of the Industrial study area. 105
4.5 Apparent surface temperature distributions for each view direction over the Industrial area during Flight 1. 107
4.6 Modelled composite temperature distribution. 109
4.7 Broadening of the apparent surface temperature distribution. 110
4.8 Comparison of apparent surface temperature distributions before and after images with a non-standard block orientation or surface cover were removed. 111
4.9 Same as Figure 1.5 except for Flight 2. 113
4.10 Same as Figure 1.5 except for Flight 3. 114
4.11 Temporal development of the distribution of T_r as indicated by the difference between surface and canyon level air temperature. Industrial area. 115
4.12 Thermal image of the Residential study area, Flight 7. 117
4.13 Surface temperature frequency distributions for the three flights over the Residential study area. 118
4.14 Same as Figure 1.5 except for Flight 7 over the Residential study area. . 120

4.15 Comparison of T_r distributions for morning flights over the Industrial and Residential study areas. 121
4.16 Same as Figure 1.15 except for early afternoon flights. 122
4.17 Same as Figure 1.15 except for late afternoon flights. 123
4.18 Comparison of T_r distributions for two primary block orientations in the Residential study area. 125
4.19 Thermal image of the Downtown study area. 126
4.20 Same as Figure 1.5 except for Flight 4 over the Downtown study area. . . 128
4.21 Comparison of T_r distributions for the Downtown, Industrial, and Residential areas. 129
4.22 Same as Figure 1.20 except for early (Downtown) and late afternoon flights (Industrial and Residential areas). 130
4.23 Temperature frequency distribution for a concrete scale model representing the Residential area. 133
4.24 Transects of apparent surface temperature across shadow boundaries. . . 135
4.25 Fitted distributions to road surface temperatures. 137
4.26 Fitted component distributions to Flight 2 over the Industrial area. . . . 139
4.27 Summary of fitted and observed distributions applied to the morning flight over the Industrial area. 140
4.28 Same as 1.27 except for Flights 2, 4, and 7. 141
4.29 Summary of fitted distributions applied to temperature frequency differences for the morning flight over the Industrial area. 145
4.30 Same as Figure 1.29 except for: Flights 2, 4, and 7. 147
4.31 Distribution of image mean apparent temperature for nadir and opposing view directions over the Industrial study area. 151
4.32 Same as Figure 1.31 except for the Downtown study area. 152

4.33 Same as Figure 1.31 except over the Residential study area. 153
4.34 Mean apparent surface temperature and standard error of each view direction for each flight. 155
4.35 Calculated mean apparent temperatures and standard errors of each view direction at the TOA for NOAA-11 AVHRR Channel 4. 159

5.1 Illustration of component areas. 167
5.2 Definition of tree structural parameters. 170
5.3 Modelled shapes for the tree types in the study area. 171
5.4 Building heights (stories); Industrial study area. 174
5.5 Frequency distribution of building heights in the Industrial study area. . 175
5.6 Building heights (stories); Downtown study area. 177
5.7 Frequency distribution of building heights in the Downtown study area. . 178
5.8 Building heights (stories); Residential study area. 180
5.9 Frequency distributions of estimated building structural parameters (Residential area). 181
5.10 Frequency distributions for the estimated tree structural parameters (Residential area). 182
5.11 Component and composite surface temperature frequency distributions. . 186
5.12 Traverse and image-extracted vertical facet temperature distributions: Flight 1, Industrial area. 188
5.13 Estimated T_c distributions; Industrial area. 190
5.14 Traverse and image-extracted vertical facet temperature distributions; Flight 2, Industrial area. 191
5.15 Traverse and image-extracted vertical facet temperature distributions; Flight 3, Industrial area. 192

5.16 Component temperature distributions (from vehicle traverses); Industrial area. 194
5.17 Complete and off-nadir apparent surface temperature distributions; Industrial area. 195
5.18 T_c distributions; Downtown study area. 196
5.19 Traverse and image-extracted vertical facet temperature distributions; Downtown study area. 197
5.20 Traverse and image-extracted vertical facet temperature distributions; Downtown study area. 198
5.21 Apparent surface temperature distributions from traverse and image sources for building walls and trees; Flight 6, Residential area. 199
5.22 Estimated T_c distributions; Residential area. 201
5.23 Apparent tree canopy temperatures extracted from off-nadir imagery; Residential area. 202
5.24 Comparison of mean image apparent surface temperatures by view direction, traverse air temperatures (T_{at}, denoted by solid diamonds), and complete apparent surface temperatures (T_{c_1}, solid triangles labelled C) for all study areas. 204
5.25 T_{at} compared with the lowest modelled temperature distribution fitted to the composite frequency distribution. 206
5.26 Same as Figure 5.25 except showing means only, and with data subdivided into shaded and sunlit facets. 207

6.1 Two-dimensional model representation of an urban surface showing input dimensions. 211
6.2 Detail of the component angles calculated in the SC model. 212

6.3 Example of SC model output. 215
6.4 Sensitivity of K↓ to D and w. 222
6.5 K↓ differences and w. 223
6.6 Observed and modelled incoming global solar irradiance for August 15, 1992.224
6.7 Comparison of mid-facet estimates of net shortwave radiation (K^*) generated using the mid-point model and the Arnfield (1982) canyon radiation routines. 225
6.8 Comparison of mid-facet and facet average estimates of K^* generated using the mid-point model and the Arnfield (1982) canyon radiation routines. . 226
6.9 Sensitivity analysis of asphalt road surface temperature. 227
6.10 Modelled and observed T_{road} in the Industrial study area. 229
6.11 Modelled and observed T_{road} in the Residential study area. 230
6.12 Modelled and observed T_{road} in the Downtown study area. 232
6.13 Roof surface temperatures. 233
6.14 Modelled and measured surface temperatures and net radiation for a grass surface in Trafalgar Park. 235
6.15 Modelled and observed surface temperatures for the Summer Equipment site (Industrial area). 237
6.16 Comparison of modelled and traverse facet temperature for the Industrial study area. 239
6.17 Comparison of modelled canyon facet temperatures obtained using hourly and daily input data (Industrial area). 241
6.18 Comparison of modelled and traverse facet temperature for the Downtown study area. 242
6.19 Estimated temporal variations of shadow ratio for vertical facets in the Residential area. 243

6.20 Comparison of modelled and traverse facet temperature for the Residential study area. 244
6.21 Surface profiles for the NE portion of the Downtown study area. 248
6.22 Surface proportions viewed: Downtown, Flight 4. 249
6.23 Modelled AGEMA scanner temperature for the Downtown study area. . . 251
6.24 Surface profiles for the Industrial study area. 252
6.25 Modelled temperature seen by the AGEMA scanner for the Industrial study area including along-canyon building spacing. 253
6.26 Modelled temperature seen by the AGEMA scanner temperature for the Industrial study area, Flight 2. 255
6.27 Surface profiles for the Residential study area. 256
6.28 Modelled temperature seen by the AGEMA scanner for the Industrial study area, Flight 6. 257
6.29 Modelled AGEMA scanner temperature for the Industrial study area, Flight 7. 258

A.1 AGEMA 880 LWB system response. Data supplied by Linnander (*pers. comm.*). 281
A.2 UBC Soil Science blackbody calibration facility. 285
A.3 Relative position of the image mode for complete and subset areas of the calibration images. 287
A.4 Comparison of AGEMA scanner temperature with average blackbody cavity temperature. (a) Calibration plot, (b) Temperature differences. 288
A.5 Relation between AGEMA Thermal Value and photon emission over the calibration range. 289

A.6 Ratio of reflected solar radiance to Earth-emitted radiance for three surface emissivities. 291

B.1 Atmospheric profiles of temperature and humidity for each flight. 301

B.2 Location of the Vancouver study area and upper air reporting stations Port Hardy, B.C. (YZT) and Quillayute, WA (UIL). 305

B.3 Comparison of the LOWTRAN 7 Midlatitude summer atmosphere model with measured profiles from station YZT. 307

B.4 Look-up table plots of atmospheric corrections. 311

B.5 Comparison of ground-sampled T_r with corrected AGEMA scanner T_r; Flights 1–12. 314

B.6 Modelled variations in apparent radiative surface temperature for a 60° FOV Everest IRT viewing a water surface. 321

C.1 Radiant power distribution received by EIRT from a surface. 326

C.2 Block diagram of EIRT. 327

C.3 Temperature differences due to conversion of T_{ev} from $\epsilon_{ev} = 0.98$ to 1.00 and differences due to using T_{det} ±1,2,5°C in place of T_{det}. 330

D.1 Study areas in Vancouver, B.C. 332

D.2 Scanned areas (by direction) and composites for Flight 1. 333

D.3 Scanned areas (by direction) and composites for Flight 2. 334

D.4 Scanned areas (by direction) and composites for Flight 3. 335

D.5 Scanned areas (by direction) and composites for Flight 4. 336

D.6 Scanned areas (by direction) and composites for Flight 5. 337

D.7 Scanned areas (by direction) and composites for Flight 6. 338

D.8 Scanned areas (by direction) and composites for Flight 7. 339

D.9 Scanned areas (by direction) and composites for Flight 8. 340

List of Symbols and Abbreviations

ABBREVIATIONS

A/D	Analog to digital
AVHRR	Advanced Very High Resolution Radiometer
EIRT	Everest Infra-red Transducer
FOV	Field of View
GRE	Ground Resolution Element
H:W	building height to street width ratio
HCMM	Heat Capacity Mapping Mission
HCMR	Heat Capacity Mapping Radiometer
IFOV	Instantaneous field of view
ITOS	Improved TIROS Operational Satellite
LAT	Local Apparent (Solar) Time
LDT	Local Daylight Time
LST	Local Standard Time
LN	Liquid nitrogen
LUT	Look-up table
LWB	Longwave Band (Scanner type used with AGEMA system)
LAI	Leaf area index

MSS	Multispectral scanner
NOAA	National Oceanic and Atmospheric Administration
PDT	Pacific Daylight Time
RMS	root mean square
SC	sensor-surface model (modified from Sobrino and Caselles (1990))
SR	Scanning radiometer
SST	Sea surface temperature
SUHI	Surface urban heat island
TIR	Thermal Infra-red
TIROS	Thermal Infrared Operational Satellite
TM	Thermal Mapper (of the Landsat satellite)
UBL	Urban Boundary Layer
UCL	Urban canopy layer
UHI	Urban heat island
YD	Year day

SYMBOLS

Areas	(m^2)
A_b	building area (roof + wall)
A_c	complete surface area
A_L	Lot area
A_o	horizontal ground-level area

A_p	plan area
A_{pr}	plan or apparent roof area
A_{pv}	plan (apparent) vegetation area
A_r	roof area
A_v	vegetation area (3-D)
A_w	wall area
B_L	building length (m)
C	subsurface volumetric heat capacity (J m^{-3} K^{-1})
c	ellipse semi-axis (Chapter 5)
c	speed of light (2.998×10^8 m s^{-1})
D	dust particles (cm^{-3})
DPD	Dewpoint depression (°C)
E	adjusted voltage for EIRT calculations (mV)
F_{hf}	fraction of total foilage height (m)
F_{gap}	ratio between 3-D vegetation area and geometric canopy bounding area
f	fractional component
H	building height (m)
h	Planck's constant (6.6262×10^{-34} J s)
h_f	total foilage height (m)
h_r	height of maximum crown radius (m)
h_t	tree height (m)

h_{tk}	vegetation trunk height (m)
h_s	sensor height (m)
IU	isotherm units (AGEMA system)
$iups$	AGEMA internal constant
$K\downarrow$	incoming global shortwave radiation (W m^{-2})
$K\uparrow$	reflected global shortwave radiation (W m^{-2})
K^*	net shortwave radiation (W m^{-2})
k	Boltzmann's constant (1.281×10^{-23} J K^{-1})
L	radiance (W m^{-2} sr^{-1})
L_c	radiance of the complete surface
L_s	sensor detected radiance
L_o	surface blackbody radiance
L_{sky}	hemispheric incoming sky radiance at the ground
L_a	atmospheric path emission (radiance)
L_s	sensor-detected radiance
L_{ev}	EIRT-detected radiance
L_{ag}	AGEMA-detected radiance
n	counter
n_A	Alley counter (SC model)
n_S	street counter (SC model)
P	photon emission (Photons s^{-2} cm^{-2} sr^{-1})

$P(\lambda, T)$	spectral photon emission for specified temperature
P_{scan}	AGEMA scanner normalized photon emission (Photons s^{-2} cm^{-2} sr^{-1})
P_{solar}	AGEMA scanner-detected photon emission due to reflected shortwave radiation (Photons s^{-2} cm^{-2} sr^{-1})
Q	energy of a photon (J)
Q^*	net radiation (W $m^{-}2$)
R_c	actual emitted radiation (W $m^{-}2$)
R_p	EIRT measured apparent radiation
RH	Relative Humidity (%)
r_c	maximum crown radius (m)
SV	sample values
T	temperature (°C or K)
TV	thermal values (IU)
T_a	air temperature
T_c	complete apparent surface temperature
T_{c_1}	complete surface temperature estimated using traverse facet temperature data
T_{c_2}	complete surface temperature estimated using image-extracted facet temperature data
T_{cav}	blackbody calibration cavity temperature
T_d	dewpoint temperature
T_{det}	detector temperature

T_{ev}	EIRT apparent temperature
T_{mod}	modelled temperature distribution
T_o	thermodynamic (kinetic) surface temperature
T_r	apparent surface temperature
T_{sky}	apparent (radiative) sky temperature
ΔT_{u-r}	urban rural temperature difference
V_{scan}	AGEMA scanner voltage (V)
W	street width (m)
W_S	street width (SC Model) (m)
W_{Ap}	alley width (SC Model) (m)
w	precipitable water (mm)
X	distance from sensor sub-point to beginning of IFOV (m)
z	length of (truncated) lower vegetation ellipse semi-axes (m)
Z	Solar zenith angle
z_o	surface roughness (m)
z_{max}	maximum radiosonde reporting height (m)

Greek

α	albedo
γ_g	angular portion of IFOV occupied by ground
γ_r	angular portion of IFOV occupied by roofs
γ_w	angular portion of IFOV occupied by walls

γ_{x_e}	end angle for x component angle calculation
γ_{x_s}	start angle for x component angle calculation
Δ	difference
ϵ	emissivity
θ	sensor view angle from nadir
$\hat{\theta}$	angle between normal to the surface (of arbitrary slope) and the solar beam
κ	subsurface thermal diffusivity ($m^2\ s^{-1}$)
λ	wavelength (μm)
ρ	reflection coefficient
σ	standard deviation
τ	atmospheric-path transmission
$\Phi(\lambda)$	relative instrument spectral response with wavelength
ϕ	Solar azimuth angle
ϕ_c	canyon azimuth angle
ϕ_s	sensor azimuth angle
ψ	view factor
ψ_s	sky view factor

Miscellaneous

$^\circ$	degree
$\hat{}$	spatial average

$\bar{}$	mean

Subscripts

a	air
c	complete (height of FOV centre; Chapter 2)
f	canyon floor (fixed site - second subscript; Chapter 2)
g	ground team
h	FOV height (Chapter 2)
t	traverse
w	canyon wall (FOV width; Chapter 2)

Acknowledgements

Without the support and assistance of many persons, this thesis could not have been undertaken.

My research supervisor, Dr. T.R. Oke, has shown unwavering support of the project from the beginning, and his encouragement has allowed me to continue to pursue this research through many difficult times. His guidance and teaching have extended beyond the academic realm and have been instrumental in my development as teacher, researcher, and person.

Thanks are also due to the roles played by the other members of my supervisory committee: Dr. P. Austin provided guidance on the atmospheric corrections and the implementation of the LOWTRAN model, as well as enduring all my questions on various aspects of workstation computing. Dr. M. Church provided a thorough review of the thesis draft and gave useful and realistic guidance in the practical matters of completing a thesis when it was most needed. Dr. R. Cole was a continual source of inspiration on the role of building-climate interactions, and our conversations always served to motivate my interest in the field.

A great many other people have helped with various stages of this thesis: Special thanks are due to Dr. S. Grimmond of Indiana University for carrying out the local radiosonde launches, and operating a second energy balance site during the observation programme. Dr. R.Spronken-Smith endured me as a lab-mate for many years and helped out with many of the observational details of the ground-truth programme. Thanks also to Drs. H.P. Schmid and M. Roth for their support and encouragement of this research.

T. Cheong, A. Mclean, T. Newton, B. Rehwald, K. Richards, and S. Smith of UBC

Geography, and M. Demanes of Indiana University provided assistance with the field observations. Pilots Graham, Steve, and Barry of Vancouver Helicopters provided smooth flights and Chris Baille patiently endured the many noise complaints during the remote sensing flights. The Ontario Laser and Lightwave Research Centre made available the AGEMA scanner and Victor Isbrucker provided extensive assistance with the operation of the instrument. Dr. A. Black of the Soil Science Department made available the temperature calibration facility and thanks are due to R. Adams for numerous consultations on the use of the Everest IRT. Jan Skapski applied his technical expertise to the installation of the AGEMA scanner in the helicopter and to the EIRT setup on the traverse vehicle. Vincent Kujala provided significant computer consultations and constructed the primary AGEMA data conversion program.

Funding for this research has been provided to Dr. T.R. Oke by the Natural Sciences and Engineering Research Council of Canada and the Atmospheric Environment Service of Environment Canada. Personal funding for this project was provided by the University of British Columbia Graduate Fellowships, Veterans Affairs Canada, and Teaching and Research Assistantships in the Department of Geography.

Some special friends have helped me to make it through some very difficult periods during the thesis. Thanks are especially due in this regard to T. Cheong, S. Rice and M. Brown. To all the others in the Department with whom I have shared lunch, icetime, or beer, many thanks. My family has provided support throughout this project. To Sandra, whose support and encouragement was immeasurable, and who sacrificed too much to help me, thank you for what you were able to provide. And finally, thanks to S. Fairburn for her encouragement during the final stages of this research.

Chapter 1

INTRODUCTION

1.1 Thermal Infra-red Remote Sensing of Urban Areas

Remote sensors operating in the thermal infra-red (TIR) portion of the electromagnetic spectrum provide detailed and spatially-continuous records of the radiative temperature of urban surfaces, information that would otherwise be difficult to acquire. Surface temperature strongly affects the lowest air layers and thus constitutes an important boundary condition for studies of the behaviour of the urban atmosphere.

TIR remote sensing has been applied to the study of urban climate almost since the advent of the first sensors. In particular, the urban heat island (UHI) phenomenon, long known to be a characteristic of the urban atmosphere, was shown to exist in patterns of surface temperature even by early, coarse resolution satellite imagery (Rao, 1972). Later series of satellite-based sensors including the (A)VHRR (Advanced Very High Resolution Radiometer) on board the NOAA series of satellites, the limited duration HCMR (Heat Capacity Mapping radiometer) carried by the HCMM (Heat Capacity Mapping Mission) satellite, and the Landsat TM (Thermal Mapper) have all been utilized in studies of urban thermal patterns as have numerous aircraft-scanner combinations. A brief summary of some of the published studies is presented in Table 1.1.

These studies focus upon three primary areas. Firstly, the relation between land surface cover and surface brightness temperature as it relates to the surface urban heat island (SUHI); secondly, the relation between remotely-measured surface temperature

Table 1.1: Summary of past urban TIR remote sensing studies. ITOS = Improved TIROS Operational Satellite, NOAA = National Oceanic and Atmospheric Administration, HCMM = Heat Capacity Mapping Mission, SR = Scanning Radiometer, (A)VHRR = (Advanced) Very High Resolution Radiometer, HCMR = Heat Capacity Mapping Radiometer, MSS = Multispectral Scanner, AGEMA = thermal scanner (trade name), TM = Thermal Mapper (on board Landsat), EIRT = Everest Infrared Radiation Transducer. T_r is the apparent surface temperature, T_a air temperature.

Study	Platform	Sensor	Objective
Rao (1972)	ITOS-1	SR	Identification of SUHI (Surface Urban Heat Island) with coarse resolution thermal imagery.
Pease *et al.* (1976)	Aircraft	M7 MSS	Surface energy balance calculation and modelling using thermal imagery.
Carlson *et al.* (1977)	NOAA-3	VHRR	Analysis of urban heating patterns. Surface energy balance calculations from day/night satellite pairs.
Matson *et al.* *(1978)*	NOAA-5	VHRR	Identification of nocturnal SUHI in 50 U.S. cities.
Price (1979)	HCMM	HCMR	Extent and intensity of daytime SUHI in New England.
Matson & Legeckis (1980)	NOAA-5	VHRR	Daytime SUHI analysis of New England cities.
Carlson *et al.* (1981)	HCMM	HCMR	Estimation of surface energy fluxes, moisture availability and thermal inertia using thermal imagery and 1-D boundary layer model.
Foster *et al.* (1981)	HCMM	HCMR	Strength of day/night SUHI in English cities.
Goward (1981)	Aircraft	MSS	Investigates thermal inertia as a cause for UHI.
Artis & Carnahan (1982)	Aircraft	M7 MSS	Variation of roof emissivity in urban areas.
Vukovich (1983)	HCMM	HCMR	Day/night, summer/winter SUHI analyses for St. Louis.
Birnie *et al.* (1984)	Aircraft	MSS	TIR survey.
Hoyano (1984)	Aircraft	MSS	Summer/winter T_r relations with type of residential area, seasonal land coverage changes.

Table 1.1 continued

Study	Platform	Sensor	Objective
Barring *et al.* (1985)	Aircraft	Scanner	Relation between canyon geometry, T_r, and T_a.
Goldreich (1985)	Aircraft	RS-25	Spatial structure of pre-dawn SUHI.
Kidder & Wu (1987)	NOAA-7	AVHRR	SUHI under snow-covered conditions.
Balling & Brazel (1988)	NOAA-9	AVHRR	Relation between land cover and surface thermal patterns.
Schmid (1988)	Aircraft	MSS	Structural analysis of T_r and surface cover.
Lewis & Carlson (1989)	HCMM	HCMR	Analyze spatial variations of energy fluxes, surface moisture availability and thermal inertia; comparison with land surface cover.
Henry *et al.* (1989)	HCMM	HCMR	Compare and model ground-level and traverse T_a, and remote T_r.
Roth *et al.* (1989)	NOAA-7 - 9	AVHRR	Day/night, summer/winter SUHI in three coastal cities.
Dousset (1989)	NOAA-6,7,9,10	AVHRR	Difference between T_r and T_a; study of microclimates.
Carnahan & Larson (1990)	Landsat-5	TM	Analysis of morning urban cool island.
Dousset (1991)	NOAA-6,7,9,10	AVHRR	Examine relation of remotely determined land cover with T_r.
Eliasson (1991)	Helicopter	AGEMA	Relation between T_r, T_a and surface geometry.
Eliasson (1992)	Helicopter	AGEMA	Effect of building geometry upon nighttime T_r.
Kim (1992)	Landsat	TM	Examine causes of urban heating. Energy balance formulation using remotely sensed products.
Stoll & Brazel (1992)	Helicopter	EIRT	T_r and T_a relations; representativeness of ground vs. remote T_r.

Table 1.1 continued

Study	Platform	Sensor	Objective
Gallo *et al.* (1993)	NOAA-11	AVHRR	Assessment of Normalized Difference Vegetation Index (NDVI) as an UHI indicator.
Lee (1993)	NOAA-9, 10	AVHRR	Comparison of satellite T_r with T_a, T_r in South Korea.
Nichol (1994)	Landsat	TM	Use of thermal imagery in tropical city planning.
Quattrochi & Ridd (1994)	Aircraft	TIMS	Variation of thermal response of different urban surface types.
Shoshany *et al.* (1994)	Aircraft	RS-25	Extraction of roof-top areas for UHI analysis.

and screen-level air temperature; and thirdly, the use of remotely-measured surface temperature to estimate surface energy fluxes in conjunction with numerical models. Based upon these studies a number of consistent observations can be made regarding the nature of the SUHI:

- Warmest daytime surface temperatures are found in industrial-commercial land use zones.
- Daytime SUHI is much stronger than the air temperature UHI.
- Daytime SUHI and intra-urban variability of T_r are greatest in the warm season.
- Nocturnal SUHI is weaker than the air temperature UHI.
- Nocturnal SUHI and intra-urban variability of T_r are much smaller than in daytime.
- Strong relation between vegetation, surface moisture and surface temperature patterns.

The results from the numerous studies attempting to relate surface and air temperatures are more difficult to interpret. Lack of correlation between these measurements

has been attributed by Roth *et al.* (1989) to three main factors: lack of simple coupling between the surface and air due to advection in the urban canopy layer (UCL); biased spatial sampling of surface temperature by remote sensors which preferentially view horizontal, unobstructed surfaces; and mismatches in the scales of measurement used. In general, aircraft-based, high-resolution thermal imagery shows better agreement with near surface air temperatures, perhaps because the scales of observation are more closely matched, than when lower resolution satellite imagery is used. Birnie *et al.* (1984), and Balick and Wilson (1980) note that trees display surface temperatures related to the profile of atmospheric temperature, thereby implicitly recognizing that the surfaces obscured may have different temperatures.

Modelling of surface energy balances using remotely-measured radiative surface temperature (Pease *et al.*, 1976; Carlson *et al.*, 1981; Lewis and Carlson, 1989; Kim, 1992) is an example of the inverse problem (Price, 1982, 1989; Becker and Raffy, 1987) in which surface parameters are inferred from the observed temperature, which is itself a function of the radiance measured by the sensor. This technique has been used to derive values of surface thermal inertia for use in geological applications (Kahle *et al.*, 1976; Kahle 1977) and to estimate evaporation from surfaces (see, for example, Huband and Monteith, 1986b; and Taconet *et al.*, 1986). Reviews of the application of remote sensors to determine surface energy fluxes and evaporation are given by Price (1982), Jackson (1988), Choudhury (1989) and Kustas *et al.* (1989).

Studies over urban areas generally find higher sensible heat flux in more built-up areas, and that surface moisture availability exerts strong control on the partitioning of energy fluxes. Spatial patterns of thermal inertia are found to be weak. There has been no validation of such modelling over urban areas, although Pease *et al.* (1976) found maps of modelled and measured surface temperature to be in general agreement. Difficulties in matching the surface represented in the model with that viewed by the

satellite have been advanced as restrictions to the testing of such models (Roth *et al.*, 1989).

1.2 Limitations of TIR remote sensing

The use of remote TIR sensors over any surface presents a unique set of problems which restrict the interpretation and application of the measurements obtained. Among these are:

- atmospheric attenuation of the transmitted radiance and re-emission;
- non-blackbody surface emissivity;
- spatial averaging of the signal over heterogenous surface areas;
- directional variations of the measured radiance (anisotropic radiance distribution; also referred to as anisotropy) which arise due to the form of the surface and the distribution of fluxes emitted (i.e., patterns of surface temperature) and/or reflected by the surface.

Over urban areas, these problems are compounded by the complex nature of the urban surface-atmosphere system: the surface is heterogenous down to relatively small scales, it is composed of a wide variety of materials with a range of radiative properties, it is essentially three-dimensional, and spatial variations in the urban atmosphere complicate atmospheric transmission.

1.3 The Urban Surface

From a climatological perspective, the surface is an important concept. The surface is the site of radiant energy receipt. Properties of the surface control the partitioning and

conversion of the energy received, so the nature of the surface strongly conditions the behaviour of the lowest layers of the urban atmosphere. Specification of surface conditions and properties is thus an important objective for study and to gain understanding of the urban atmosphere.

The complete (or true) urban surface is composed of a myriad of individual surface elements, ranging from a blade of grass or tree leaf to a sidewalk or road. These elements may be combined to form larger component surfaces. The description of the complete urban surface is hindered because of its complexity (Oke, 1984) but this can usually be simplified by considering only some of the elements, combining elements, or generalizing to consider only their macroscopic surface structure. The definition and areal limitation of the urban surface may be dependent upon the process(es) under study and the scale of the investigation, both temporal and spatial (Grimmond, 1988).

Several possible urban surface definitions are presented in Figure 1.1 (Oke, *pers. comm.*). The position of observation may affect the parameterization of the urban surface. For example, a representation of the urban surface from a ground-based observation point may not include roof tops (Figure 1.1b), and that taken from an overhead aerial position may omit vertical surfaces (Figure 1.1d). Very simplified conceptual definitions of the urban surface have been made in order to simplify the urban surface in numerical models. These conceptions differ considerably from the complete surface, and in some cases, they may not actually be true atmosphere/solid interfaces at all (e.g., Figure 1.1e). One-dimensional UBL models often represent the urban surface in this way (e.g., Carlson *et al.*, 1981).

The regular geometric patterns of common elements which characterize urban areas have been used to simplify and generalize the three-dimensional urban surface through the use of various length scales which represent the height, spacing and density of those elements. These are defined for an idealized three-dimensional urban surface in Figure 1.2.

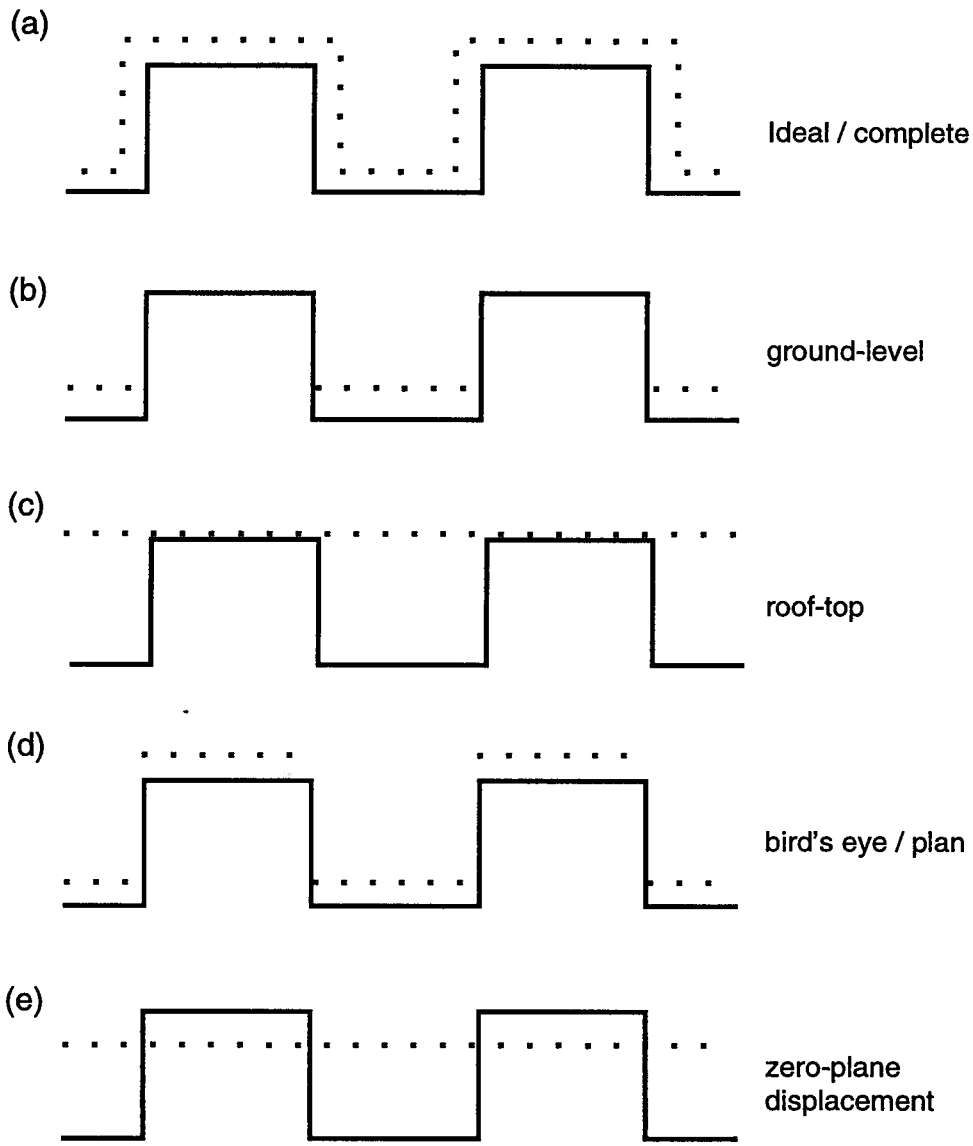

Figure 1.1: Various definitions of the urban surface. (a) ideal/complete, (b) ground-level, (c) roof-top, (d) bird's eye/plan view, (e) zero-plane displacement.

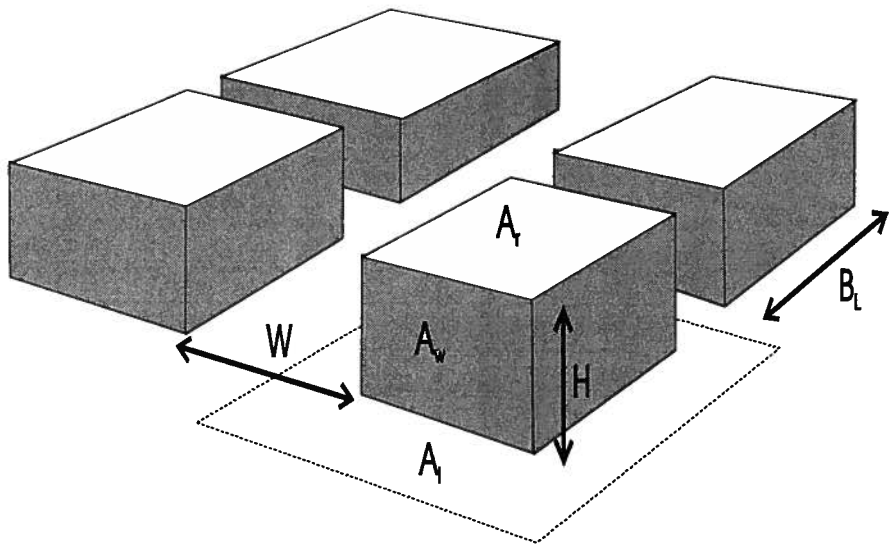

Figure 1.2: Length scales used to simplify and generalize the three-dimensional urban surface: H - building height, W - street width, B_L - building length, A_r - roof (plan) area, A_l - Lot area, A_w - wall area.

1.4 TIR Remote Sensing of the Urban Surface

In order to fully understand remotely-sensed data, an understanding of the surface(s) viewed by the sensor is needed. Over urban areas, the complex three-dimensional nature of the surface poses a difficulty in determining what the sensor views. The qualitative appraisal of Roth *et al.* (1989) suggests there may be potential for significant biases between remotely-observed surface temperature and the complete or "true" surface temperature over urban areas, which actually conditions the urban atmosphere. These biases are likely to arise because remote sensors, when viewing straight downwards (at nadir), preferentially view horizontal surfaces and undersample vertical surfaces and obstructed horizontal surfaces (e.g., beneath tree canopies). Alternatively, for off-nadir viewing angles, a biased subset of vertical surfaces may be included in addition to the plan view.

Resultant biases will also depend upon the Sun-sensor-surface geometry, as this controls the temperature of the various component surfaces. Preferential viewing of surfaces with particular thermal properties (e.g., roofs and tree tops which are characterized by low thermal inertia) can also contribute to potential biases; in the case of low thermal admittance surfaces, the diurnal range of surface temperature will be unduly large.

Understanding directional variations in space and time is therefore important for the interpretation of remotely-sensed measurements and identification of potential biases. It also allows the expansion of spatial and temporal coverage via off-nadir sensing, and may yield improved or additional information about the surfaces viewed (Kimes *et al.*, 1984).

While direct investigation of the existence and magnitude of the suspected biases has not been carried out over urban areas, there have been a number of studies over agricultural and forest canopies to address similar questions. The following section reviews the results of these studies.

1.5 TIR Remote Sensing of Agricultural and Forest Surfaces

Agricultural crops generate composite scenes in remotely-sensed imagery because the sensor's field of view is a mixture of vegetation and substrate components and the regular spacing of row crops lends a three-dimensional structure to the crop surface, not unlike that of a street canyon. In order to infer the properties of a crop, the effects of the different components must be separated. Efforts have been directed to resolving component temperatures of the different surfaces. When near-nadir measurements are taken, the resultant temperature is a composite of the vegetation and soil or substrate material between the rows. Thus the objective, which is to extract vegetation temperature from the composite response, cannot be achieved under most conditions (Kimes and Kirchner 1983). One approach to this problem is to use multiple measurements at different

viewing angles in order to infer attributes of the scene components, and to calculate the directional response of sensors to crop types (Kimes and Kirchner, 1983; Kustas *et al.*, 1990). The multiple measurements are then combined in a modelling framework in which physically-based models of sensor response are devised (Kimes, 1981, 1983; Otterman *et al.*, 1992.)

Sensor-surface relations have been investigated over vegetated surfaces, especially crops and, more recently, forest canopies (Sader, 1986; McGuire *et al.*, 1989). Studies of the response of sensor radiance to view angle, azimuth and crop geometry for different vegetation covers have been conducted by a number of research groups. Reviews of many of the experiments conducted are given by Nielsen *et al.* (1984), Boissard *et al.* (1990) and Paw U (1992). Table 1.2 summarizes the results of a number of studies investigating longwave anisotropy over a variety of agricultural and forest surfaces.

In general, effects of longwave anisotropy giving directional and/or angular variations in apparent radiative temperature are minimized over full-cover, homogenous crop or forest canopies, and are maximized when a row structure dominates. This conclusion supports the suggestion by Roth *et al.* (1989) that such effects may be present over urban areas.

1.6 Modelling of Thermal Emissions over Plant Canopies

The geometrical description of vegetative surface elements used in agricultural studies is more advanced than that of urban surfaces due to the many modelling studies of radiative transfer in vegetation canopies. In detailed vegetation surface parameterizations, canopy leaves may be modelled as randomly distributed elements of a given shape, with prescribed distributions of inclination and orientation angle over a canopy volume, so that probability theory may be used to describe the radiation field statistically (Norman,

Table 1.2: Examples of observed longwave anisotropy over agricultural and forest surfaces. Max. - Maximum observed temperature difference with view direction/angle, RMS - root mean square difference of temperatures, Azim. Max. - maximum difference difference during azimuthal rotation.

Authors	Surface type	Anisotropy			View
		Max.	RMS	Azim Max	angle[a]
Monteith and Szeicz (1962)	Grass	3	1	1	0-80
Fuchs *et al.* (1967)	Sudan grass	0.6	0.3		15-75
	Alfalfa/bromegrass	1.8	0.7		15-75
	Soybeans	1.7	0.7		15-60
Kimes *et al.* (1980,1983)	Cotton rows	16.2			0-80
	Wheat rows	13.0			
	Lodgepole pine	2.2	0.7		5-85
Nielsen *et al.* (1984)	Soybeans			1.5	0-75
Balick and Hutchison (1986)	Oak-hickory forest	7		5-10	0-70
Paw U *et al.* (1989)	Sunflower		0.4	9.3	0-90
McGuire *et al.* (1989)	Oak-hickory forest	3.2		6.8	10-85
Lipton (1992)	Mountainous	3[b]			46-65
	terrain	6[c]			

[a]measured from nadir
[b]realistic viewing conditions
[c]relative bias; 2 satellites

1975). This model type is most useful for homogeneous crop covers (Boissard *et al.*, 1990). The primary structural information needed is the total leaf area per unit soil area in the different canopy layers. This, together with some additional information on stand parameters such as plant distribution and density, can be used to derive the probability of interception or non-interception of radiation by an element in a given layer of vegetation. These probabilities have been used to formulate a thermal infra-red exitance model of a plant canopy (Kimes *et al.*, 1981). The Kimes *et al.* (1981) model has been extended and refined by Smith *et al.* (1981) and McGuire *et al.* (1989) to incorporate the variation of the probability of interception due to changes in view angle and azimuth (although the three-dimensional surface function was not actually incorporated in the model).

Still more complex models of radiative transfer in plant canopies, using a weighted-random approach, are available (e.g., Norman and Welles, 1983) which combine probability theory with a simplified geometric representation of individual vegetation elements (such as spheres, ellipsoids etc.) in order to model discontinuous vegetation canopies.

From an energy-balance approach, a number of models are available which can estimate longwave emissions. The simplest of these are single or multiple-layer "big-leaf" models which can be used to describe anisotropic emissions. Complex models coupling parameterized plant canopy turbulence and energy budgets with view angle geometry have also been developed (Paw U *et al.,* 1985).

In contrast, very simplified abstractions of vegetative surfaces have been made by Sutherland and Bartholic (1977), Kimes and Kirchner (1983), and Caselles and Sobrino (1989) in considering thermal radiance models of orchards and row crops. These studies use extended rectangular surfaces to represent the overall vegetation structure. These so called "geometric projection models" combine canopy structure information and component temperatures with a given remote sensor IFOV (Instantaneous Field of View) to model apparent sensor temperature.

Geometric projection models have been devised by Jackson *et al.* (1979), Kimes *et al.* (1981) and Caselles and Sobrino (1989). Kimes and Kirchner (1983) have validated a simplified version of the Jackson *et al.* (1979) model. Agreement between measured and modelled sensor response was within 1°C RMS deviation. The Caselles and Sobrino (1989) model is used to derive the temperature of oranges in an orchard using thermal information from the different components of the orange grove, and is used for frost prediction purposes.

Geometric projection models can be used to optimize the directional view of sensors for specific canopy structures and to investigate optimal inversion strategies for inferring component temperatures (Kimes, 1983; Kimes and Kirchner, 1983). Geometric projection models form an appropriate basis for developing a model for urban surfaces, due to the similarities exhibited between crop row structures and urban canyons. The development of such a model is detailed in Chapter 6 of this thesis.

1.7 Objectives

The overall objective of this thesis is to investigate how the three-dimensional form of the urban surface temperature distribution affects observations of radiative surface temperature by thermal infra-red remote sensors. Specific objectives of this research are to:

1. collect direct observations of the temperatures of vertical surfaces (typically undersampled in remotely sensed data) in selected urban areas, and characterize their spatial and temporal variations;

2. compile complete (or "true") three-dimensional surface temperature information for selected urban land-use areas;

3. use thermal remote sensing observations over selected urban land-use areas to determine the extent of directional variations (anisotropy) of urban surface thermal emissions;

4. investigate the suitability of available two-dimensional geometric projection models to the prediction of apparent sensor temperature for remote sensors viewing typical urban surfaces.

1.8 Methodology

The objectives set out in Section 1.7 are implemented using an intensive observational programme of selected sites in Vancouver, B.C. The observational programme consists of three main components.

1. Remote observation of urban surface temperature, at different viewing angles and azimuths, using a portable thermal scanner carried on board a helicopter. These observations were made at times when preliminary ground-based data suggested the potential for maximum variation.

2. Mobile sampling of the surface temperatures of vertical building facets using vehicle-mounted infra-red transducers. Traverses were made on a regular basis throughout the daytime period to determine the heating and cooling patterns on the different facet orientations. Traverses also monitored road surface temperature and in-canyon air temperature (at a height of approximately 1.5 m).

3. Sampling of component surface temperatures with hand-held infra-red thermometers by ground teams, to determine the variation of temperature at the microscale at the time of remote sensing data acquisition.

In addition, a number of supporting observations were made or obtained including:

- the vertical profile of atmospheric pressure, temperature and humidity in order to allow correction of the remote thermal imagery for atmospheric absorption and re-emission;
- surface temperature measurements of homogeneous calibration surfaces for comparison with remote observations;
- emissivity measurements of the calibration surfaces;
- concurrent surface energy balance measurements (at two sites);
- thermal satellite imagery (NOAA-11) as available.

To support model development, and for comparison with observations over the study sites, a brief scale modelling exercise using concrete blocks to represent buildings was performed. In this component of the study, the thermal scanner was mounted on a mobile platform and viewed simple surface geometries constructed in an open, flat parking lot.

1.9 Study Sites

The observational programme was carried out using three primary study areas within the city of Vancouver, B.C. (Figure 1.3).

The sites were chosen based upon a number of considerations including:

- the importance of the surface type as a fraction of the total urban area, (and implicitly, its associated weight with respect to its influence upon the urban atmosphere);
- variations in the magnitude of surface structure as expressed by measures such as the plan to active surface area, and street height to width (H:W) ratios;
- areas where topographic surface variations are small with respect to the urban surface structure;

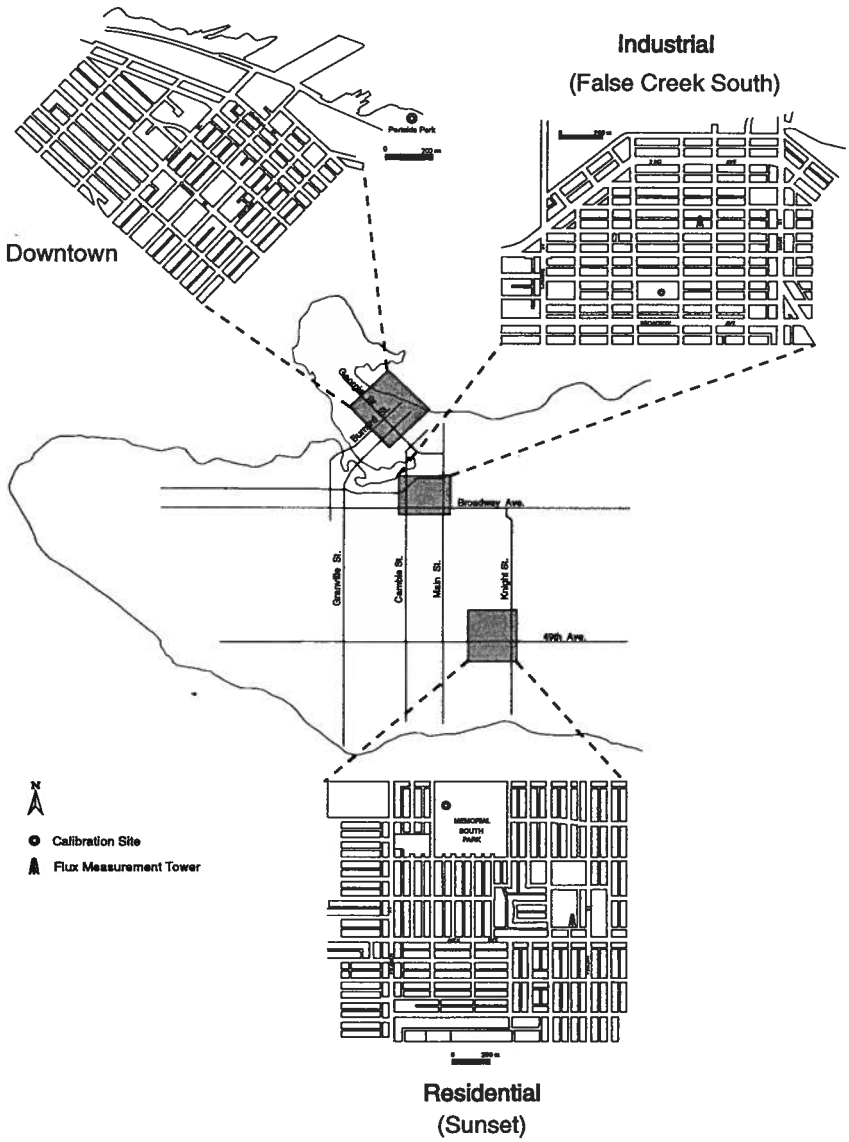

Figure 1.3: Location of the three study areas within the city of Vancouver, B.C.

- the ability to define a representative sample of the surface for detailed study. For example, the representative area concept introduced by Schmid (1988) for residential land use types in which the contribution to the total variance attributed to specific surface structures is analyzed;
- structural simplicity of the surface structure; a real surface is selected to closely resemble model surface representations in order to provide a link between the modelling and observational components. Such a surface is characterized by box-like buildings with fairly homogeneous facet material distributions, a lack of vegetation and a regular surface geometry;
- previous remote sensing coverage, database development, or coincident parallel research.

1.9.1 Industrial (False Creek South)

This area is an inner city light industrial district of fairly limited extent (Figure 1.4).

The area is typified by very rectangular, flat topped buildings of between 1 and 3 stories. Commonly, buildings adjoin one another and are arranged on blocks with their long axis oriented E-W. Blocks are separated by relatively wide streets. Alleyways parallel the long axis of the block. There is very little vegetation, particularly trees, which leads to relatively simple geometric street canyon configurations. The topography shows a gentle slope trending upwards to the SE.

1.9.2 Downtown

The downtown study area fulfills the requirement for an area with very large vertical development where vertical walls become a large fraction of the total surface area (Figure 1.5).

Figure 1.4: The Industrial study area (False Creek South). View is to the west.

Building heights approach 150 m for some office towers. Building facades are complex, and contain large amounts of glass. Large office towers dominate the southern part of the study area while blocks to the north are characterized by older, adjoining 5 - 7 story buildings. Blocks are oriented NE-SW with some square blocks and some with their long axis in the NE-SW direction. Some blocks are characterized by NE-SW alleyways. Vegetation in the form of trees is fairly prevalent along the streets, although for the most part it is immature. The topography slopes downwards to the water in a NE direction.

1.9.3 Residential (Sunset)

The Sunset area is an urban residential neighbourhood located in South Vancouver with some commercial and institutional developments interspersed, particularly along major streets (Figure 1.6).

The housing is primarily 1 or 2 story detached dwellings, relatively closely spaced along the street. In the area most extensively studied for this project, two block orientations are present; an E-W long axis alignment south of 49th Ave, and a N-S long axis alignment north of 49th. Buildings are set back significantly from the street and garages border alleyways which divide the blocks along their long axis. Roofs generally have a shallow pitch; many have a simple peak roof with the long axis perpendicular to the block axis. Vegetation of all forms is extensive.

The Sunset study area has a long history as the base for many local atmospheric studies (Steyn, 1980; Schmid, 1988; Grimmond, 1988; Roth, 1989) and is the location of a free-standing tower used as an instrument platform for those studies.

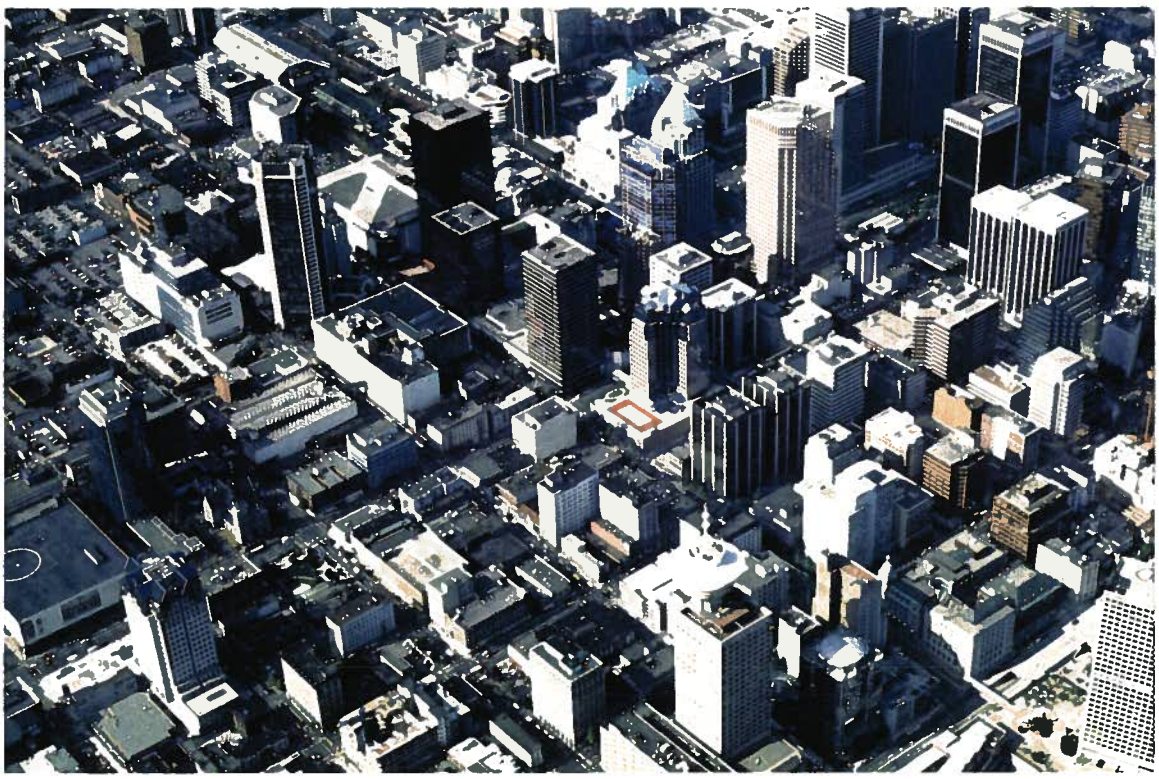

Figure 1.5: The Downtown study area. View is to the west.

Figure 1.6: The Residential study area (Sunset). View is to the northwest.

1.10 Prevailing Climate

The Vancouver area is characterized in summer by persistent anticyclonic systems which yield extended periods of fine weather suitable for remote sensing work. Surface analyses for the primary study period of August 15-17 1992 are presented in Figures 1.7, 1.8, 1.9. During this period an offshore ridge of high pressure gave rise to clear skies and a synoptically induced northwesterly flow at the surface.

Local observations of radiation, temperature and wind (Figure 1.10) show practically identical radiation regimes for the three study days.

Incident shortwave radiation at the surface approaches 850 W m^{-2} and daytime net radiation (taken from a 22 m tower in the Residential area) is close to 500 W m^{-2}. Air temperatures from two of the study sites (measured at 9 m and 10 m at the Industrial, and Residential sites respectively) and the Vancouver airport (screen-level observations) show the third day to be somewhat warmer than the first two, especially in the Residential area and the second day to be slightly cooler than the first. August 15 shows evidence of a local seabreeze development with evening and morning easterly winds shifting to westerly or southwesterly in the afternoon and remaining steady until evening. August 16 is characterized by a stronger northwesterly flow influenced by a steepening of the coastal pressure gradient associated with the offshore ridge and inland low pressure areas (Figure 1.8). August 17 shows daytime winds from a more westerly or southerwesterly direction (especially at the residential site) and with lower velocities than for August 16.

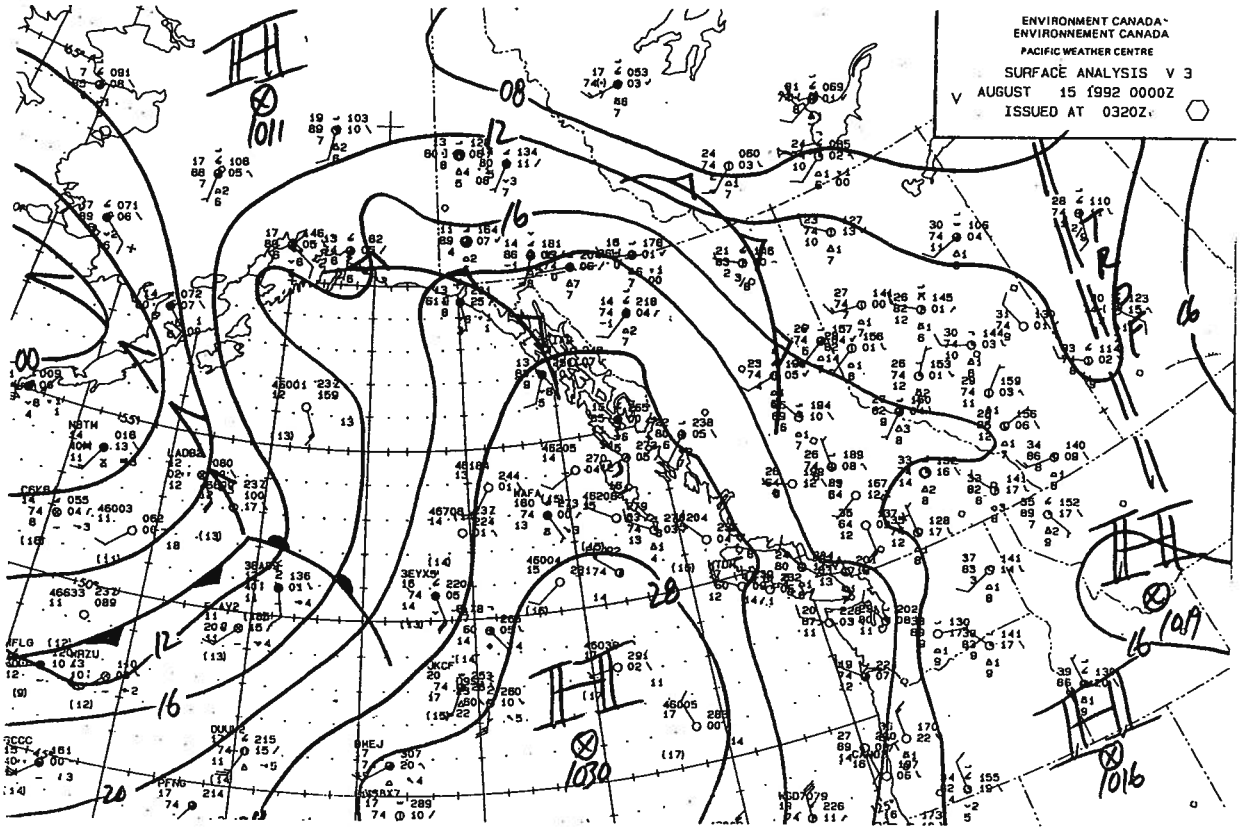

Figure 1.7: Pacific Weather Centre surface analysis for August 15, 1992.

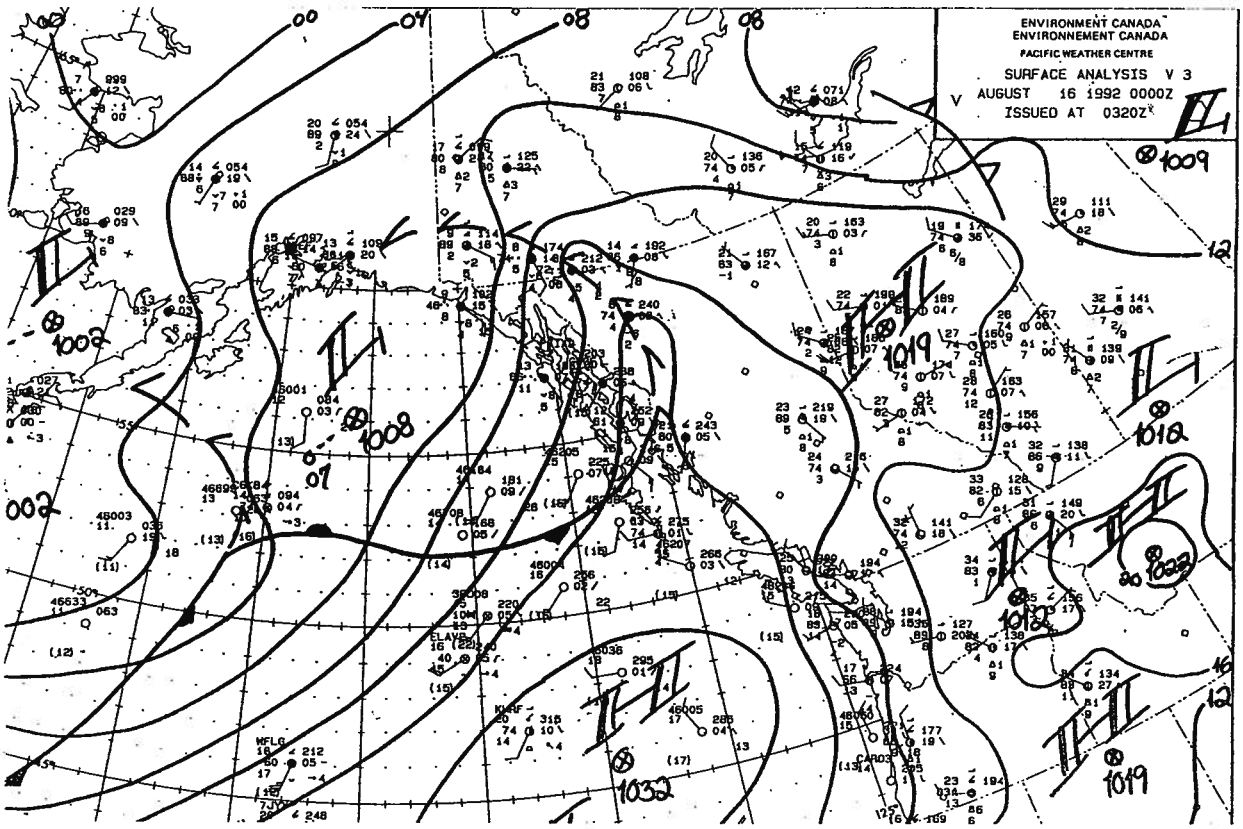

Figure 1.8: Pacific Weather Centre surface analysis for August 16, 1992.

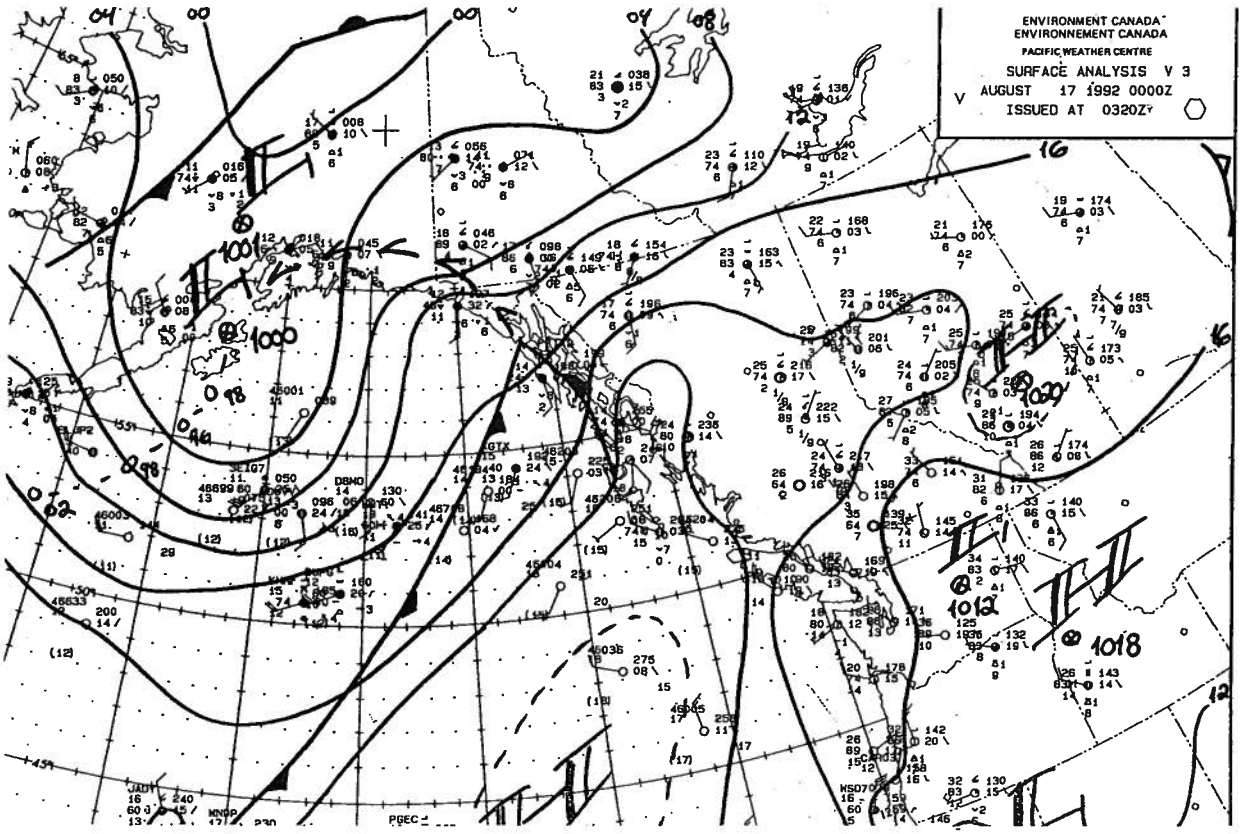

Figure 1.9: Pacific Weather Centre surface analysis for August 17, 1992.

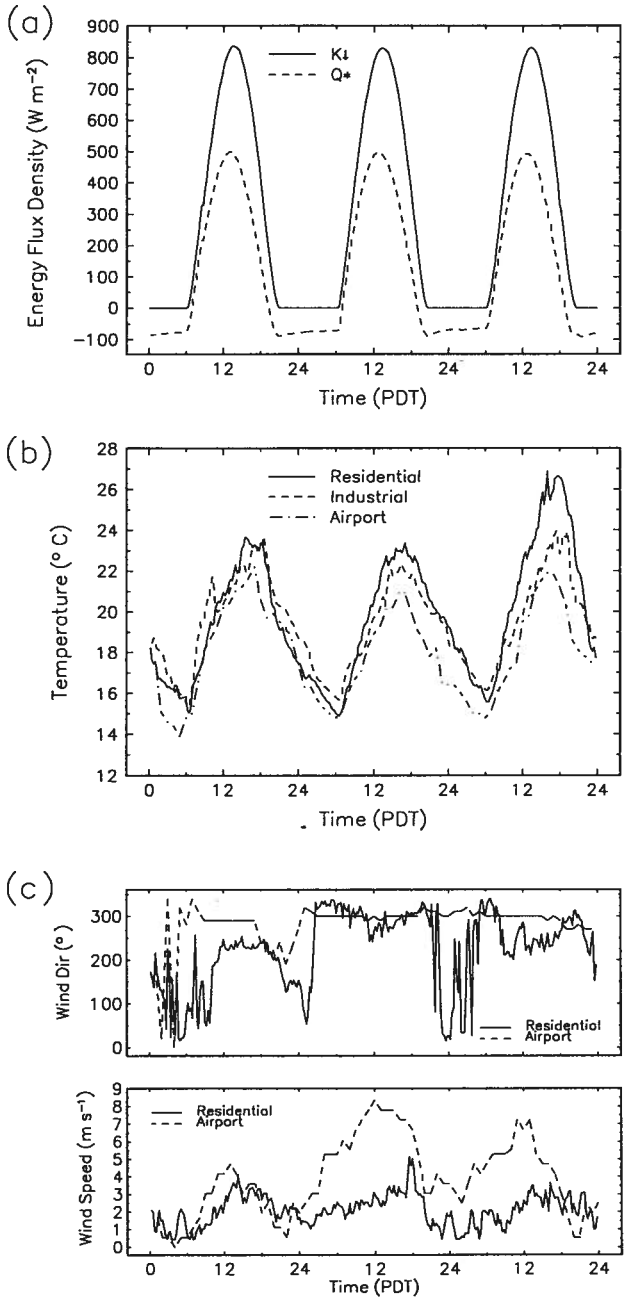

Figure 1.10: General weather conditions on the three study days: August 15 - 17, 1992. (a) incident shortwave radiation and net radiation from the Residential site, (b) air temperatures (Residential - 10 m, Industrial - 9 m, airport - 1.5 m), (c) windspeed and direction (10 m).

Chapter 2

AUTOMOBILE TEMPERATURE TRAVERSES

2.1 Introduction

This chapter presents the aims, methodology, and results of vehicle surface temperature traverses. The primary aim of the traverses is to specify, for a particular land use area, typical surface temperatures of the vertical building facets (i.e., walls), surfaces which are often undersampled in remotely-sensed imagery. In addition, the roadway surface temperature and UCL air temperature (at approximately 2 m) were also monitored during the traverses.

Traverses were conducted along major streets and alleyways in order to obtain representative samples from a range of buildings. Traverses were designed so that all major facet orientations (4 are assumed) were sampled. Stratification of the data by facet orientation allows identification of times when strong azimuthal variations in surface temperature between different facets occur. This information is used to schedule remote sensing missions at times when differences of observed temperature with view direction are maximized.

Facet orientations are defined by their relative position to the centre of a building (e.g., the east wall faces east), which appears to be the most conventional definition. Note however, that if the point of observation is within a street canyon, it is not unreasonable to define facet orientations with respect to the canyon centre; (e.g., the north canyon facet is actually a south-facing building wall). For consistency and to reduce confusion

the former definition is used throughout this thesis.

2.2 Method

2.2.1 Sensor Configurations

Surface temperature measurements were made using an array of 15° FOV infrared transducers (Everest Interscience Model 4000A, hereafter referred to as EIRT) mounted on a pickup truck. Technical details of the EIRT are provided in Appendix C.

Two primary configurations were employed (Figures 2.1 and 2.2): in the first, 4 EIRTs were mounted facing to one side of the vehicle at angles of 0, 15, 30, and 45° above the horizontal. The second had two pairs of EIRTs at angles of 0 and 10-15° mounted facing outwards to the right and left. Both configurations also have a single EIRT facing to the rear and downward (at approximately 45° below the horizontal) to measure road surface temperature, and a shielded and aspirated thermocouple (26 - 30 awg) to monitor air temperature.

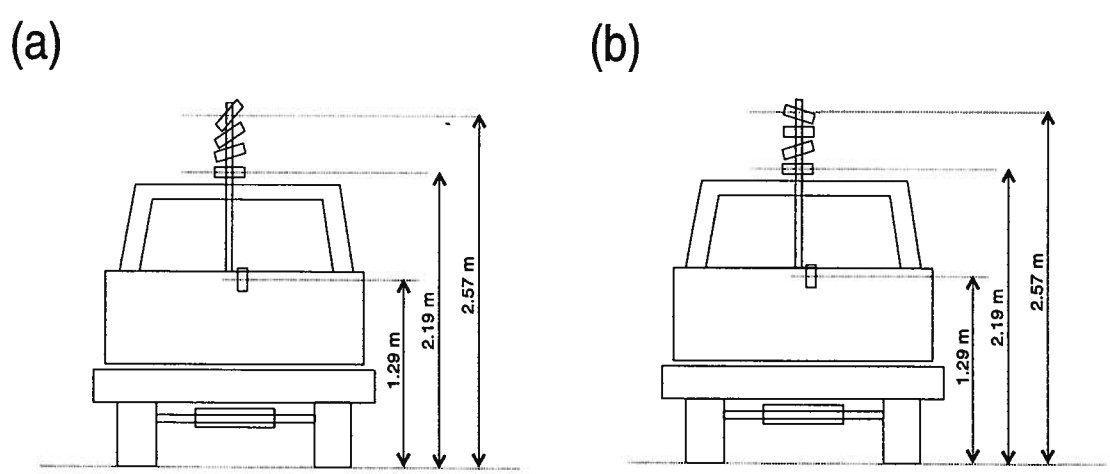

Figure 2.1: Traverse configurations used to sample surface temperatures. (a) configuration 1, (b) configuration 2.

The first configuration is optimized for use in urban areas characterized by large H:W street canyons. This configuration obtains temperatures from only one canyon facet and therefore requires two traverses to obtain complete canyon facet temperature information. The second configuration allows expanded coverage, or more frequent traverse intervals within areas characterized by low H:W street canyons.

2.2.2 Sampling Methodology

A wheel-mounted magnet-sensor array interfaced with a Campbell Scientific (CS) 21X datalogger was used to generate digital pulses at a rate of one per full revolution of the truck wheels. Surface temperatures were sampled when the accumulated pulse count reached a pre-set number. The minimum spatial sampling interval is set by the circumference of the wheel, nominally 2.38 m. The magnet-sensor array and datalogger sampling interval limit the maximum useful traverse speed to approximately 60 km hr^{-1}. However, the EIRTs have an internal calibration procedure which obscures the field of view each 0.5 s for 0.25 s during which the temperature value is not updated. This limits the maximum traverse speed to 17 km hr^{-1} when one sample per wheel rotation is desired. Generally, traverses were conducted with sampling conducted after every second wheel rotation, allowing traverse speeds of approximately 34 km hr^{-1}, i.e., samples spaced at 4.76 m. The number of samples obtained for different structural units of the urban surface in the three study areas is outlined in Table 2.1. A written record of the truck position and time during traverse was kept, with entries made at the start and end of each street, or alleyway. To more closely establish position along the street a digital record was kept by toggling a switch on the datalogger when the truck was in an intersection between blocks. This procedure also allows those observations to be removed from the record if desired, although, as will be demonstrated later, lag in the response of the instrument results in the displacement of within-intersection temperatures to outside the flagged boundaries.

Figure 2.2: The traverse vehicle outfitted in traverse configuration 2.

Table 2.1: Sampling intervals per urban surface structural unit.

Study Area	Structural Unit	Sampling Intervals per structural unit
Residential	building	2
	block	40 (N/S), 30-40 (E/W)
Downtown	building	2 - 4
	block	17, 32
Industrial	building	2 - 4
	block	17 (N/S), 37 (E/W)

2.2.3 Projected FOV

When the EIRT FOV is projected onto street canyon walls, the area viewed is that of an ellipse. In the limiting case of the horizontal EIRT the projected FOV is a circle (if the ground surface is not "seen"). The size and elongation of the ellipses increase with sensor angle above the horizontal (Figure 2.3a). Ellipse dimensions for the sensor to surface distances along the traverse routes are presented in Figure 2.3b. As the building set-back distance increases, overlaps between adjacent samples can occur, otherwise adjacent samples are separated by gaps (Figure 2.3c). Because of the manner in which an EIRT operates, the portrayal of the FOV as an ellipse is true only for a stationary sensor. With movement, the signal is obtained as the FOV moves across the building facets during the time the EIRT optical aperature is open for viewing (0.250 s each 0.5 s, see Appendix C).

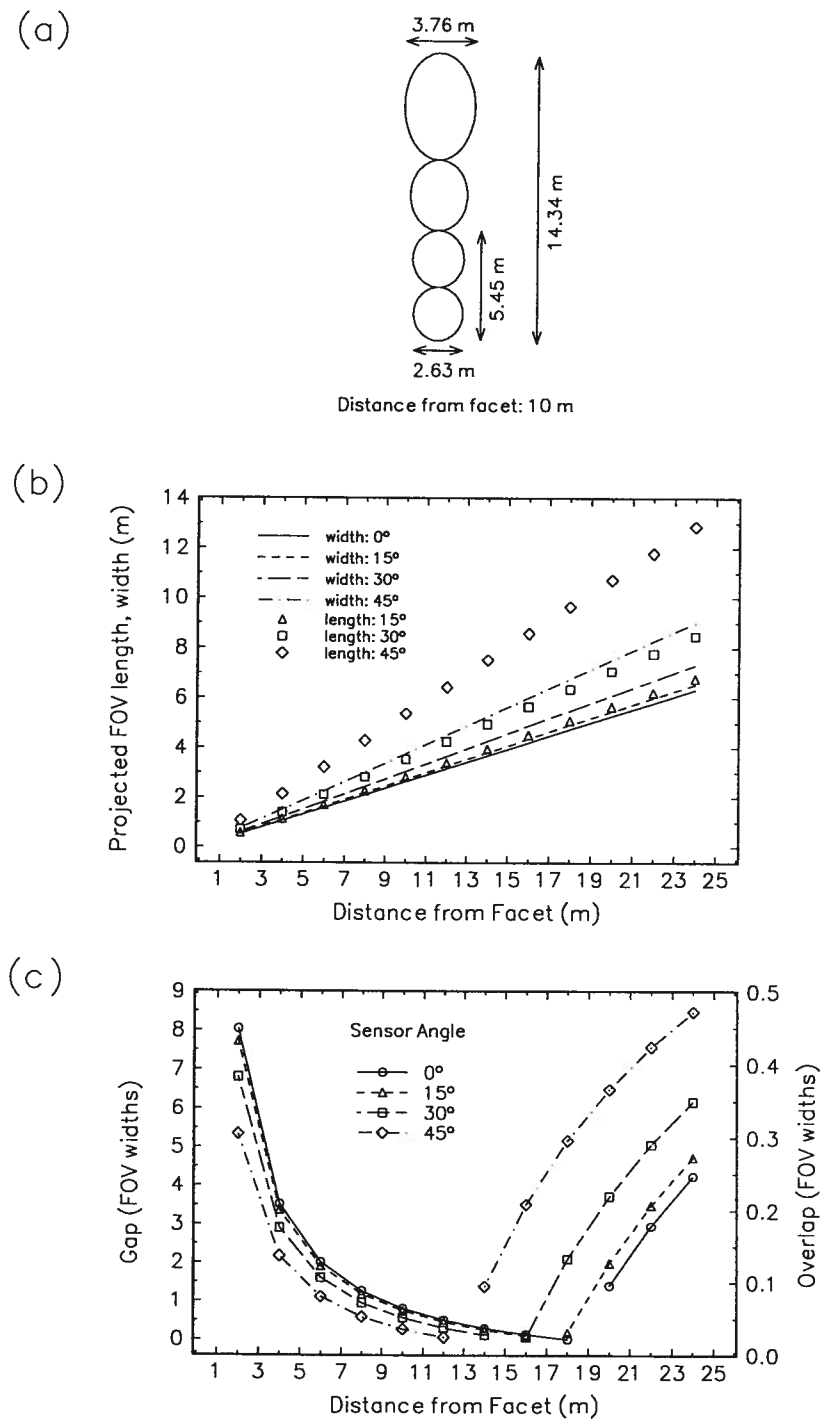

Figure 2.3: (a) Projected EIRT FOV for traverse configuration 1 and 10 m from wall. (b) Projected FOV dimensions with distance from facet. (c) Projected FOV gaps (left) and overlaps (right) for given sensor-facet distances.

2.2.4 Processing

The data were corrected using calibration information for each EIRT. The record was also checked to ensure samples were not taken more frequently than that limited by the chopper frequency. Samples taken at more frequent intervals were considered as "missing" values and assigned a code. The written traverse record was used to search for the nearest actual sampled value and a file (navigation file) was created of those times, street positions, and facet orientations viewed. Using the navigation file and the cleaned data file, the data were separated according to facet orientation.

2.3 Surface Emissivity

Naturally occuring surfaces have emissivities less than unity. Therefore, measurements made using thermal infrared radiometers incorporate both thermal emissions from the surface and reflected radiance. The range of emissivities in urban areas is relatively large due to the variety of surface materials used in building construction. In general we may expect to view surfaces with emissivities ranging from 0.7 or less, for window materials with special coatings, to 0.98 or higher for some painted surfaces and vegetation. Table 2.2 presents a summary of the emissivities present in urban areas according to values in the literature. When infrared surface temperatures of a horizontal surface are viewed from above, surface emissivities less than unity lower the apparent surface temperature (T_r). This arises because the source of reflected radiance is primarily the sky (assuming the surface is relatively unobstructed and behaves as a diffuse reflector). This is typical of airborne or spaceborne observations of surface temperature over relatively flat areas. In urban areas, horizontal within-canyon surfaces have an reduced sky view factor (ψ_s), so that radiance emitted from buildings replaces that from the sky. The reduction in surface brightness temperature is therefore less, because some sources of reflected radiance have

Table 2.2: Surface emissivities for surface materials in urban areas. After Oke (1987); additions from Arnfield (1982).

Surface Material	emissivity, ϵ
concrete	0.71 - 0.9
asphalt	0.95
brick	0.9 - 0.92
stone	0.85 - 0.95
wood	0.9
glass	0.87-0.94 zenith angles<40°
	0.87-0.92 40° < Z <80°
paint: black	0.9 - 0.98
paint: white, red, brown, green	0.85 - 0.95
roofing shingles	0.9 - 0.92
tar-gravel roof	0.92
tile roof	0.90
slate roof	0.90
yard (90% lawn, 10% soil)	0.968
short grass	0.97 - 0.99
urban areas	0.85 - 0.96; average 0.95

a radiative temperature close to that of the surface viewed. Another way to interpret this effect is to consider the canyon to increase the effective ϵ of the system due to internal multiple reflections (e.g., Sutherland and Bartholic, 1977; Arnfield, 1982; Caselles *et al.* 1992). For the case of vertical canyon facets viewed from a position low within the canyon, the source of incident radiance upon the facet includes significant portions from the ground (canyon floor), the opposite canyon wall, and relatively less from the sky (Table 2.3). The canyon H:W data of Table 2.3 are representative of the three study areas: the Residential values are H:W 1:4–1:2 and the Industrial area values are H:W 1:2–1:1 for streets and alleyways respectively. The Downtown area has H:W ratios which vary significantly; values for several of the canyons traversed ranged from 1:1-2:1.

Table 2.3: View factors for the mid-point on the floor of a canyon and a point low (3 m above floor) on the canyon wall for canyon H/W representative of the three study areas (for a discussion see text). Canyon widths are 25 m (H:W 1:1, 2:1), 35 m, (H:W 1:4), 20 m (H/W 1:2).

View factor	Canyon H:W			
	1:4	1:2	1:1	2:1
of walls for floor	0.10	0.30	0.55	0.75
of sky for floor	0.90	0.70	0.45	0.25
of floor for wall	0.45	0.43	0.44	0.44
of opposite wall for wall	0.12	0.24	0.39	0.50
of sky for wall	0.43	0.33	0.17	0.06

To determine the effect of $\epsilon < 1$ on the traverse measurements, view factors typical of the canyon geometries in the study areas are calculated and surface temperatures assigned based upon an examination of the initial temperature histograms. Using these temperatures as "true" values and applying different ϵ, the wall T_r is calculated including

a single reflection event from the other canyon facets.

Results for canyons typical of the Industrial study area (Table 2.4) mostly show T_r decreases, but some increases occur when the EIRT views a cool wall and the opposing wall is hot. Differences vary with time and facet orientation. As canyon H:W decreases,

Table 2.4: Facet temperatures (estimated from traverse data for the Industrial study area) with calculated apparent temperature for wall 2 using canyons with H:W = 1:1 and 1:2. Apparent sky temperature, (T_{sky}) is set at −20°C, $\epsilon = 0.95$ all facets. T_{ow1}, T_{ow2}, T_{of} are the true temperatures of wall 1,2 and the canyon floor respectively. T_{rw2} is the calculated apparent temperature for wall 2.

Time	Wall Pair	T_{ow1}	T_{ow2}	T_{of}	T_{rw2} H:W = 1:1	δT_{rw2}	T_{rw2} H:W = 1:2
0745	S-N	17	22	17	21.5	+0.5	21.2
	N-S	22	17	17	16.8	+0.2	16.5
	E-W	19	19	18	18.7	+0.3	18.4
1035	N-S	26	21	32	21.0	0.0	20.7
	S-N	21	26	32	25.7	+0.3	25.4
	E-W	21	32	32	31.4	+0.6	31.2
	W-E	32	21	32	21.2	-0.2	20.8
1405	N-S	35	23	44	23.4	-0.4	23.0
	S-N	23	35	44	34.6	+0.4	34.3
	E-W	28	26	42	26.1	-0.1	25.7
	W-E	26	28	42	27.9	+0.1	27.6
1740	N-S	25	24	39	24.0	0.0	23.7
	S-N	24	25	39	25.0	0.0	24.7
	E-W	26	22	36	22.1	-0.1	21.8
	W-E	22	26	36	25.8	+0.2	25.5

T_r values are generally less than true surface temperatures (T_o), due to the greater ψ_s. The decrease in T_r with lower H:W may be somewhat offset in heavily vegetated areas

where the overall canyon ϵ may be higher (Table 2.5).

Table 2.5: Difference between true and apparent wall temperatures at select times for a H:W = 1:4 canyon (typical of the Residential area) for $\epsilon_1 = 0.95$ and $\epsilon_2 = 0.97$. Input temperatures obtained from traverse data.

Time	ΔT_{ϵ_1}	ΔT_{ϵ_2}	Time	ΔT_{ϵ_1}	ΔT_{ϵ_2}	Time	ΔT_{ϵ_1}	ΔT_{ϵ_2}	Facet Pair
0830	0.7	0.4	1030	0.4-0.7	0.3-0.4	1330	0.6-0.7	0.3-0.4	N-S
	0.8	0.5		0.7-0.9	0.4-0.5		0.9-1.0	0.5-0.6	S-N
	1.0	0.6		1.0-1.1	0.6-0.7		0.8-0.9	0.4-0.5	E-W
	0.7	0.4		0.5-0.7	0.3-0.4		0.7-0.8	0.4-0.5	W-E

A case where ϵ effects could lead to substantially lower T_r arises with specular reflection of sky radiance from the facets of buildings (especially the Downtown site) for the EIRT mounted at 30° and 45°. This effect has also been observed in other field studies (Verseghy and Munro, 1989). Figure 2.4 presents a transect of temperatures at increasing elevation angles, using a hand-held IRT with a narrow FOV, for an office tower clad in copper-coloured reflective glass.

Correction of surface temperatures for ϵ on a point by point basis is impossible because the ϵ of the viewed surface is unknown, the temperature of the surroundings must be estimated, and the exact canyon geometry is usually unknown. Application of emissivity corrections is deferred until summary statistics of apparent temperature for each facet are available. Then, using the mean apparent temperatures for opposing facets, an estimated sky radiant temperature, and approximate values for canyon floor temperature and canyon geometry, the actual emitted radiation of a facet is estimated using

$$R_{c_{w2}} = \frac{1}{\epsilon_{w2}}[R_{p_{w2}} - (1-\epsilon_{w2})(R_{p_{w1}}\psi_{w1,w2} + R_{p_{sky}}\psi_{sky,w2} + R_{p_f}\psi_{f,w2})] \qquad (2.1)$$

where R_p is the apparent radiation determined from the apparent temperature measurements made by the EIRT, R_c is the actual emitted radiation, and ψ are view factors

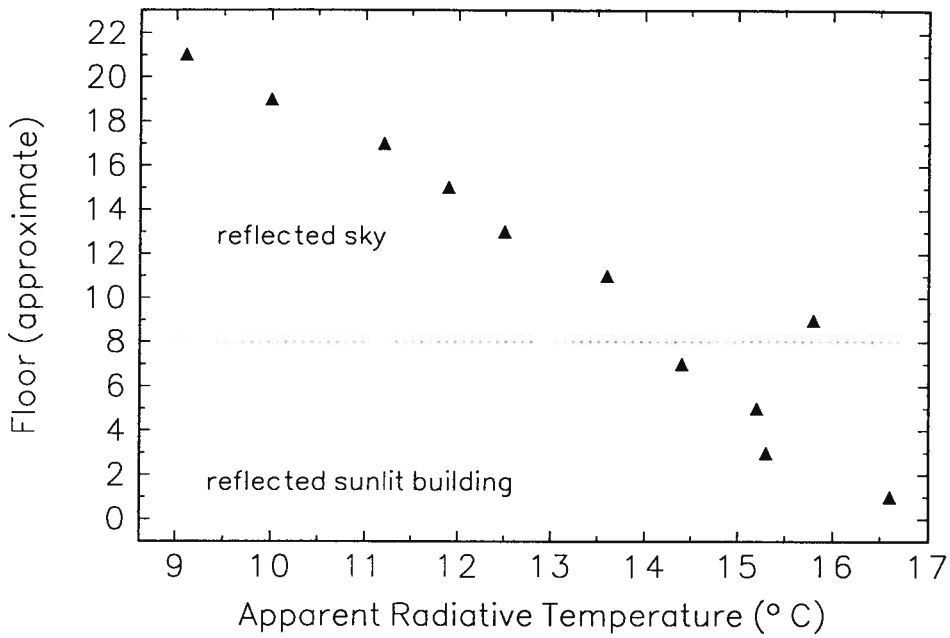

Figure 2.4: Vertical transect of T_r up the face of a north-facing wall of a glass-clad office building.

of the first subscripted facet for the second subscripted facet. Facet designators are w_1 and w_2 for wall 1 and 2 respectively, f for the canyon floor, and sky for the sky. Radiation values are calculated using the Laguerre-Gauss quadrature method (Johnson and Branstetter, 1974) and T_o determined from R_c are obtained by interpolation in a pre-calculated look-up table.

2.4 Everest - AGEMA Scanner Comparisons

A limited number of short traverses were conducted in which the AGEMA THV 880 LWB scanner used for acquiring airborne measurements was placed alongside an EIRT mounted on the traverse vehicle. Various tests were conducted; those described here utilize a sampling frequency of 12.5 Hz for the AGEMA scanner and a single pulse interval for

the EIRT sampling. EIRT observations more frequent than the 0.5 s limit are discarded from the analysis. The AGEMA scanner output (140 × 140 pixels) is averaged over the image with the EIRT FOV weighting applied to the image. Comparison of the time series from the two instruments (Figure 2.5 shows a short section of one such test) demonstrates generally good agreement, although the EIRT response is slightly lagged. The presence of a lag is important only if the temperature value measured is to be related to structure on the ground. For example, the elimination of samples taken during passage through intersections may result in the removal of some observations near the start of the intersection which actually apply to buildings sensed just prior to the intersection. The EIRT tends to underestimate (overestimate) the highest (lowest) scanner values.

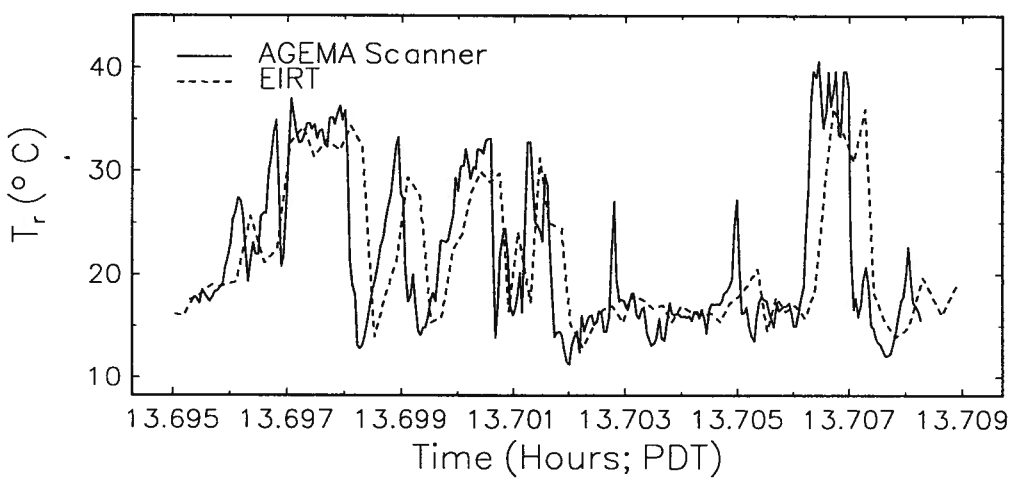

Figure 2.5: Surface temperature time series using EIRT (dashed line) and AGEMA scanner (solid line).

Where these are related to small surface features, they are not picked up in the EIRT trace. However the response to features of the scale of typical buildings is, in most cases replicated by the EIRT. Distributions of sampled temperatures for the AGEMA scanner and EIRT for two traverses (Figure 2.6) show generally good agreement. It was expected

that the AGEMA, with its slightly smaller FOV and fast sampling period, would show greater frequencies at high and low temperature classes relative to the EIRT. There is some evidence of this, but it is not strong, and based upon the tests conducted, the EIRT is accepted as providing an adequate representation of the vertical surface facet temperature.

2.5 Temperature Distributions

2.5.1 Traverse Configuration 1

The traverse system samples temperatures, irrespective of the position of the projected FOV at the sampling time. Thus, samples often include combinations of surfaces, including the sky. Plotting traverse results in the form of distributions illustrates this effect. In Figure 2.7 results are separated by facet orientation (panels a - d), and further broken down into the angle of the EIRT, and the side to which the EIRT was facing with respect to the direction of the traverse (left or right; recall that two EIRT are oriented in each direction in traverse configuration 1; Figure 2.1). Also plotted is the distribution of air temperatures (broken down into classes of 0.25°).

A common feature of the four plots is the presence of a bimodal distribution with a small peak at temperatures between 0–12°C and a larger peak at higher temperatures. The cooler set is interpreted as originating from samples taken when a large portion of the projected FOV is occupied by sky. The warmer set is comprised of samples which view non-sky surfaces; here assumed to be primarily vertical surfaces. The shape of the warmer distribution varies with facet orientation. Shaded facets (north facets (a)) are characterized by narrow, sharply peaked T_r distributions. Facets exposed to direct beam solar radiation show a dramatic increase in the range of surface temperatures. In this case, sunlit or shaded surface possibilities exist resulting in a broad peak of temperatures

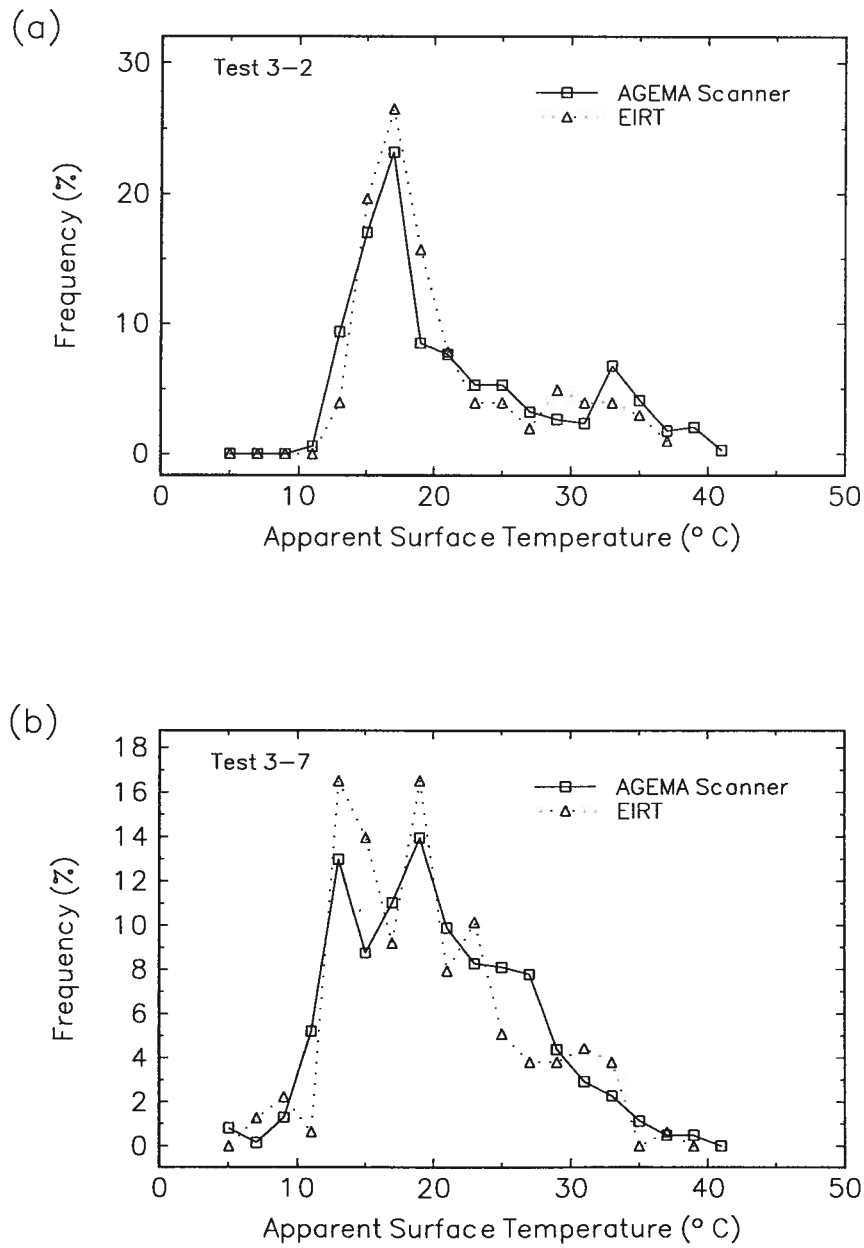

Figure 2.6: Apparent surface temperature distributions for the AGEMA scanner and EIRT obtained from the traverse tests.

with a tail towards higher values (east facets (c)).

As the angle of the EIRT above horizontal increases, there is a shift towards a greater proportion of observations in the lower portion of the distribution, because more samples include sky in the FOV. Separation by direction of the EIRT accounts for the differences in the distance to the facet between the left- and right-facing EIRT; the left-facing EIRT is further from the facet and therefore has a greater chance of having some portion of the FOV occupied by sky (since the projected FOV is larger). This effect is only weakly expressed in the results; it is best viewed as an increase in the frequencies of occurences of left-facing samples in the lower distribution.

In the Industrial and Residential study areas, traverses were conducted on both streets and alleyways. In both areas, the geometry of the alleyways differs from that of the street (generally lower H:W for the street canyon compared to the alley), because alleyways are narrower and generally have a smaller building set-back distance (although this distance tends to be much more variable than for the street canyon in these areas). Figure 2.8 compares alley and street temperature distributions in the Industrial study area for a mid-morning traverse. Results from left- and right-facing instruments are combined because, due to the manner in which the traverse was conducted, relatively few observations were obtained for some facet-instrument pairings.

South facets show slightly greater proportions of higher temperatures in the street canyons compared to the alleys, especially for the 10° EIRT. This may be due in part to (early morning) differences in solar access because of the different canyon H:W and/or a smaller and lower projected FOV within the alley canyon which may be more likely to view the shaded portions of walls. This may also account for the enhanced frequencies of sky or mixed sky and building observations in the alleys which occur counter to that expected due to canyon H:W differences. The overall shapes of the distributions are similar and the apparent position of the peaks are not too dissimilar.

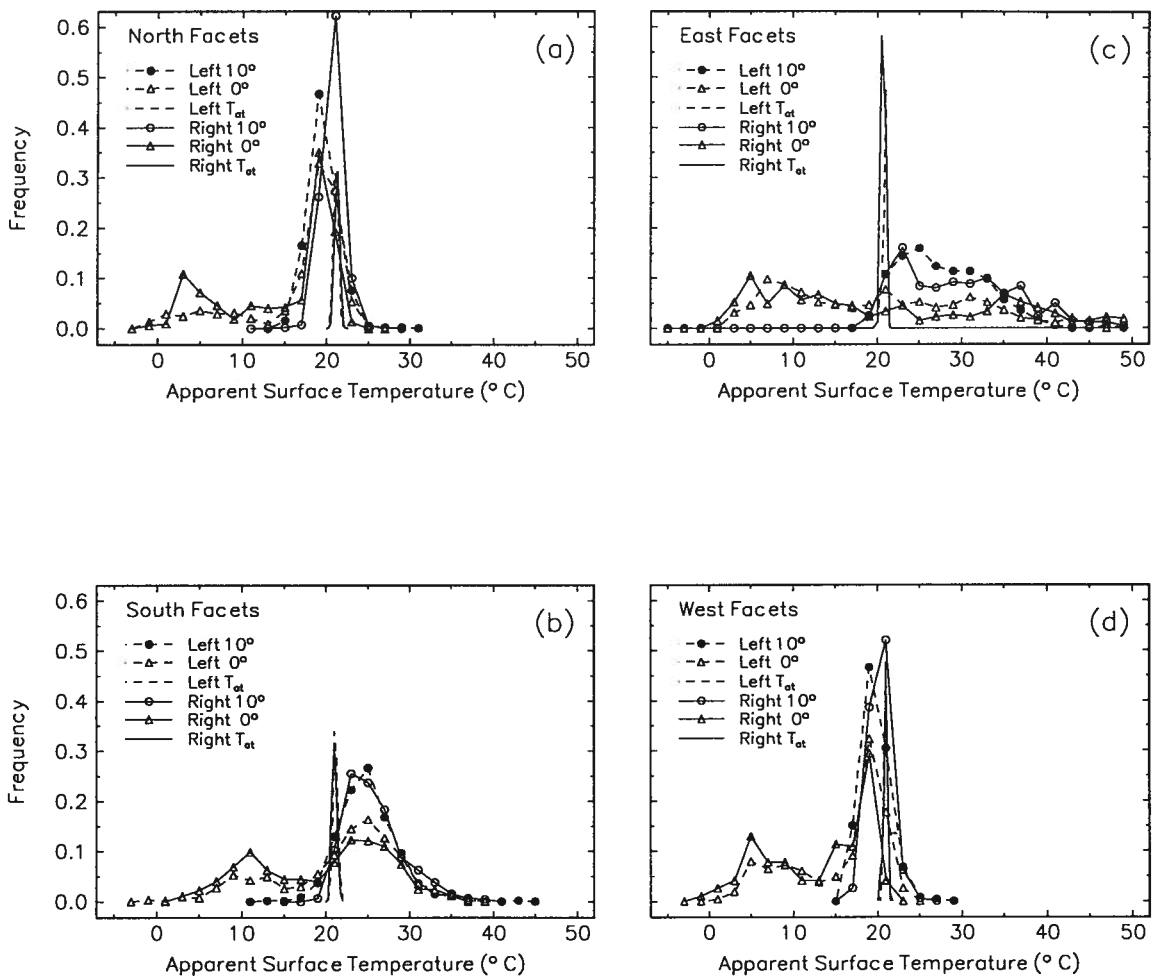

Figure 2.7: Frequency distributions of T_r obtained during a mid-morning (1025-1048 PDT) traverse of the Industrial study area for: (a) north, (b) south, (c) east, (d) west facets.

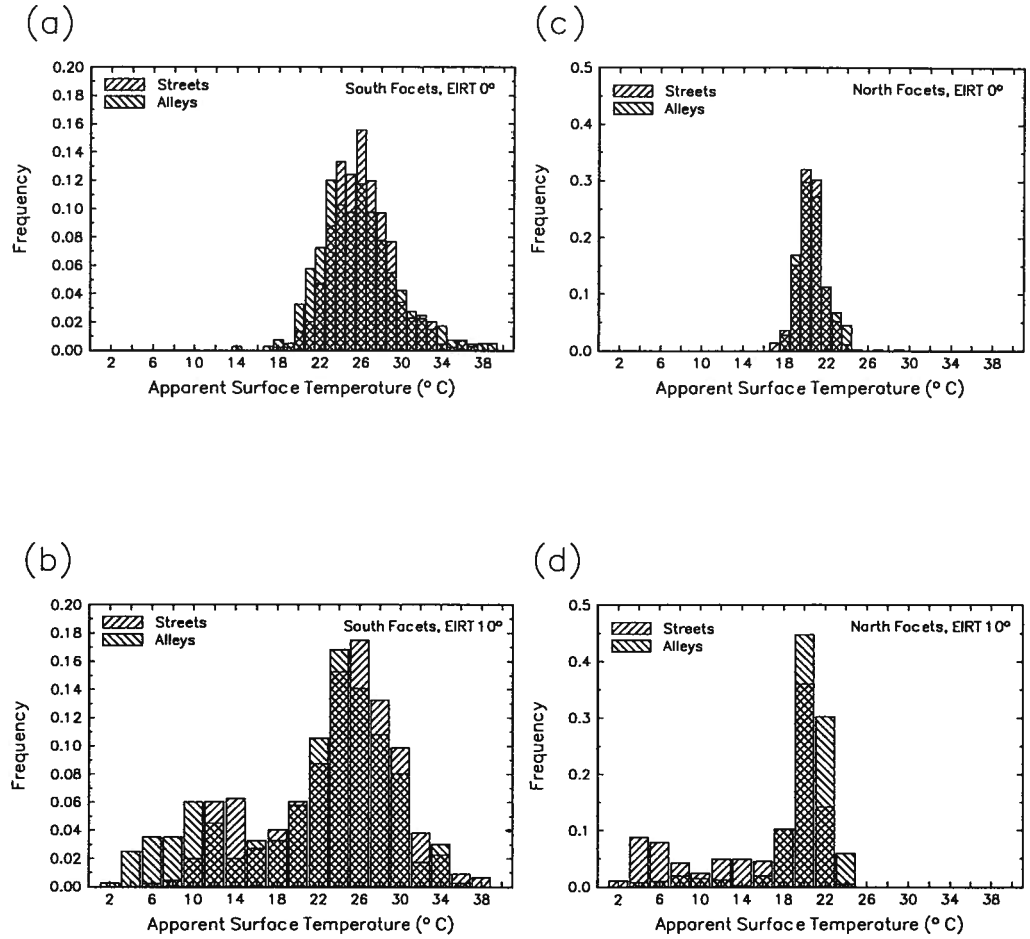

Figure 2.8: North and south facet temperature distributions for 0 and 10° EIRT in alleys and streets in the Industrial area. Note the variation in ordinate scale.

North facets have similar distributions for the 0° EIRT. The 10° EIRT shows a tendency for streets to have more observations which view sky or mixed sky and building as may be expected from the H:W differences, but the distribution shapes are similar, especially in the range of likely surface temperatures. Early and late evening traverses were checked to determine if any enhancement in distribution differences occurred because higher local zenith angles at these times could potentially create greater solar access differences. No significant differences in the shapes of the distributions were noted. Based

on these results it is concluded that alley facet temperatures need not be separated from street facets in the Industrial study area.

In the Residential area, results from an early morning traverse (Figure 2.9), show more significant differences, especially for the directly irradiated east facets which show a strong tendency for alleys to be significantly warmer than the streets for both the 0 and 10° EIRT. A similar difference exists for north and south facets as viewed by the 0° EIRT. The shaded (west and north) facets as viewed by the 10° EIRT at this time show streets to be slightly warmer, the difference between streets and alleys for west facets are especially striking. This effect may be due to the presence of many large trees within the north-south street canyons which are viewed by the 10° EIRT.

2.5.2 Traverse Configuration 2.

Figures 2.10 and 2.11 illustrate results obtained using traverse configuration 2 in the Downtown study area. The general trend of the results is similar to that described earlier; the addition of the EIRTs at larger elevation angles yields a greater range of low temperature values. Separate peaks relative to the sensor angle are sometimes apparent (Figure 2.11 (b) northeast facets). These are related to the decrease of apparent sky radiative temperature with increase in elevation angle.

2.5.3 Modelled Temperature Distributions

A simple model of T_r as obtained from the traverse sampling methodology was formulated to create hypothetical temperature distributions for comparison with the observed distributions. The model requires surface structural information on the typical height, length, and spacing of buildings along a city block. Each block contains a number of buildings equally spaced along the length of the block plus an "intersection" with no buildings. Each building is assigned a height drawn from a distribution with a mean and

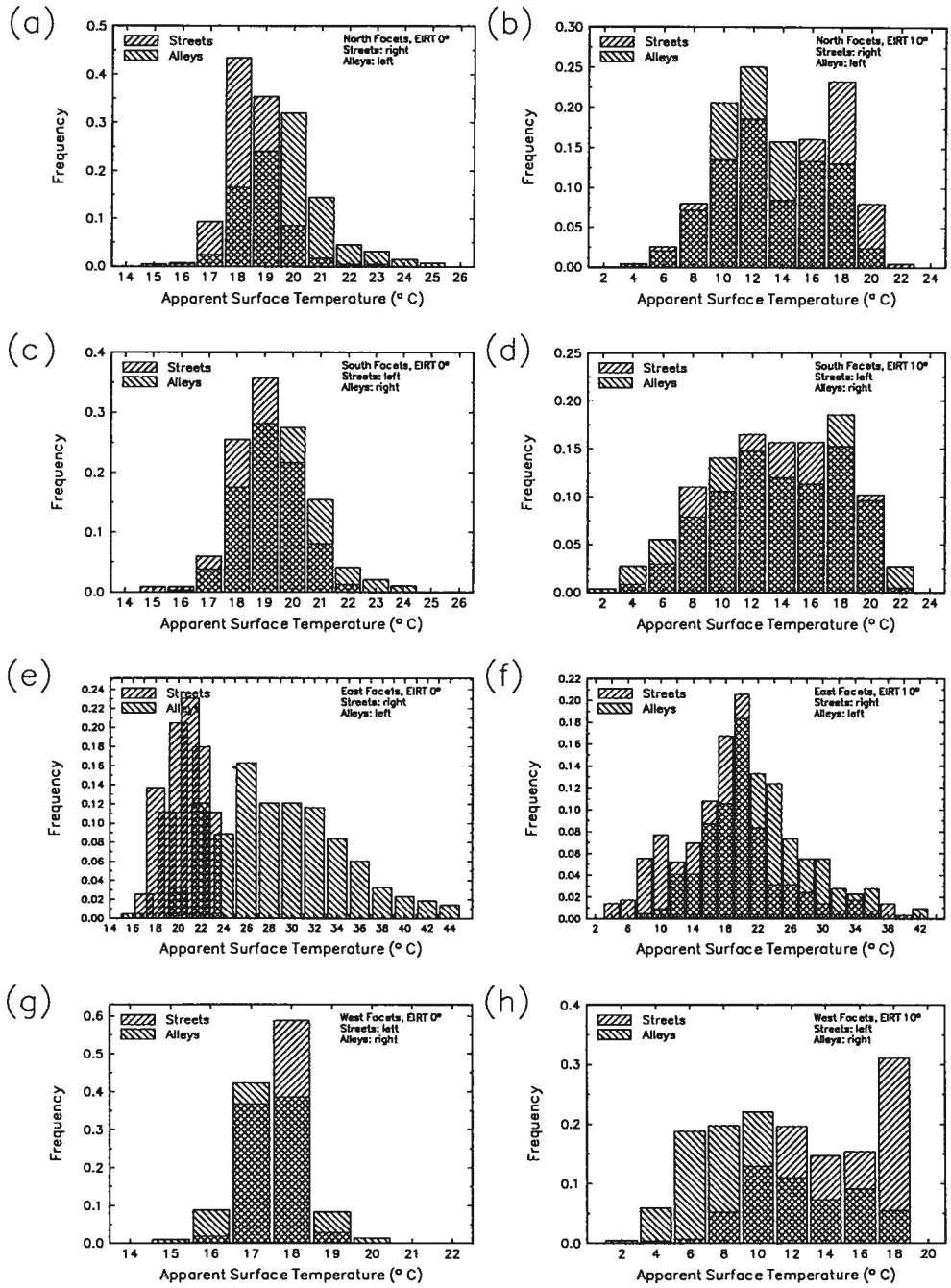

Figure 2.9: Facet temperature distributions for streets and alleys in the Residential area. Note variation in frequency scales.

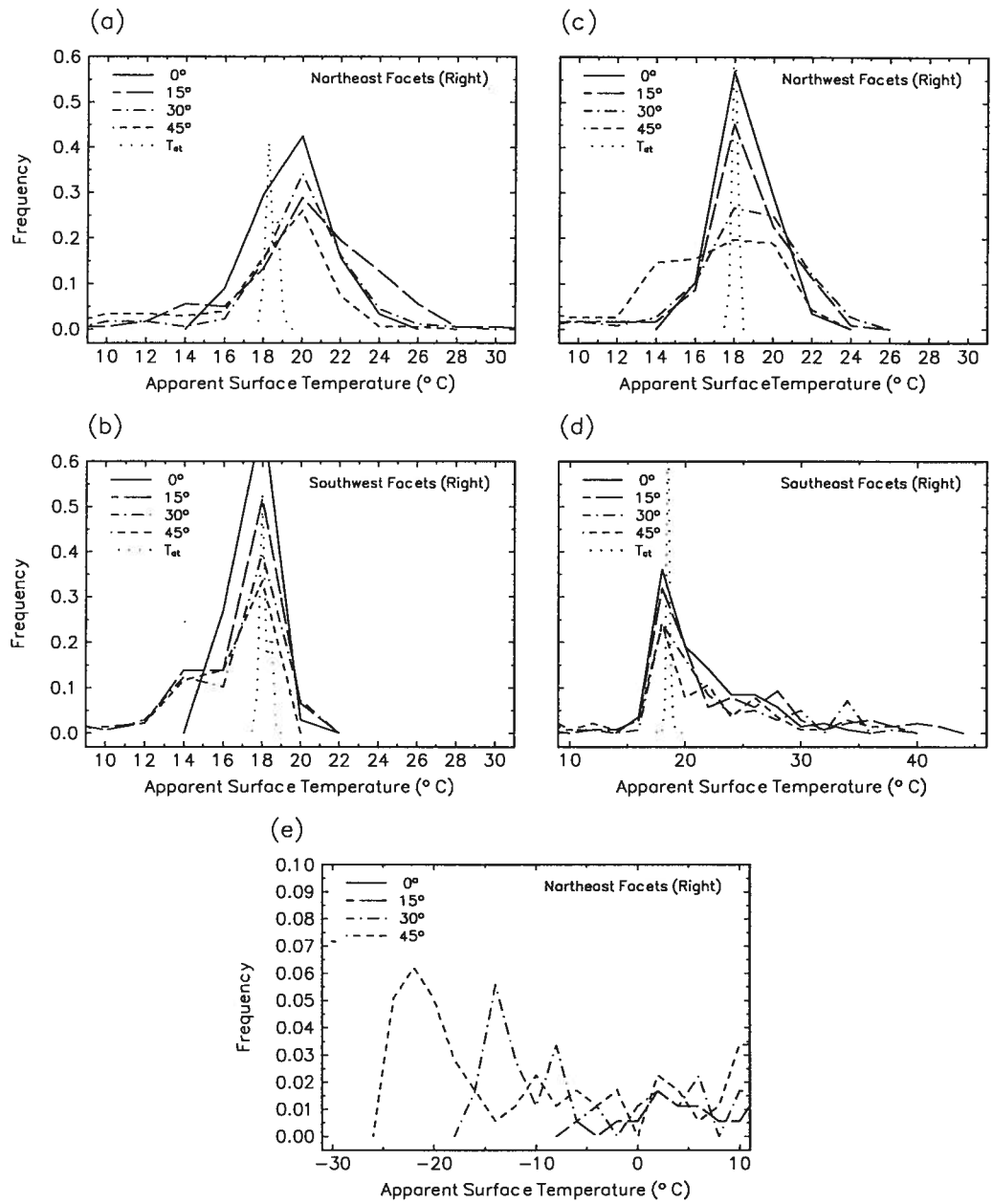

Figure 2.10: Frequency distributions of T_r obtained during a mid-morning (1025-1048 PDT) traverse of the Downtown study area. Right-facing EIRT for: (a) northeast, (b) southwest, (c) northwest, (d) southeast facets, (e) northeast facets (low temperature range).

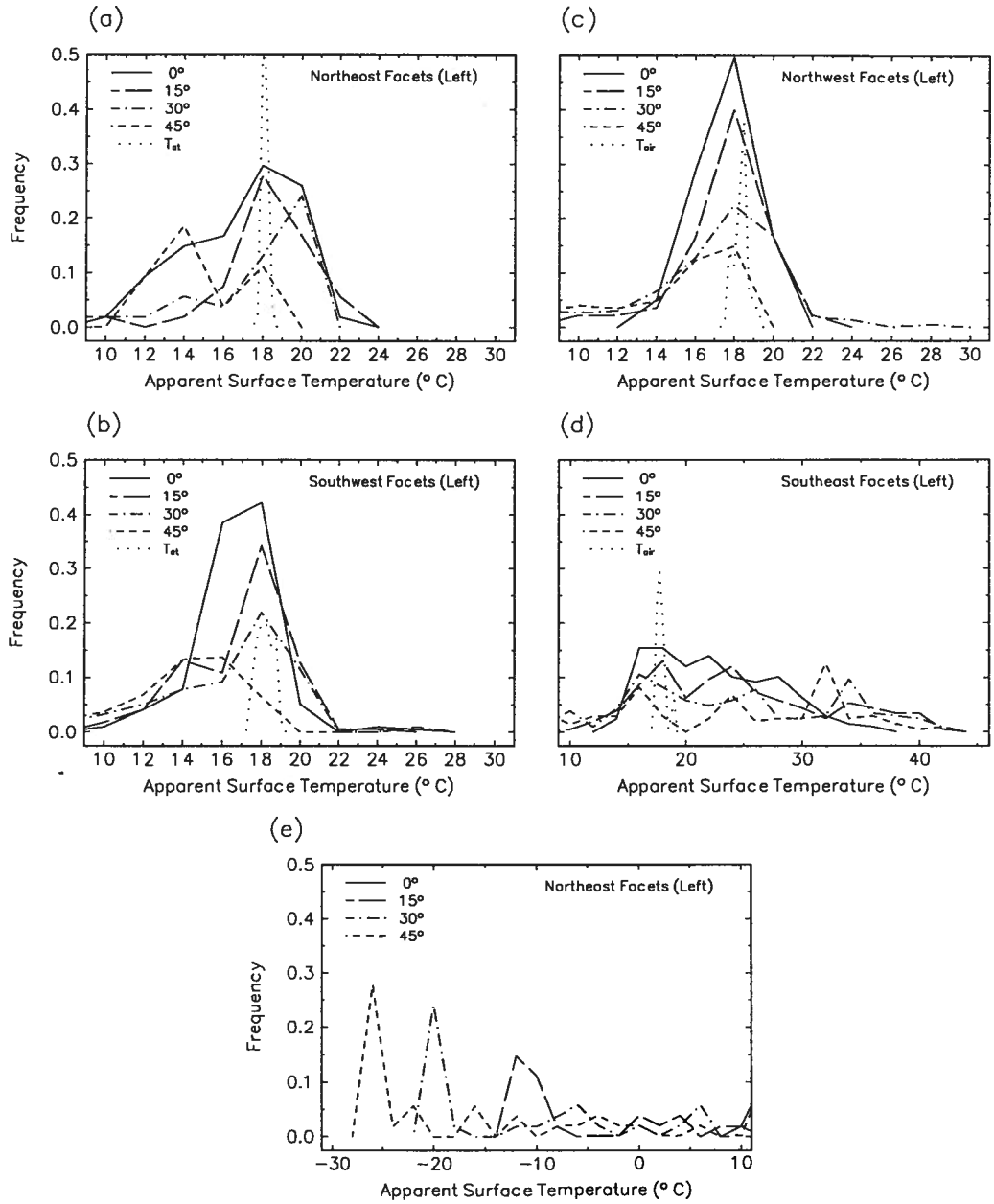

Figure 2.11: Frequency distributions of T_r obtained during a mid-morning (1025-1048 PDT) traverse of the Downtown study area. Left-facing EIRT for: (a) northeast, (b) southwest, (c) northwest, (d) southeast facets, (e) northeast facets (low temperature range).

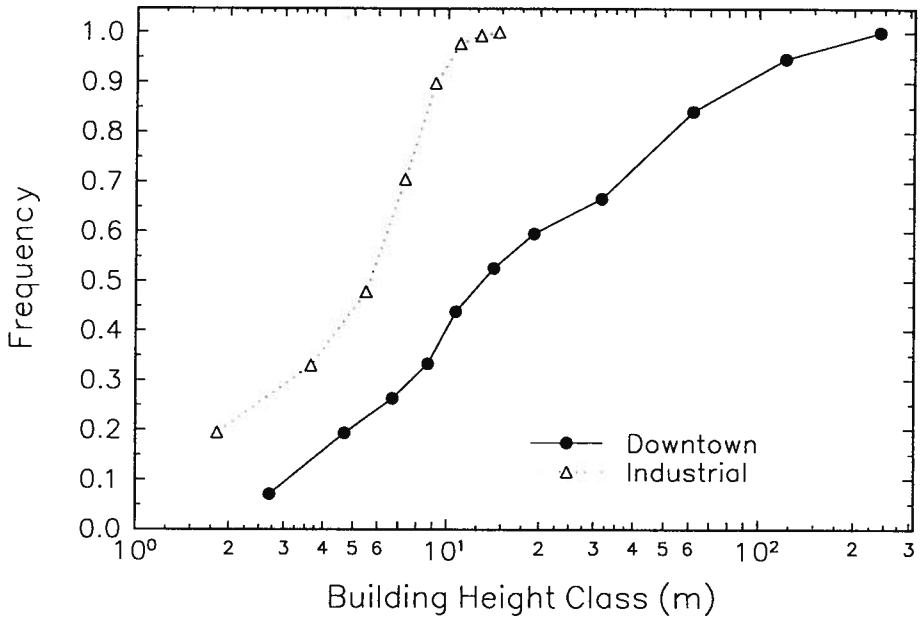

Figure 2.12: Cumulative frequency distribution of building heights for Downtown (traversed northeast facets only) and Industrial (north street and alley facets).

standard deviation based upon measured height classes (Figure 2.12). Temperatures of building facets (T_w) and sky (T_{sky}) are generated from a normal distribution with a specified mean and standard deviation. Modelled T_r is obtained by weighting the equivalent building radiation and sky radiation by the the proportion of the projected FOV that is occupied by building and sky components to produce an equivalent temperature. For simplicity, the FOV is assumed to be rectangular, rather than elliptical and the size and projected height of the FOV is set by the distance between the EIRT and the building facet, and the EIRT angle.

Modelled temperatures are calculated along the block using a given traverse sampling interval with a random starting position (between 0 and one sampling interval). The block-intersection sampling sequence is repeated for a given number of iterations. Two

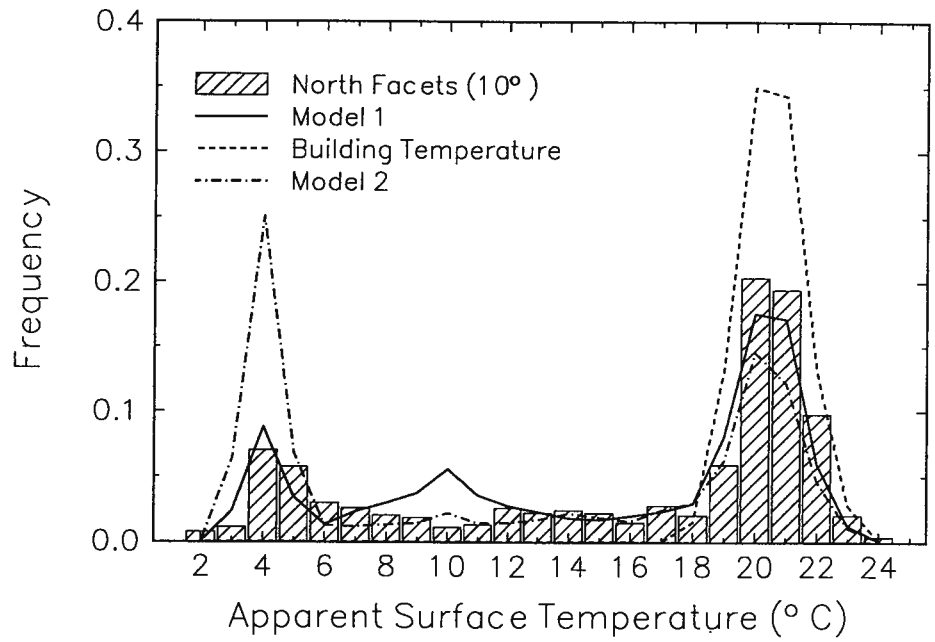

Figure 2.13: Modelled and measured EIRT temperature distributions for north facets during a mid-morning traverse in the Industrial study area. Model 1 sets all building heights to a minimum of 3.66 m. Model 2 uses height classes as measured.

sequences are used: one to represent sampling conditions on main streets, the other for alleyways (e.g., for east-west traverses in the Industrial study area). Model parameters used in the case studies are presented in Table 2.6 and the measured and modelled temperature distributions for shaded facets in the Industrial and Downtown study areas are shown in Figures 2.13 and 2.14 respectively. The "building temperature" is the distribution which would be measured if each sample contained a FOV consisting of only a building.

Building height classes in the Industrial area were categorized into the number of stories (0 - 4, in 0.5 increments) and converted into heights (assuming 3.66 m (12′) per story). Assignment to the 0 and 0.5 classes may be deceptive, because, despite the absence of a building in the foreground, background buildings may fill the projected

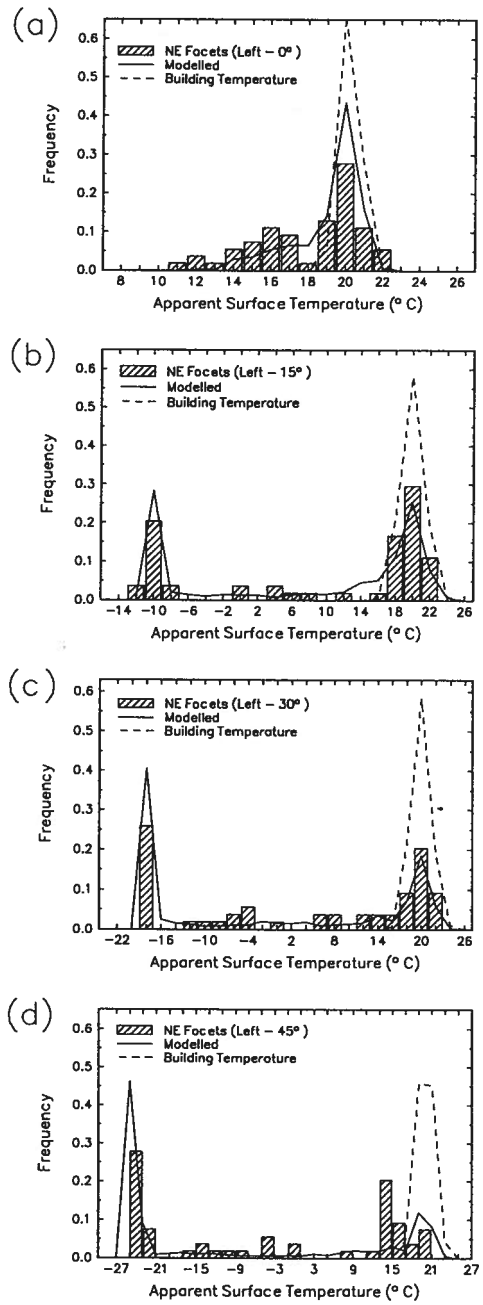

Figure 2.14: Modelled and observed EIRT temperature distributions for a mid-morning traverse in the Downtown study area (Southwest facets only). (a) 0° EIRT, (b) 15° EIRT, (c) 30° EIRT, (d) 45° EIRT.

Table 2.6: Model parameters used in EIRT distribution modelling. A - Industrial: EIRT angle 10°; dff (distance from facet) 12. 5 m (streets) and 5 m (alleys). B-E Downtown:EIRT angles 0,15,30,45° dff 15 m.

Parameter	Description (Units)	A	B	C	D	E
FOV_{w1}	Field of View width (m)	3.34	3.95	4.09	4.57	5.63
FOV_{h1}	Field of View height (m)	3.40	3.95	4.24	5.30	8.04
FOV_{c1}	Height of FOV centre (m)	4.20	2	6.02	10.6	17
FOV_{w2}		1.35				
FOV_{h2}		1.35				
FOV_{c2}		2.88				
BLKL	Block Length (m)	125	83	83	83	83
INTL	Intersection Length (m)	20	20	20	20	20
BLDGL	Building Length (m)	15	21	21	20	20
NBLDG	Number of Buildings	8	4	4	4	4
BLDGSP	Building Spacing (m)	0.6	0.8	0.8	0.8	0.8
NIT_1	Number of Iterations	60	100	100	100	100
NIT_2		50				
T_w	(°C)	20.5	20	20	20	20
σ_w	(°C)	1.0	1.5	1.0	1.0	1.0
T_{sky}	(°C)	4.0	16	-10	-18	-23
σ_{sky}	(°C)	0.5	0.5	0.5	0.5	0.5

FOV. Similarly, intersections, assumed to have 0 building height, may include horizontal or vertical surface elements within the FOV such as when distant buildings are viewed or if the topography slopes upwards. In the Downtown area, building heights were obtained from inclinometer measurements and put into a number of classes.

North facets have been chosen for the initial modelling efforts as they exhibit a narrow unimodal distribution of building temperatures, due to the absence of direct solar radiation (Figure 2.7). Results from the Industrial area show a strong sensitivity to the specification of the building height classes. Using the classes as measured, the model greatly overestimates the proportion of observations with temperatures near that of T_{sky},

underestimates those near T_w, and slightly underestimates intermediate temperatures. Assuming a minimum building height of 3.66 m results in a much better agreement between the observed and modelled distributions with the exception that there is a local peak near 10°C. This peak may be a result of excess observations in the 3.66 m class, in combination with the surface structure.

Results from the Downtown study area show a similar overestimation of the sky temperature class and underestimation of the building temperature. Again, this may reflect some bias in the low building height classes: for EIRT angles of 30 and 45° we expect negligible viewing of any surfaces in the intersections, yet, the overestimation in this class remains high or even increases relative to the observed distribution. The offset between the modelled and observed building temperatures for the 45° EIRT may represent an actual temperature decrease on the upper portion of the buildings (the 45° right-facing EIRT shows good agreement with the building temperature). Note that the number of observations for the left-facing EIRT in this portion of the traverse is not large (54). Extending the modelling analysis to other facets, Figure 2.15 presents results for the south, east and west facets in the Industrial area. The surface structure differs for the east and west facets because the block length is shorter, and each block contains an alleyway as well as an intersection. Up to three temperature distributions are used in the model. Proportions for each temperature population are listed in Table 2.7. Mean temperatures, standard deviations and proportions are estimated in order to achieve a "best fit" with the observed data. The model generally performs well for the east and west facets, despite the fact that the building height distributions were measured only on the north and south sides of the street, therefore assuming the distribution of building heights by street direction is invariant. T_{sky} is under-represented in the observed data for the south facets. Block length, building length, and the number of buildings were adjusted to represent the differing character of the north-south streets.

Table 2.7: Model parameters for EIRT distribution modelling. Industrial area, mid-morning traverse, south, west, east facets.

Parameter	(Units)	South	West	East
FOV_{w1}	(m)	3.34	3.34	3.34
FOV_{h1}	(m)	3.40	3.40	3.40
FOV_{c1}	(m)	4.20	4.20	4.20
FOV_{w2}	(m)	1.35		
FOV_{h2}	(m)	1.35		
FOV_{c2}	(m)	2.88		
BLKL	(m)	125	83	83
INTL	(m)	20	20	20
BLDGL	(m)	15	18	18
NBLDG		8	4	4
BLDGSP	(m)	0.6	2.8	2.8
NIT_1		60	110	110
NIT_2		50		
T_{w1}	(°C)	23.5	20.3	23.2
σ_{w1}	(°C)	1.25	0.55	0.25
T_{w2}	(°C)	29.0		37.5
σ_{w2}	(°C)	1.75		2.0
T_{w3}	(°C)			46.0
σ_{w3}	(°C)			2.5
% Bldg1		45	100	5
% Bldg2		55		75
% Bldg3				20
T_{sky}	(°C)	5.0	5.0	5.0
σ_{sky}	(°C)	1.5	1.5	1.5

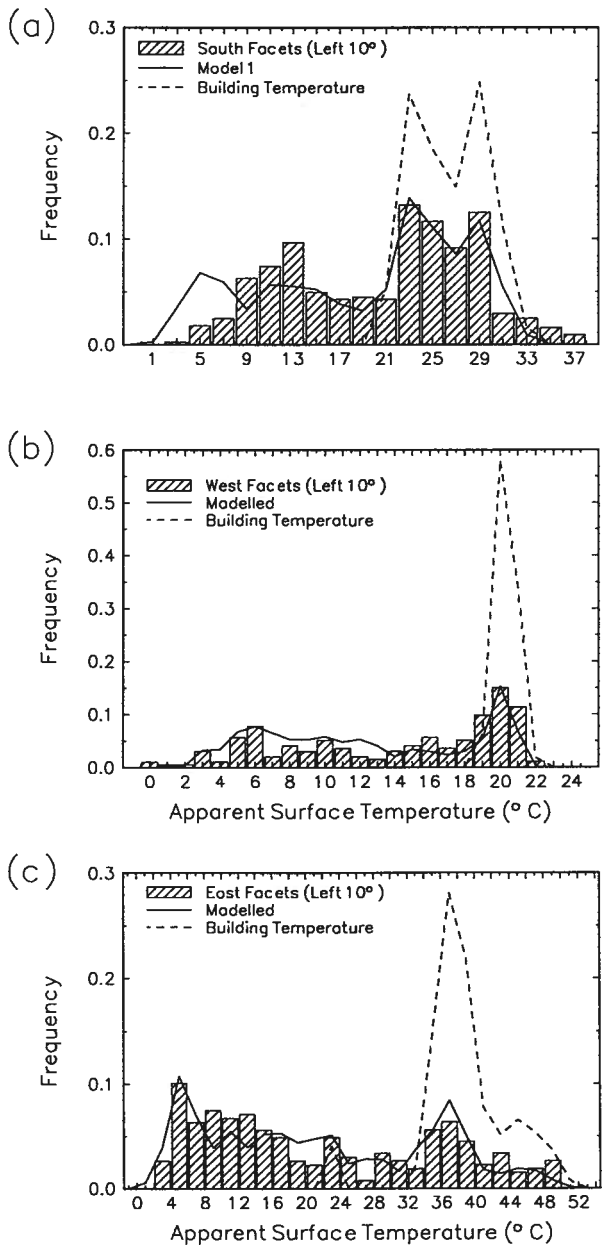

Figure 2.15: Modelled and observed 10° left-facing EIRT temperature distributions for a mid-morning traverse in the Industrial study area. (a) north, (b) east, (c) west facets.

2.6 Summary

Spatial sampling of the surface temperatures of vertical facets, the road surface temperature and air temperature was carried out using automobile traverses in three land-use areas of Vancouver. This is the first such study to characterize street canyon temperatures on this scale. Previous studies generally were confined to single street canyons. Traverses included both streets and alleyways within the study area. Results are summarized in the following list.

- Distributions of apparent surface temperature show changes with time and facet orientation; facets under direct solar irradiation show a much broader range of temperatures than do shaded facets which are characterized by very narrow distributions. All distributions are complicated by the presence of observations from IFOV which view the sky or mixed building and sky scenes.

- There is a lag in the response of the EIRT as shown by tests against the AGEMA fast response thermal scanner, so that the resultant temperature is not a direct function of the projected IFOV at that instant. This has implications in the removal of observations using the navigation record.

- Surface emissivities are not considered on a sample basis but rather are applied to the spatial averages using a simple model of canyon radiative exchange.

- Spectral reflection by low emissivity surfaces may pose a problem in the Downtown area as evidenced by vertical transects of apparent surface temperature made by ground teams using hand-held EIRT.

- A simple model of the apparent surface temperature distributions was shown to give qualitative agreement with observed distributions. More precise agreement would

be expected with improvements in the representation of the surface structure.

Chapter 3

AVERAGE TEMPERATURES OF CANYON FACETS

In order to determine a representative temperature for the vertical facets of a given orientation, it is necessary to remove from the sampled data those points for which the projected FOV contains sky radiation. Two approaches were attempted: truncation of the surface temperature distribution followed by the compilation of summary statistics on the remainder of the distribution, and mixed distribution modelling with or without pre-truncation of the temperature distribution (statistical separation of the composite distribution into a number of component populations).

3.1 Distribution Truncation

A method to remove surface temperature observations which originate from sky, or mixed sky and building, scenes is to truncate the distribution and discard all observations below the threshold. This approach assumes the combination of sky and building surface radiance within the instrument FOV reduces T_r below that which might be reasonably expected, whereupon it is discarded. A difficulty with this method is that a combination of a small fraction of sky radiance, combined with large fraction of high surface temperature, cannot be distinguished from a surface having a slightly lower temperature. This means that the resulting truncated distribution may be biased towards slightly lower temperatures than are actually present (although model results tend to show this is not a large problem). The use of air temperature (T_a) data as the truncation point was investigated. This is based on the assumption that surfaces cannot be far below the ambient

air temperature. Therefore, relationships between T_r obtained from automobile traverses, T_a and remotely-sensed surface temperatures are investigated for selected shaded facets to determine typical minimum surface temperatures.

The surface temperature is controlled by the surface energy balance as influenced by the properties of the surface material. Directly irradiated facets are expected to show substantial positive differences between surface and air temperatures. For shaded facets the differences are likely to be much smaller, or even negative (Nakamura and Oke, 1988) due to the lag in the thermal response of building materials with high thermal inertia (Figure 3.1). Similar results were found in the scale model canyon of Voogt (1989) where T_{wo} - T_a was -0.8 to -1.3°C soon after sunrise.

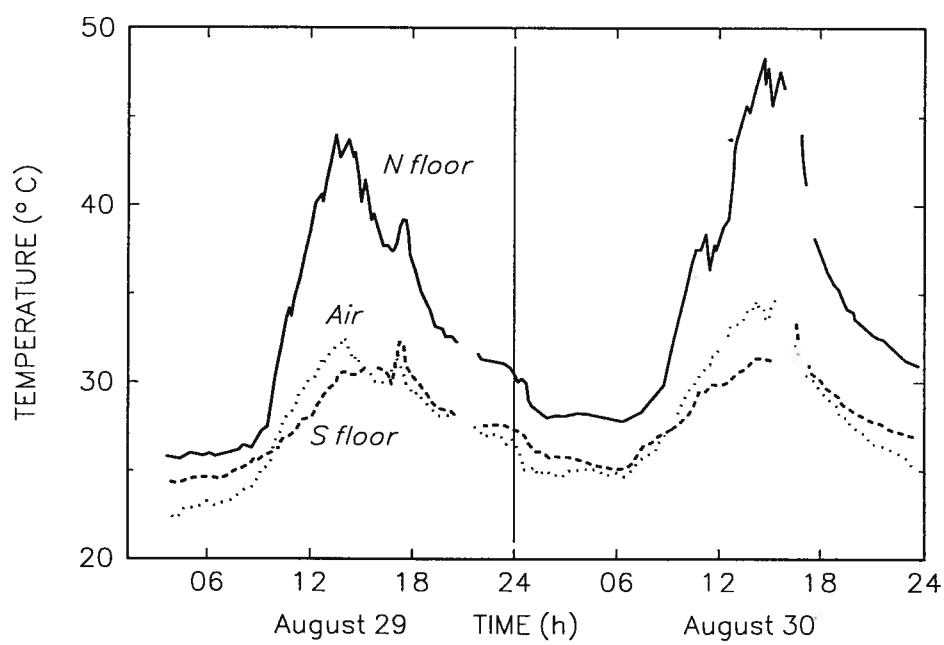

Figure 3.1: Temporal variation of canyon floor surface temperatures in an east-west oriented street canyon compared with 0.5 m air temperature. (After Nakamura and Oke, 1981).

3.1.1 Surface/air Temperature Relations in the Study Areas

3.1.1.1 Industrial Area

As part of a parallel study on the storage heat flux in the Industrial area, the surface temperatures of selected building facets were monitored for several days. These provide an independent set of facet measurements which may be compared to the traverse measurements. Other independent sources of data include: apparent surface temperature measurements made by ground team members equipped with hand-held IRTs, and facet temperatures from the airborne scanner. Each set is compared to the select subset of traverse temperatures. The traverse temperatures are screened by hand with "obvious" mixed-pixel values removed, and statistics calculated on the remaining points.

Figure 3.2 presents the results for an alleyway within the Industrial study area; symbols are defined in Table 3.1. Error bars are used to plot $\pm 1\sigma$.

The temporal trend of T_{wf} shows a smooth curve excepting a period following sunrise when some direct solar radiation is received by the wall resulting in a sharp rise in the surface temperature followed by a leveling off for about two hours. $\hat{T}_{wt}$ for the same block is warmer (by 1-2 °C) for most of the day, but the standard deviation (plotted as error bars) indicates that the traverse sample contains a reasonable number of observations with temperatures similar to that of the building wall. $\hat{T}_{wa}$ is slightly lower than $\hat{T}_{wt}$, and has a larger standard deviation. Images show coolest temperatures near the base of the shaded walls which extends onto the ground surface so that including these in the sample may lower the mean. The greater variation may be due to the inclusion of a few pixels from warm roofs, or smearing of roof pixels into upper wall areas.

Minimum surface temperatures extracted from the airborne imagery are substantially below both air temperatures and T_{wf} and except for the first flight, are lower than T_{wgmin} (although the latter is a very small sample). T_{wgmin} correlate reasonably well with those

Table 3.1: Description of symbols used in Figures 3.2, 3.3 and 3.4.

Symbol	Description
w	facet (wall)
f	fixed observing site
a	air (first subscript), airborne platform (second subscript)
t	traverse
g	ground team
$\hat{}$	denotes a spatial average
T_{wf}	apparent building facet surface temperature obtained from the fixed monitoring site
$\hat{T}_{wt}$	mean apparent building facet surface temperature from the traverse vehicle for the same block (screened as described above);
T_{at}	the modal air temperature class (0.5 °C width) obtained from the vehicle traverses done in the study area (approx. 2 m level)
T_{af}	air temperature at 9 m above the ground
T_{wgmin}	minimum recorded apparent surface temperature from north-facing walls obtained from samples taken by ground teams
T_{wg}	mean apparent surface temperature from north-facing walls taken by ground teams
$\hat{T}_{wa}$	mean apparent facet temperature of selected buildings taken from off-nadir airborne imagery
T_{wamin}	minimum recorded apparent facet temperature of selected buildings obtained from the off-nadir airborne imagery

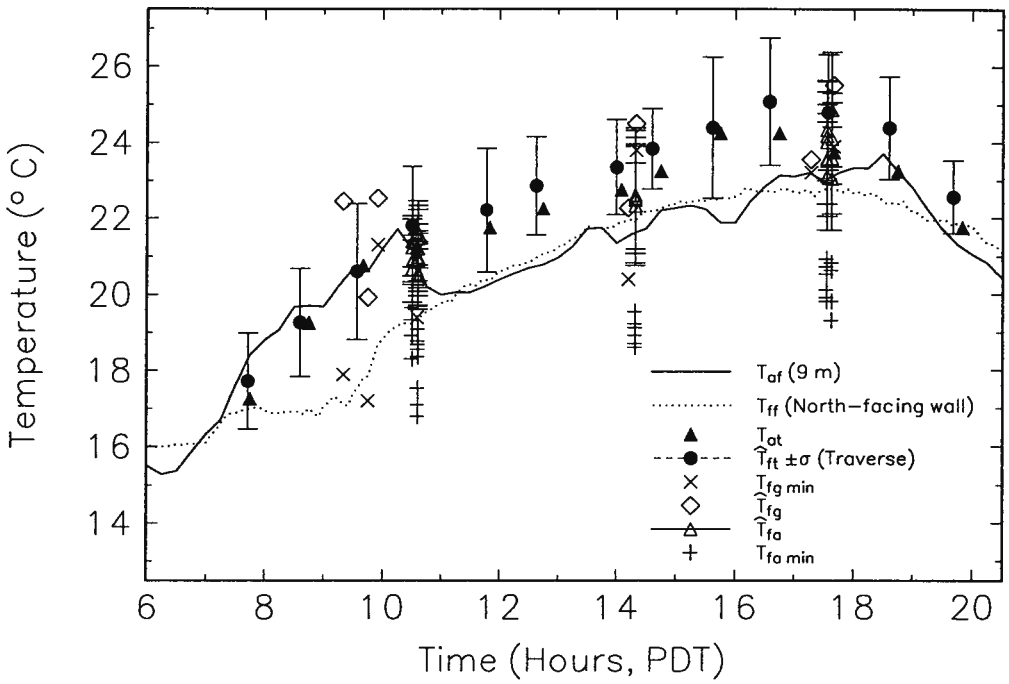

Figure 3.2: North-facing alley facet temperatures and air temperatures in the Industrial study area.

of the fixed monitoring site in the morning, but show more scatter later in the day. The means of these points generally fall within $\pm 1\sigma$ of $\hat{T}_{wt}$. T_{at} is slightly less than $\hat{T}_{wt}$ for almost all traverses but is higher (by 1-2°C) than $\hat{T}_{wt}$ at all times, except for the first and last traverses when the two values are in close agreement. The 9 m air temperature (T_{af}) agrees well with T_{at} up until approximately 1030 PDT, when T_{af} shows a sharp drop, possibly associated with the onset of a local sea breeze. Following this drop, T_{af} remains close to the north-facing building surface temperature until approximately 1600 when it becomes warmer for approximately 2 hours. The difference between the T_{af} and T_{at} points to a possible decoupling of the canyon level (microscale) air volume from the UBL (mesoscale) air.

By itself, T_{wf} provides an independent measure to truncate the distribution, under

the assumption that it is representative of the coolest surfaces available. For any other facet orientation, this limit also holds (i.e., for shaded portions of directly irradiated facets). However, the airborne and hand-sampled data appear to indicate significantly cooler surfaces do exist in the study area. The relation between T_{at} and T_{wf} indicates that T_{at} is generally warmer requiring the specification of an offset of 1-2°C for most times in order to utilize T_{at} as a truncation measure for this facet. For directly irradiated facets, the specification of an offset is not as critical because the bulk of the surface temperature distribution lies well above air temperature.

The use of minimum temperature as a truncation point may be suitable for the 0° EIRT as they rarely view the sky (except at intersections), so the statistics are relatively stable. However, for the 10° EIRT, this cutoff may include significant numbers of mixed sky-building pixels. Using T_{at} with an additional (negative) offset (denoted by DTA (°C)) the effect on the statistics of the traverse record was investigated as DTA is changed from 0 to 5. The results indicate that for the 0° EIRT, DTA greater than 2 incorporate most of the data set and statistics tend to stabilize. For DTA less than 2, $\hat{T}_{wt}$ increases exponentially; differences in $\hat{T}_{wt}$ between DTA = 0 and DTA = 2 are not large in absolute terms (generally less than 1°C). The 10° EIRT tend to show a more linear decrease of $\hat{T}_{wt}$ as DTA increases, absolute differences are again less than 1°C. There are differences between the EIRT with angle; for directly irradiated walls, the 0° EIRT tend to be cooler than the 10° EIRT, possibly due to increased shading by awnings, vegetation lower on walls, and decreased solar access nearer the ground. For north-facing facets, traverses during the day show good correspondence between 0 and 10° EIRT for DTA ≈ 2. At this time of day little or no temperature variation with height on this wall is anticipated so this may be a satisfactory truncation point. Earlier and later in the day, when this wall may be exposed to short periods of direct solar irradiance, the upper EIRT may show preferentially warmer values. Nevertheless, based upon the above considerations, $T_{at} - 2$

is used as a truncation limit for all facets, at all times, for this traverse.

3.1.1.2 Downtown

No fixed monitoring of building surfaces was conducted for the other study areas so comparisons are between traverse, hand-sampled, and airborne data. The Downtown traverse data is for two blocks of northeast-facing facets (Figure 3.3). The plot shows $\hat{T}_{at}$ to be slightly below the average T_{wt} (except in the late afternoon, early evening period). But the $\pm 1\sigma$ of surface temperature often falls below the $\pm 1\sigma$ ($\hat{T}_{at}$) again indicating that some surfaces fall below air temperature.

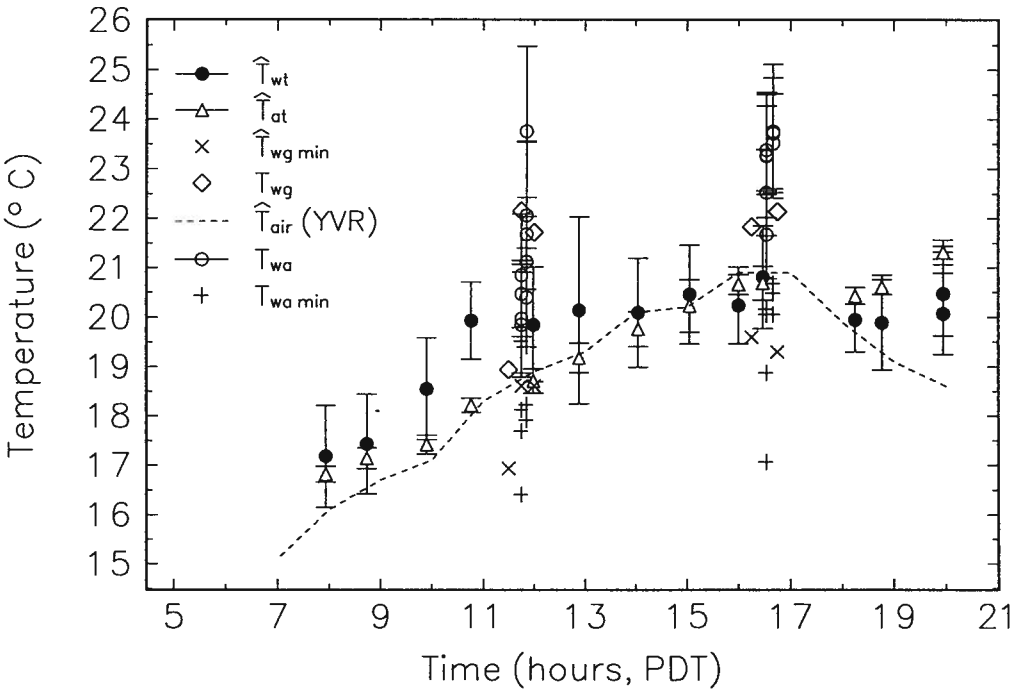

Figure 3.3: Subset of northeast-facing facet and air temperatures in the Downtown study area.

Airport air temperature (YVR) compares well with that measured in the study area except for the morning and late evening traverses. These may be associated with the

nocturnal UHI. Hand-sampled values for this area show minima which tend to be close to $\hat{T}_{wt} - 1\sigma$ and means generally warmer than $\hat{T}_{wt} + 1\sigma$. The number of points involved is small, but the relatively warm average value may point to the presence of surfaces with low ϵ (such as glass) affecting $\hat{T}_{wt}$. Facet temperatures derived from the airborne imagery tend to be substantially higher than those obtained from the traverse subset. This may be due to a greater proportion of pixels originating from the upper part of walls in the imagery, compared to the traverse subset which uses temperatures from near the base of walls. Specular reflection from low emissivity surfaces may also contribute to a higher mean for the airborne imagery. The source of the reflected radiance is the surface or opposite canyon wall, which in this case is quite warm. For the Downtown area, the truncation measure used is the minimum of either $\hat{T}_{wt} - 1\sigma$ or $T_{at} - 1\sigma$ for each traverse.

3.1.1.3 Residential

The results from the Residential area (north-facing side of 50th Ave) (Figure 3.4) consistently show $\hat{T}_{at}$ warmer than $\hat{T}_{wt}$ at all times, with differences of up to 3°C in the late afternoon. Air temperature measured at the 10 m level of the Sunset Tower ($\hat{T}_{wa}$) is much lower than $\hat{T}_{at}$ and is lower than the $\hat{T}_{wt}$ until late afternoon, when it approaches and then exceeds $\hat{T}_{wt}$.

Mean airborne facet temperatures agree well with the traverse values for the morning and afternoon flights; the early afternoon flight shows means slightly lower than $\hat{T}_{wt}$. Standard deviations are much larger, but are probably related to difficulties associated with extracting wall temperatures from the image data. Hand-sampled minimum temperatures show significant scatter and are, in several cases, substantially below the traverse surface temperatures, but are in approximate agreement with T_{wamin}. This finding is not surprising when the FOV of the traverse EIRT is considered. The sensor to facet distance is large in the Residential area because of the small canyon H/W, which means

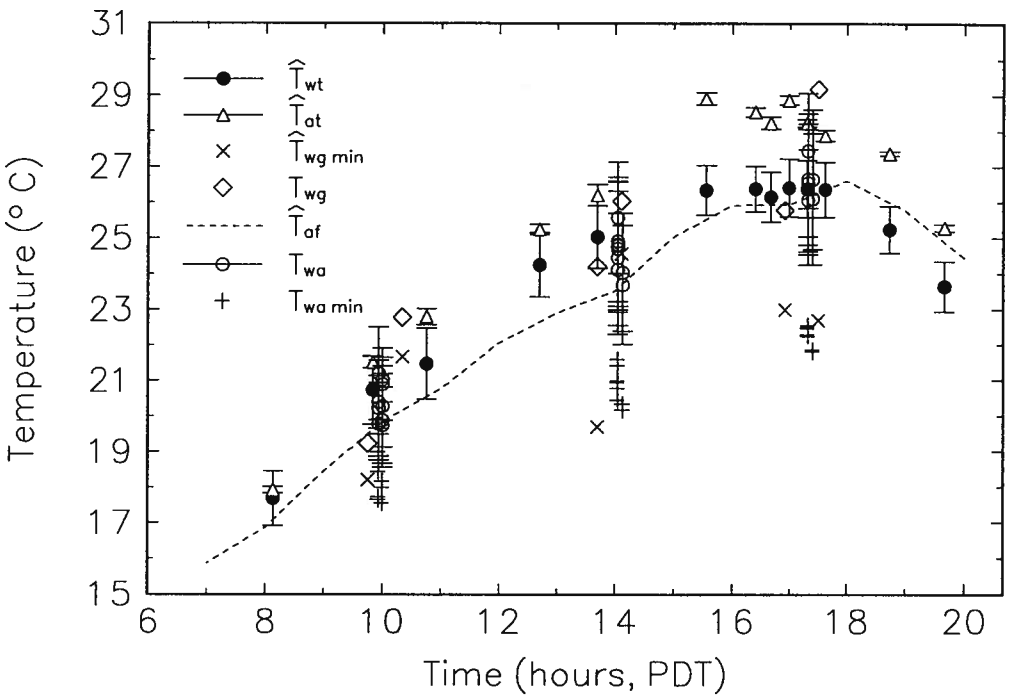

Figure 3.4: Subset of north-facing facet and air temperatures in the Residential study area.

the projected FOV is large relative to the size of the buildings. This is likely to give a better spatial average. The hand-sampled observations involve a narrow FOV radiometer and are taken much closer to the target facet. They are therefore more likely to register anomalously warm or cool spots. The truncation point for this site is specified as $\hat{T}_{wt}$ -2σ. Because of the small H/W and building set-back from the road, 10° EIRT rarely view walls alone. The distributions contain most of the observations that are well below air temperature, probably as a result of viewing mixed vegetation and sky. They are not considered in the determination of averages for this area.

3.1.2 Results

Using the distribution truncation limits defined previously, the traverse data are averaged by facet orientation for each portion of the traverse route as defined by the navigation file (a block or sequence of blocks along a street) and also for the entire traverse. Observations made within an intersection, and the first observation following an intersection, were discarded, regardless of whether they met the truncation criteria. The overall facet mean for this area is obtained by combining the 0° and 10° EIRT. In the figures which follow the solid symbols are mean temperatures with the emissivity correction applied.

3.1.2.1 Industrial Study Area

Figure 3.5 presents the mean facet temperatures for east-west and north-south facet pairs, and the difference between the corrected mean temperatures. The east-west facet pairs show two periods with large temperature differences between the means. The afternoon differences are slightly smaller, due to the overall warming of the non-directly irradiated facets. The north-south facet pair show a single peak with differences maximized near 1400 PDT, which lags solar noon (1317 PDT) by approximately 45 minutes. Standard deviations of the shaded facets are much smaller than those from the irradiated facets. The latter typically show standard deviations of 4-5°C. Shaded facets tend to closely follow the trend of air temperature, except for the west facets in the afternoon, which are slightly warmer, probably due to the release of heat stored when they were sunlit in the morning.

Averages for each street in the traverse (3-4 blocks for north-south facets, 5 blocks for east-west pairs) are shown in Figure 3.6. Again variation between blocks is highest when directly irradiated. Three north facets are cooler than the remainder; two of these are alleys and the other is a street (8th Ave). It is suspected that the cooler temperatures

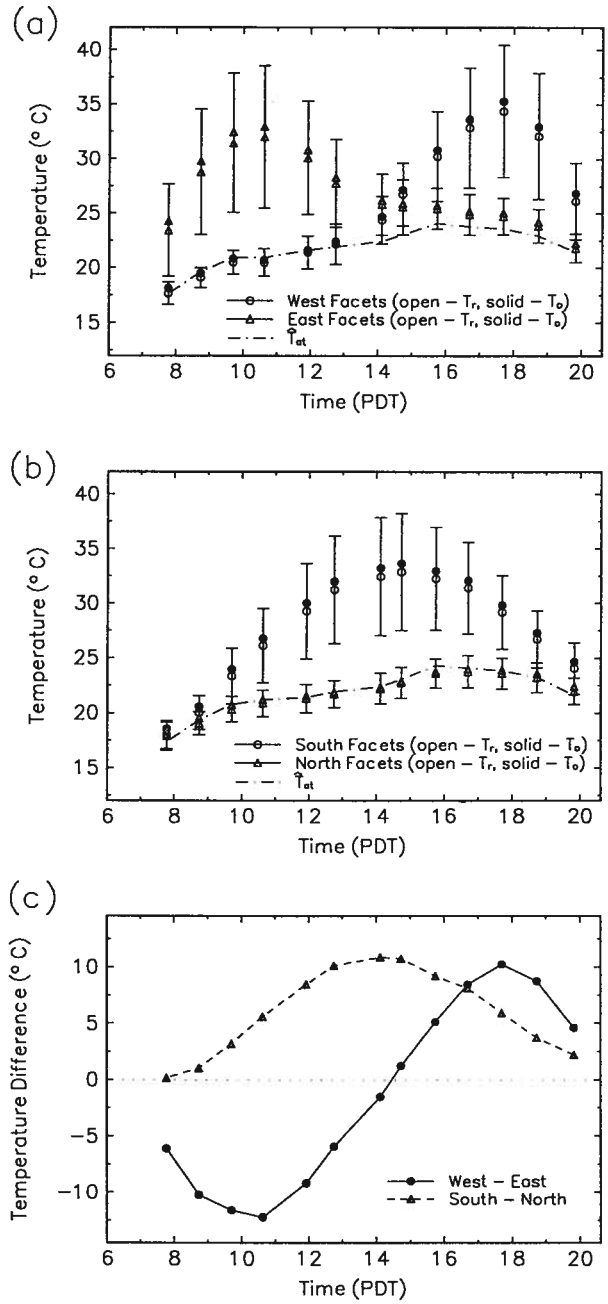

Figure 3.5: Mean facet temperatures (apparent and corrected) and standard deviations following distribution truncation in the Industrial study area for (a) east and west facets, (b) north and south facets and (c) mean temperature differences.

are due to these alleys being narrower than the others, and the street may be somewhat cooler due to the presence of a large park for one block so that the recorded temperatures may be that of distant buildings and some ground surface.

3.1.2.2 Downtown

Results for the Downtown site differ from the Industrial area because of the different street orientation (Figures 3.7 and 3.8).

The northeast-southwest facet pairing (the 15° EIRT data are plotted) shows only small differences in the early morning followed by a reversal and the creation of large differences in the mid- to late afternoon. Northwest-southeast facet pairs show only a large late-morning to noon peak. Shaded facets are slightly warmer than the air temperature for the most part, except late in the day. Standard deviations are large for directly irradiated facets and overlap those of the shaded facets, probably due to mixed shade-sunlit facets in the deep canyons.

There is a large variation in the mean block to block sequence temperatures especially for the irradiated facets (Figure 3.8). This is attributed to the relatively large range of local canyon H/W ratios and possibly to ϵ variations. Figure 3.9 embellishes Figure 3.8 by including each of the EIRT angles used. In general, the warmest facet temperatures are obtained with the 30 or 45° EIRT when viewing an irradiated facet. Again, this is probably due to shading in the lower parts of the street canyons because of canyon geometry and the presence of awnings and building overhangs at lower levels. When facets are shaded, there is some tendency for the larger angle EIRT to view a slightly lower temperature; this may be a function of specular reflections from the sky or a true decrease in temperature with height.

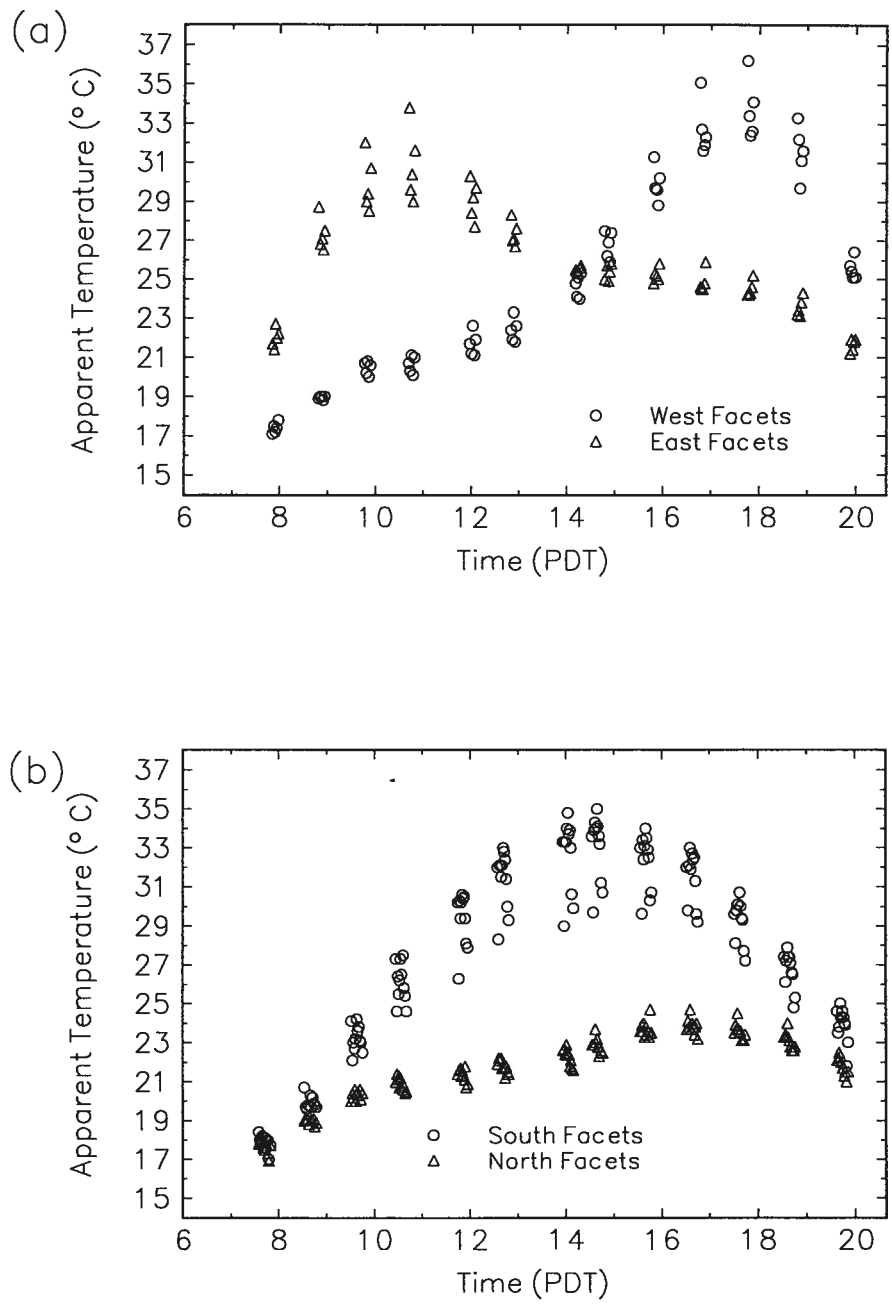

Figure 3.6: Mean facet temperatures of each street in the Industrial study area; (a) east and west facets, (b) north and south facets.

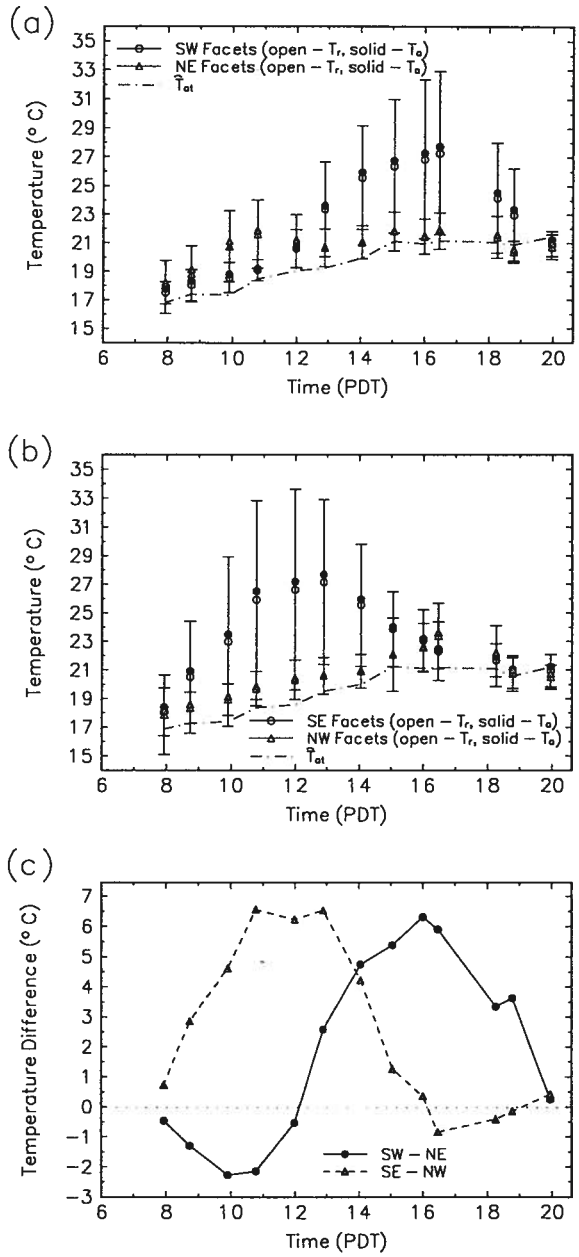

Figure 3.7: Mean facet temperatures (apparent and corrected) and standard deviations following distribution truncation in the Downtown study area for (a) northeast and southwest facets, (b) northwest and southeast facets and (c) mean temperature differences.

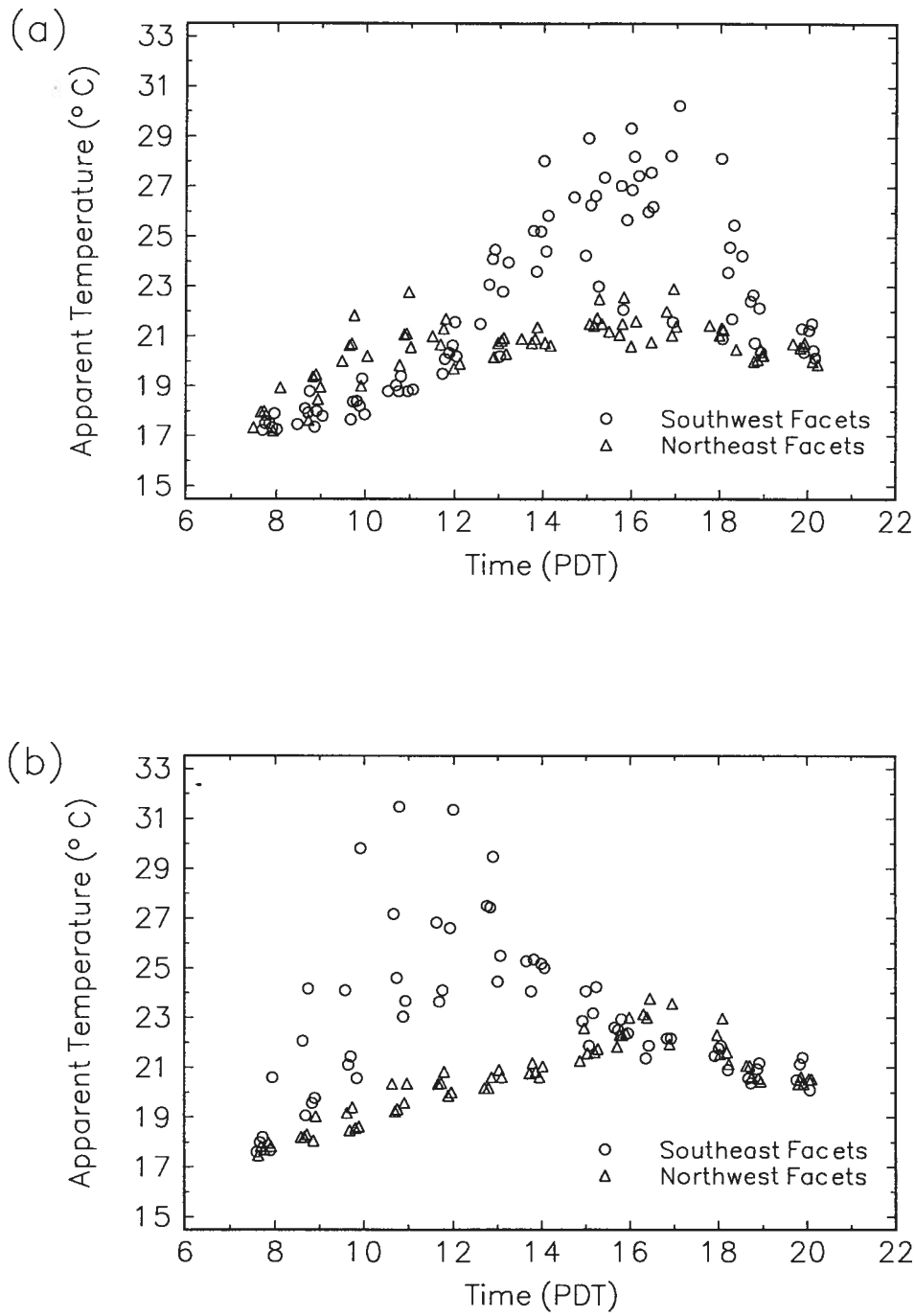

Figure 3.8: Mean facet temperatures of blocks or block sequences in the Downtown study area; (a) northeast and southwest facets, (b) northwest and southeast facets.

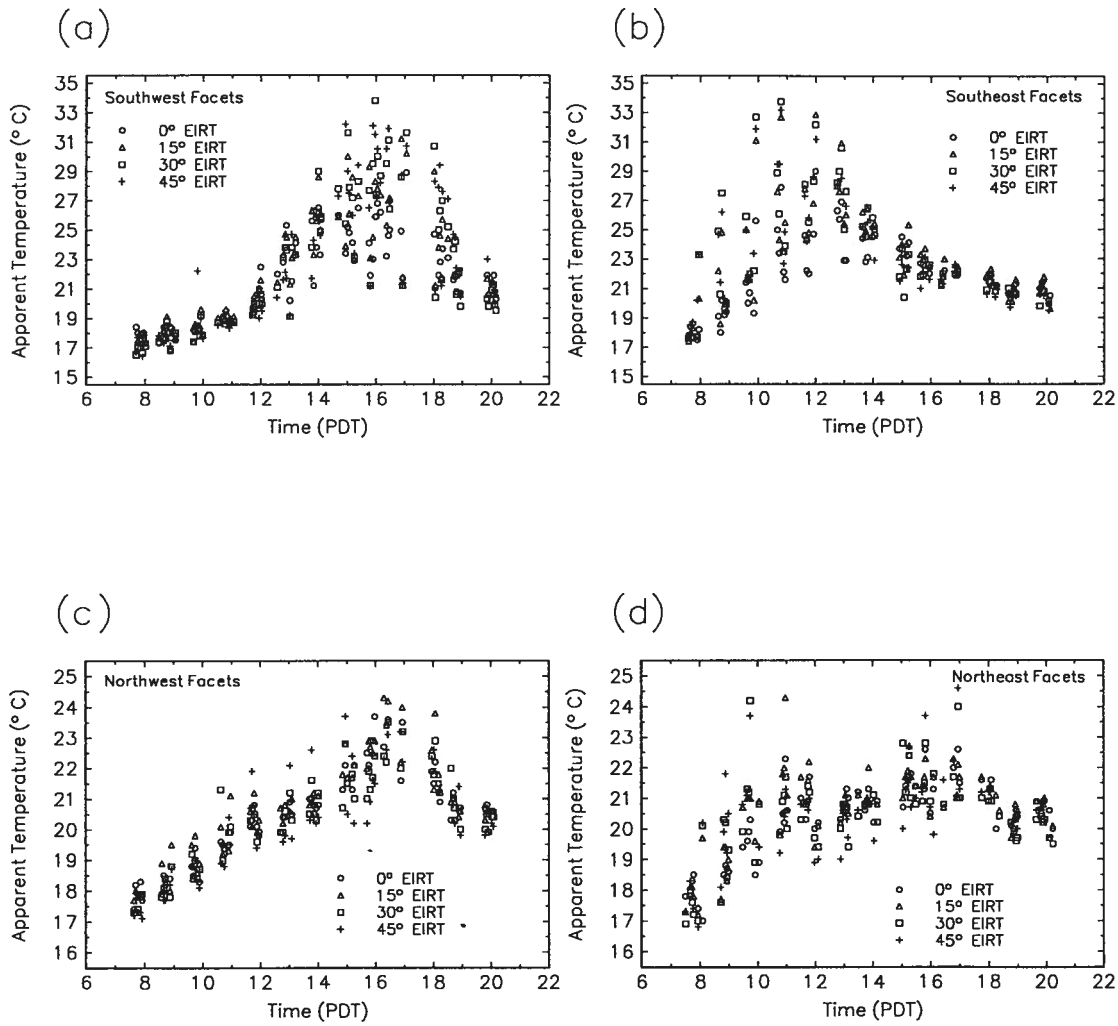

Figure 3.9: Mean facet temperatures of blocks or block sequences in the Downtown study area for each EIRT. (a) northeast, (b) northwest, (c) southeast, (d) southwest facets.

3.1.2.3 Residential Area

Results from the Residential area follow the general pattern described for the Industrial area, but show somewhat smaller differences, and greater variation. Overall mean differences (Figure 3.10c) are smaller, especially for the north-south facet pairing, and for the east-west pairing in the afternoon. Mean facet temperatures (Figure 3.11) show some dependency upon the orientation of the EIRT relative to the facet: south facets viewed by a left-facing EIRT and north facets viewed by the right-facing EIRT, each have a warm bias. For the former case, the EIRT may be viewing some low-sloping roofs, and in the latter, the shorter facet to sensor distance increases the likelihood of a warmer temperature.

3.2 Mixed Distribution Modelling

Mixed distribution modelling allows component populations to be extracted from a composite distribution. It has a close analog in the separation of cloudy, or partly cloudy, pixels from clear pixels in remote observations of sea surface temperature (SST). Figure 3.12 illustrates typical temperature histograms from a clear, and a partially cloud contaminated, thermal image.

Several methods are available to estimate the temperature of the sea surface from the mixed distribution (Crosby and Glasser, 1978; Smith, 1985). All methods generally assume that the sea surface temperature is only slowly varying in space, that it can be represented by a Normal probability density function, and that the presence of clouds within the sensor FOV will lower the measured radiance. The techniques attempt to determine the statistics of the SST using either the maximum slope of the Normal probability density function (using a system of equations to solve for the statistical parameters), or by fitting (by least-squares) a Normal probability function to points at the

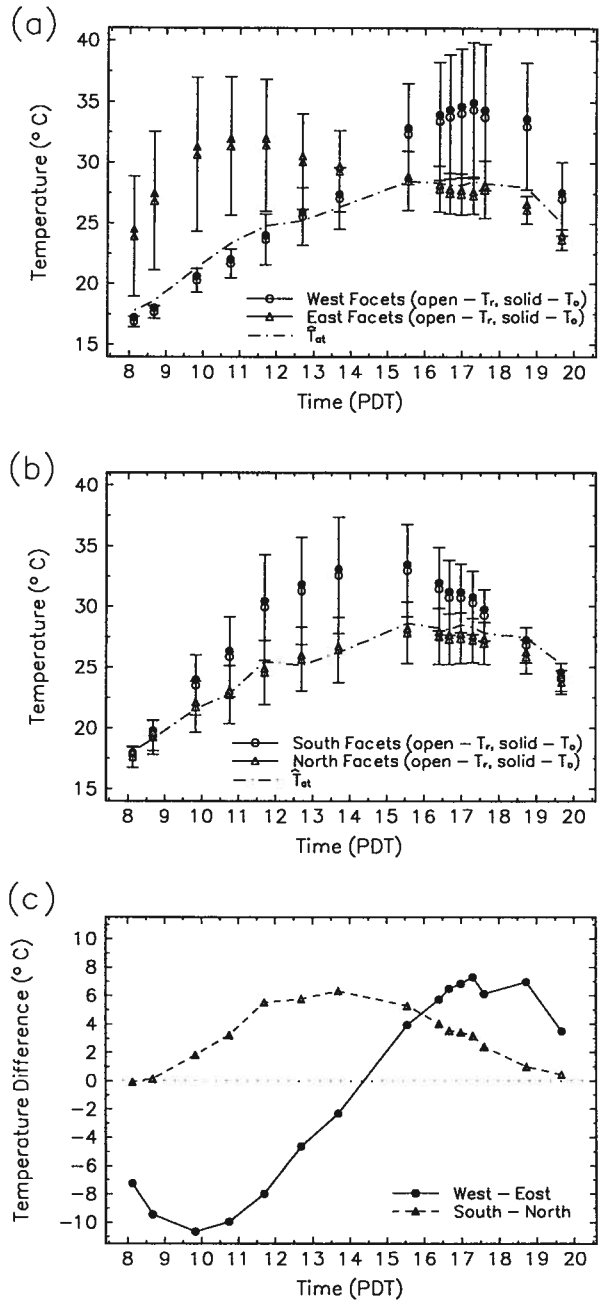

Figure 3.10: Mean facet temperatures (apparent and corrected) and standard deviations following distribution truncation in the Residential study area for (a) east and west facets, (b) north and south facets and (c) mean temperature differences.

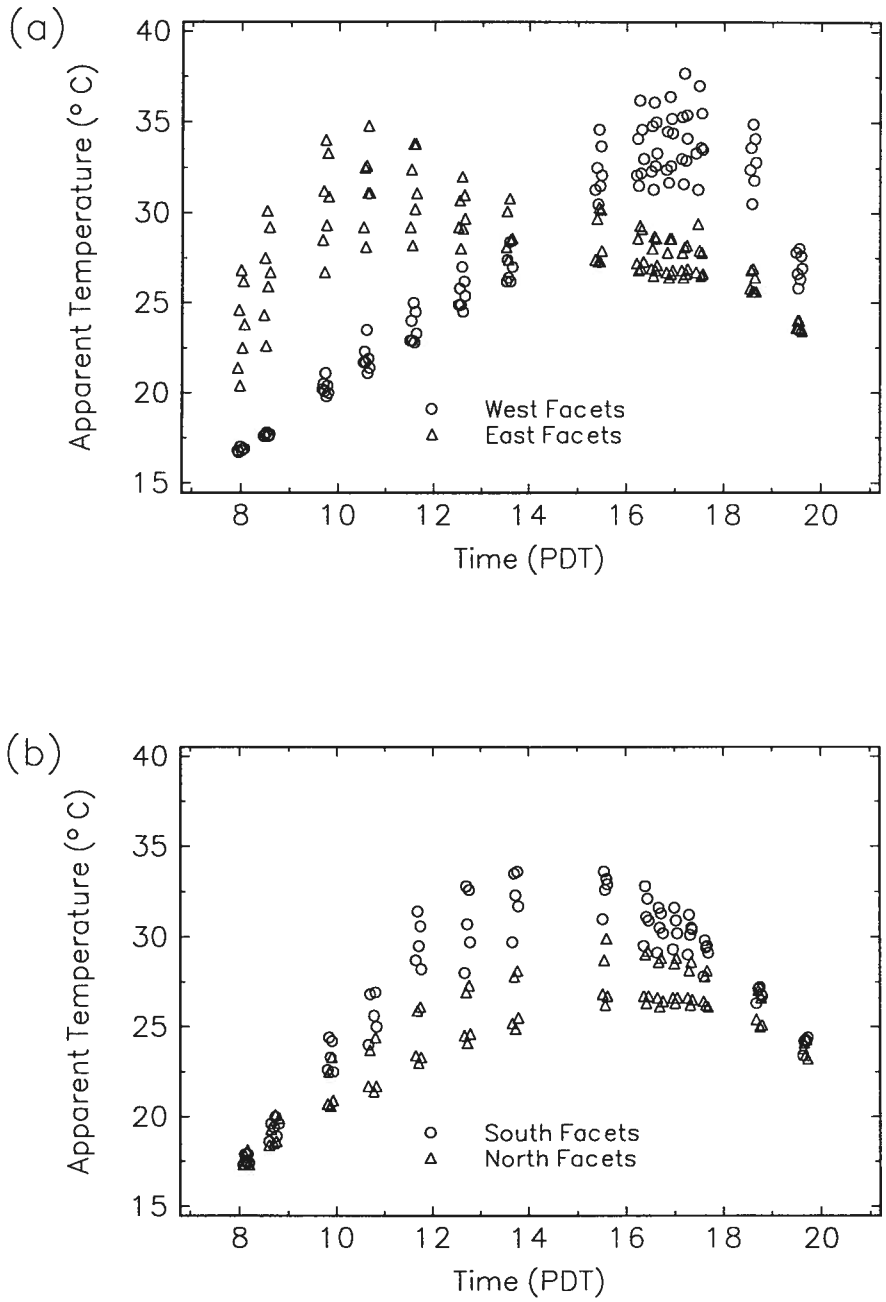

Figure 3.11: Mean facet temperatures of each street in the Residential study area; (a) east and west facets, (b) north and south facets.

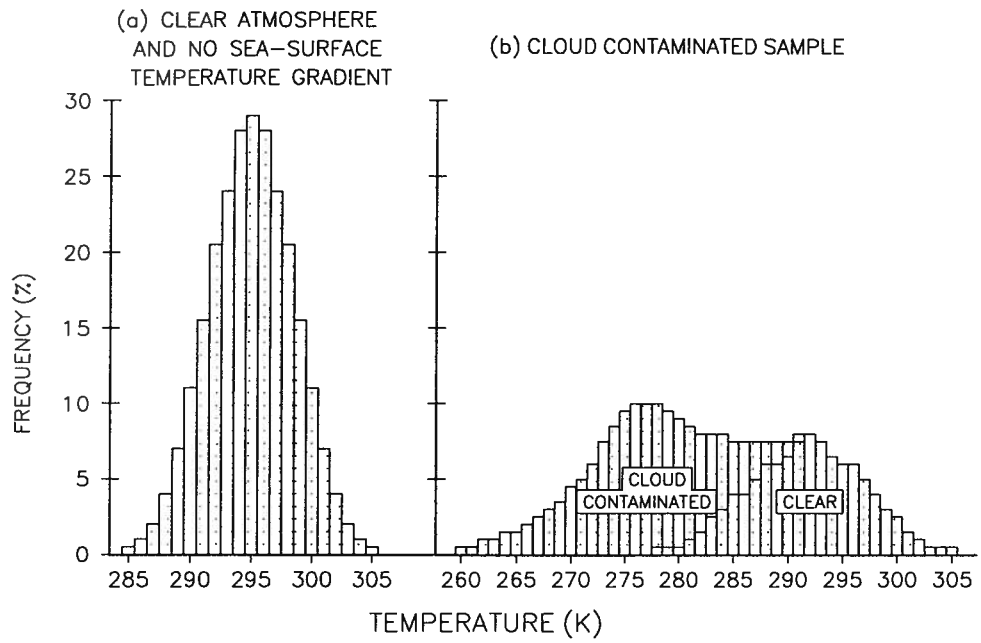

Figure 3.12: Temperature distribution from a satellite image characterized by: (a) clear sky, (b) cloud contaminated. From (Smith, 1985).

end of the observed frequency distribution.

The case of the vehicle traverse observations differs from the cloud removal case in that the underlying surface temperature distribution shows much greater spatial variation than does the SST. For shaded facets, the range of surface temperatures is quite narrow, but the surface temperature of directly irradiated facets is strongly conditioned by the thermal and radiative properties of the materials and any local shading. Because canyon facets are generally distinctly inhomogeneous the resultant temperature distribution becomes very broad. In the limit, where different surface types are separated, and repeated temperature measurements made of each type, it is anticipated that each surface type would be characterized by a Normal distribution of temperatures. If, in the canyons traversed, the facets are composed of only a few major classes of surface types, it may be possible to represent the observed temperature frequency distributions (or at least the upper portion away from the mixed sky-building part of the distributio) with

a combination of normal probability curves. This method is referred to here as mixed distribution modelling. The technique is not new. Harding (1948) describes a graphical method for separating a number of mixed populations with examples drawn from animal science and Sinclair (1976) describes geochemical applications. Presently, computer applications of the technique are available which allow selected probability distributions to be fit to observed data in order to represent the overall distribution. The successful application of mixed distribution modelling allows decomposition of a multi-modal data distribution into its component populations, and to define thresholds which separate the data into groups corresponding to the component populations. It assumes there is an underlying physical model for the process generating the data. The goal is to identify the values of the parameters in the model equation because they have physical meaning. The prime requirement is that the model equation be correct, otherwise the values of the parameters will not be physically meaningful.

Here, mixed distribution modelling is applied to the temperature frequency distributions obtained from the vehicle traverses to recover the component populations represented in the temperature distributions, and in some cases to remove mixed sky/building pixels from the analysis. For the Downtown study area, in which traverse configuration 1 was used, the distributions of the 15, 30 and 45° EIRT were pre-truncated to remove the obvious sky and mixed sky pixels prior to implementing the analysis. The mixed distribution modelling procedure used was the computer program PROBPLOT (Stanley, 1987). The number of classes was selected in order to achieve a good visual fit. The fit was then optimized using a maximum likelihood procedure.

3.2.1 Road Surface Temperature

Road surface temperatures (T_{road}) offer the simplest application of mixed distribution modelling to the observed temperature frequency distributions. Assuming that the road

surface material is reasonably constant over the traverse route, the main control upon the measured surface temperature is the presence or absence of shading. However, there are probably some variations in road surface properties due to asphalt of differing ages within the study area, and variations in the local slope of the road surface. In addition, the length of time the road surface has been shaded results in further variations in surface temperature. Figure 3.13 presents a road surface temperature distribution from a morning traverse in the Industrial area. The distribution is well represented by three Normal curves. The lowest temperature distribution has a fairly narrow standard deviation, and is thought to represent those sections of the road surface not yet heated by direct solar irradiance. The uppermost distribution comes from the road surface which has undergone direct heating, and the middle distribution may represent surfaces in transition. In this example, the curves were fit using the PEAKFIT^{TM} non-linear curve fitting program which implements the Marquardt-Levenberg algorithm for minimizing the sum of the squared deviations. This program provides significant advantages over the PROBPLOT software in terms of the types of distributions which may be used and the control over the fitting procedure.

Results from the mixed distribution modelling of the road surface in the three study areas are presented in Figures 3.14, 3.15, and 3.16. Results are separated by street orientation. The figures give the number of components, and the mean and standard deviation of each of the component populations for each traverse. The position of the mean is indicated by the plotted number which represents the percentage of the total population made up by that component.

In general, the distributions show fewer component populations early in the day with a stronger distinction between the means. This is probably due to the strong temperature contrast between shaded and irradiated portions of the road surface in the morning. Later in the day, when previously shaded portions have been warmed, and previously

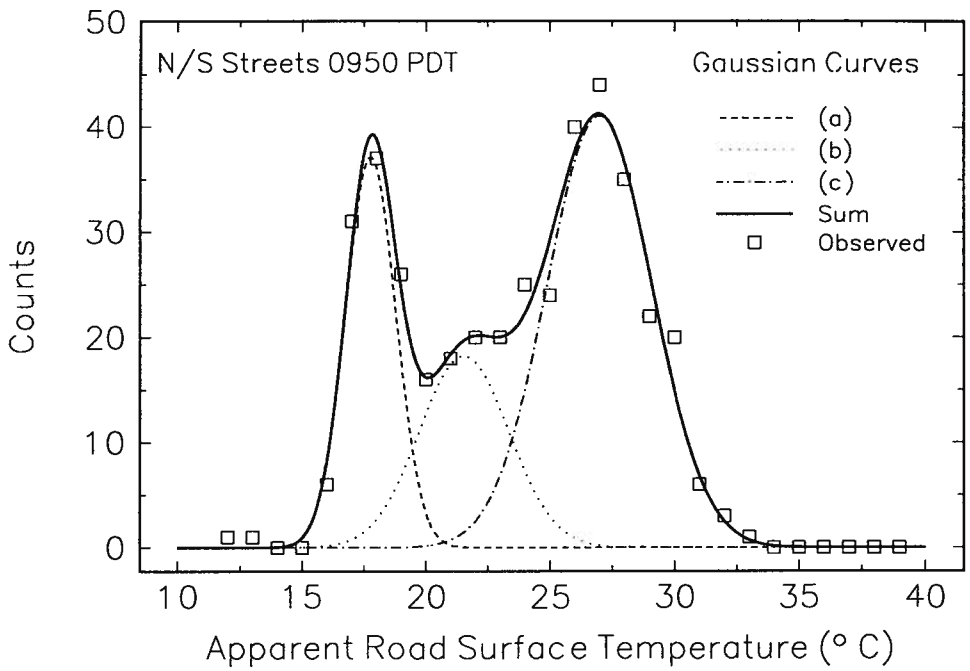

Figure 3.13: Distribution of road surface temperatures in the Industrial study area from a morning traverse showing bimodal distribution characterized by shaded and sunlit road portions.

irradiated portions are shaded (especially evident for N/S street orientations and the Downtown street orientations), the distinction between the means is less. Often there are three or even four component populations. These generally constitute a relatively small percentage of the total data and are thought to be due to areas undergoing transition from shaded to irradiated, or in some cases small areas of extreme temperature, perhaps due to variations in road surface material (i.e., new "blacker" asphalt).

The Industrial area shows a high proportion of the E/W streets in the uppermost temperature class. This is because the small canyon H/W means few shadows are cast onto the road, except early and late in the day. The N/S streets show a higher percentage of shaded temperatures early in the day, but shift to almost entirely high temperatures

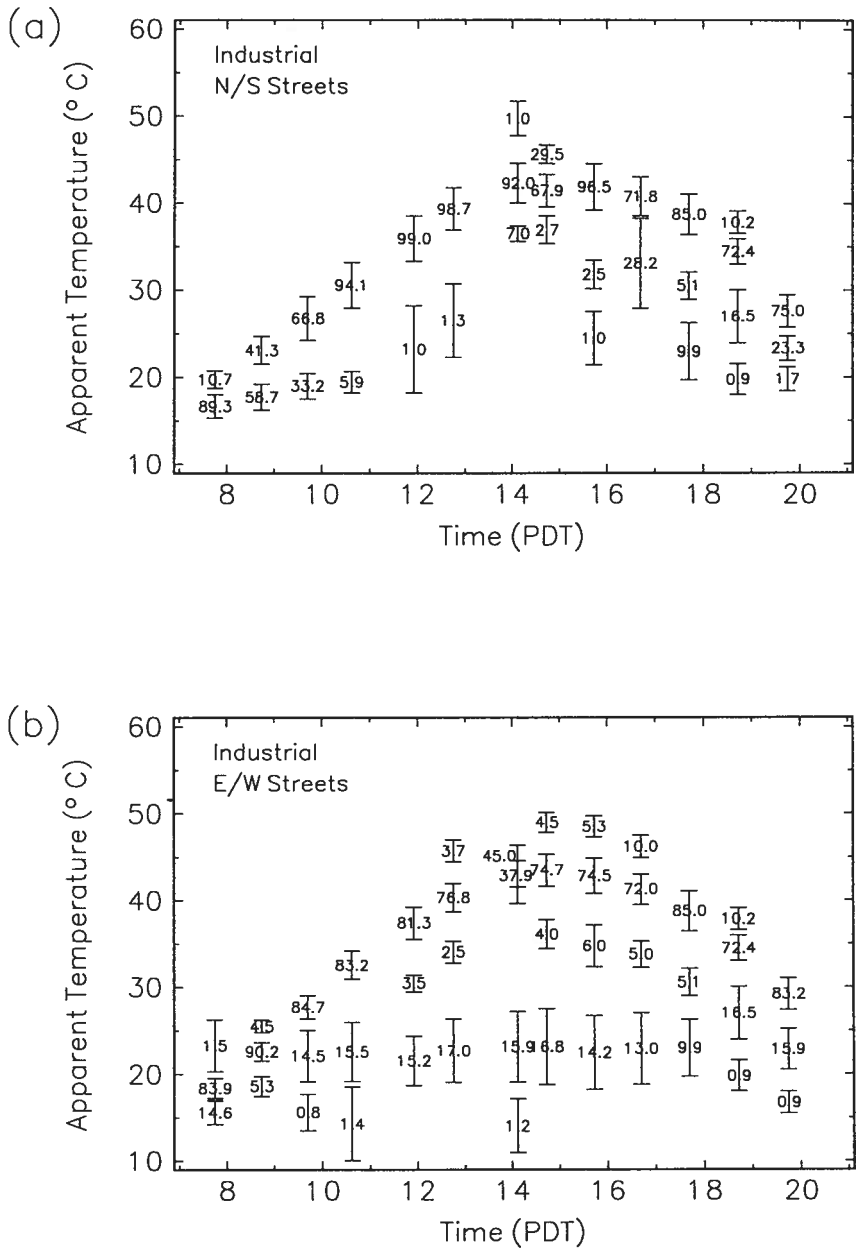

Figure 3.14: Road surface temperature statistics for the component populations derived from mixed distribution modelling for the Industrial area: (a) N/S streets, (b) E/W streets. The number of bars at each time indicates the number of component populations, the plotted numbers are percentages of the total population and are located at the mean of each component. Error bars are $\pm 1\sigma$.

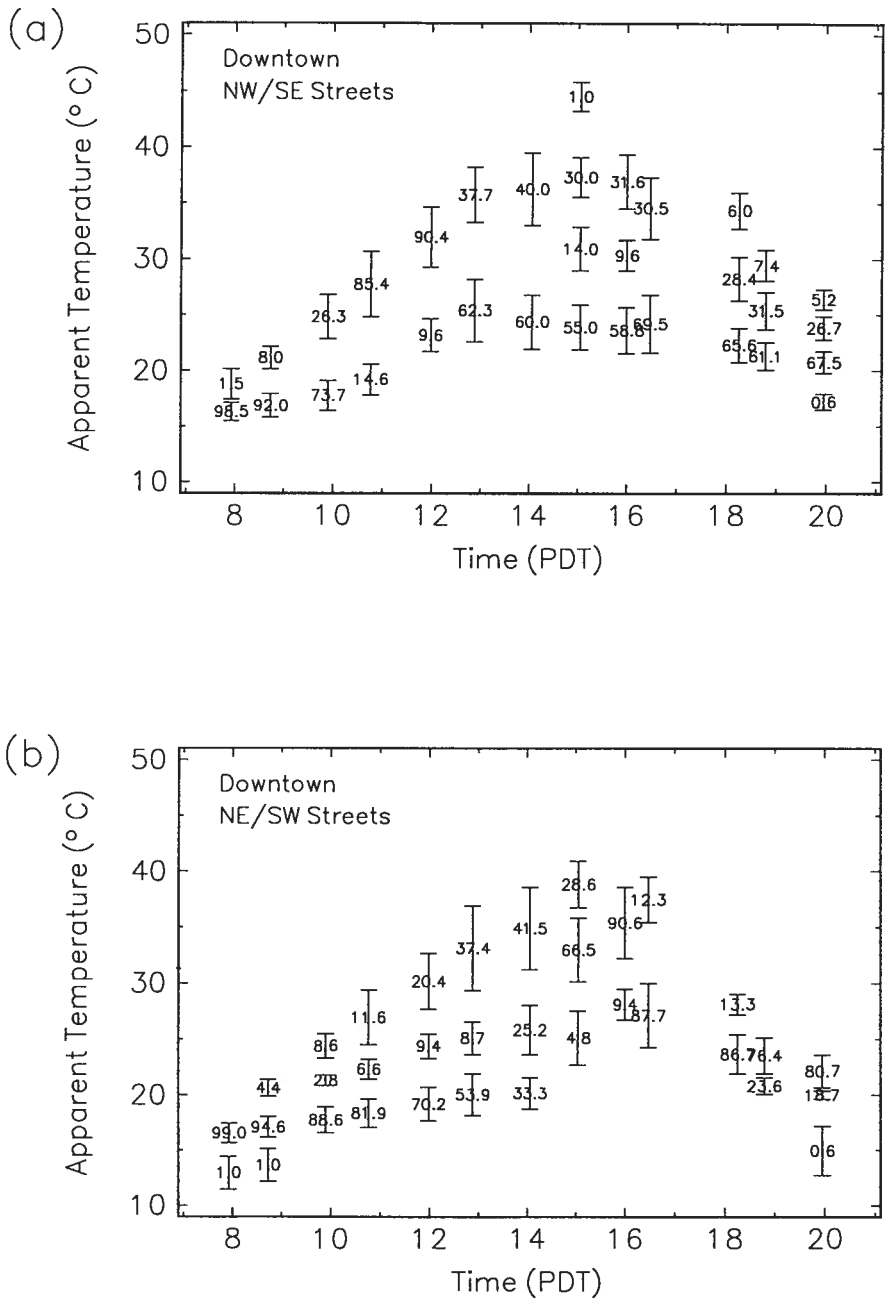

Figure 3.15: Road surface temperature statistics derived from mixed distribution modelling for the Downtown study area: (a) NE/SW streets, (b) NW/SE streets.

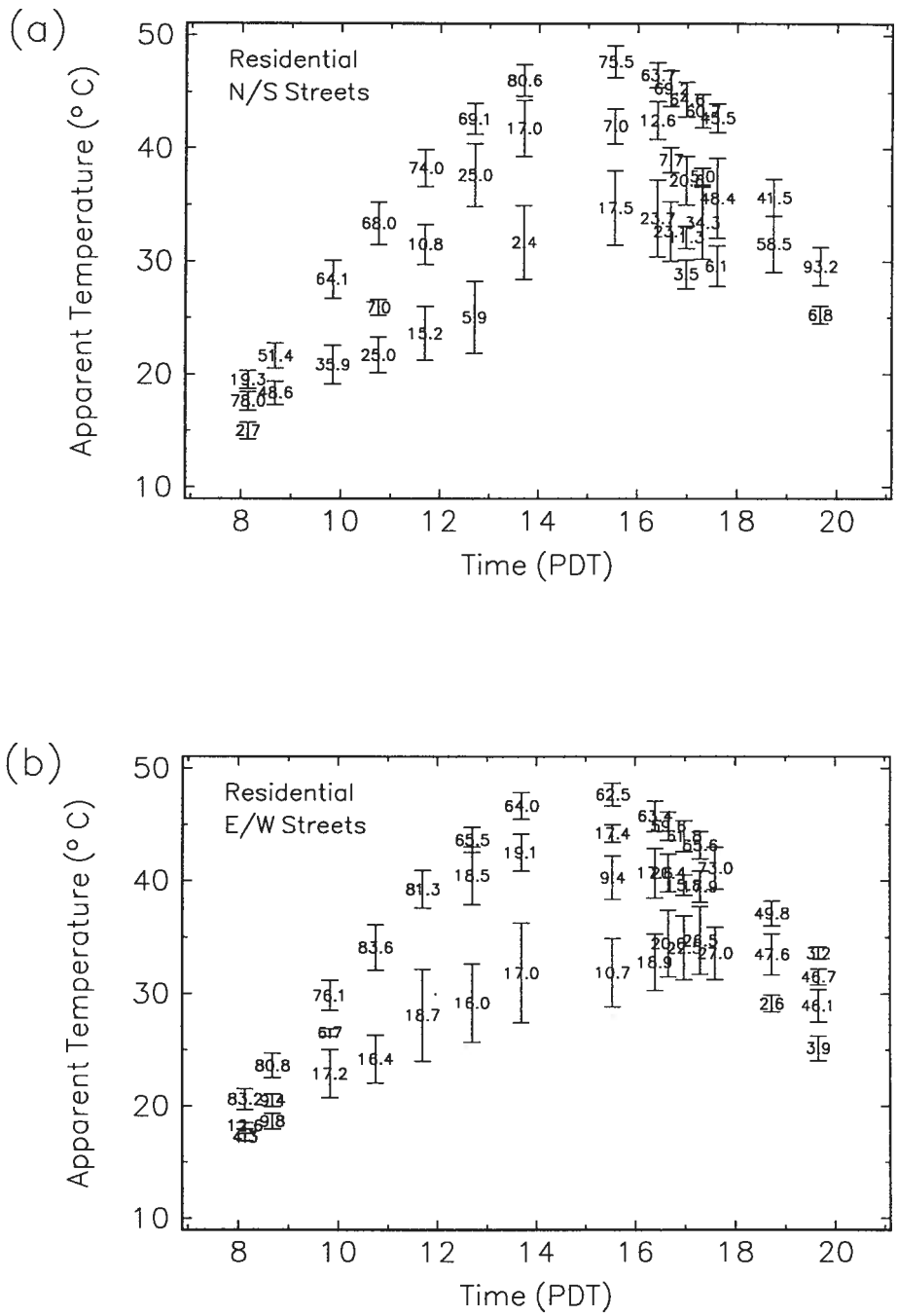

Figure 3.16: Road surface temperature statistics derived from mixed distribution modelling for the Residential study area: (a) N/S streets, (b) E/W streets.

toward mid-morning in accord with increased solar access to the canyon floor. The Downtown study area, with its deep street canyons shows a generally higher percentage of the low temperature distribution except for a short period when the solar azimuth is aligned with the canyon axis and permits direct solar access to the canyon floor. In the Residential area, the N/S streets show a decrease of the percentage contained in the lowest temperature class through the morning and an increase in its standard deviation. At the same time there is an increase in the percentage contained in the highest temperature class. From early afternoon, the warmest temperature class dominates but falls off later. The means of the lowest temperature class remain approximately constant but their percentage increases, and the distinction between the class means decreases with time. The E/W steets show a relatively small shaded fraction in the morning, with some increase in the afternoon. A survey of the study area indicates much greater shading of the road surfaces by mature trees on the N/S streets compared with the E/W streets so direct comparison of these street orientations is limited by the fact that the shading regimes differ.

3.2.2 Wall Surface Temperatures

Wall (canyon facet) surface temperatures present a more complicated application for the mixed distribution modelling technique. Here it is assumed that there exists at least one, and in some cases multiple populations of wall surface temperature, together with sky, and mixed sky and surface, temperature observations. The case of directly irradiated facets poses a particular challenge. The long tail extending towards higher surface temperatures probably represents multiple surface types with high temperatures, and is also probably a function of the FOV of the instrument since that incorporates some averaging of the surface temperatures. In order to better separate these populations, truncation of the distribution at the lower end can be utilized in cases where sky and

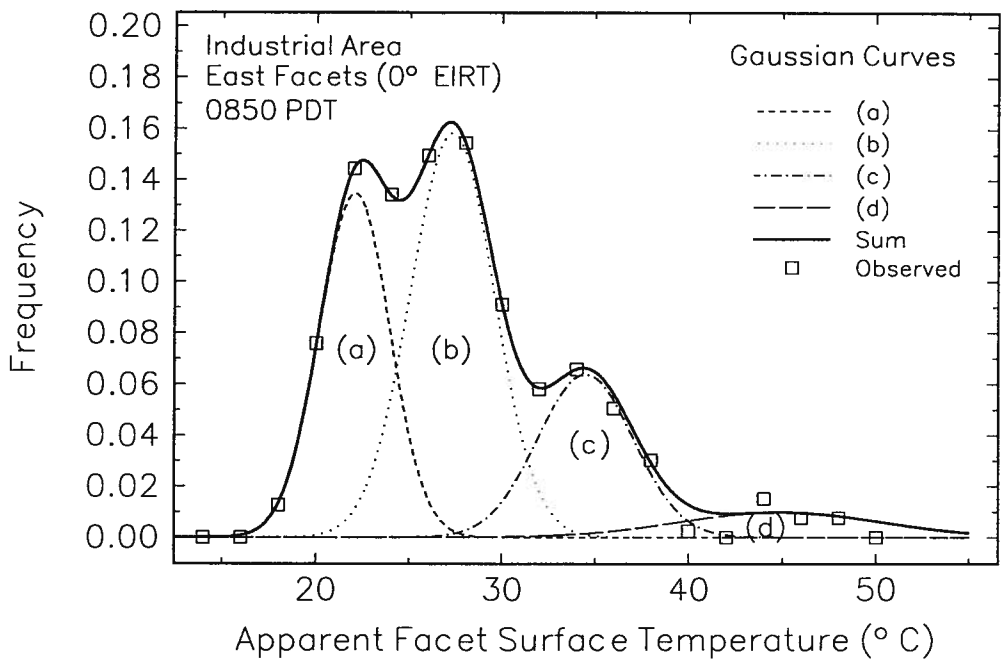

Figure 3.17: Morning east-facing facet temperature distribution with component populations from the Industrial study area.

mixed FOV temperatures are obvious.

Figures 3.17, 3.18 and 3.19 present results for three traverses which view facets experiencing direct solar heating. Figure 3.17 is for a west (east-facing) facet in the Industrial area taken in the early morning (0845 PDT). Three main components represent the majority of the distribution. A fourth, small, high temperature distribution is also added, but it is not well represented in the measured distribution. Figure 3.18 is a west-facing wall taken during the late afternoon (1730 PDT) and again is well represented by three component distributions.

Figure 3.19 illustrates a particular case in which the number of individual distributions becomes large, and/or there is significant overlap between distributions, possibly created due to averaging effects within the sensor FOV. The distribution may be fit by a finite

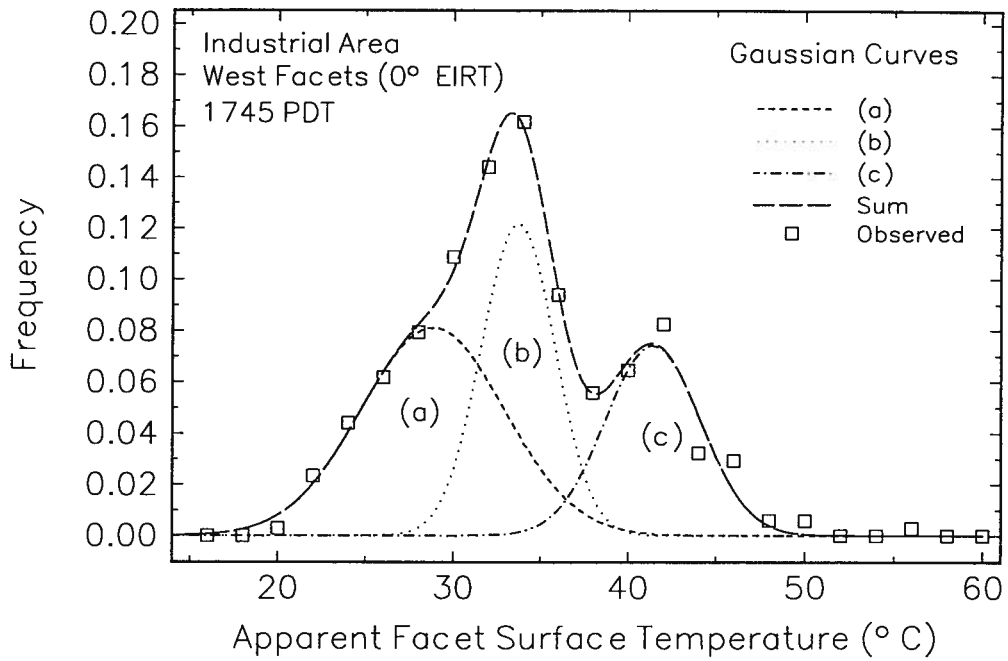

Figure 3.18: Late-afternoon, west-facing facet temperature distribution and component populations from the Industrial study area.

number of Normal distributions, in this case 4, or, alternatively the overall distribution can be represented fairly well by a single exponentially-modified Gaussian. The use of exponentially-modified Gaussian may thus be more appropriate when the sensor IFOV is large with respect to the areas of component temperatures.

The simple model for estimating EIRT temperatures (Section 2.5.3) was used to determine if the mixed distribution modelling could accurately recover the model temperatures. Table 3.2 compares the model input and mixed distribution results for a 10° EIRT viewing each facet in the Industrial area during a mid-morning traverse. As a test of the procedure, the simple EIRT response model was used to generate some model temperature distributions. Input was provided by several normal distributions of selected mean and standard deviation to represent different surface temperature classes. The

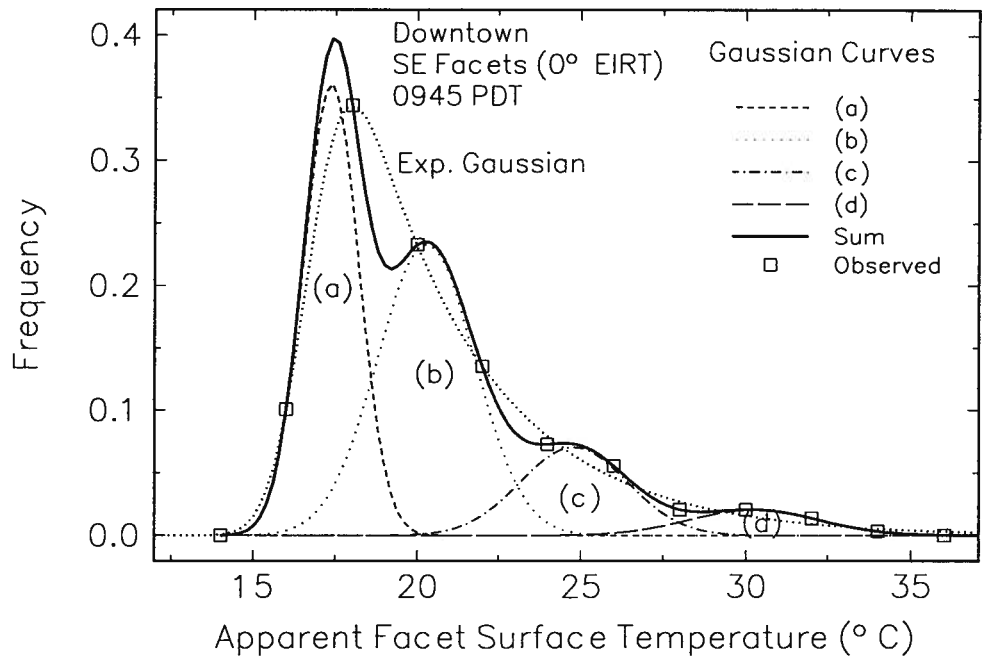

Figure 3.19: Morning southeast-facing facet temperature distribution from the Downtown study area showing representation by multiple normal distributions and a single exponential Gaussian distribution.

output was submitted to the PROBPLOT program to see if the original input statistics could be recovered in the presence of the mixed sky and building pixels. The results (Table 3.2) show that the procedure can recover fairly closely the original temperature distribution statistics, but that the number of classes needed to achieve a good visual fit is often higher than the number of classes specified. This is probably due to the mixed FOV temperatures. Standard deviations are generally larger than those specified, although truncating the distribution results in a better agreement between the recovered and specified values.

Results from the three study areas are presented in Figures 3.20, 3.21 and 3.22. Pre-truncation was performed for the Downtown study area only. In the Industrial area, north

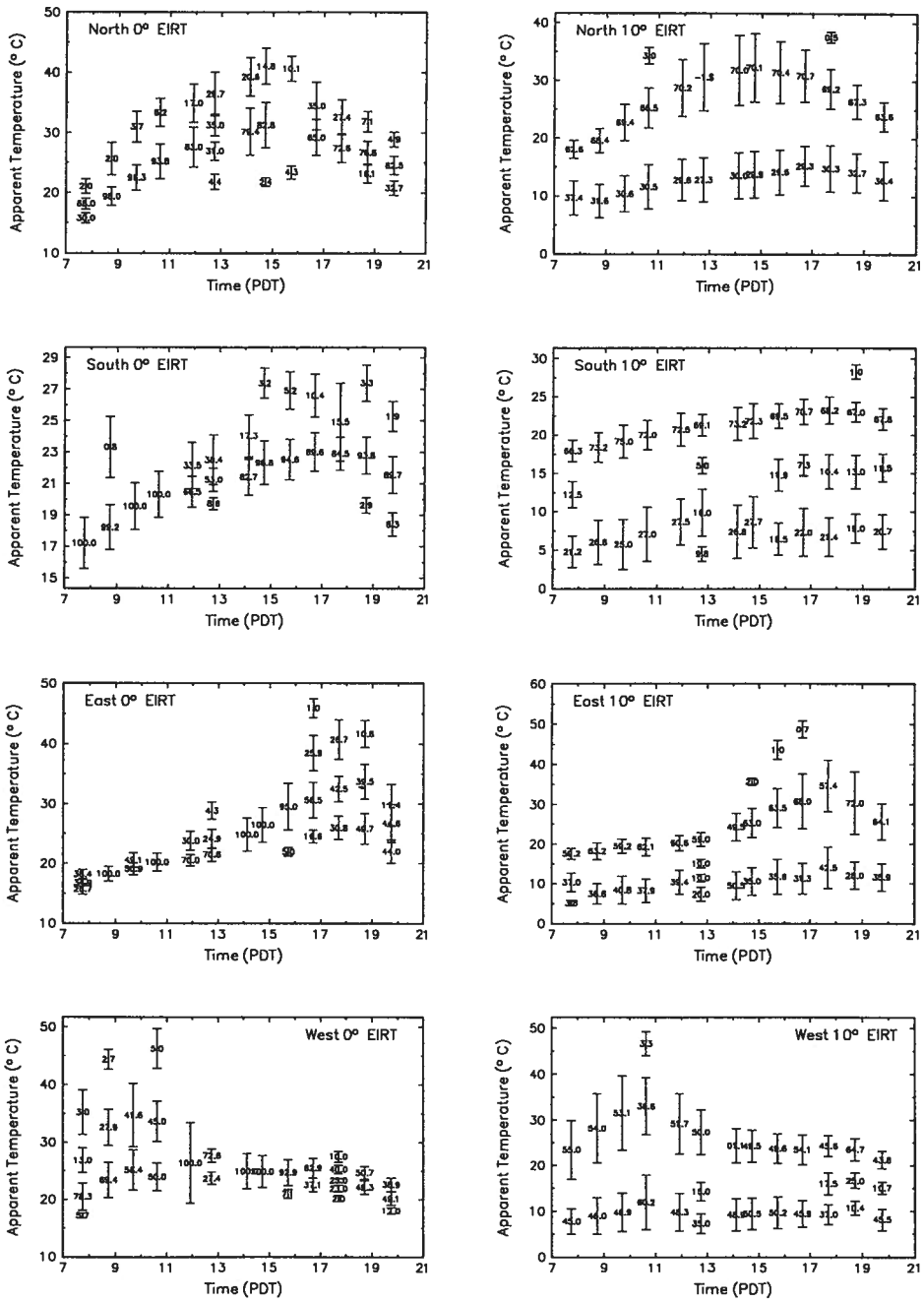

Figure 3.20: Facet surface temperature statistics derived from mixed distribution modelling for the Industrial study area separated by facet and EIRT angle. No pre-truncation of the distribution was carried out.

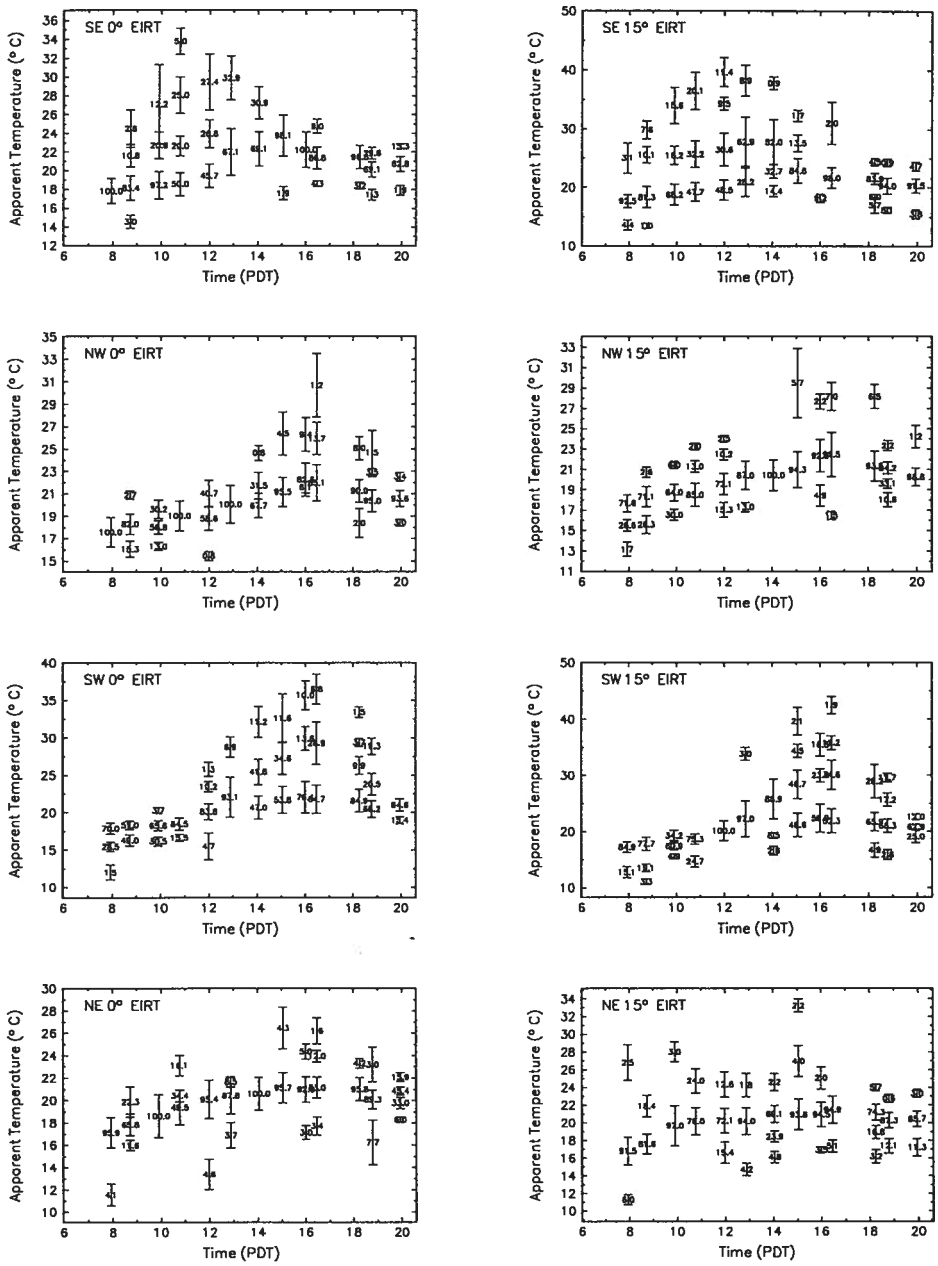

Figure 3.21: Facet surface temperature statistics derived from mixed distribution modelling for the Downtown study area separated by facet and EIRT angle. Distributions were pre-truncated.

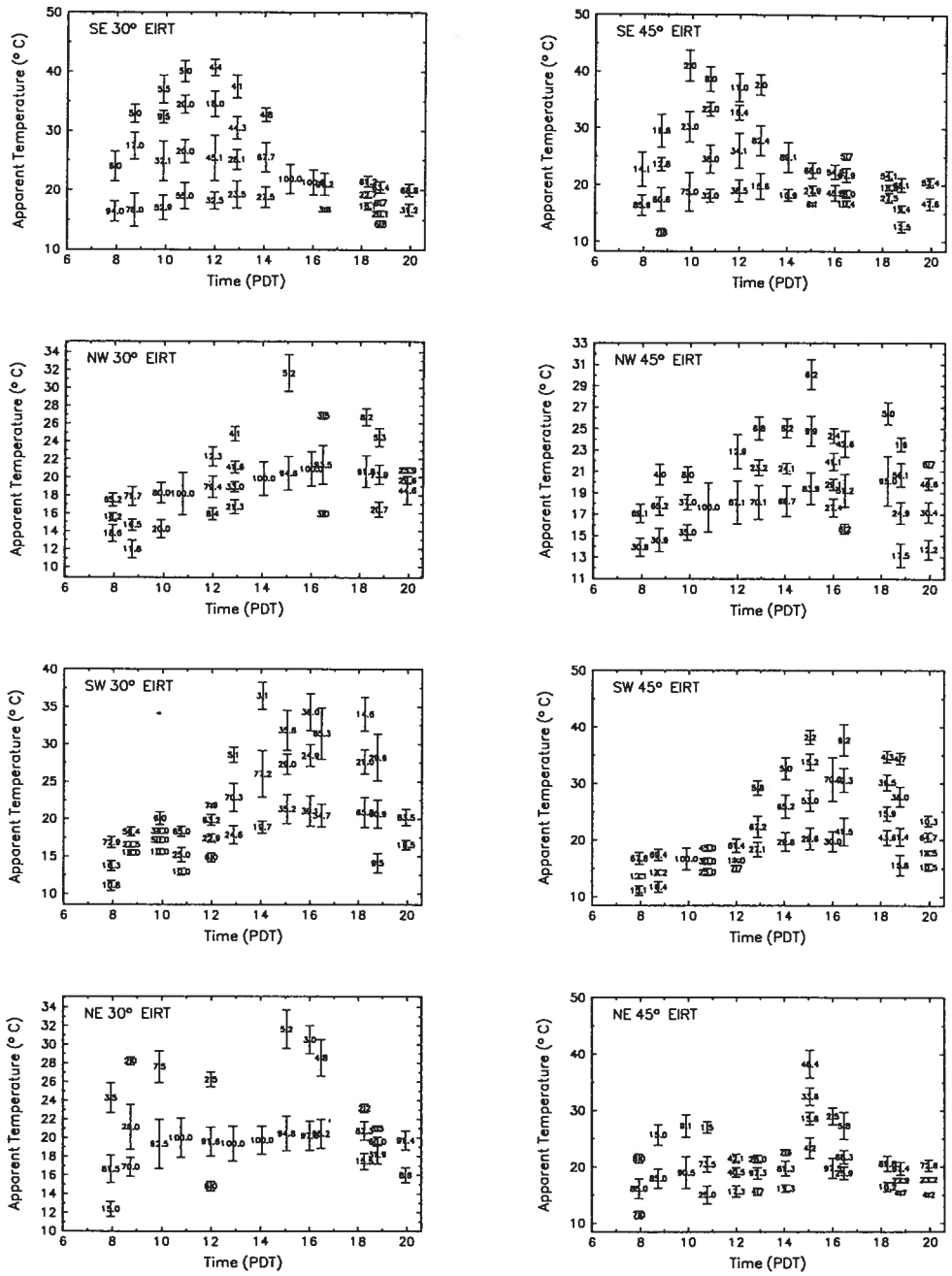

Figure 3.21 (*Continued*). Mixed distribution statistics for the Downtown study area: 30 and 45° EIRT.

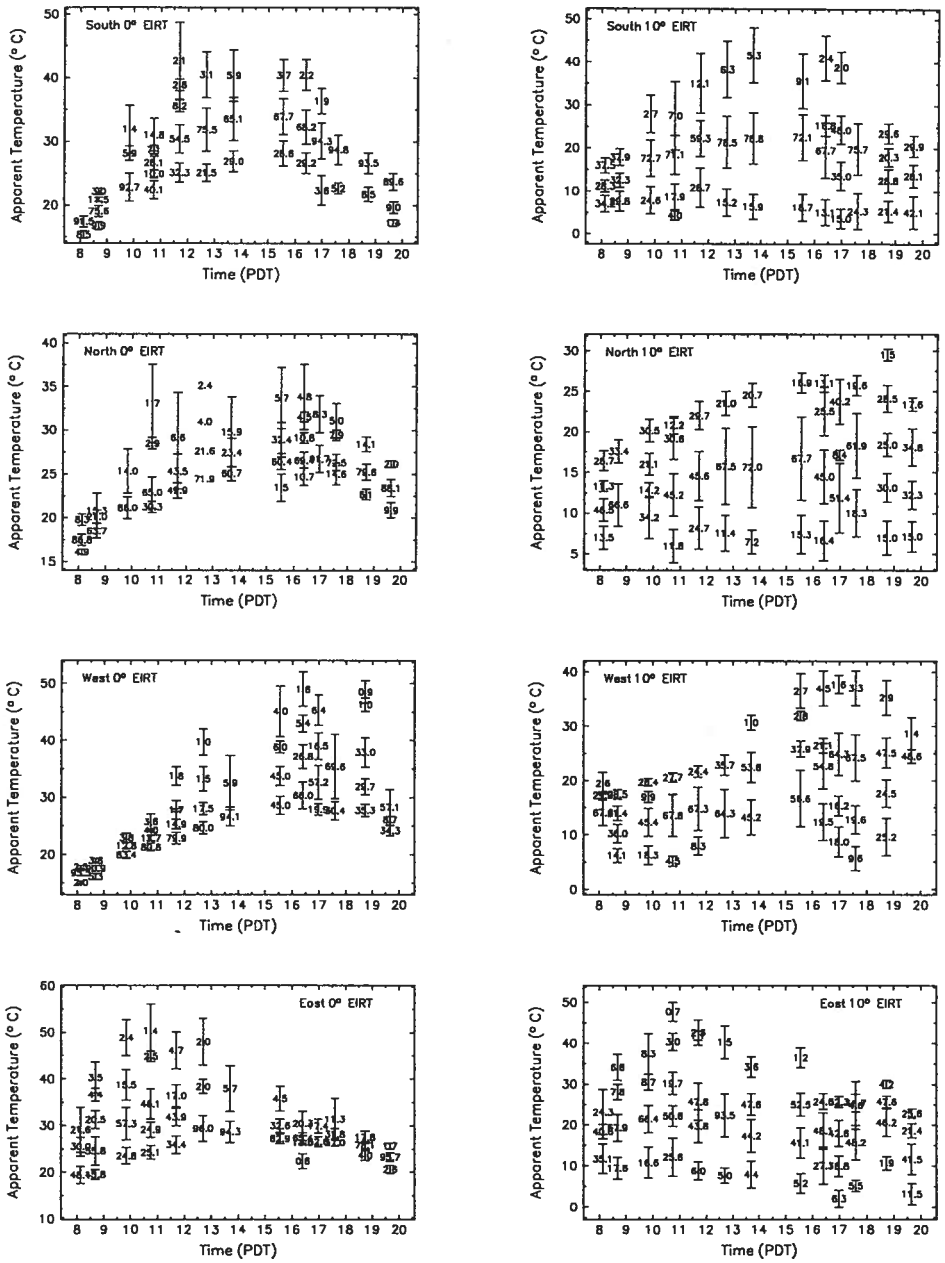

Figure 3.22: Facet surface temperature statistics derived from mixed distribution modelling for the Residential study area separated by facet and EIRT angle. No pre-truncation of the distribution was carried out.

and south facet temperature distributions are generally characterized by two populations, while the east and west facets show one or two narrow distributions during the time they are shaded and an increase in the number and standard deviation of the components when irradiated. Interestingly, the north facets (south-facing), which are directly irradiated for much of the day, do not show as great a variation or number of component populations as do the east and west facets when they are directly irradiated. This may be due to the reduced influence of direct-beam radiation due to the small local zenith angle at these times, or perhaps to greater use of shade devices which reduce the area directly irradiated. The 10° EIRT differs from the 0° in that there is an obvious separation of the distribution into facet and non-facet temperatures; with the lower temperature distribution assumed to be representative of sky or mixed sky/building temperatures. The percentage of this population varies with facet orientation; it is approximately 20-30% for north and south facets and 35-50% for east and west facets. This difference is ascribed to a greater building set-back and the absence of alleyways in the traverses observing east and west facets. There also appears to be a tendency for the facet temperatures to be represented by a single component with a fairly large standard deviation; this may be a function of the resolution of the mixed distribution program during the initial fitting of component populations. Pre-truncation of the 10° EIRT may allow further separation of the facet temperatures into further components.

In the Downtown traverse (Figure 3.21) facets under direct irradiance show three or four well separated component populations. Shaded facets sometimes have a small warm component the origin of which is uncertain. In some cases it may be due to reflected radiation or in others to temporary obstruction of the instrument FOV by a passing tall vehicle, which was known to occur. Small, low temperature components may be an artifact of the truncation procedure, which used a relatively conservative truncation point to minimize the loss of any real facet temperature data. Results from the Residential area

Table 3.2: Temperature distributions assigned to a simple model of EIRT response ($\bar{T}_m$, σ_m), and results from mixed distribution modelling on the EIRT model output using the entire temperature distribution ($\bar{T}_p$, σ_p) and a truncated distribution ($\bar{T}_{pt}$, σ_{pt}).

Facet	Assigned		Mixed Distribution Modelling			
			Entire Set		Truncated Set	
	$\bar{T}_w$	σ_w	$\bar{T}_w$	σ_w	$\bar{T}_w$	σ_w
WEST	5.0	1.5	5.4	1.7	28.9	1.3
			18.3	6.5	36.4	2.6
	37.5	2.0	36.4	3.2	45.8	2.2
	46.0	2.5	46.2	1.6		
EAST	5.0	1.5	6.5	2.2	16.6	0.3
			13.2	2.7	17.8	0.3
	20.2	0.7	19.9	0.9	19.9	0.8
NORTH	5.0	1.5	5.7	2.0	18.5	1.2
			13.5	2.8	23.3	1.5
	23.5	1.25	23.1	2.0	29.2	1.7
	29.0	1.75	29.4	1.6		
SOUTH	4.0	0.5	4.1	0.6	10.8	0.7
			11.2	2.9	14.3	1.5
	20.5	1.0	20.1	1.4	20.2	1.2

(Figure 3.22) show a tendency for a greater number of components required to represent the total distribution. The 10° EIRT shows a very small percentage of the observations in component populations whose temperature is above air temperature, indicating this instrument provides little information about canyon facets. The behaviour of the east and west facets, as they change from shaded to sunlit, is similar to that described for the Industrial area.

3.2.3 A Single Model for Canyon Facets

An alternative to extracting model components is to model the complete distribution under the assumption that the small scale heterogeneity is too great to allow adequate separation of individual components. Such an approach has been adopted by Holbo and Luvall (1988) in which Beta probability distributions were used to model surface temperature distributions obtained from an airborne thermal scanner over a forested region. Their observed distributions often showed non-Normal shapes which were attributed to small scale variations in the surface type and orientation; e.g., openings in the forest canopy which reveal isolated very warm soil or rock surfaces of differing orientations.

Surfaces, if sufficiently categorized, would be represented by Normal distributions. However the number of components can become very large so that overlap between distributions creates an essentially smooth continuum of temperatures. The Beta distribution is used to represent these distributions because it allows a wide variety of shapes to be represented. This approach makes no assumptions about the number of underlying component distributions, instead it considers the spread of temperature to be related to small scale variations in wall properties which are too numerous to subdivide. Distributions at any time or for any facet orientation may be modelled using a single model, whereas the number of component populations required is higher for strongly irradiated surfaces. The difficulty in using this approach is relating the parameters of the Beta distribution to the more commonly used statistical moments of the mean and standard deviation of each facet.

3.3 Summary

Two methods were examined in order to remove those surface temperature observations from the mobile traverses which have mixed building and sky or sky in their FOV:

truncation of the distribution, or mixed distribution modelling. Following the application of these methods, the spatial and temporal variation of the mobile traverse temperature data were examined for each of the study areas in order to determine the magnitude and timing of maximum temperature differences between vertical facet pairs. The results indicate the following.

- Distribution truncation investigated a subset of surface temperatures from a north or northeast facet which was shaded for most of the day and compared these with various parameters including: air temperature from the traverse vehicle, fixed air temperature sensors, hand-sampled temperatures from ground teams, and temperatures from the airborne thermal imagery in order to determine a reasonable lower limit for the apparent surface temperature.

- Truncation measures differed for each study area: in the Industrial area $\hat{T}_{at} - 2°C$ is used, in the Downtown study area the minimum of $\hat{T}_{wt} - \sigma$, $\hat{T}_{at} - \sigma$, and in the Residential area $\hat{T}_{wt} - 2\sigma$.

- Temperatures of the facets show large increases in variance when directly irradiated and means for each block show much greater variation under these conditions.

- Temperature differences between facet pairs are greater than 10°C in the Industrial area and slightly less in the Residential, with the largest difference occurring mid-morning between east and west facets. Other times of maximal temperature differences between facet pairs occur within approximately 1 hour after solar noon between north and south facets and in the late afternoon between east and west facets. In the Downtown area, the different street orientation yields one time period with a large facet temperature difference and a second where the differences are minor, with results showing a fairly high degree of symmetry.

- Mixed distribution modelling is demonstrated for road surface temperatures where the number of component populations is related to areas of the road which have been shaded or irradiated for some time, and areas which have recently changed from one radiation regime to the other. Morning distributions in particular are well represented by two component populations, later in the day generally three populations are required.

- Modelled surface temperature distributions were used to determine how the technique would behave in the presence of mixed sky and building temperatures. Any bias towards low temperatures caused by mixed pixels not discarded appears to be minor.

- Application of the mixed distribution modelling to vertical facet temperatures results in most distributions requiring between two and four component populations. The technique is less successful when facets are directly irradiated because the number of underlying distributions of temperature is potentially very large due to differences in surface material combined with varying radiation regimes.

- Results from the Industrial area show, without pre-truncation of the distribution, there is less sensitivity in the method for the 10° EIRT, but there is a clear separation of a low temperature population.

- The Downtown area is characterized by a greater separation of component populations than the other two study areas; the Residential area requires more components and results show the 10° EIRT to be of limited use for representing facet temperature.

Chapter 4

AIRBORNE TIR OF SELECTED LAND-USE AREAS

4.1 Introduction

An airborne thermal scanner was used to provide detailed surface temperature information in each of the study areas to complement that obtained by ground-based sampling. The airborne scanner allows direct observation of the extent of anisotropy in surface long-wave emission over selected urban land-use areas and also allows the compilation of a complete urban surface temperature distribution, through the acquisition of images from different view directions. The approach adopted provided benefits in terms of flexibility, cost and detailed coverage of small areas.

This chapter details the methods and equipment used to obtain the imagery, post-acquisition corrections to the imagery, and the results of analyses performed. Details of the instrumentation and correction techniques are provided in appendices and are referred to where appropriate. It is not the aim to provide an exhaustive accounting of the thermal response of different surface types (see e.g., Quattrochi and Ridd, 1994). Instead, the emphasis is upon a description of how the distributions of temperature for the land-use areas vary with time and view direction and how the temperature distributions of component surfaces combine to form the overall distributions.

4.2 Methods

4.2.1 Thermal Imaging System

The thermal imaging system used was the AGEMA Thermovision 800 BRUT System equipped with a model 880 LWB scanner. System components are illustrated in Figure 1.1; full description of the specifications and operating details of the scanner are provided in Appendix A. A brief summary of the main features is provided here.

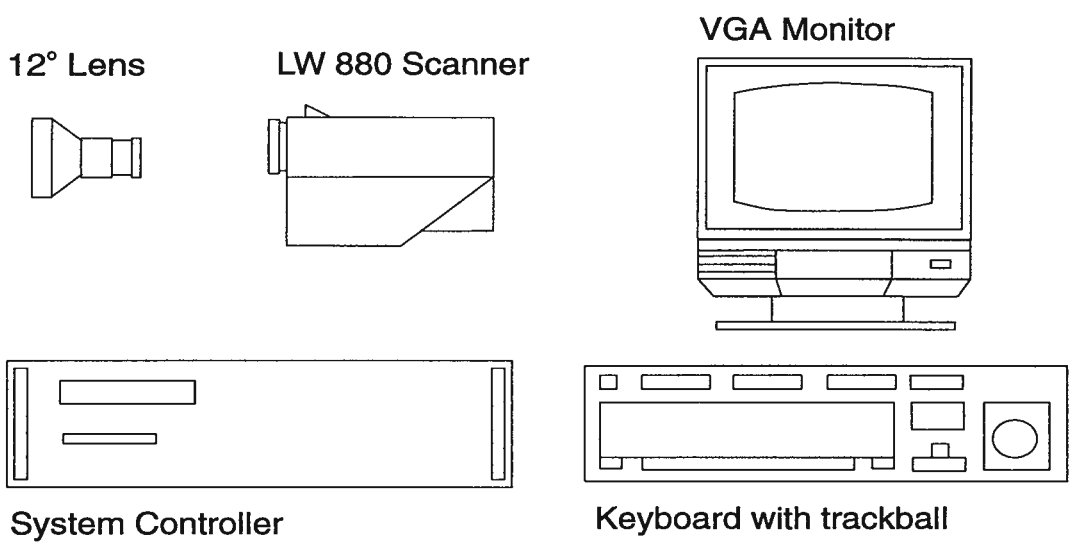

Figure 4.1: AGEMA 880 system components.

The scanner uses a cryogenically-cooled detector which is sensitive primarily in the 8–14 μm waveband, and is capable of measuring surface temperatures between −30°C and 1300°C with a sensitivity of 0.05°C at 30°C. The scanner was fitted with a 12° FOV lens with a geometric resolution of 1.2 mrad. Images were obtained by scanning a set number of lines (140 or 280) across the FOV. Each line consists of 140 pixels. The images were stored digitally on an internal hard disk and later transferred to other computer systems for processing and analysis.

4.2.2 Helicopter-AGEMA Installation

The AGEMA system was installed in a Bell 206B JetRanger helicopter. The system controller and monitor were placed in the front passenger seat together with a portable power supply consisting of two deep-cycle 12 V batteries and a DC-AC power inverter. The system operator occupied the left back seat and directed operations via the system keyboard and the internal helicopter communication system (Figure 1.2).

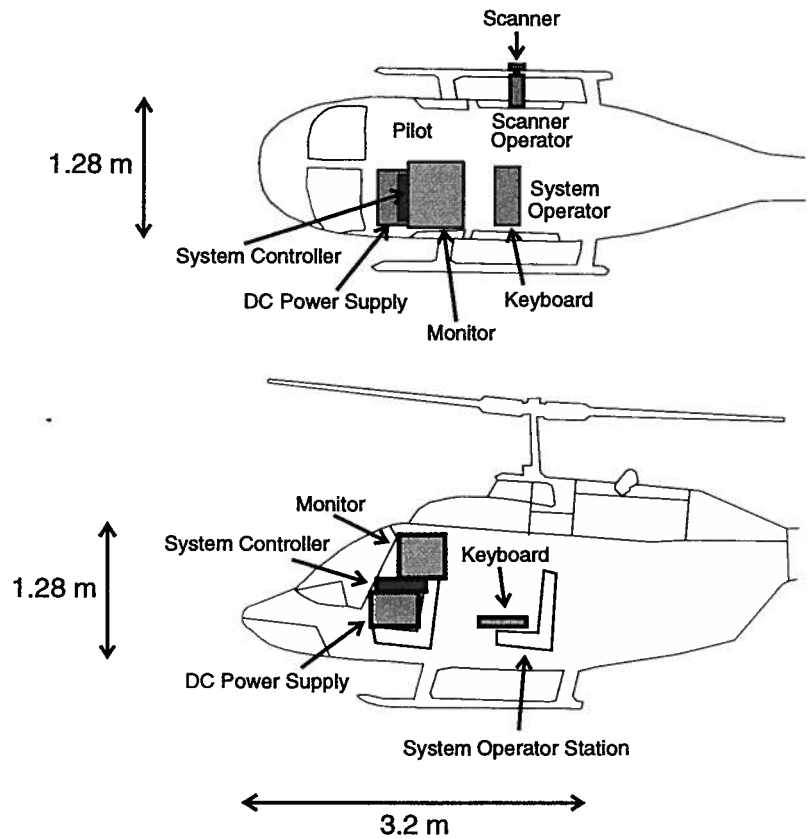

Figure 4.2: Thermal imaging system installed in the helicopter. Top: top view, Bottom: side view.

The scanner was mounted on a custom-built harness worn by a second operator. The harness was strapped over the operator's shoulders and the scanner was mounted

on an adjustable camera mount fixed to a plate projecting forward from the harness (Figure 1.3). Using body position and an attached level, the scanner operator directed the scanner towards the ground at right angles to the flight path at the required viewing angle. The scanner operator was in communication with the system operator and pilot, so that by adjustment of the flight path and scanner direction, the required ground areas were imaged. To avoid viewing the helicopter skid during nadir flight lines, the scanner operator stood on the skid and leaned outwards to ensure an unobstructed view of the ground.

4.2.3 Remote Sensing Flights

Eight primary flights were made in support of the objectives outlined in the introduction. A series of four additional flights was made in support of other research objectives. Details of each flight are listed in Table 1.1. Flights originated and terminated at Vancouver International Airport. Times listed for Flights 1–8 are for the period of image acquisition, including imaging of the ground calibration sites carried out prior to, and following coverage of the selected land-use area. For Flights 9–12 the times refer to the sequence of continuous scanning between the rural area (Delta) and downtown Vancouver. Overflights of several urban parks were carried out following this sequence.

The time of the flights was determined from an analysis of preliminary auto-traverse data which identified the times at which vertical facet temperature differences were maximized for the canyon orientations in each of the study areas.

On each flight, the nadir view flightlines were flown first, followed by the off-nadir lines. Because the scanner was fixed on one side of the aircraft, the four off-nadir view directions were scanned in a rotational sequence to conserve flight time, (e.g., east, south, west and north). Two to four rotations were necessary to achieve the required coverage. The ground speed of the helicopter varied depending upon wind direction and speed

Table 4.1: Flights conducted to acquire airborne thermal imagery.

Flt	Date	Time (PDT)	Location(s)	Alt (m)	SA[a] (°)
1	08/15/92	1000–1100	False Creek S.	647, 457	0, 45
2	08/15/92	1345–1430	"	647, 457	0, 45
3	08/15/92	1705–1745	"	647, 457	0, 45
4	08/16/92	1115–1210	Downtown	689, 488	0, 45
5	08/16/92	1605–1645	"	689, 488	0, 45
6	08/17/92	0940–1005	Sunset	975, 548	0, 45
7	08/17/92	1345–1415	"	975, 548	0, 45
8	08/17/92	1705–1730	"	975, 548	0, 45
9	08/24/92	1520–1550	Urban/rural	2134	0
10	08/24/92	2015–2045	"	1524	0
11	08/24/92	2345–0010	"	1524	0
12	08/25/92	0450–0520	"	1524	0

[a]SA-scan angle

but was generally between about 60 and 80 km hr^{-1}. Images were sampled so that a minimum 75% overlap was maintained. Maps of the actual area covered by the images obtained are presented in Appendix D.

Each flight included coverage of one or more ground calibration sites, generally both prior to and following the coverage of the selected land-use area. These sites, located at urban parks, were imaged and compared with ground-based observations of surface temperature over several surface types in an effort to confirm the appropriateness of the calculated atmospheric corrections. Surfaces scanned included water, grass, concrete and asphalt in order to obtain a range of surface temperatures. Details of the methods and results are presented in Appendix B.

Figure 4.3: Scanner mounting arrangement.

4.3 Atmospheric Corrections

The airborne thermal imagery is influenced by the processes of atmospheric absorption and re-emission by atmospheric gases, primarily water vapour, but also ozone, carbon dioxide, nitric oxide, carbon monoxide and methane, which serve to alter the apparent temperature measured by the scanner compared to that observed at ground level. In general, this leads to an underestimate of the surface temperature, for most surfaces under typical daytime conditions (high radiant input, lapse profile). Correction for these processes used the single infrared channel method (Becker and Li, 1990) in which a vertical description of the atmosphere (in terms of pressure, temperature and humidity) is used in conjunction with an atmospheric radiation transfer model to estimate atmospheric absorption and re-emission in the spectral range of the instrument. The model used was the LOWTRAN 7 Atmospheric Transmittance/Radiance model (Kneizys *et al.*, 1988). Measured vertical profiles of pressure, temperature and humidity were made by radiosondes. The lowest layers of the atmosphere were measured by locally launched radiosondes, while upper atmosphere information was obtained from one of the two nearest upper air reporting stations, Port Hardy B.C., or Quillayute WA. Details of the measured profiles, methods and results are presented in Appendix B. Final corrections, in the form of a polynomial approximation, were determined for each altitude/scanner angle combination and applied to images prior to further processing.

4.4 Surface Temperature Analysis

4.4.1 Industrial Area

A thermal image taken at a 45° off-nadir angle towards the south during the morning overflight of the Industrial area is shown in Figure 1.4. The original 280×140 image has

been re-configured to a square 280×280 image for display purposes.

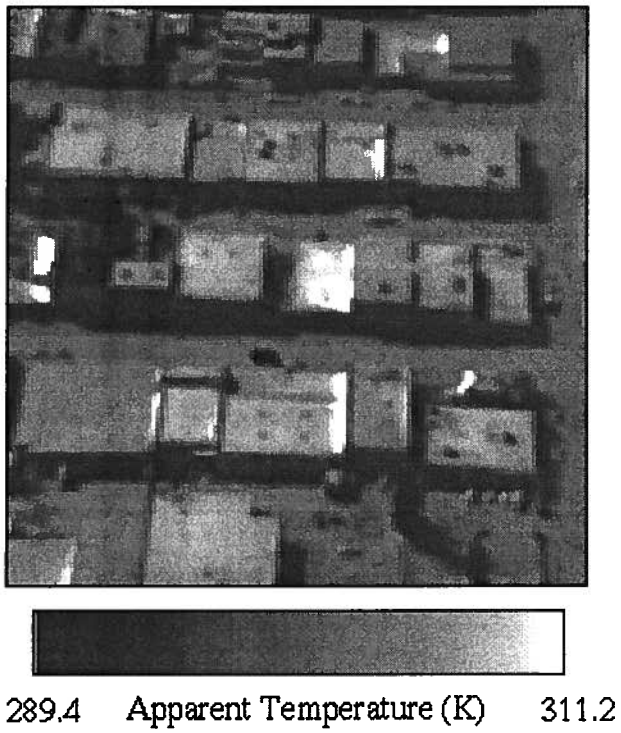

Figure 4.4: Thermal image of the Industrial study area, Flight 1 (1030 PDT). View is southwards at a 45° off-nadir angle.

The flat-topped, rectangular buildings clearly show very warm roof areas; roof temperatures are generally homogeneous for individual buildings but differ between buildings, probably due to material and construction differences. Isolated darker features on roofs are generally related to low emissivity (aluminum) heating/cooling equipment or ducts. Where adjacent buildings are of different heights, some areas of the roof are also cast in shadow.

Road surfaces tend to show a fairly narrow temperature range, except on the N/S street where cooler areas near shadows exist. These are thought to be related to areas formerly in shadow which have recently become directly irradiated. Some vehicles may

be identified as very dark (cool) areas (one is located on the E/W street near the middle of the image); these are trucks with polished aluminum cargo boxes. Painted vehicles are not so easily identifiable; trucks parked at the loading dock of the building in the lower right-hand corner of the image display temperatures as warm as, or warmer than the road surface.

The associated temperature distributions, separated by view direction, are presented in Figure 1.5. The composite image temperature distributions (solid line) are overlaid with temperature distributions from the major surface types present in the study area (flat roofs, roadways, walls and shaded ground). These were extracted from select images by digitizing the component areas and aggregating the temperature values. Areas were defined solely on the spatial pattern of temperature. This may lead to some bias, based upon expected thermal patterns relative to the surface structure, e.g., defining the vertical extent of the walls can be difficult when both they and the ground are shaded. Each frequency distribution is normalized by its maximum class frequency. The position of the component distributions may then be used to determine which surfaces are responsible for the shape of the composite distribution.

The plots show a strongly demarcated low temperature peak for the south, east, and vertical view directions, which is related to shaded wall and ground surfaces. In contrast, the north and westward views show only a minor peak or shoulder at these temperatures. All view directions exhibit a second, clearly defined mode as well as a shoulder of higher temperatures. The distribution of road surface temperatures approximately matches the main peak of the composite distribution but is shifted towards warmer temperatures, especially for the south and east view directions. The upper shoulder is due to roof surfaces, and in the westward viewing case, west (east-facing) walls. The position of the wall temperature distribution varies with view direction and it therefore alters the subsequent shape of the composite distribution. In the east and south view directions wall

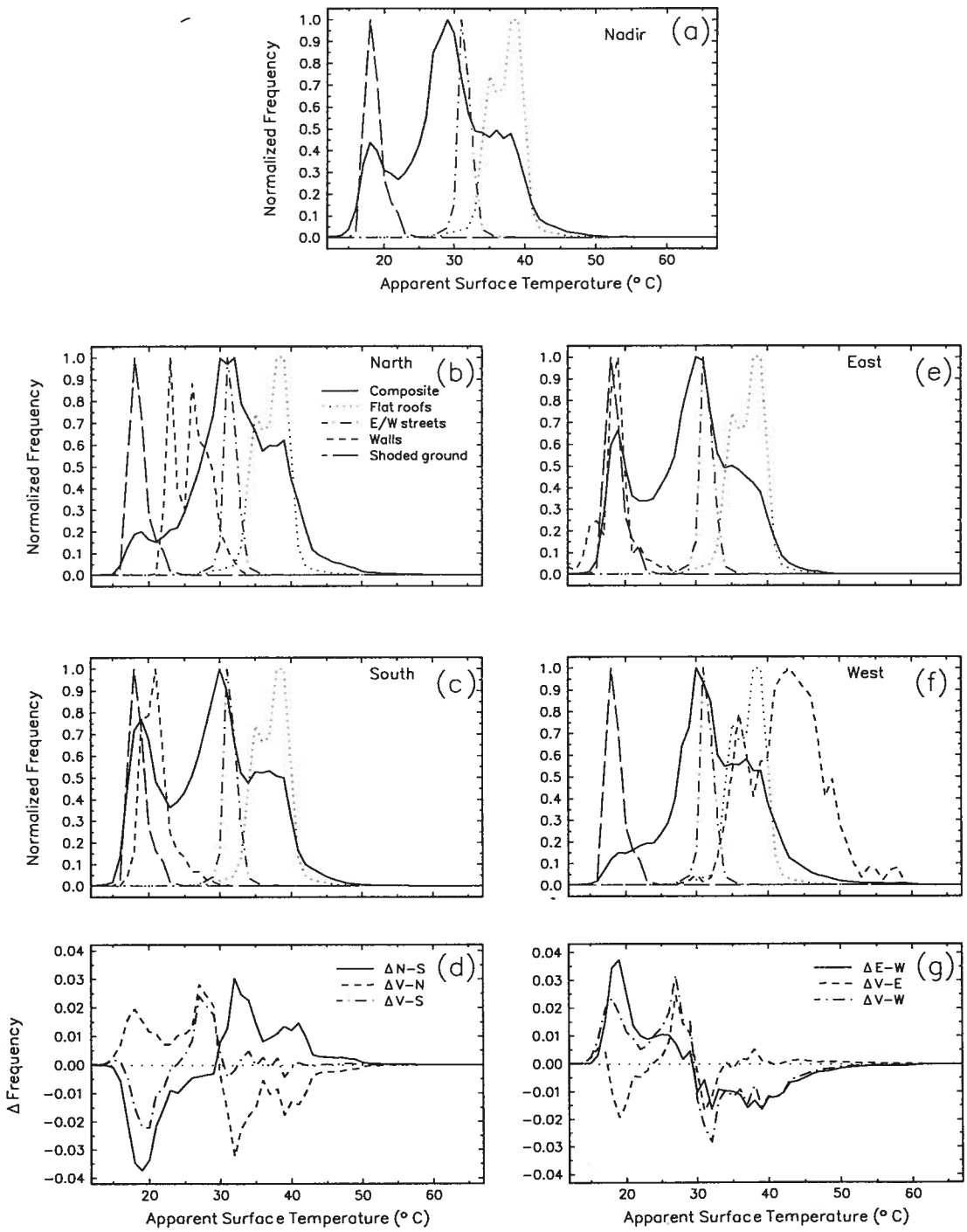

Figure 4.5: Apparent surface temperature distributions for each view direction over the Industrial area during Flight 1 (morning).

temperatures lie very close to that of the shaded ground resulting in a sharply defined peak in the composite distribution, (more so for the east than the south direction). The warm west facets contribute to the upper temperature shoulder in the composite distribution, enhancing the effect of the roof temperatures. North facet temperatures lie midway between the shaded ground and sunlit streets, resulting in a broadening of the main peak of the composite distribution.

There exists a gap in the component distributions as they relate to the composite for temperatures less than the sunlit road surface temperature, but warmer than the shaded ground. For some view directions (north, south), wall temperatures occupy part of this intermediate position, but there is clearly a large fraction of surfaces in a temperature range not incorporated by any of the component surfaces extracted from the images. This is further confirmed in Figure 1.6 which uses approximate weightings derived from images for each of the extracted components and sums the weighted component distributions in comparison with the observed South 45° composite distribution.

Examination of the range of "missing" temperatures on select images reveals that it is associated with what may be characterized as partly shaded surfaces. A large fraction of these are road surfaces which have recently changed from shaded to sunlit, while others are seen near boundaries between walls and roofs.

Differences between the frequency distributions for opposing view directions and nadir versus off-nadir flightlines are summarized in the final plots of Figure 1.5. These show the temperature ranges in which the frequencies differ the most. Differences are strongly related to the presence or absence of shaded surfaces, as evidenced by the strong peak at 18°C (i.e., close to air temperature). Differences between the off-nadir and nadir views show large frequency differences for temperatures in the range 27–29°C.

The highest frequency peak shows some offset between the four off-nadir view directions and the vertical view; this may be a result of warming during the time needed to

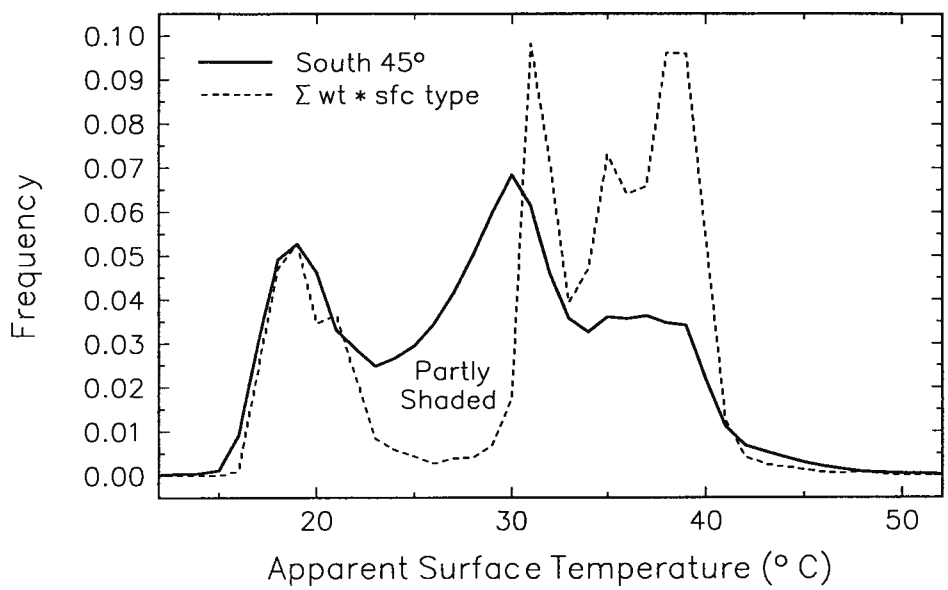

Figure 4.6: Modelled composite temperature distribution using component temperature distributions weighted by their occurrence within the sensor FOV.

cover each of the nadir flightlines. (The vertically scanned flight lines were flown before the off-nadir). There is little or no offset among the off-nadir view directions because of the rotational sequence in which they were sampled. Warming or cooling during the time required to complete the flightlines may act to broaden the distributions somewhat; warming/cooling rates calculated from ground and remote observations can be large for road and roof surfaces, especially in the morning and afternoon.

The degree of broadening in the composite distribution due to warming in the Industrial area during the morning flight (Flight 1) is investigated in Figure 1.7.

Assuming similar surface structure and materials among the flightlines, differences in the frequency distribution are attributed to warming between runs. The main and upper temperature peaks associated with road and roof temperatures respectively show a substantial offset (taken to be associated with a warming of these surfaces) between the

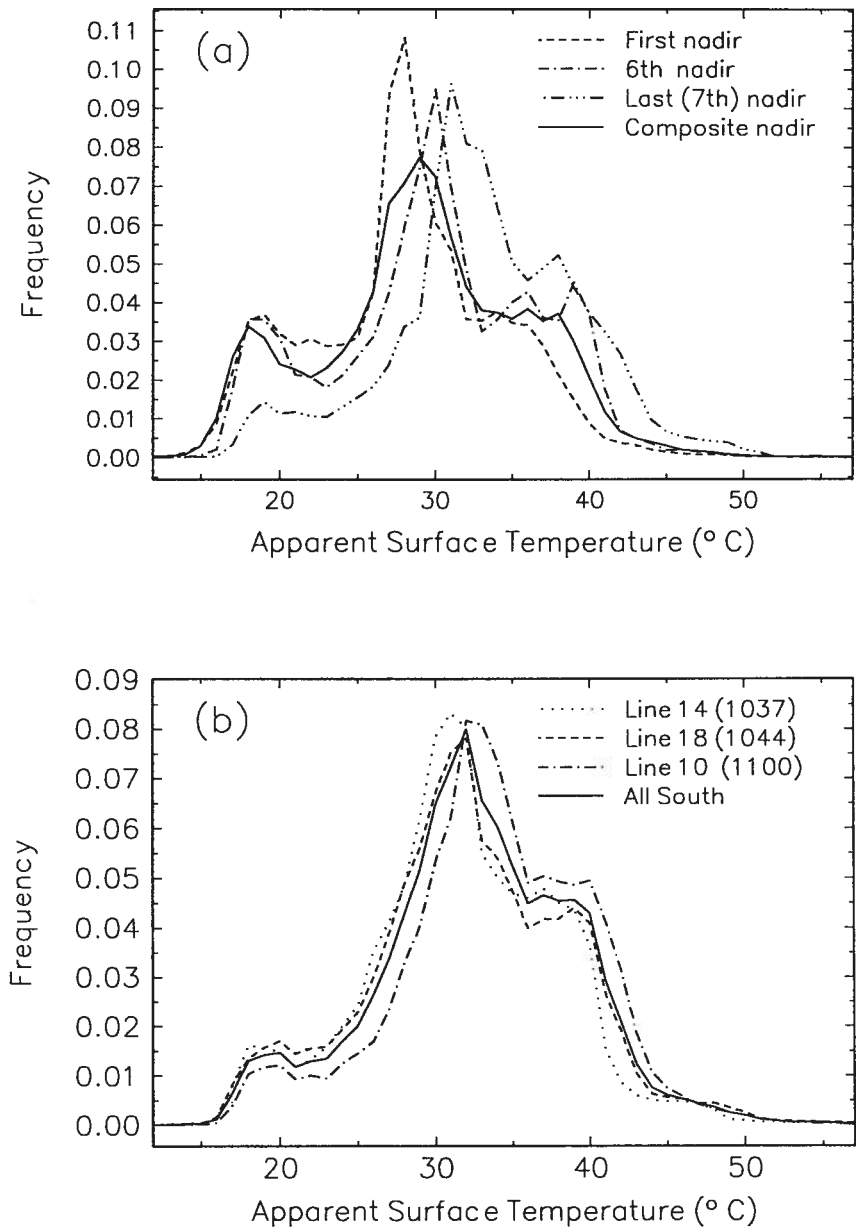

Figure 4.7: Broadening of the apparent surface temperature distribution attributed due to surface warming during data acquisition of the morning flight over the Industrial area.

first and last nadir flightlines (Figure 1.7a), while frequencies of the lowest temperatures decrease, in proportion to the reduction of shaded areas. Distributions for the north view direction (Figure 1.7b) show a shift in the main peak (road temperatures) towards warmer temperatures with time, a reduction (increase) in the frequencies of the coolest (warmest) temperatures associated with shaded (roof top) areas.

No attempt was made to correct the imagery for this warming or cooling during the time of the overflight because different surfaces warm and cool at different rates depending upon their orientation and thermal properties. However, because some surfaces undergo substantial warming with time, comparisons between ground and remote observations should take the time periods over which they have been made into consideration. A second factor to be considered is the inclusion of areas of "non-standard" surface cover (here defined as block orientations different from the rest of the study area, or areas such as parks or large open areas not included in the categorization of the area). This effect is investigated in Figure 1.8 which compares the complete composite distribution with a distribution obtained when all images containing non-standard block orientations (present in the NW portion of the study area), Jonathan Rogers Park, and areas to the south of the study area (many large trees) are omitted from the analysis.

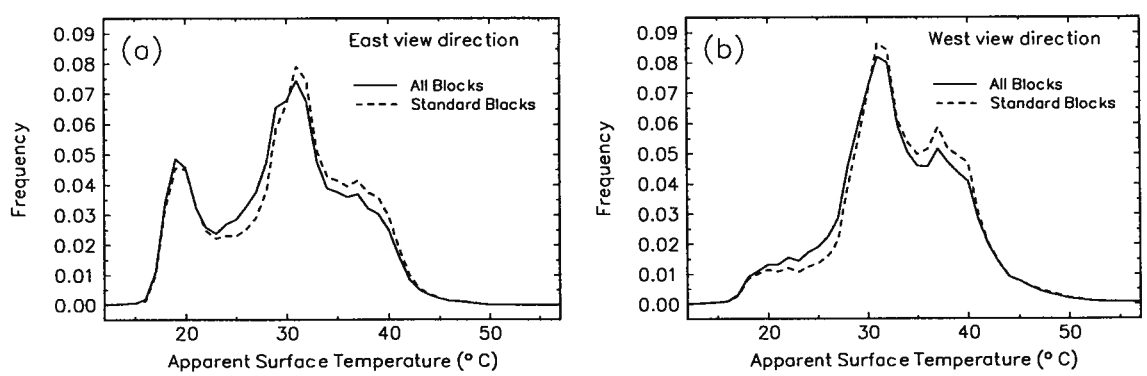

Figure 4.8: Comparison of apparent surface temperature distributions before and after images with a non-standard block orientation or surface cover were removed.

The distributions show a reduction in frequencies at low temperatures (associated with the removal of the vegetated areas), a slight narrowing and increase in frequencies of the mid-range peak, and enhancement of the upper portion of the distribution (for all off-nadir view directions). The effects are best seen in the east and west view directions as these flightlines had proportionally a greater number of non-standard images.

The early afternoon flight (Figure 1.9) shows distributions with features similar to those described for the morning flight but with somewhat less well defined peaks. The smearing of the peaks is attributed to the overall warming of all surfaces and the transition of many surfaces from shaded to sunlit status which gives more surfaces with intermediate surface temperatures.

The "shoulder" of warmer temperatures above the main peak is still present but less well defined than in the morning flight. This appears related to a greater overlap in the temperature distributions of these components; similar results were obtained by Quattrochi and Ridd (1994).

The east and west view directions present almost identical distributions, and differ from the vertical only by slightly higher frequencies of low temperatures and lower frequencies of warm temperatures (Figure 1.9). Shaded areas are minimized at this time giving a smaller low temperature peak for the southward view. Images obtained with a northward view show an almost complete absence of temperatures in the range for shaded ground, and the composite distribution is a unimodal, almost symmetric shape.

The late afternoon overflight (Figure 1.10) shows much less distinction between roof and road surface temperatures and between roof and sunlit wall surface temperatures compared with previous flights.

This is evident by the absence of the warm temperature "shoulder" of the morning and early afternoon flights. The low temperature peak associated with shaded surfaces is less well defined at this time; it is to be anticipated that the range of temperatures in

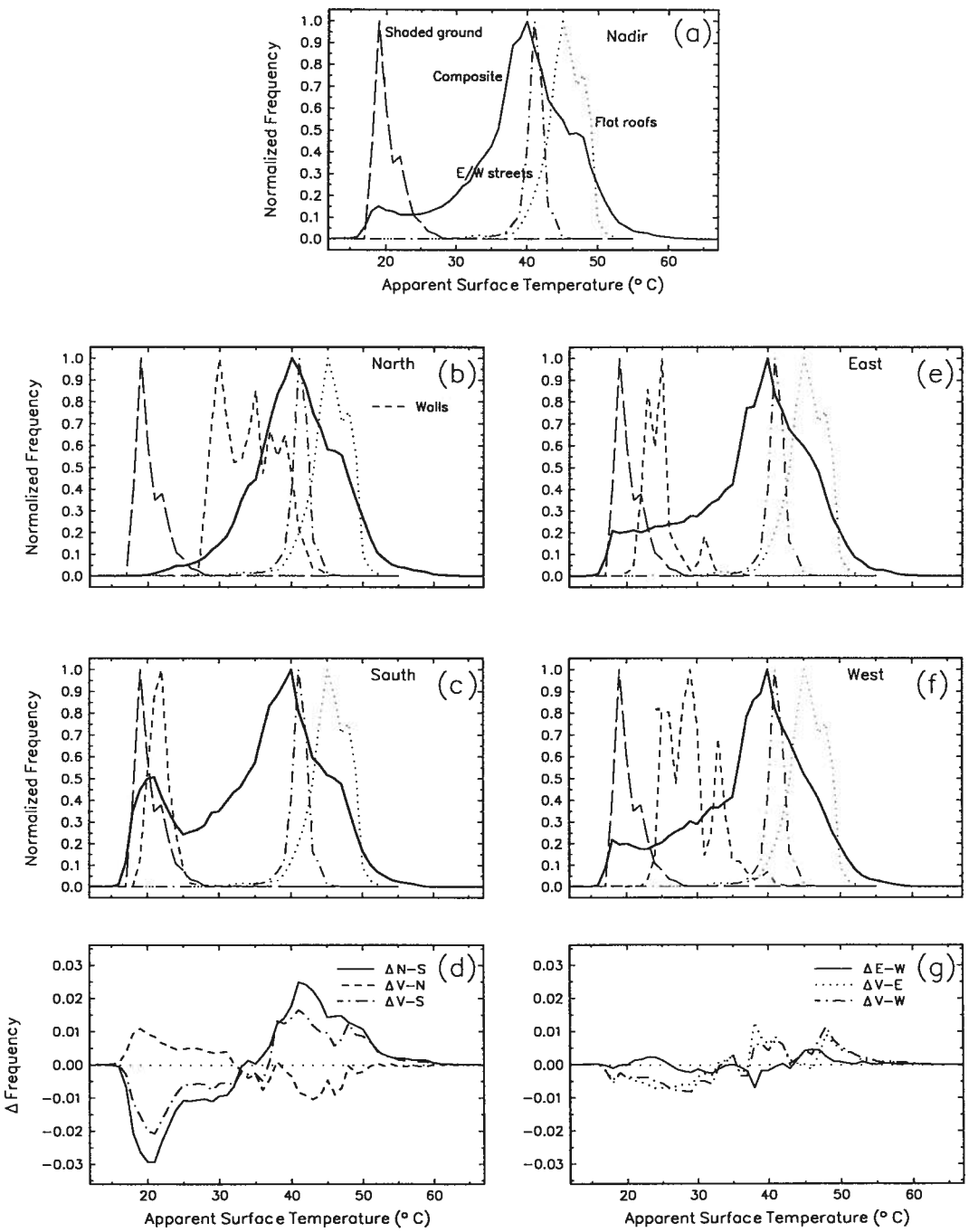

Figure 4.9: Same as Figure 1.5 except for Flight 2 (1345-1430 PDT).

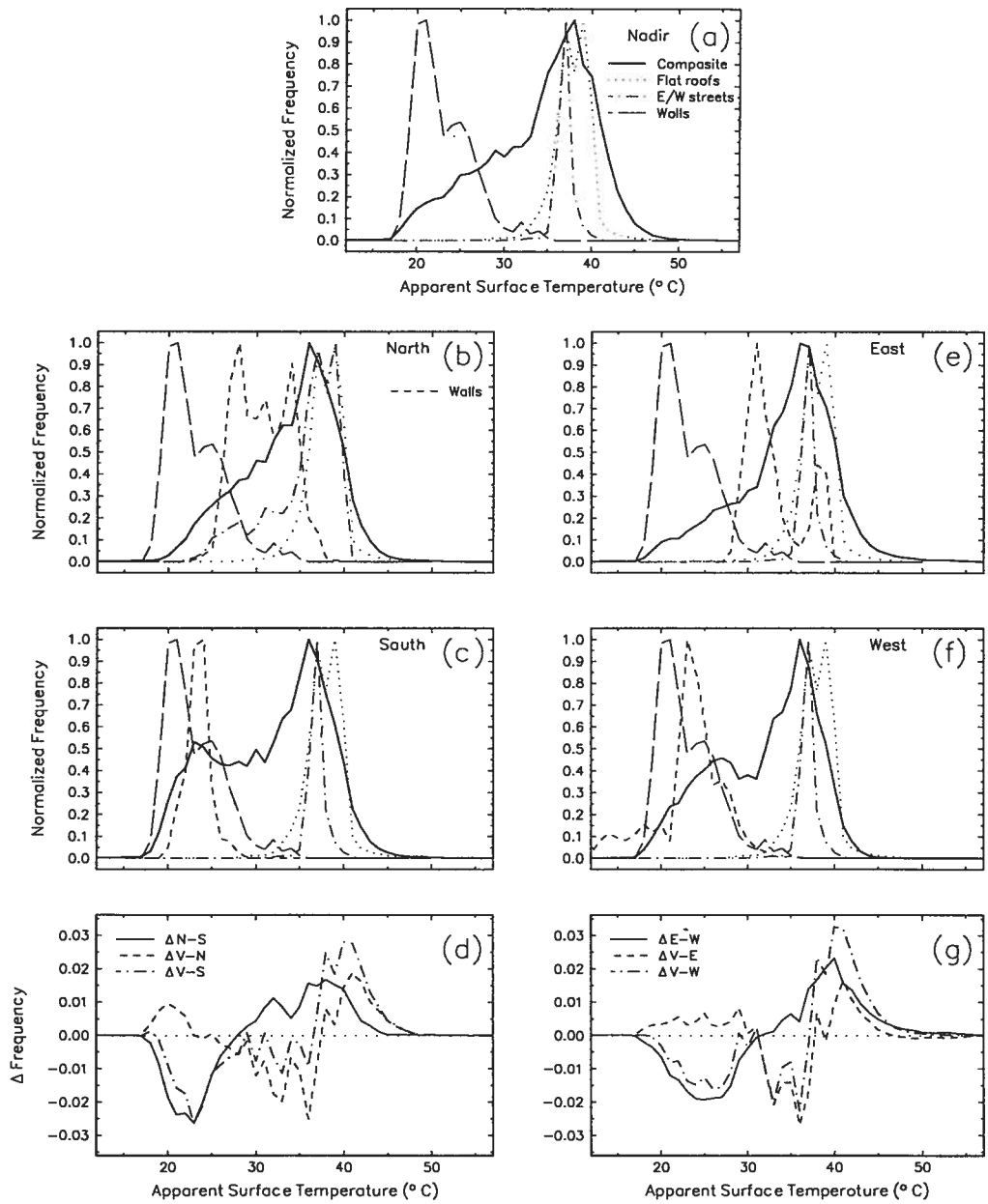

Figure 4.10: Same as Figure 1.5 except for Flight 3 (1705–1745 PDT).

areas classified as shaded will be larger in the afternoon because many of these surfaces were previously sunlit and are in the process of cooling; the range of temperatures will become narrower with time as cooling progresses. This effect extends to the shaded ground on the south sides of E-W canyons which become exposed to direct radiation in the late afternoon and undergo some warming, further smearing the low temperature peak.

Temporal development of the temperature distributions is summarized in Figure 1.11 which shows the difference between apparent surface temperature, and the canyon-level air temperature from the traverse vehicle, for each view direction.

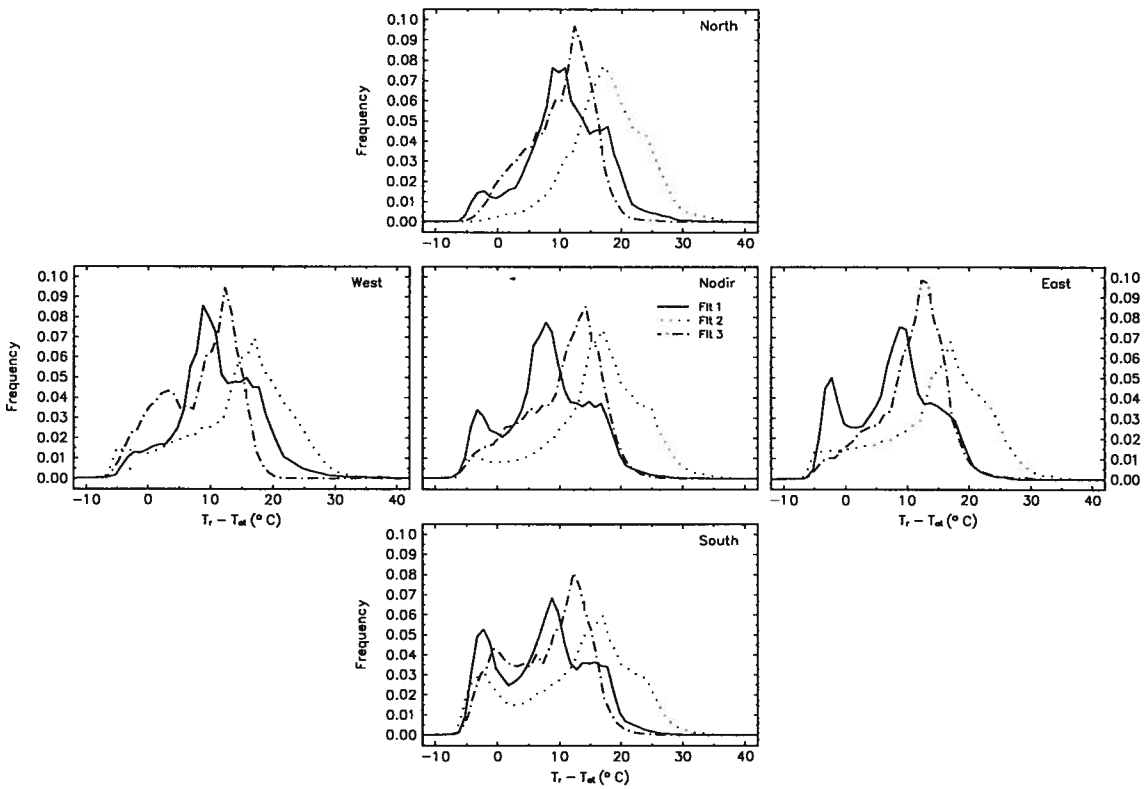

Figure 4.11: Temporal development of the distribution of T_r as indicated by the difference between surface and canyon level air temperature. Industrial area.

The shift and change in the features of the distributions is easily traced. At all times,

the majority of the surface temperatures greatly exceed the canyon-level air temperature. Those features of the distributions attributed to shaded surfaces tend to have temperatures slightly less than that of the air (2.5 degrees). The lower bound of the distributions is fairly consistent with time; the cutoff is approximately 6 degrees below air temperature. This may represent the temperature of those surfaces shaded throughout the day. The upper bound varies strongly with time of day.

4.4.2 Residential

In the Residential study area, thermal images clearly show the cool vegetated surfaces, including tree crowns and grass, and a greater variety of roof temperatures, due in part to variations in the pitch and orientation of the mostly non-flat roofs (Figure 1.12).

The ability to view building walls depends upon the building and block orientation. North-facing walls are clearly evident on buildings aligned N/S along E/W streets, but the small inter- building spacing hides most of the N-facing wall from view for buildings aligned E/W along N/S streets. The temporal development and shape of the temperature distributions (Figure 1.13) is similar to that described for the Industrial area: The morning flight shows a bimodal distribution of temperatures with a sharply defined lower cutoff and a more gradually decreasing tail of warmer temperatures. The peaks are less well separated than for the Industrial area and there is no distinct plateau or shoulder of warm temperatures as seen in the Industrial area. This appears to be related to a greater range of temperatures for the building roofs, which occurs because many roofs are pitched rather than flat. This serves to increase the range of temperatures above that due solely to material or construction differences.

Component temperature distributions observed during Flight 7 (1345-1415 PDT) (Figure 1.14) are presented for 8 major component surfaces in the N-S block orientation

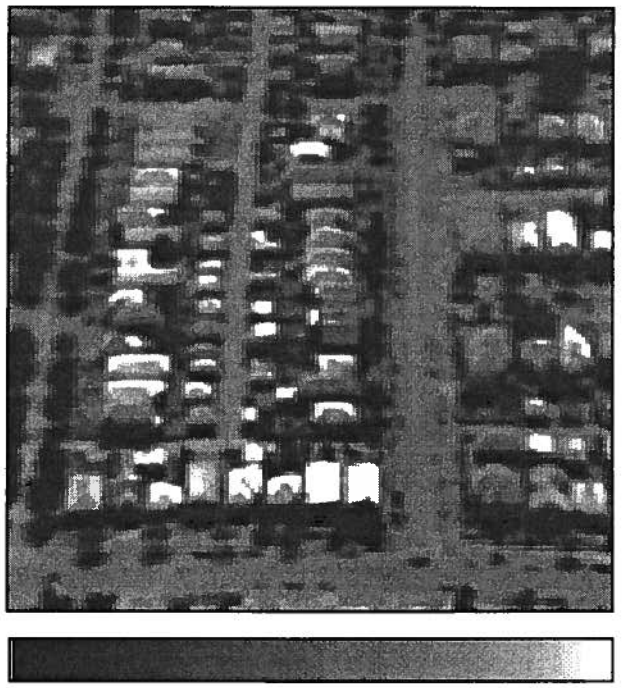

Figure 4.12: Thermal image of the Residential study area, Flight 7 (1400 PDT). View is southwards at a 45° off-nadir angle.

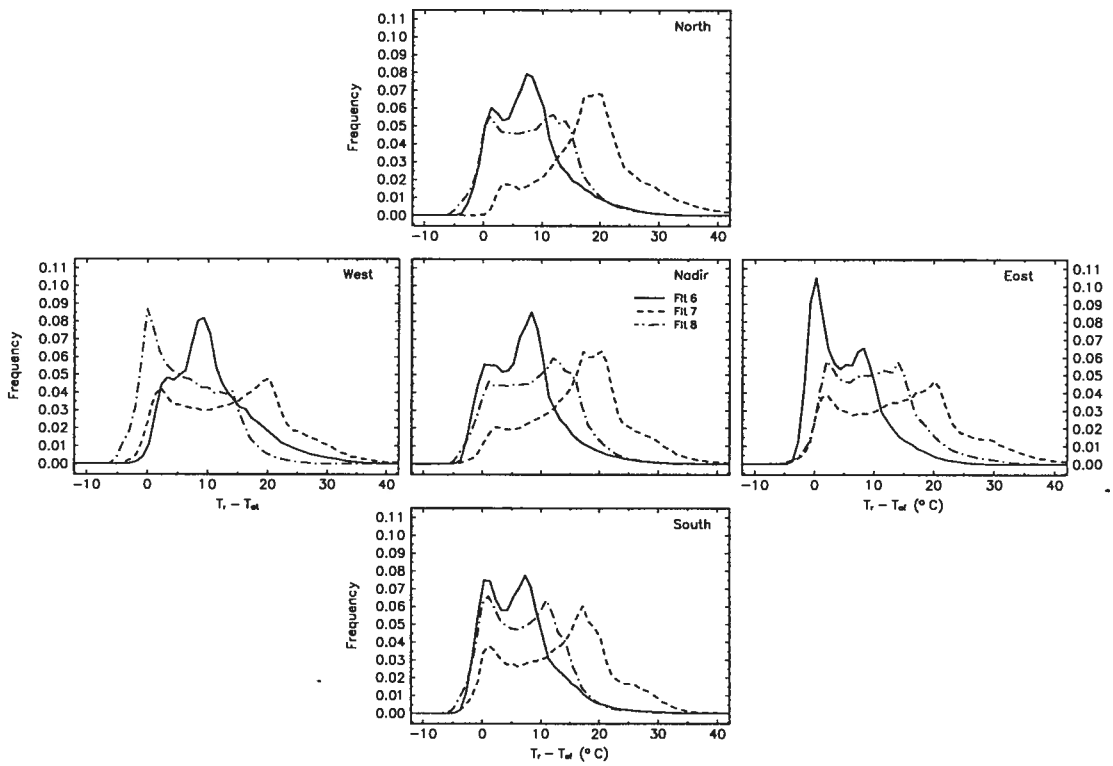

Figure 4.13: Surface temperature frequency distributions for the three flights over the Residential study area: solid line (0945 PDT), dash-dot (1400 PDT), dash (1730 PDT).

area: shaded ground, tree crowns, grass, streets (asphalt), walls (separated by orientation), flat roofs and north and south pitched roofs. To clarify presentation, those components common to all view directions are shown together with the nadir composite. Each off-nadir view direction adds only those components unique to that direction; primarily the walls, but also the north and south-pitched roofs.

The range of temperatures for some components is large, especially roof areas. A clear separation is evident between roofs classified as north- and south-pitched, but each contains significant overlap with the flat roof category. North-pitched roofs, which are cooler than flat or south-pitched roofs have temperatures very similar to those obtained for road surfaces and south-facing walls. The low temperature peak of the bimodal distribution appears to be a combination of three surfaces: tree crowns, shaded ground areas, and, where visible, north-facing walls. Grass surfaces show similar frequencies over a fairly wide range of temperatures (7°C) which overlaps the range of north, east and west walls, and of the north-pitched roofs, and leads to the relatively high frequencies in the composite distribution between the two peaks. East and west walls have very similar distributions. West walls show a slightly narrower distribution and a tail of warm temperatures as these facets cool, and east walls warm, with time in the afternoon. The similarity in their composite distributions is confirmed by the difference plot (Figure 1.14(g)) which shows essentially random variations around 0.

Differences between nadir and east and west distributions are also very similar. The relative reduction in low temperature frequencies appears to be correlated with the east and west wall temperature distribution; the source of enhancement for temperatures at 40°C is less clear, presumably it is related to a more direct view of the pitched roof surfaces. North-south differences are stronger and show a narrow peak at approximately 25°C related to the presence or absence of north-facing walls and shaded ground between the two views, and also to temperature differences across the tree crowns. The more

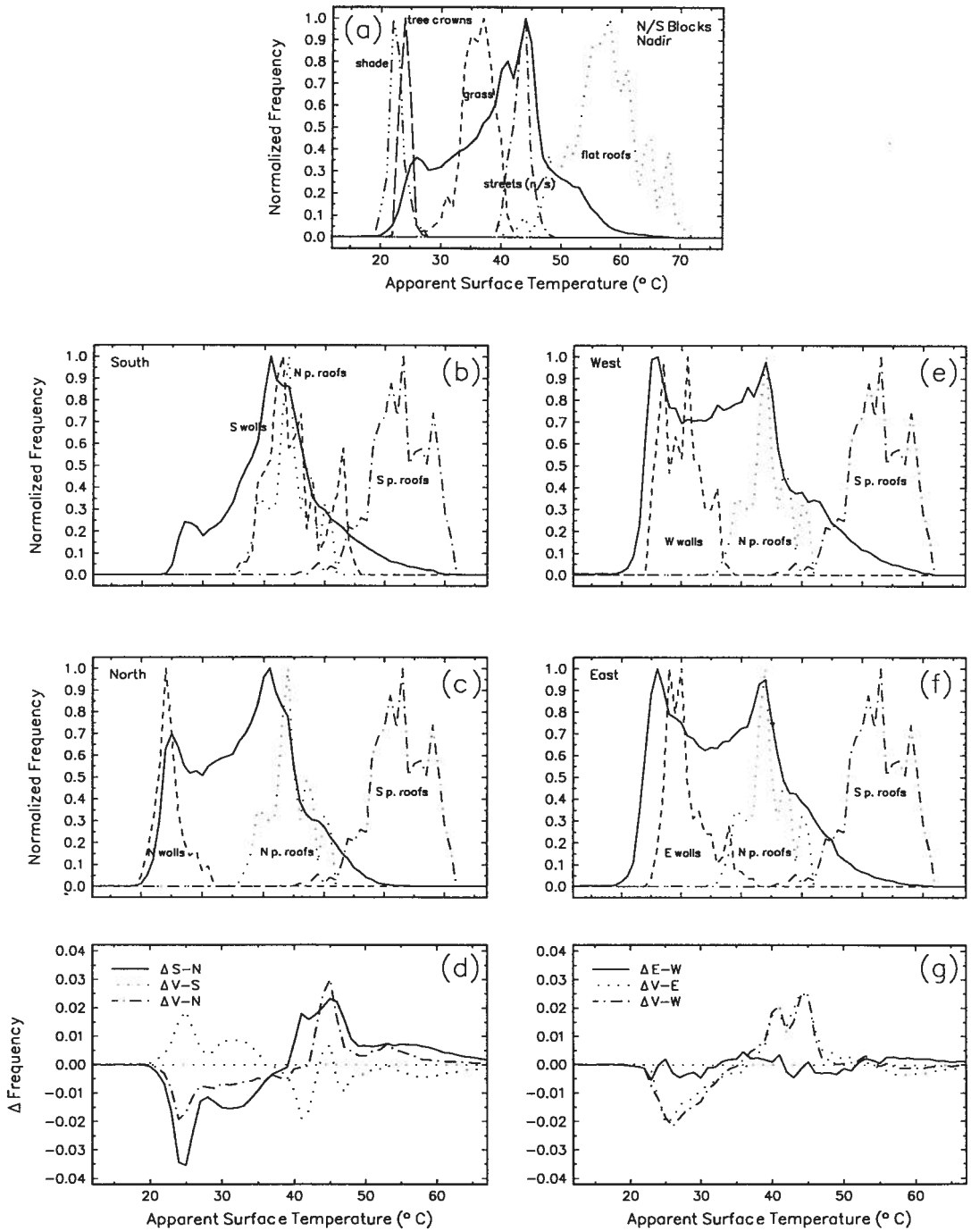

Figure 4.14: Same as Figure 1.5 except for Flight 7 (1345–1415 PDT) over the Residential study area.

exposed view of the south-pitched roofs accounts for the plateau of positive differences at high temperatures. The enhancement of temperatures between 40 and 50°C appears to be linked to the south-facing walls.

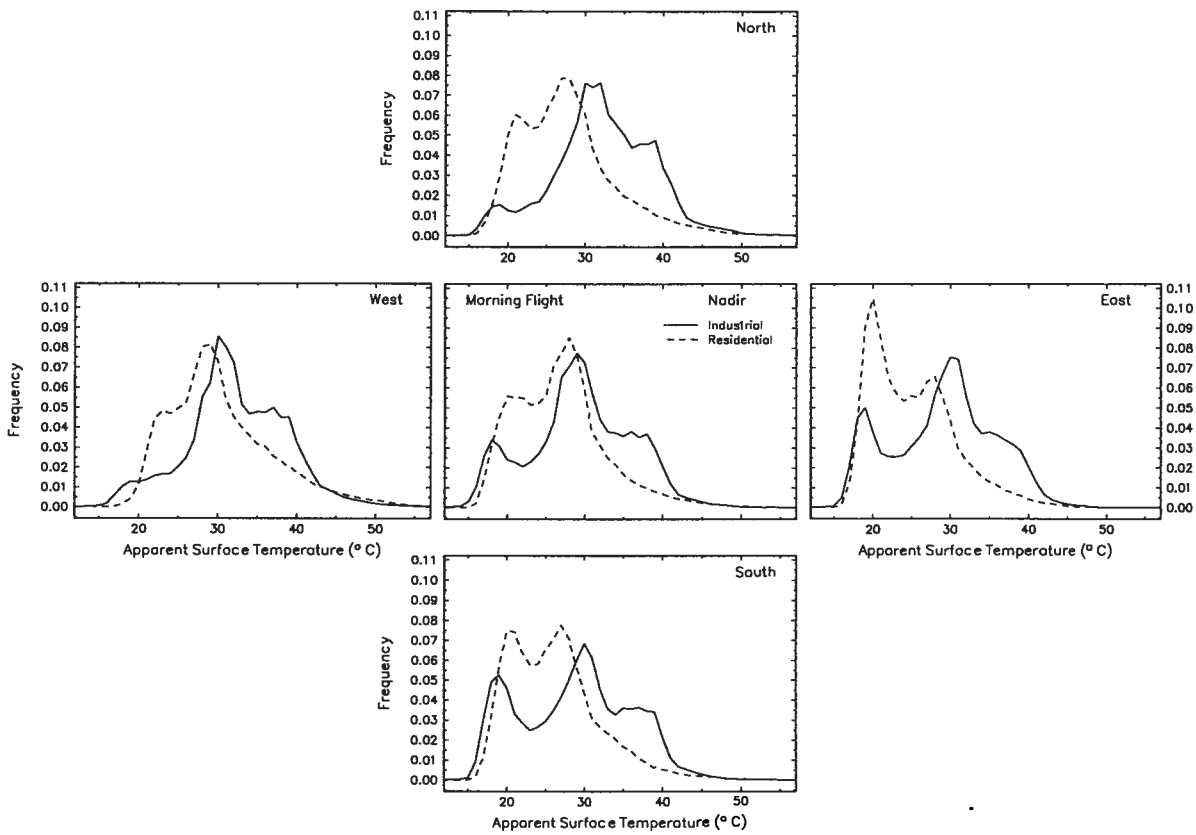

Figure 4.15: Comparison of T_r distributions for morning flights (Flights 1 and 6) over the Industrial and Residential study areas.

Comparison with the Industrial area (Figures 1.15, 1.16, 1.17) shows that the Residential area exhibits greater frequencies for the low temperature peak, presumably due to greater amounts of vegetation and/or shading. The relative magnitude of this peak is almost comparable to, or in the case of the eastward-viewing direction, exceeds the frequency of the warm temperature peak.

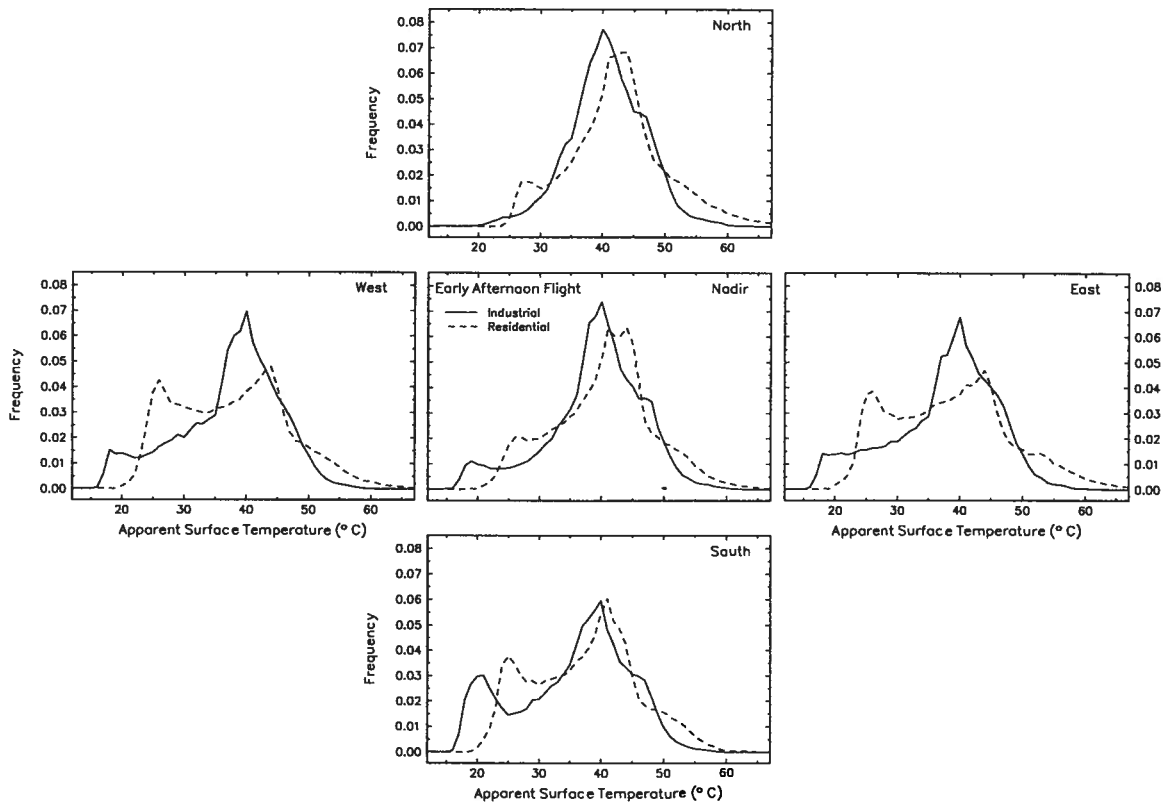

Figure 4.16: Same as Figure 1.15 except for early afternoon flights (Flights 2 and 7).

The early afternoon flight shows evidence of a shoulder of warm temperatures developing. Vertical, north and southward distributions are otherwise generally similar except for a greater frequency of low temperature classes. Peaks in the distribution are offset due to the warmer temperatures on this day. East and westward views are again similar at this time, and the relative magnitude of the peaks is almost comparable, in contrast to that of the Industrial area.

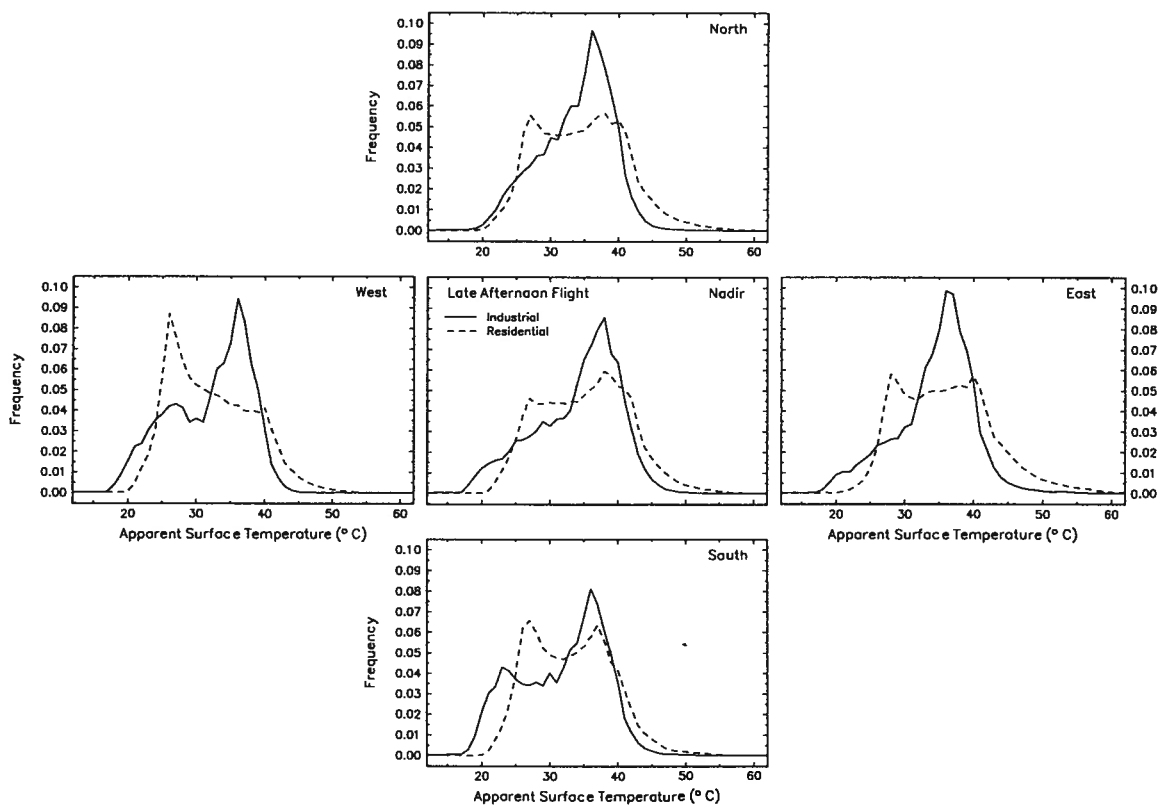

Figure 4.17: Same as Figure 1.15 except for late afternoon flights (Flights 3 and 8).

In the late afternoon, the north-, south- and eastward distributions are characterized by bimodal distributions with the classes between the peaks exhibiting relatively high frequencies (Figure 1.17). Compared to the Industrial area, the warm temperature peak is reduced in magnitude and the cool temperature peak enhanced. Sharp drop-offs in the

distribution shape are evident at both warm and low temperature ends of the distribution. A complicating feature of the Residential area is the presence of two distinct areas of differing block orientations. North of 49th Ave. blocks have their long axis oriented north-south. Buildings are oriented E/W with a small inter-building spacing in the N/S direction. Two-sided pitched roofs are preferentially oriented N/S because the long axis of most buildings is east/west. Streets are lined with large mature trees. South of 49th Ave. most blocks are oriented east-west and there is less mature vegetation.

Images for Flights 6–8 were categorized according to the primary block orientation and the frequency distributions were recalculated (Figure 1.18). Images with mixed orientations were removed from the analysis. Nadir images consistently show higher frequencies at low temperatures for the N/S oriented blocks.

This is taken as evidence of larger amounts of vegetation in this portion of the study area. Morning eastward and afternoon westward views in the N/S block orientations exhibit higher frequencies of low temperatures which are attributed to the greater apparent wall area exposed along the streets compared to that in the E/W oriented blocks where east and west walls are less easily viewed due to the small inter-building spacing. Northward-looking views from the morning flight over E/W blocks were characterized by higher frequencies of warm temperatures, possibly due to the more open south-facing facets in this area. The late afternoon flight shows a similar effect but for southward views. East and westward views during the early afternoon flight show higher frequencies of warm temperatures in the E/W blocks which are attributed to fairly equal temperatures on the pitched roofs in this block orientation compared to those in the N/S blocks, where north-pitched roofs are cooler than the south-pitched ones.

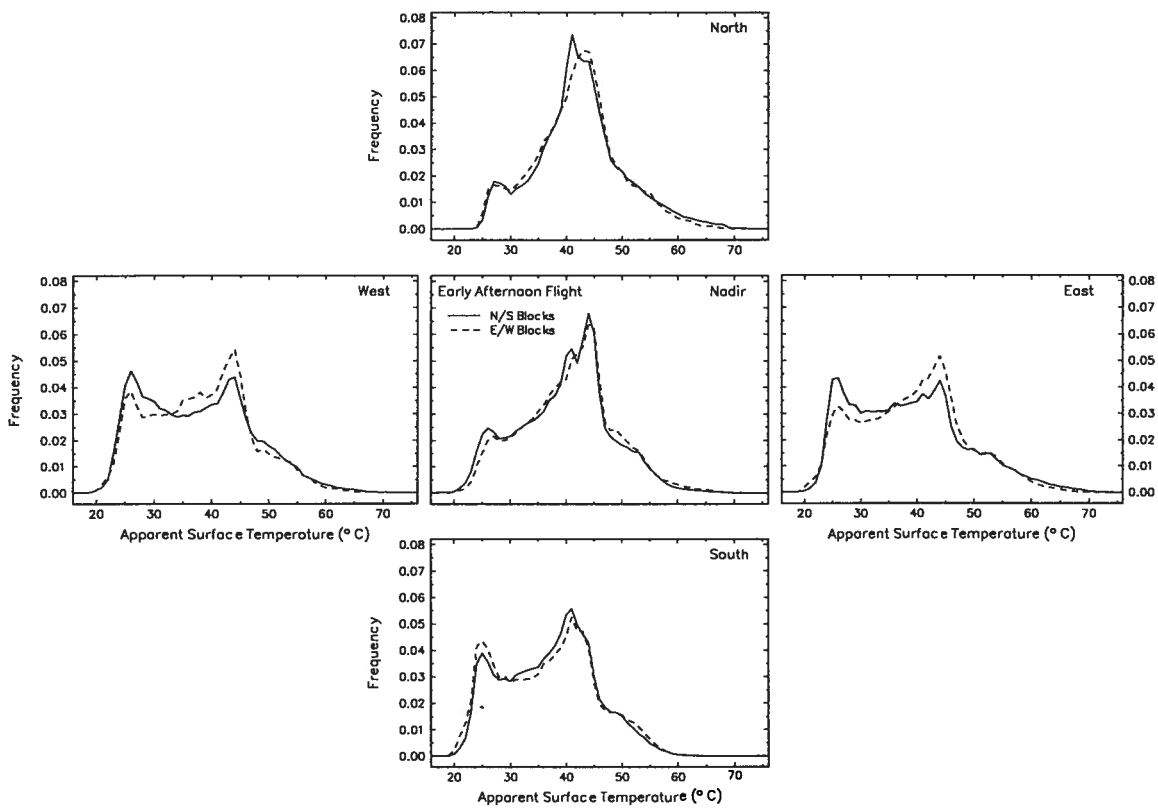

Figure 4.18: Comparison of T_r distributions for two primary block orientations in the Residential study area. Data for the early afternoon flight (Flight 7).

4.4.3 Downtown

The large building structure in the Downtown area is well illustrated by Figure 1.19. This image was taken looking towards the southwest, as evidenced by the shadow patterns visible on the street on the left-hand side of the image. Note that the tall buildings for the most part obscure the streets which parallel the flight direction, and the roofs of shorter buildings are obscured by tall buildings. This leads to a reduction in the frequencies of warmer temperatures in these view directions. Building roofs tend to be more structurally complicated than the other two land-use areas, so that the roofs often contain areas of shadow or apparent temperature differences due to low emissivity materials. The relative proportion of roof area to the entire image is smaller than in the other two areas.

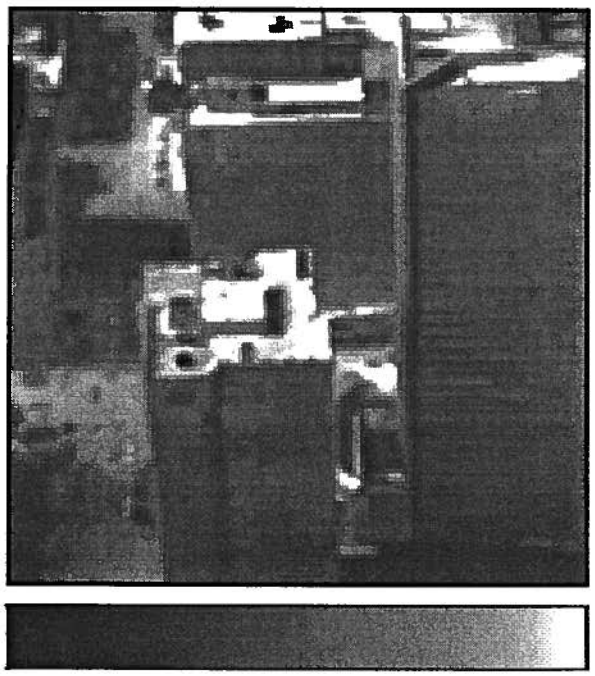

286.2 Apparent Temperature (K) 303.4

Figure 4.19: Thermal image of the Downtown study area, Flight 4 (1130 PDT). View is to the southwest at a 45° off-nadir angle.

The image was collected using scanner mode 3, in which only 140×140 pixels were sampled, thus no interpolation has been required but the image is somewhat coarser than that of corresponding Figures 1.4, and 1.12. Temperature distributions from the morning Downtown overflight (Figure 1.20) show distributions dominated by low temperatures, except in the direction of the most directly sunlit facet (NW at this time). The nadir view shows a bimodal distribution with the lower temperature peak slightly larger. The low temperature peak is related to shaded areas on the ground, and the warm temperature peak is derived from the warm roof and street areas. In this figure, temperature distributions for roadways are not limited to sunlit areas, samples were taken along the length of the visible streets (in the direction of the sensor view) and thus include both shaded and sunlit road surfaces.

There is strong differentiation between the NW and SE view directions. The NW distribution is unimodal; the frequency of shaded surfaces viewed by the sensor is very small. There is little difference between the NE and SW distributions at this time, each having a large low temperature peak and a weakly expressed warmer mode. The dominance of the low temperature classes occurs because the walls and streets include a high proportion of shaded areas. The view angle in combination with the tall buildings effectively restricts viewing NW/SE streets which are characterized by relatively little shading at this time. The NE/SW oriented streets are primarily shaded except at intersections.

Temperature distributions from the afternoon flight (not shown) are reversed from those of the morning. The largest difference is the shape of the nadir temperature distribution which is no longer bimodal; the upper peak is replaced by a gradual tail-off of frequency.

Comparison with the other sites is difficult because the different street orientations alter the time of the maximum vertical facet temperature differences. An alternative is to use times at each site when the relative solar azimuth with respect to the street

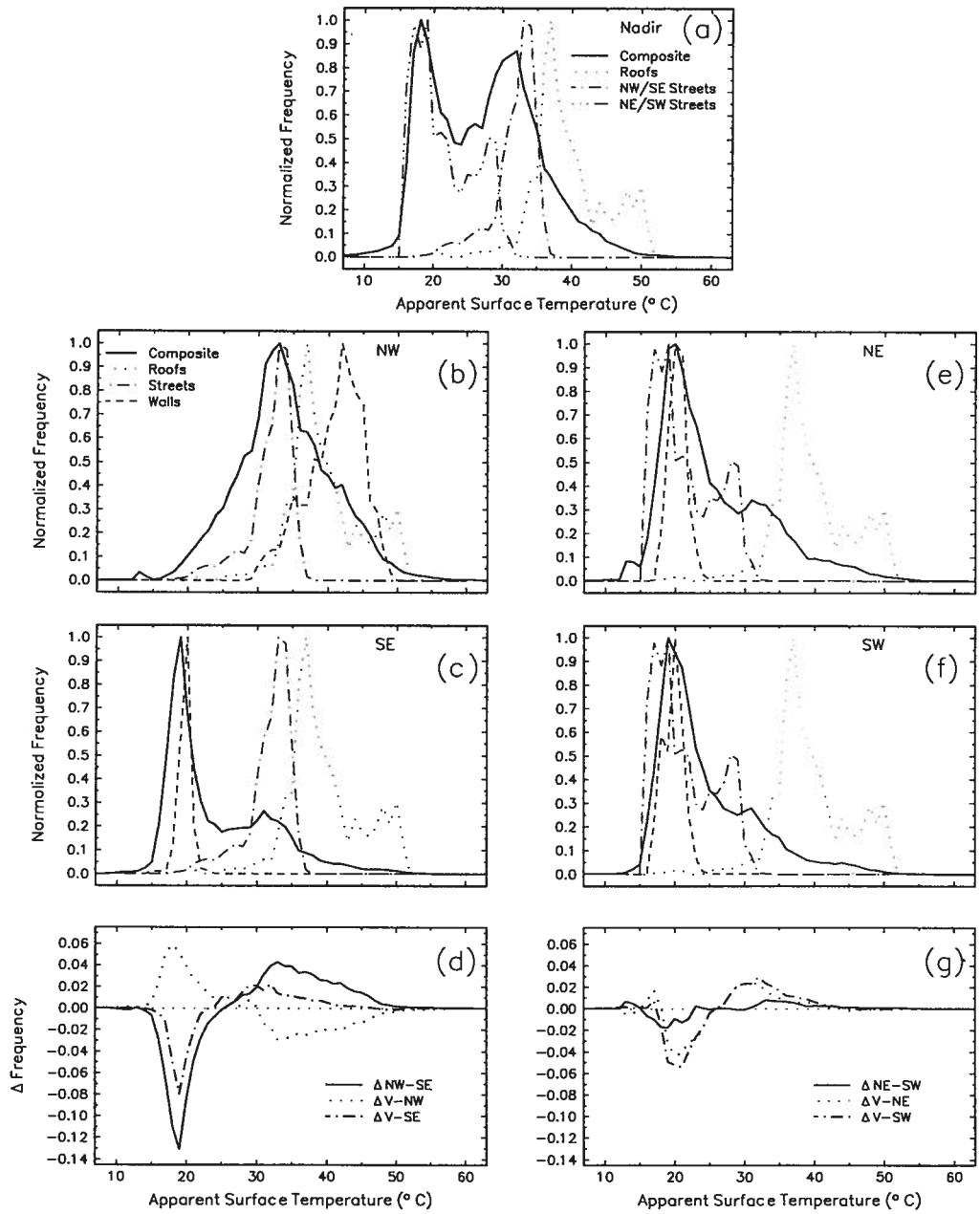

Figure 4.20: Same as Figure 1.5 except for Flight 4 (1130 PDT) over the Downtown study area.

orientation is similar for the Downtown and another site. However, it should be noted that since solar zenith angles are different there are differences in the angle of incidence of the solar beam with the building facet. The closest comparisons possible, based upon relative solar azimuth to the canyon facets, are shown in Figures 1.21 and 1.22.

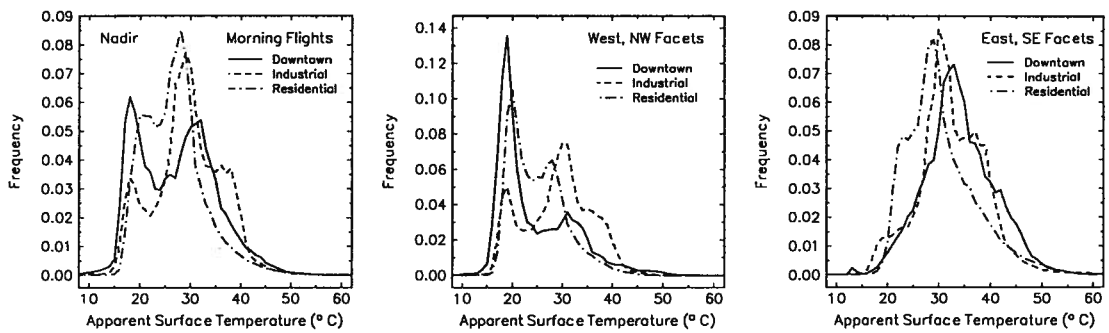

Figure 4.21: Comparison of T_r distributions for the Downtown (Flight 4), Industrial (Flight 1), and Residential (Flight 6) areas. Comparison based upon relative solar azimuth to canyon orientation.

The dominance of shaded surfaces in view directions SE (Flight 4) and SW (Flight 5) is very apparent. A much smaller fraction of the FOV intersects the ground or roof surfaces compared with the other study sites, and, even when horizontal surfaces are viewed they are in many cases shaded by tall buildings. The increase in shaded ground area is also apparent in the enhanced frequencies of low temperatures in the nadir views (Figure 1.21(a), 1.22(a)).

When viewing the directly sunlit facet, the distributions appear more similar to those from the other study areas; and become more unimodal.

4.4.4 Summary

High resolution thermal images of the three study areas were used to show spatial temperature patterns. Road surface temperatures tend to be relatively homogeneous except for

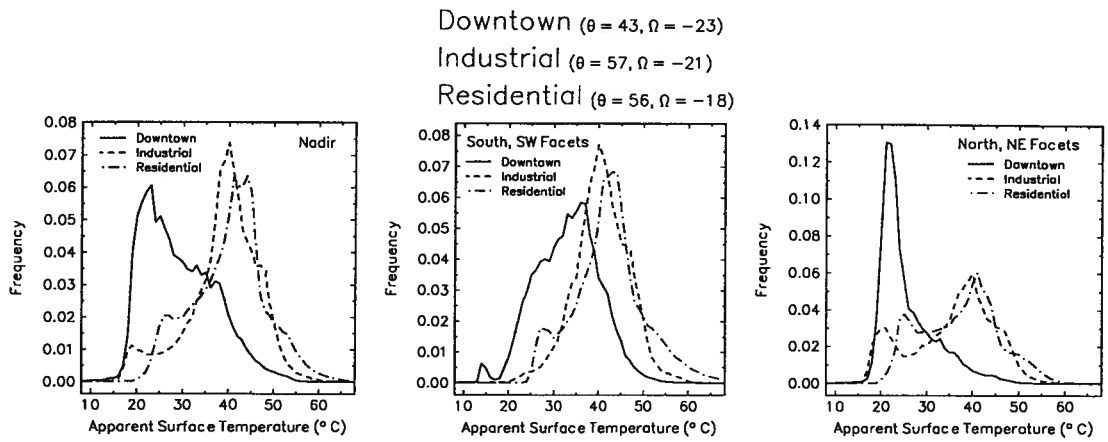

Figure 4.22: Same as Figure 1.20 except for early (Downtown) and late afternoon flights (Industrial and Residential areas).

shaded areas. Roof temperatures show variations related to materials and construction and especially to roof pitch. Distributions of surface temperature tend to be bimodal; the distributions are most sharply defined during the morning when differential heating creates the largest temperature differences between surfaces.

The lower peak of the distribution is associated with shaded surfaces and varies in strength depending upon the view direction. Shaded surfaces exhibit their narrowest temperature range in the morning.

The composite temperature distribution may be used to discriminate between land-use types: in Residential areas characterized by a wide variety of surface covers, the temperature distribution is less well defined and shows more constant frequencies across a wide range of temperatures. In commercial/Industrial land-use areas, the larger roof and paved areas enhance narrow ranges of temperature.

4.5 Modelling the Distribution of Surface Temperature

4.5.1 Introduction

The composite image surface temperature frequency distributions show features related to the surface structure and materials. Where the surface structure is relatively simple (e.g., the Industrial area), the distributions are shown to be composed of relatively few individual distributions, each arising from a component surface (e.g., wall, roof, road, shaded ground). In more structurally complex areas (e.g., the Residential areas), the overall distributions show fewer distinct features, because the number of component distributions increases and there is greater overlap between distributions. This section investigates the possibility of modelling the composite distributions as a mixture of distributions using the techniques described in Chapter 3. Of particular interest is whether the composite distribution can be modelled so that the component surface temperature distributions can be recovered without having to resort to intensive extraction of small scale features within an image (e.g., see Quattrochi and Ridd, 1994), or the use of coincident multispectral imagery.

In some respects, the question is: How successfully may surface type be classified upon the basis of temperature ? Where different surface components exist with similar temperatures, discrimination will not be possible. Where a surface type is represented by a wide temperature distribution due to variations in surface properties at small scales (e.g., different roof types), problems will also arise due to substantial overlap with other surface categories (e.g., walls or road surfaces). Discrimination between components is also expected to depend on the time of day; relative differences in thermal and radiative properties produce the most sharply defined composite distributions during the morning heating period.

4.5.2 Modelling a Simple Case

A simple composite temperature distribution, obtained from a thermal image of a set of concrete blocks on an asphalt surface, is shown in Figure 1.23a.

This model simulates the general surface structure of a Residential area in terms of the dimensions and spacing of the blocks and buildings. It obviously greatly simplifies the surface in terms of material type; only asphalt and concrete are present. Temperature variations are therefore largely constrained by the surface orientation and shading. Overlain on the composite distribution are the component distributions obtained by extracting selected surfaces from the image; in this case the image is subdivided into roofs (top of concrete blocks), walls (only the west wall is viewed), and the asphalt surface (shaded and unshaded components). The form of the composite distribution is most different from that obtained over the Residential area in that the roof temperatures are much lower than either the walls or unlit asphalt surface. The composite distribution was then fitted with four component curves using the PEAKFIT^{TM} program (Figure 1.23b,c). In the first example, all component curves were Gaussian. In the second, Beta distributions were used for the wall and shaded surfaces, to better represent the asymmetry displayed by those distributions as extracted from the image. Comparison between the statistics of the extracted components and modelled components is given in Table 1.2. The agreement is very good; (R^2 values are 0.993 and 0.963) however, the most accurate fitting requires tuning the position and shape of the individual components prior to starting the fitting iterations. This is especially true with the Beta distributions.

4.5.3 Modelling Road Surface Temperatures

A second example examines (as in Chapter 3) mixed distribution modelling of the road surface temperatures. The airborne thermal imagery is used this time instead of the

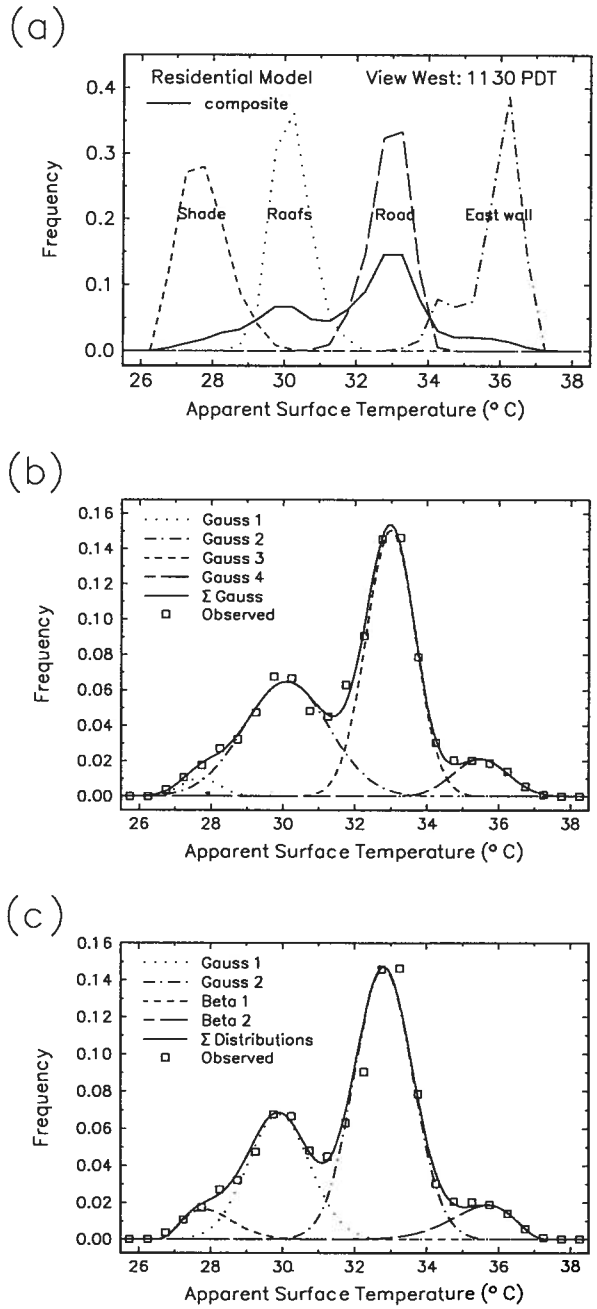

Figure 4.23: Temperature frequency distribution for a concrete scale model representing the Residential area showing the complete image distribution (solid line) and selected component surfaces. View is to the west.

Table 4.2: Comparison of component temperature distributions for an image of a simple scale model. (All values °C).

	Extracted		Modelled [a]		Modelled [b]			
Component	Mean	SD	Mean	SD	Cntr	Wid1	Wid2	Wid3[c]
Wall	35.82	0.75	35.49	0.76	35.70	13.01	18.01	3.51
Roof	30.19	0.53	30.10	1.18	30.05	1.08		
Asphalt (sunlit)	32.89	0.55	32.98	0.68	32.95	0.73		
Asphalt (shaded)	27.75	0.67	27.71	0.53	27.76	13.01	2.51	14.51

[a]all surfaces Gaussian
[b]wall and shaded surfaces Beta
[c]Wid1, Wid2, Wid3 are adjustable paramters for the Beta Distribution

vehicle-mounted EIRT. Road areas were selected from an image, (in this case a N/S road from the morning flight over the Industrial area which shows both shaded and non-shaded areas). As described in Chapter 3, road surfaces are relatively homogeneous in terms of their thermal properties and orientation (this can be important at small scales due to the camber of the road, and at larger scales due to topography), so that temperature differences are most strongly conditioned by shading. The surface temperature of both shaded and sunlit streets may be assumed to be represented by a Normal distribution if they have not recently undergone a change from one irradiance regime to the other (analogous to the approach taken in Chapter 3). However, inspection of the images showed significant areas with temperatures intermediate between that of the shaded and sunlit portions. These sections appear to have recently become sunlit (or shaded). They exhibit a temperature distribution where the frequency of temperatures is related to the time since the change in irradiance. The temporal response is expressed spatially as a non-linear change in temperature across a shaded/non-shaded boundary. The rise is most rapid near the boundary and tails off with distance (Figure 1.24(b)); more of the area is characterized by temperatures close to those of unshaded than shaded areas. Physically

this may be related to the large temperature gradient imposed near the surface when the surface becomes sunlit. The temperature rise will be initially be rapid as the large temperature gradient is confined to a shallow layer near the surface. However, as the asphalt layer warms, the temperature gradient will be reduced and the temperature will more gradually approach the new value. Note that this effect appears to be limited to morning hours on the north-south streets where the area of shadow changes most rapidly; on east-west streets, the area undergoing a shading change is smaller and appears to have less bias towards either shaded or unshaded temperatures.

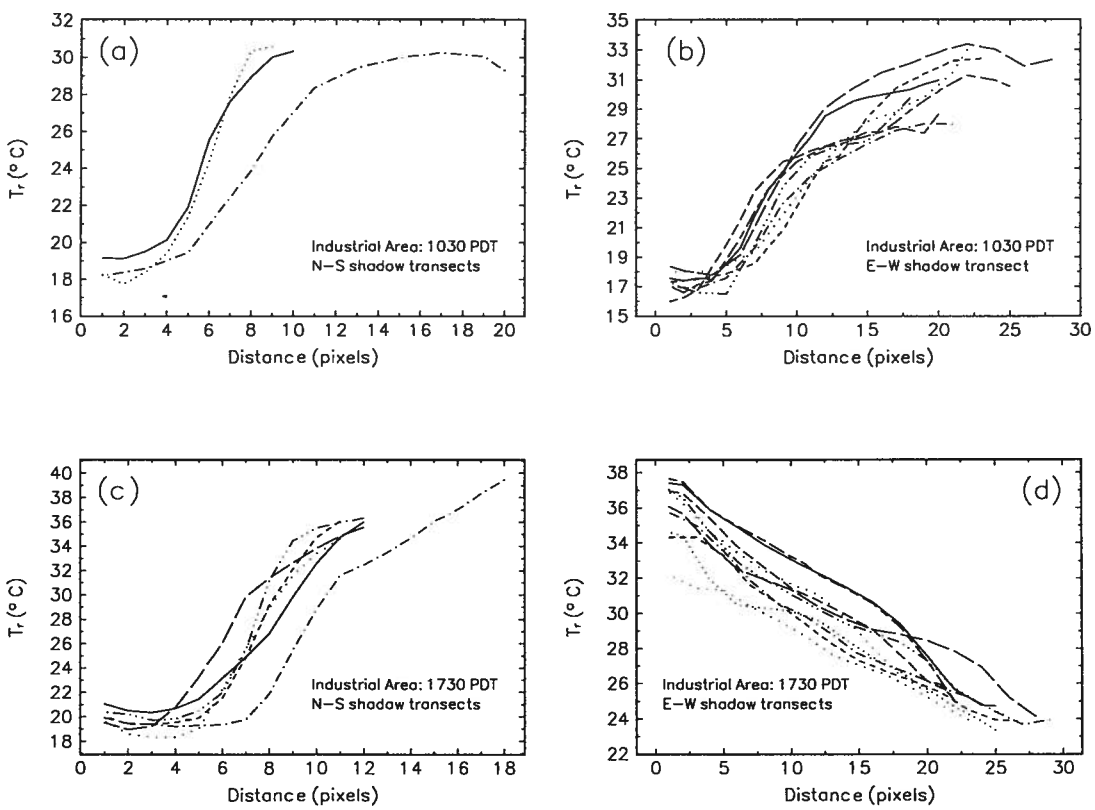

Figure 4.24: Transects of apparent surface temperature across shadow boundaries.

The afternoon extension of shadows onto the N-S streets yields a much more linear

transect; several profiles show a more rapid drop off from the unshaded temperature which is the inverse of the results from the morning, but the effect is subtle. To represent the observed morning bias in the modelled distributions two approaches may be adopted: First, the composite distribution may be represented by two distributions in accordance with the number of radiation classes (i.e., shaded or sunlit). Assuming the pixel size is sufficiently small to make the number of mixed shaded/sunlit pixels insignificant, each class can be represented by a Beta distribution. This accounts for the asymmetric shape incurred by those areas which have recently undergone a change in radiation regime; i.e., shaded areas have a warmer tail, and sunlit areas have a cool tail. Results (Figure 1.25a) indicate this approach has some trouble achieving a fit to temperatures intermediate between the two modes.

Second, shaded and non-shaded surfaces which are not undergoing rapid temperature changes with time due to a recent change in the radiation regime can each be represented by Gaussian distributions. A third distribution, representing those areas recently shaded or non-shaded (the latter dominates at this time but is not the sole class because the shadow position rotates and shortens as the solar zenith angle decreases), is added. This third distribution may be represented by a Beta distribution. The combined curves (Figure 1.25b) yield a good fit across most of the observed temperature range, except for temperatures from 21–25°C where observed frequencies are under-represented. The observed frequencies in this and other examples show a range of surface temperatures between the two main peaks, for which almost equal frequencies were observed, and increasing frequencies towards the main, high temperature peak. This suggests a general shadow pattern which consists of a linear portion beginning at the shaded/sunlit border, and a decrease in the slope as the directly-irradiated surface is approached. In this case the lower temperatures might be better represented by a rectangular distribution, and the upper portion by a Beta distribution, while retaining Normal distributions for the

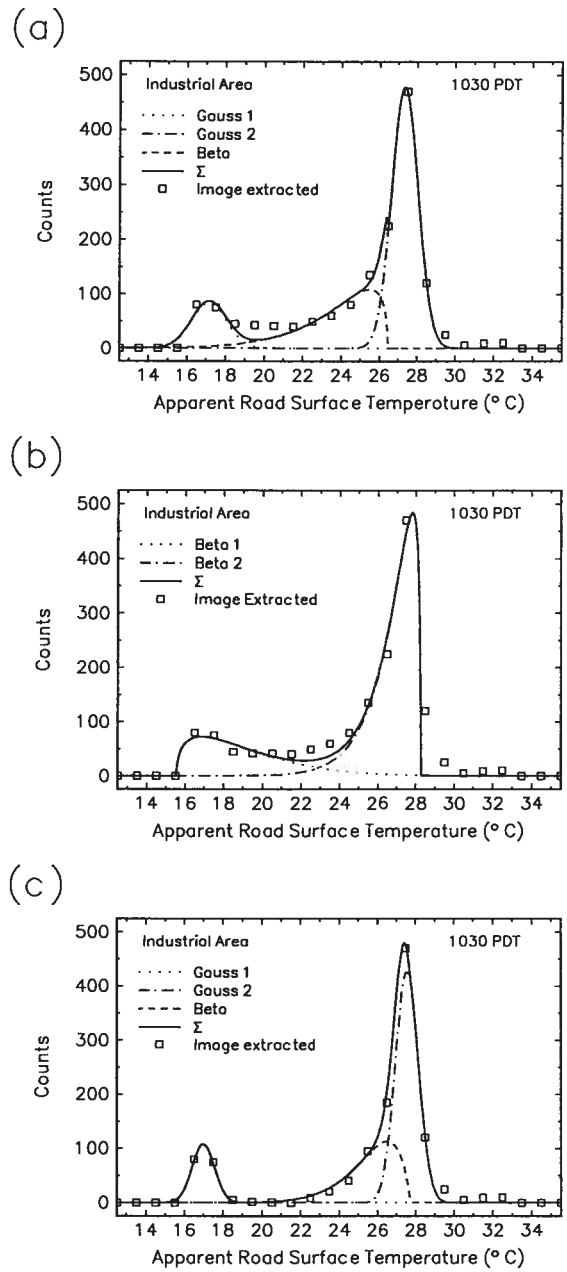

Figure 4.25: Fitted distributions to road surface temperatures (a) using Gaussian distributions for shaded, and sunlit surfaces and a Beta distribution for areas recently unshaded, (b) using Beta distributions for shaded and unshaded surface classes, (c) same as (a) except that a rectangular distribution has been subtracted from the observed distribution between 18.5 and 25.5°C.

shaded and sunlit surface temperature classes. To implement this, a constant count was subtracted from the temperature classes between 18.5 – 25.5°C to represent the rectangular distribution, and two Gaussian and a single Beta distribution were fitted to the adjusted data (Figure 1.25c). The agreement between the combined curves and the observed results is excellent.

4.5.4 Modelling the Study Area Distributions

4.5.4.1 Temperature Frequency Distributions

Selected composite distributions were analyzed to determine the success of modelling with mixed distributions and the relation between these distributions and the statistics of selected component surfaces obtained by extraction from images or from the traverse data.

Two examples of fitted component distributions are shown in Figure 1.26. In the first, component distributions were selected as Gaussian or exponential Gaussian (extreme value) which has a negative skew to the distribution (a tail of higher frequencies towards higher temperatures). The use of the exponential Gaussian provides a good fit to the upper portion of the composite distribution. Both distributions are fitted with three adjustable parameters: the amplitude, centre and width of the distribution. The advantage of using an exponential Gaussian distribution over a Beta distribution is that it is fully described by a mean and standard deviation, while the Beta distribution requires four parameters. The second example retains a Beta distribution and includes an extra Gaussian distribution to better represent the shape suggested by the main peak of the observed data.

Comparison with component surface temperatures extracted from the image suggest that the uppermost distribution is related to roof surface temperatures, the main peak

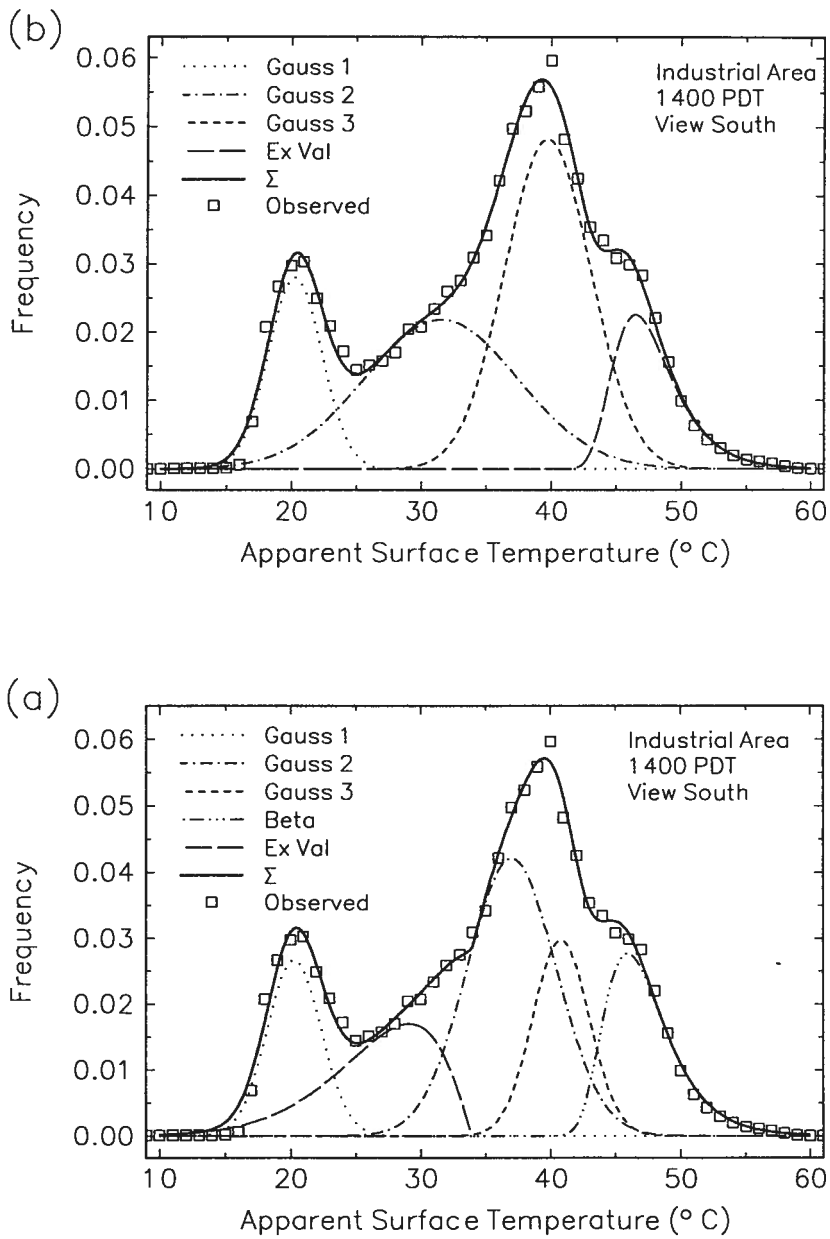

Figure 4.26: Fitted component distributions to Flight 2 (early afternoon flight over the Industrial area). (a) using only Gaussian or exponential (extreme value) Gaussian distributions, (b) including Beta distributions.

(upper peak of the two in the second example) relates to sunlit road and the low temperature peak is a composite of the shaded horizontal and south wall surfaces. The intermediate peaks are less easily correlated with any one component surface.

Results from the application of the technique to composite distributions from Flights 1 and 2 (Industrial study area) Flight 4 (Downtown) and Flight 7 (Residential) are summarized in Figures 1.27 and 1.28.

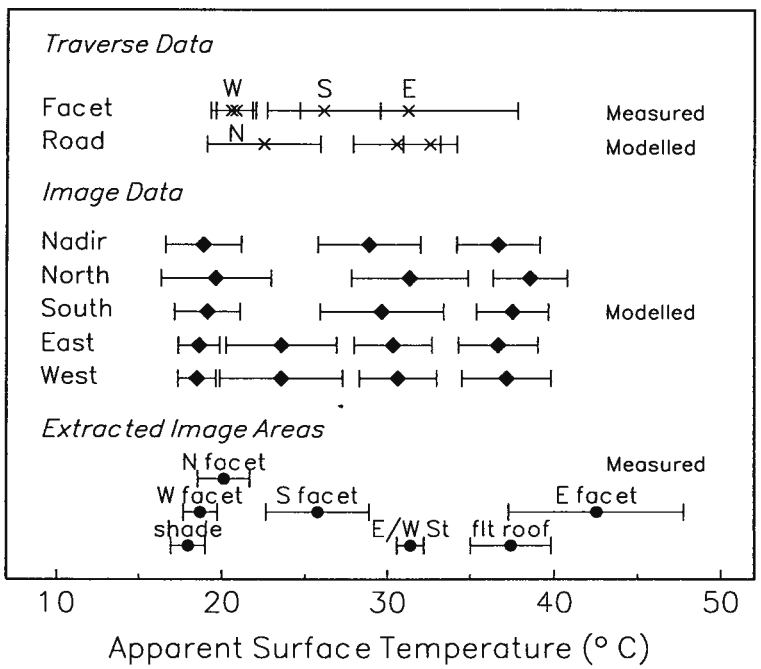

Figure 4.27: Summary of fitted and observed distributions applied to the morning flight over the Industrial area. Facet traverse data are means and standard deviations of the truncated data set for each facet, road data are the means and standard deviations of the fitted distributions. Image data are fitted distributions to the composite surface temperature frequency distribution for each view direction. Extracted Image areas are observed frequency distributions for select pixel categories.

The fitted distributions (described by a mean and standard deviation) for each view direction are plotted horizontally in the middle of the figure. Generally, between three

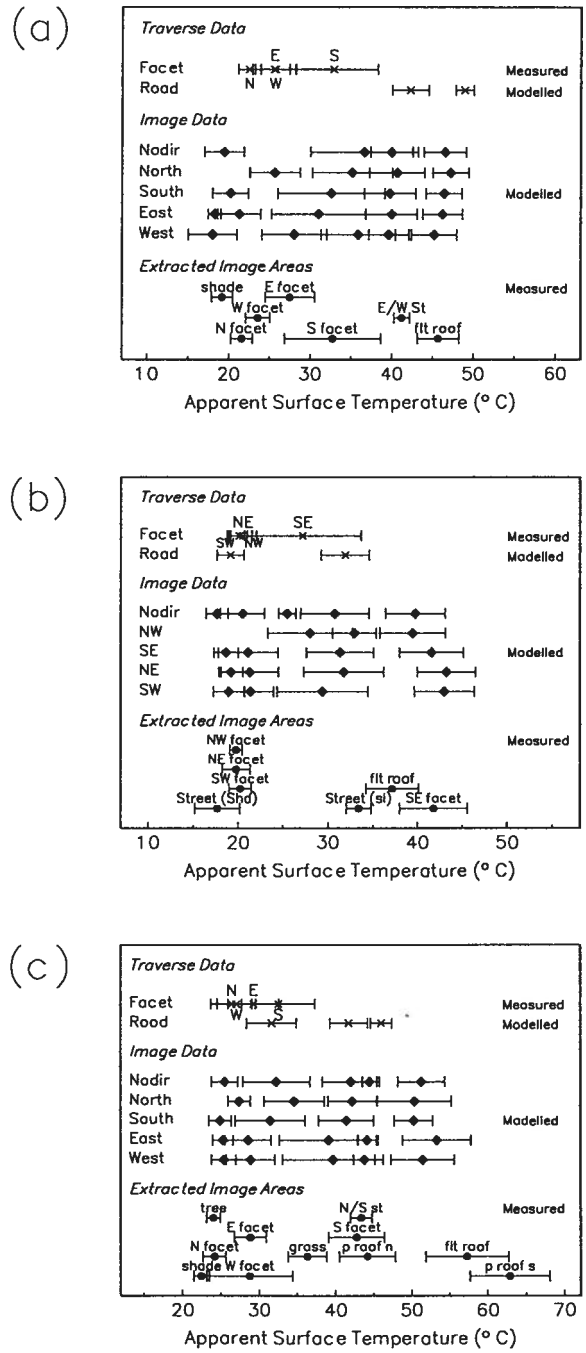

Figure 4.28: Same as 1.27 except for (a) the early afternoon flight (Industrial), (b) noon flight (Downtown), (c) early afternoon flight (Residential).

and five distributions are required to achieve a close fit. Some "tuning" of the procedure (initial adjustment of individual distribution position and parameters) was carried out prior to allowing the fitting procedure to iterate. R^2 values for the modelled curve were always greater than 0.95 and generally above 0.99. Only Gaussian and exponential Gaussian curves were used; the use of Beta distributions requires substantial tuning of the shape to fit the curve and was generally not well related to any one component surface. Summary statistics for component surfaces extracted from select images are plotted at the base of the figure and the means and standard deviations for facet temperatures obtained from the traverse vehicle and road surface temperature components (estimated via mixed distribution modelling of the road surface temperature) are provided at the top of the figure for comparison. These plots allow inspection to assess the agreement between positions of the modelled, component, and traverse distributions.

The plot for the morning flight over the Industrial area (Figure 1.27) shows good correspondence between the means of the flat roof temperature and the uppermost modelled distribution, the sunlit street temperatures and the second highest modelled distribution, and the shaded areas with the lowest modelled distribution. There is a tendency for the modelled distributions corresponding to the street and shaded temperatures to have a greater standard deviation than that of the extracted components. There is no clear correspondence between the facet temperature components and any of the modelled distributions; in part this is because several of the facet temperatures closely overlap other component surface temperature distributions. For example, the south and east canyon facets are very close to the shaded ground temperature, and the west facet overlaps the roof temperatures.

Results from the early afternoon flight also show fairly good correspondence between the roof and sunlit street components with the two warmest modelled distributions, although the modelled distribution most closely matched with the street is represented by

a lower mean and larger standard deviation than indicated by the extracted component. Shaded surfaces match well for all view directions which have a significant shaded surface area (i.e., not including the north view direction). At this time there is a better match between modelled components and facet temperature distributions for the east, west and north view directions. For several view directions, the number of modelled components exceeds that of the assumed component surface types. The additional distribution has a wide standard deviation and has a mean value several degrees below the distribution most closely associated with the street temperatures.

4.5.4.2 Frequency Distribution Differences

Mixed distribution modelling was also applied to the frequency distribution differences. It is hypothesized that facet temperature frequency distributions should be more apparent when differences between view direction are considered. A simple two-dimensional approximation to the average street canyon sequence (N-S transect across a building-canyon-building sequence) in the Industrial area was used to determine the changes in the fraction of the FOV subtended by each component surface (Table 1.3). Shading effects were included by using a solar zenith angle representative of the time of Flight 2. Between opposing off-nadir (north or south) view directions, there are significant changes in the total angle subtended by the sunlit and shaded components of the canyon floor, as well as the change in the canyon facet viewed. The angle subtended by roof areas remains constant; however, if the assumption of flat roofs is not met, (e.g., there are structures on the roof which cast shadows), then the roof contains shaded and sunlit areas which vary with view direction.

Differences in the component angles for nadir versus off-nadir views show large changes in the fraction of wall viewed as well as changes in the area of sunlit floor (especially for the south view direction) and the shaded canyon floor (north view direction). Changes

Table 4.3: Percentage of the FOV occupied by component surfaces of a N-S transect in the Industrial area. Z = 36°, FOV = 12°.

	View Direction		
Surface	Nadir	North	South
Roof	65.2	67.9	67.9
Wall	1.1	14.9	14.9
Floor (shaded)	22.6	17.2	6.6
Floor (sunlit)	11.1	0.0	10.6

in apparent roof area are rather small for the conditions tested. These results suggest that at least three and perhaps four or five component distributions should be apparent in the difference distributions due to the change in apparent area of major component surfaces.

Mean and standard deviations of the fitted distributions are presented in Figures 1.29 and 1.30, along with those for the extracted component surfaces and the overall mean and standard deviation of apparent facet temperatures obtained from the vehicle traverse. The sign of the difference for the fitted distributions is represented by the symbol: an open symbol indicates a negative difference and a solid symbol a positive difference.

The number of distributions required for Flights 1 and 2 is generally 3 or 4, in agreement with that expected due to differences in the apparent component surfaces. The identification of facet surface temperature distributions is inferred by comparison with the component distributions and the traverse statistics.

For Flight 1, the south, west, and east facet temperatures appear to be represented. The west facets appear warmer when viewed by the airborne scanner rather than the EIRT; this is probably due to the ability of the airborne scanner to view the differential wall areas which occur along the blocks where buildings of different heights are adjacent,

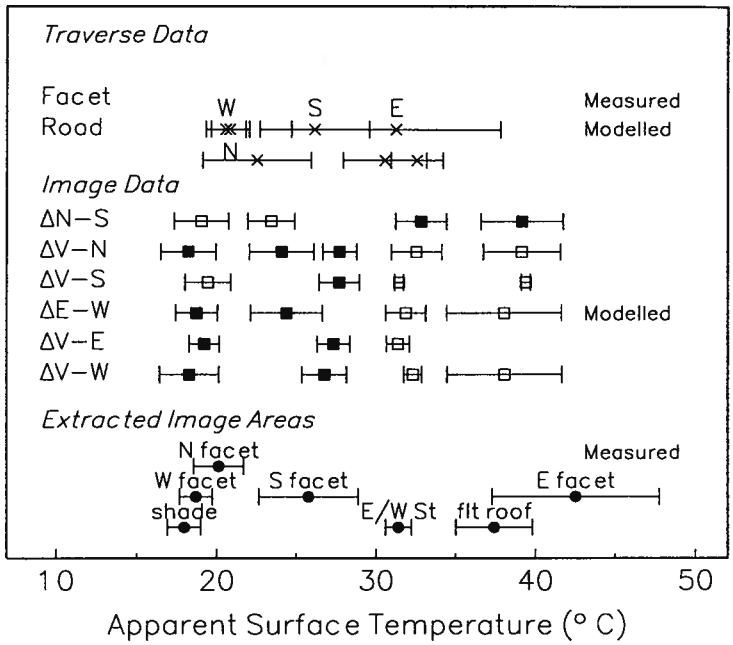

Figure 4.29: Summary of fitted distributions applied to temperature frequency differences between pairs of view directions for the morning flight over the Industrial area. Open symbols for the fitted distributions indicate a negative value for the difference between the view directions, solid symbols represent a positive difference.

but which are not seen from the traverse route, which is limited to the exposed facets of buildings at the ends of the blocks. The east and south facet components viewed by the airborne scanner tend to be cooler. This may be due to inclusion of some surface temperatures at the base of the walls which are cooler and/or the limitation of the EIRT to view only a portion of the wall. The N/S and nadir/S differences show good agreement between the lowest modelled difference distribution and the extracted south facet component. Similarly, the E/W and nadir/E differences are characterized by a low temperature distribution which correlates well with that of the east facet component. Vehicle traverses obtain mean values for the east and south facets which are slightly

warmer than either the modelled or extracted distributions. The uppermost distribution of the E/W and nadir/W differences is assumed to be related to west facet temperatures, but the mean is substantially lower than that of the extracted west facet temperatures, and warmer than that obtained by the ground traverse. North facet temperatures are not as obvious in the N/S and nadir/N differences; the best match is with the second lowest distribution of each, but these are somewhat cooler than suggested by the traverse and component surface temperatures.

All the view direction difference pairs have a peak associated with the sunlit road surface temperature; this occurs due to the reduction or increase in apparent area of this surface with view direction. Somewhat surprisingly, the differences obtained with the N,S and nadir directions also contain a distribution most closely associated with the roof component. This may be due to different viewed proportions of sunlit and shaded roof areas, caused by roof structures or buildings of different heights, or perhaps due to the temperature distributions on pitched roofs.

The results for Flight 2, (Figure 1.30a) are in general agreement with those suggested by the 2-D analysis. All facet temperatures except for north facets appear to have a component distribution well correlated with both the traverse and extracted temperatures. North facet temperatures obtained from the vehicle traverse and extracted from select images show good agreement but are not well correlated with the component distributions used to model the differences between north/south and nadir/north view directions. The reasons for this are not clear.

Road surface temperatures correlate reasonably well with one of the components in each of the view direction pairs; generally this is the second highest temperature distribution. However, traverse results suggest a component of road surface temperatures exceeding the temperature of the flat roof component so the uppermost modelled distribution may also be related to changes in the apparent area of this component.

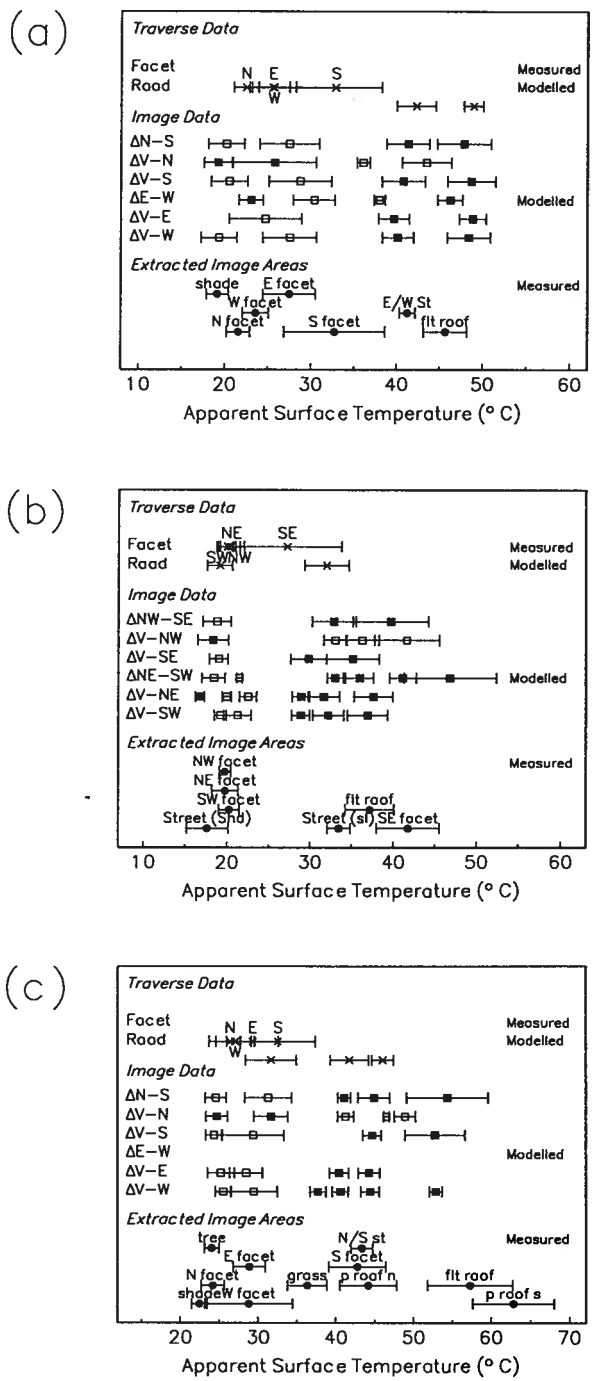

Figure 4.30: Same as Figure 1.29 except for: (a) the early afternoon flight (Industrial), (b) noon flight (Downtown), (c) early afternoon flight (Residential).

More modelled distributions are required to fit the frequency distribution difference curves from the Downtown and Residential areas than were required for the Industrial area. Assignment of modelled components to surface types is therefore more difficult, especially where several modelled distributions lie close together and where some component surfaces (e.g., sunlit canyon facets, building roofs) may have a wide range of temperatures which could be modelled by multiple distributions. Facet temperatures obtained from the vehicle traverse, and by extraction from individual images, show good agreement for the three facets not directly irradiated. These can also be relatively easily identified in the modelled distributions. Overlap between the temperature distributions of shaded road surfaces and shaded facets (refer to the extracted image component temperatures and traverse temperature distributions) makes distinction between these components difficult, although several pairs distinguish two or three low temperature components. Of these, the nadir-NE difference most closely matches the extracted component temperatures and has the expected sign of the change correct (i.e., the shaded road surface percentage is higher for the nadir view and the shaded facet component percentage is greater in the off-nadir view).

The temperature of the most directly irradiated facet (NW) shows a significant difference in the mean temperature as described by the traverse data compared with that extracted from select images (the traverse data are much cooler). This may be due in part to spectral emissivity differences and the fact that the traverse instrument points upwards (the 30° EIRT results are shown), while the airborne sensor is pointing downwards. This means that the reflected component of radiance from low emissivity surfaces originates from the sky for traverse data but from within the canyon (probably the road) for the airborne data. Fitted distributions for the NW-SE and nadir-NW differences show fairly good agreement between the uppermost modelled distribution and the NW facet image-extracted temperature.

Sunlit road surface temperatures obtained by extraction and from the traverse data correlate well with modelled distributions. The roof surface temperatures show a high variability in the study area due to the complex structure of many of the building roofs and the wide variety of roofing materials used. The best match between modelled and extracted roof temperatures is with the nadir-NE and nadir-SW differences.

In the Residential study area, the large number of component surfaces and their overlapping temperature distributions complicates the task of assigning modelled distributions to a surface component. The results shown in Figure 1.30(c) are from the northern part of the study area which is characterized by a north/south block orientation.

East, west and south facets show generally good correspondence between modelled and observed distributions. Road surface temperatures overlap with several other components and are somewhat more difficult to distinguish but appear to be linked with modelled components in several of the view direction pairs. The most directly irradiated facet (N) again shows a large difference in the mean temperature obtained from the traverse results compared with those extracted from images. This may be due to a bias in the selection of facets when analyzing the images and/or the inclusion of surfaces other than the north facets by the traverse vehicle. Where the interbuilding spacing is small, the apparent viewed area of north walls may be higher for nadir views than for off-nadir, and the sign of the modelled distribution difference which matches the traverse results most closely supports this.

4.5.4.3 Summary

The use of mixed distribution modelling on image frequency distributions and distribution differences suggests some component surface temperatures can be identified. While a statistically good fit is obtained with a relatively small number of distributions to the temperature frequency distributions, the apparent link between these distributions

and component surface temperatures desired is weak. Comparison of Figures 1.28 and 1.30 suggest that the use of the temperature frequency differences allows better correlation between the modelled distributions and the component and traverse estimates of facet temperatures, i.e., the hypothesis holds. The results improve as the simplicity and regularity of the surface structure increases.

The ability to confirm the results is limited by the differences in the view between the traverse vehicle instruments and that of the airborne scanner, and with difficulties in obtaining a representative sample from the images for some component surfaces, especially canyon walls in the Residential area, and roof tops in the Downtown area. Particular difficulties are noted for several of the flights in the relation between airborne and ground-based estimates of the most directly irradiated wall surface temperature.

4.6 Surface Temperature Anisotropy

4.6.1 Observational Results

For each of the three study areas, distributions of image means, taken from a set of images covering the study area, were constructed (Figure 1.31, 1.32, 1.33) to illustrate the anisotropy of surface longwave emissions.

These results show the degree of anisotropy which may be experienced by sensors with IFOV covering a block or more (i.e., those that sample an area which contains most of the variance over that land-use area (Schmid, 1988)). It is assumed that each image fulfills this requirement, so that the variation between image means is weak. As the IFOV decreases (averaging the image over a reduced subset of lines and columns), the overall mean should become more dependent upon the position of the projected FOV on the ground and the distributions of the means show a much wider range. Performing this operation for several images showed differences between means of images remained

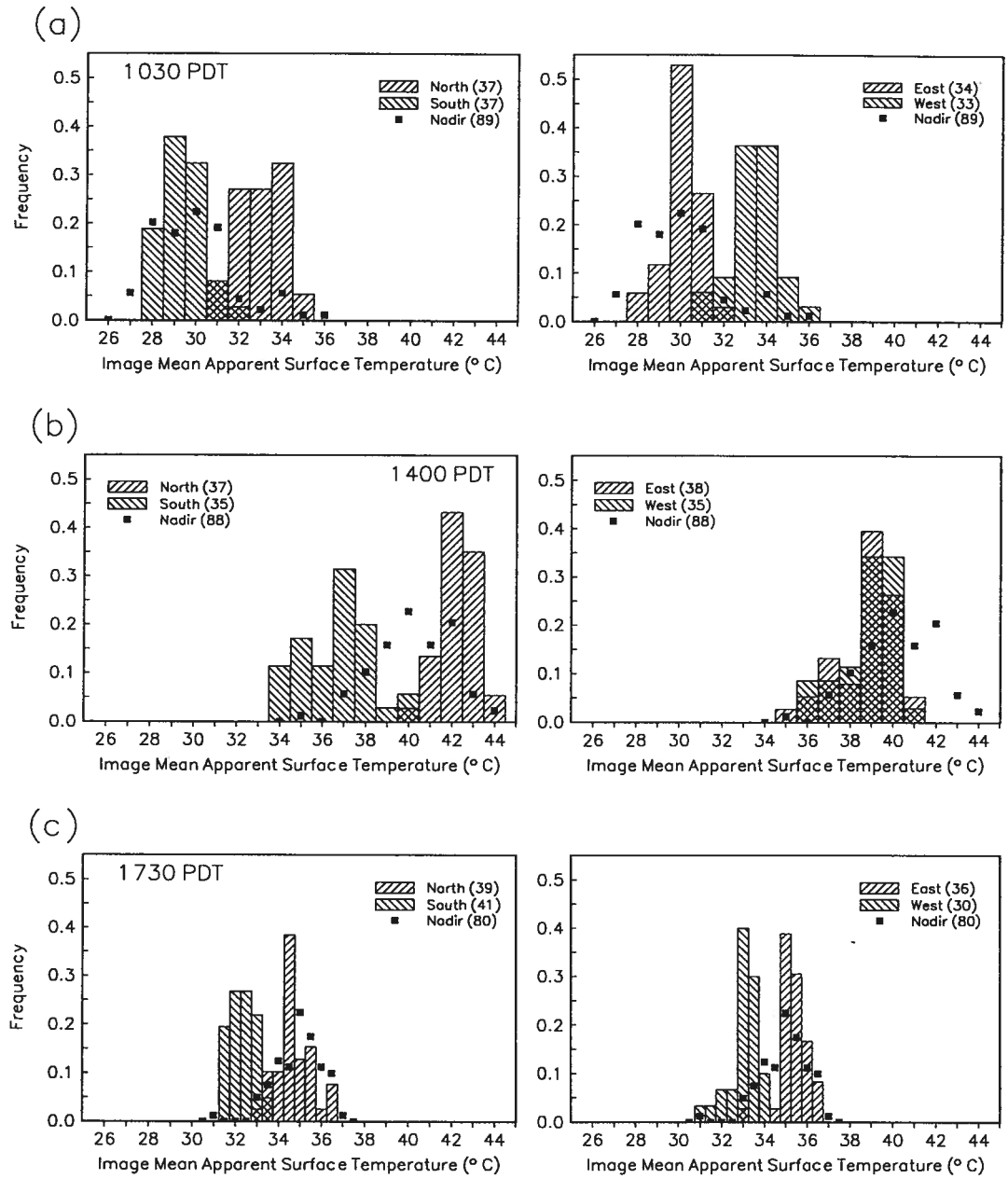

Figure 4.31: Distribution of image mean apparent temperature for nadir and opposing view directions over the Industrial study area. (a) Flight 1, (b) Flight 2, (c) Flight 3. Bracketed numbers in this and subsequent figures are the number of images used to create the frequency distribution.

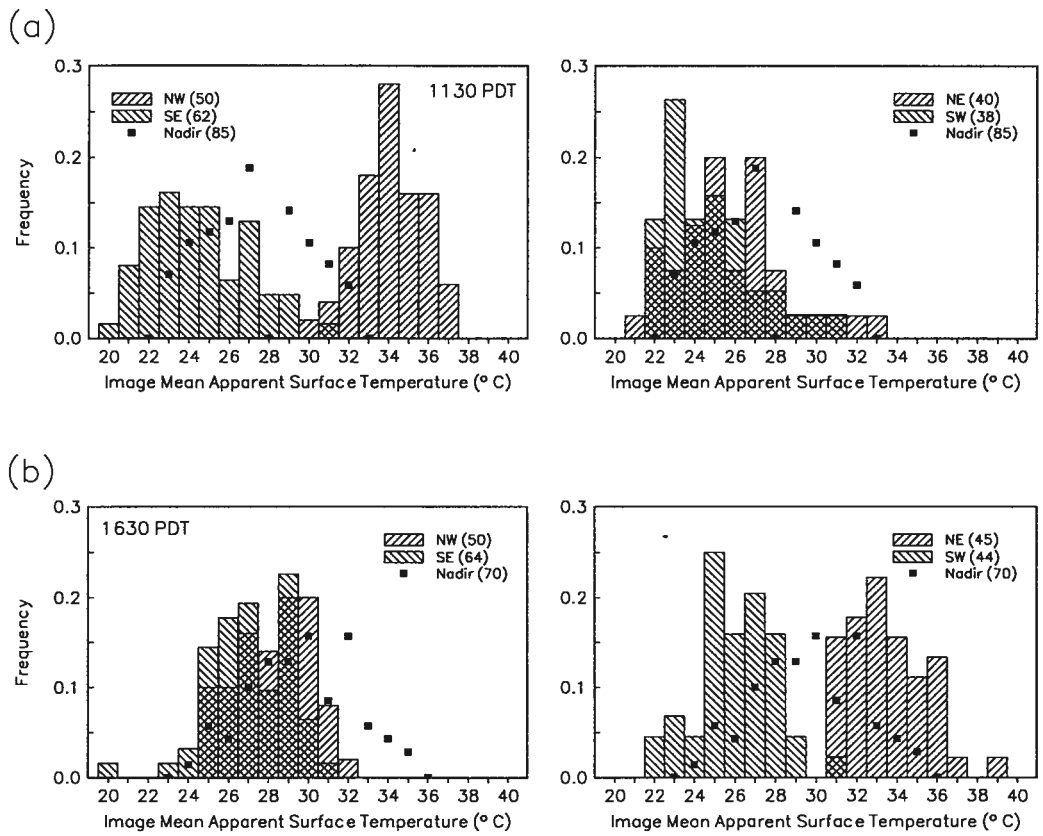

Figure 4.32: Same as Figure 1.31 except for the Downtown study area. (a) Flight 4, (b) Flight 5.

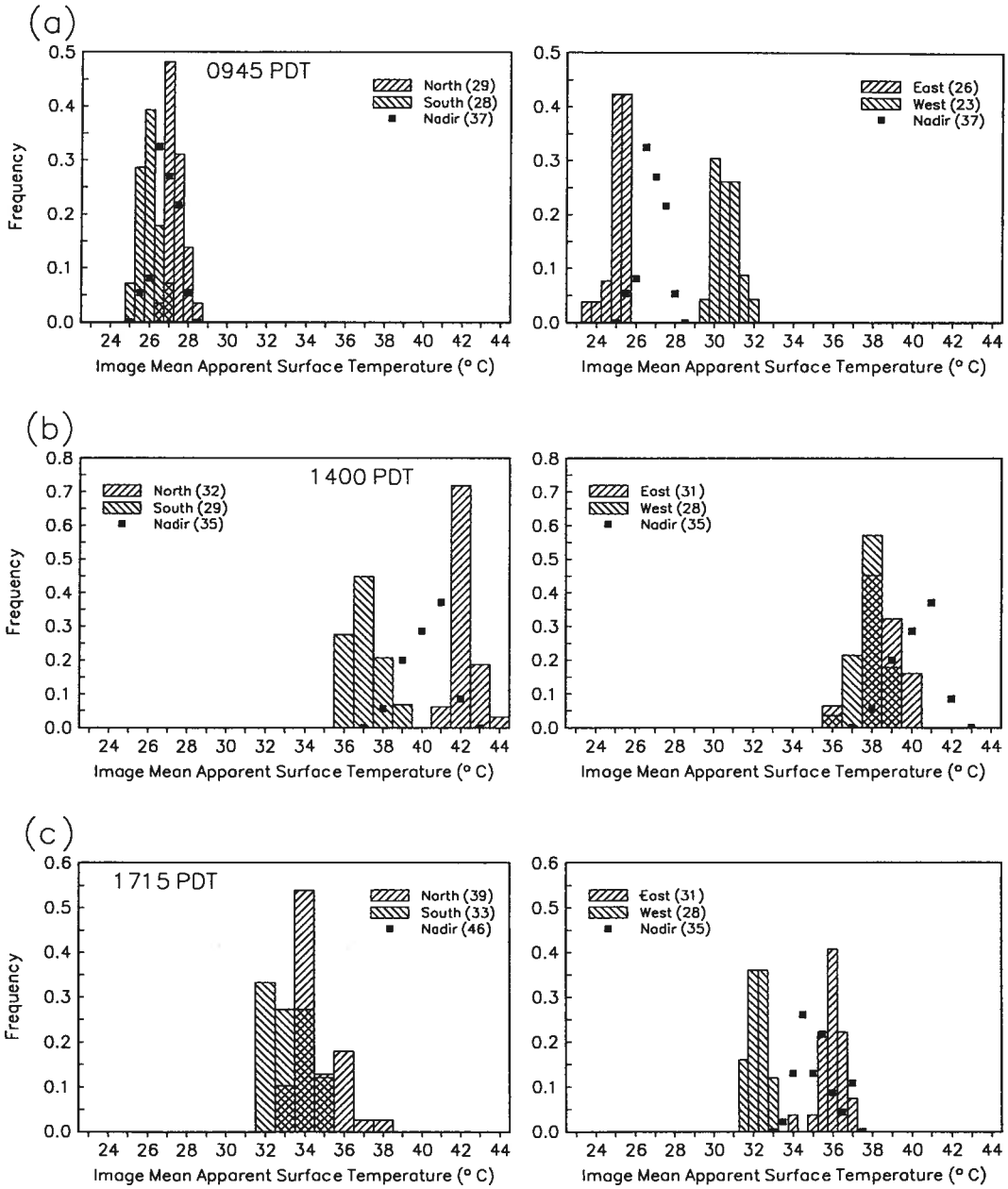

Figure 4.33: Same as Figure 1.31 except over the Residential study area. (a) Flight 6, (b) Flight 7, (c) Flight 8.

small until the image FOV covered approximately 80 m^2.

Results are separated into opposing view angle directions. In each figure, the distribution of image means for the nadir view angle is also presented for comparison. The plots have been constructed by averaging the image photon emittance (corrected for atmospheric influences) and converting to an equivalent radiant (apparent) temperature. This may be considered to be a measure of the "true" anisotropy of the surface; i.e., that which would be observed in the absence of an atmosphere. Actual observations by sensors with a FOV equivalent to, or larger than the image size may differ because the sensor averages the radiance over the IFOV and atmospheric corrections would be applied to the apparent temperature derived from the total radiance received. Corrections vary depending upon the spectral response of the instrument.

Images containing non-standard surface cover (parks, irregular block orientations) have been removed from the analysis. Clear separation of the two distributions and their modes is taken as evidence of anisotropy; (i.e., the distributions are characterized by different mean apparent temperatures).

Differences between the means of the distributions are summarized in Figure 1.34 which gives the mean temperature and standard error for each viewing direction of each flight, and Table 1.4 which summarizes all the differences between pairs of viewing directions.

The majority of differences between pairs of viewing directions were found to be significant to a high level of confidence as described by the T-test for two samples with unequal variance (Table 1.4). Of the 80 pairs tested, 6 fail the significance test at the 0.1 level, 7 at the .05 level and 13 fail the significance test at the 0.01 level.

Results between opposing off-nadir viewing directions show the anticipated differences. Strong east/west differences occur in the morning and late afternoon flights and there is little difference for the early afternoon flight. North-south differences follow an

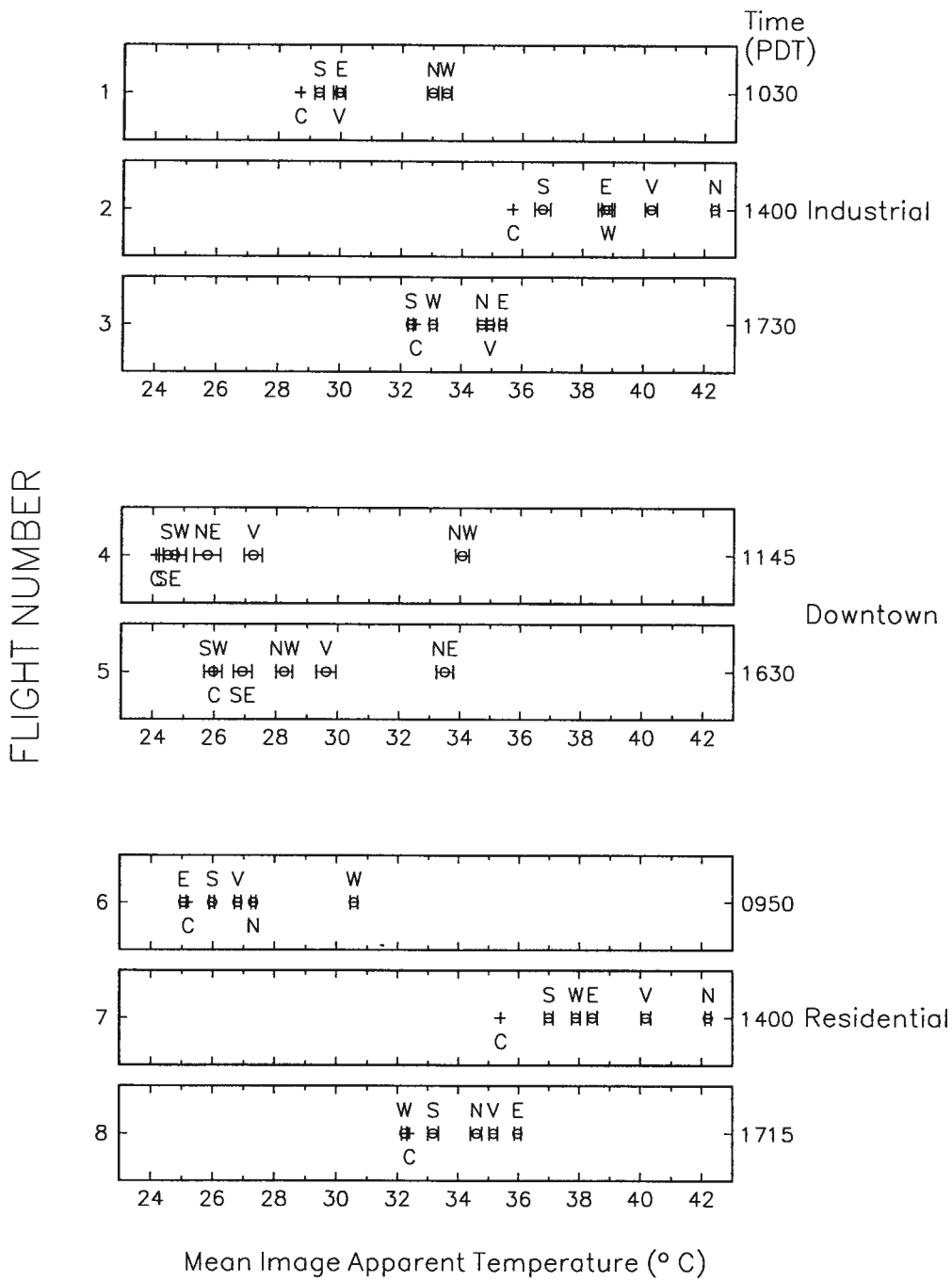

Figure 4.34: Mean apparent surface temperature and standard error of each view direction (V = nadir, C = complete temperature) for each flight.

Table 4.4: Temperature differences between means for pairs of view directions; differences NOT significant (0.01 level) are italicized.

FLT	N-S	E-W	V-N	V-S	V-E	V-W	N-E	N-W	S-E	S-W
1	3.71	-3.46	-3.06	*0.65*	*-0.06*	-3.52	3.00	*-0.46*	-0.70	-4.17
2	6.68	*0.98*	-2.09	4.59	1.51	*2.49*	3.60	4.59	-3.08	*-2.09*
3	2.33	2.31	*0.29*	2.62	*0.41*	1.90	0.70	-1.61	3.03	-0.72
6	1.34	-5.53	-0.51	0.83	1.77	-3.76	2.28	-3.25	0.94	-4.59
7	5.21	*0.55*	2.03	3.18	1.75	2.29	3.77	4.32	-1.44	-0.89
8	1.43	3.74	*0.56*	1.99	-0.81	2.93	-1.37	2.37	-2.80	0.94
FLT	NW-SE	NE-SW	V-NW	V-SE	V-NE	V-SW	NW-NE	NW-SW	NE-SE	SW-SE
4	9.59	*1.04*	-6.98	2.61	1.29	2.33	8.27	9.31	*1.32*	*0.28*
5	*2.67*	7.53	1.36	4.03	-3.87	3.66	-5.23	2.30	7.90	*0.37*

inverse pattern, (i.e., strongest differences at midday, less in the morning and later) but show clear differences between distributions at all times, with the exception of the late afternoon flight over the Residential area. The east-west differences are larger in the Residential area and north-south differences are greater in the Industrial area during the morning and late afternoon flights. These differences may be a result of the relatively low east/west wall areas in the Industrial area where most of the buildings directly join with their neighbours. East and west walls are therefore only visible for buildings at the end of blocks and where adjoining buildings have a height differential. The preferential E-W block orientation with alleys also increases the visible north and south wall areas relative to the east and west walls.

The images from the Residential area have not been stratified according to the block orientation, and the strength of the observed differences with direction was somewhat

surprising, given the low building height, small inter-building spacing and greater fraction of vegetated surfaces. The strong east-west differences are maintained through a combination of large temperature differences on east-west oriented peaked roofs in the south portion of the study area, and the differences in vertical facet temperatures which are seen in the north part of the study area.

Distributions of nadir means are generally normal, although Flight 1 exhibits some positive skewness. This was found to be a result of images from the last flightline taken over the northern boundary of the study area which was characterized by a few large, hot buildings in the sample images. It is also the flightline which has had the most time to warm relative to the other nadir flightlines. The position of the nadir distributions relative to the off-nadir varies with time, due to the large temperature changes on the vertical facets. Morning flights generally show a closer correspondence with the shaded facet, and the late afternoon flights show better agreement with the heated facet. Midday flights show the nadir mean to be substantially cooler than the north view direction, but warmer than all other view directions. Because of the dynamic nature of the temperatures of the different facet orientations (e.g., see facet temperatures changes from truck traverses), these results likely differ substantially with time.

In the Downtown area, the morning flight shows the most directly irradiated facet to be most different in temperature from the facets seen in the other three view directions, the most shaded of which are very close in temperature. The afternoon flight shows a greater separation between the temperatures of each view direction but a reduction in the difference between the warmest view direction and nadir.

As an example of observed anisotropy by a satellite sensor, the analysis for Flights 1–3 were repeated using channel 4 of the NOAA-11 AVHRR. Image apparent temperatures were corrected to true apparent temperatures using the AGEMA LUT relations derived in Appendix B and subsequently converted to apparent surface temperatures using a

calculated LUT for the satellite sensor. Results are shown in Figure 1.35.

The effect of the atmosphere is to reduce the apparent temperature differences. However, significance as calculated by T-tests remains identical because the same transformation is applied to each view direction and the ratio of variances remains constant before and after the transformation.

4.6.2 Comparison with Other Surfaces

These observations constitute the first attempt to directly measure the anisotropy of thermal radiation over an urban surface. Prior investigations have studied the anisotropy at local scales over agricultural (row crops) or natural surfaces (forest canopies) and at larger scales in mountainous terrain (c.f. Chapter 1). Comparison with Table 1.2 shows the observed variation with view direction over cities is large relative to the natural and agricultural surfaces listed, being similar in magnitude to those reported for an oak-hickory forest and a sunflower crop. Two major factors are responsible for the degree of observed anisotropy: the regularity of the surface structure, and the creation of large temperature differences on the different surface components viewed by the sensor.

Anisotropy for vegetated surfaces without a regular geometric surface structure also can be large, when canopy cover is incomplete and the sensor IFOV includes portions of vegetation and soil which change with sensor viewing angle (more vegetation is seen at larger zenith angles, i.e., longer paths through the canopy).

In urban areas, anisotropy is dominated by the regular geometric structure of the surface. The anisotropy arises due to temperature differences on the vertical facets generated by differences in absorbed solar radiation and thermal properties and due to variations in the amount of shaded and sunlit horizontal surfaces viewed. Based upon these considerations, anisotropy should be maximized in areas of the city where the block and building orientation is very regular, the area of vertical facets is large, and considerable

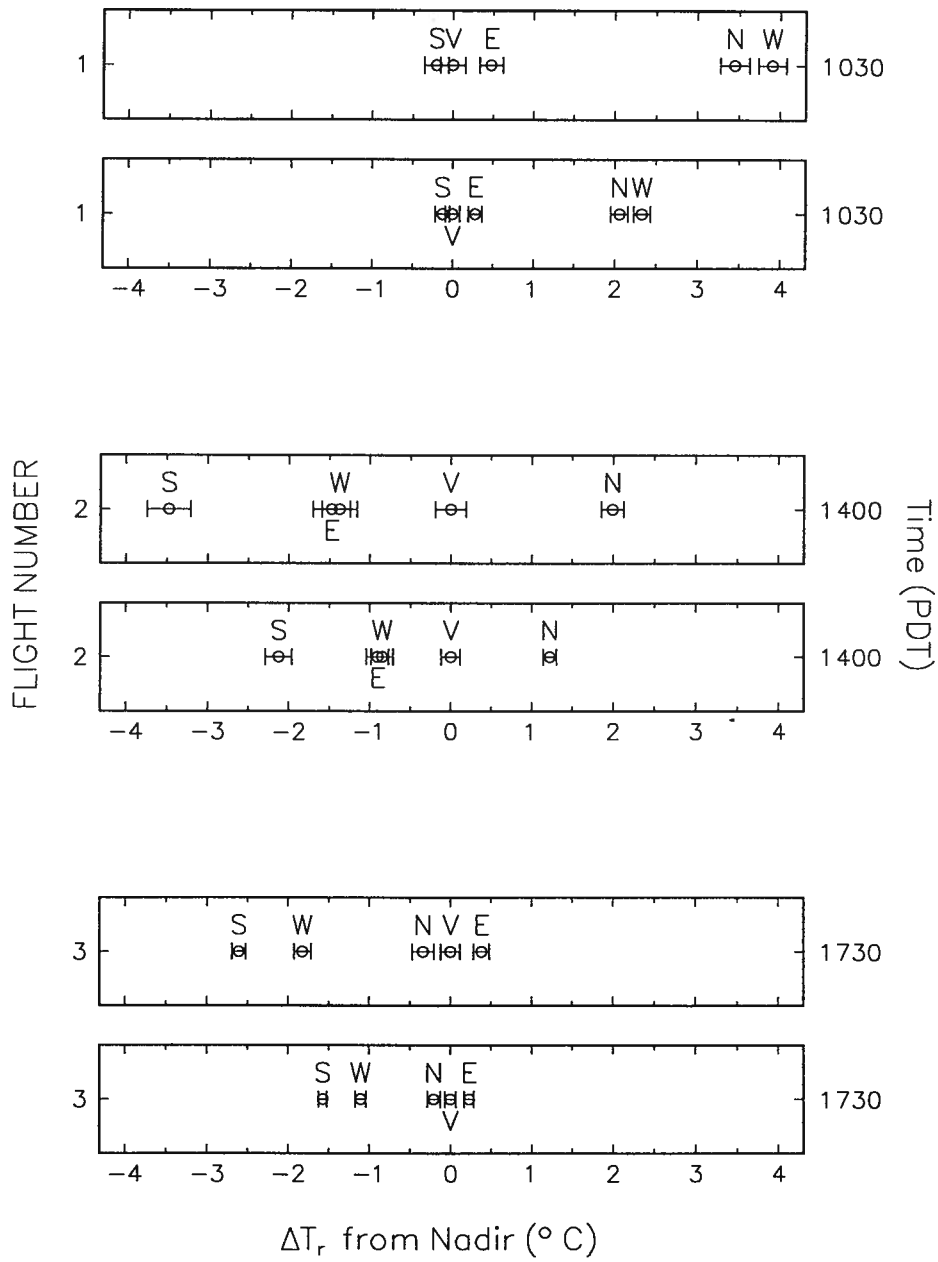

Figure 4.35: Calculated mean apparent temperatures and standard errors of each view direction at the TOA for NOAA-11 AVHRR Channel 4. Flights 1–3 only.

differences in the amount of shaded and sunlit horizontal surfaces with view direction can be observed. The results from the three study areas confirm the Downtown area has the largest apparent temperature differences with direction, although because of the different street orientation, direct comparison with the other study areas is not straightforward. A mitigating factor in both the Downtown and Industrial areas is the close spacing of buildings which limits the view of wall areas and/or cast shadows onto facets which would otherwise be directly irradiated. These effects reduce anisotropy. The spacing of the buildings is therefore an important factor in the creation of large apparent temperature differences.

In the Residential area, small scale structural features (peaked roofs) appear to enhance anisotropy which otherwise was expected to be relatively small because of smaller wall areas relative to horizontal areas, and reduced regularity in the block and building structure. The occurrence of large vegetative elements in the Residential area enhance anisotropy because they cast shadows and because the tree crowns have spatial temperature variations associated with the receipt of solar radiation. Image analysis shows tree crowns are warmer by approximately 2°C when viewed on the side receiving direct solar radiation compared with the shaded side. Similar results were obtained by Balick *et al.* (1987) over a mixed deciduous forest canopy. Like buildings, the spacing of the trees is probably important if the tree crowns are to develop temperature differences and ground-shaded areas remain distinct. As the canopy closes a more uniform top surface is presented, the temperature differences are reduced, and shaded areas beneath the canopy are obscured.

The presentation of the frequency distribution of image means (Figs. 1.31– 1.33) and the tabulation of the difference between the overall means by direction (Table 1.4) provide a more conservative statistical measure than the use of simple maximum differences with directions often reported for other studies (Paw U, 1992). An estimate of the maximum

difference to be expected can be obtained from the frequency distributions. As observed in previous studies, differences vary with time and sensor orientation. In contrast to row crops, which show a single temporal maximum, urban surfaces with street canyons oriented in orthogonal directions show large differences at two or more times during the day, depending upon the street orientation and sensor view direction.

Differences due to the variation in viewing angle are restricted to nadir and 45° off-nadir comparisons, therefore no comment can be made regarding the angle at which differences are maximized from the nadir. This angle depends on the local surface geometry and the solar position as it affects the pattern of surface heating. Qualitatively, it is anticipated that with increasing angle from the nadir when viewing a shaded facet, the mean temperature will drop due to an increase in the view of the shaded wall and loss of view of a portion of the canyon floor. The image mean temperature will likely decrease until the view of the shaded wall/floor area becomes restricted, at which time the mean temperature should rise again. For a view direction towards a sunlit facet the trend will be reversed.

4.6.3 Scale of Anisotropy

The observed biases are a function of the resolution of the sensor. As described by Lipton (1992) for a satellite sensor viewing mountainous terrain, the observed bias will increase as sensor resolution decreases and the proportion of steep slopes viewed increases. The limiting case suggested for a sensor where the IFOV consists entirely of terrain made up of parallel ridges aligned NE/SW was estimated to be 19°C during the morning. Increasing proportions of terrain with different slope orientations decreases the observed anisotropy. The local control on the anisotropy is the temperature difference between the different slope orientations of the terrain as determined by the energy balance of those surfaces (higher for less vegetated, drier surfaces).

In urban areas, anisotropy is also conditioned by surface structure. In this case the regularity and relative extent of vertical (or sloped) surfaces to horizontal surfaces is important (e.g., proportion of wall or sloped roof surfaces to horizontal surfaces). Anisotropy is reduced as irregularity in the surface structure (e.g., street pattern) increases, so proportions of cities characterized by twisting streets are expected to show less anisotropy than those with a more regular street pattern. Increase in the vertical extent of buildings increases anisotropy because a greater proportion of surfaces have larger temperature differences. It is assumed the remote sensor has an IFOV sufficient to view an area large enough to contribute most of the temperature (and by association surface structural) variance. It does not make sense to define the anisotropy at very small scales: high resolution instruments, will, in the limit, resolve individual surface elements and the variations in surface temperature become visually apparent (as in the thermal images presented here). Successive degradation of images showed evidence of the warm roofs and cool shaded areas at pixel sizes of up to approximately 6 m^2 (a peak in the local variance occurs; see Woodcock and Strahler (1987)) which is indicative of maximum variation in the temperatures of adjacent pixels. As pixels become larger than this size, they begin to average across the scale of maximum temperature differences and the variance between adjacent pixels decreases. Of importance is the anisotropy at scales where the surface structure is unresolved by an individual IFOV.

It seems likely that there will exist a range of scales (surface area) for which the anisotropy remains constant or very nearly constant; these correspond to areas of similar surface structure which generate a particular frequency distribution of temperatures; i.e., homogeneous areas. The lower bound of this range of scales is probably no larger than the scale suggested by Schmid (1988) to be representative of the surface temperature and structural variance (200 m diameter in a Residential area similar to that studied here). It may be substantially smaller. Schmid (1988) found the main contribution to the spatial

variance of surface temperature occurred at 25 m (street/alley to house row spacing) and 50 m (street to alley spacing).

Anisotropy is expected to remain relatively constant as scales increase up to the point where the IFOV begins to cover different land-use areas (and/or different surface structure patterns) at which point it is expected that compensation of directional variations should begin to take place. The similarity of single image temperature frequency distributions with that for all images within a study area lends some support to the hypothesis that anisotropy is constant over the range of scales encompassed by a single image (150 m^2) to that of the entire study area (1 km^2).

4.6.4 Anisotropy Relative to Other Influences Upon Remotely Sensed Surface Temperature

The directional temperature variations observed in this study are compared with the magnitude of other factors which influence a remote measurement of surface radiative temperature; atmospheric absorption, and surface emissivity (Table 1.5). Both factors may show spatial variability in cities.

In their consideration of errors, Roth *et al.* (1989) suggest spatial temperature errors of up to 1.5 K are possible due to variations in urban-rural surface emissivity. Horizontal variability in atmospheric water vapour and pollutant concentrations is suggested to yield errors of 1 K (Carlson, 1986).

It is worth noting that the assumption that atmospheric corrections need not be applied to determine urban/rural temperature differences is not true; calculated LUT corrections show strong variations with temperature. Appendix B indicates corrections of -1–$+8$°C are required over the range of observed surface temperatures for the AGEMA scanner (8–12μm). Applying atmospheric corrections to Figure 1 of Roth *et al.*(1989)

Table 4.5: Magnitude of temperature differences produced by processes affecting remote thermal measurement of an urban surface.

Process	Magnitude (°C)	Comments
Surface emissivity	2–2.5	average urban emissivity of 0.95 (Arnfield, 1982)
Atmospheric absorption/emission	4 – 7	mid-latitude summer atmosphere
Anisotropy	up to 10	45° off-nadir, coinciding with up- and down-Sun directions

(Vancouver daytime heat island; NOAA- 9 AVHRR Channel 4) for the standard mid-latitude summer atmosphere (contained within the LOWTRAN program) increases the apparent surface temperature by 4 K in rural areas and up to 7.5 K in the heat island core. Urban - rural surface temperature differences are therefore enhanced due to these corrections; in this example an increase from 11 to 15.5°C is calculated. Errors due to anisotropic emissions will likely vary on a pixel by pixel basis depending upon the surface structure and relative sensor position, and can be large within individual land-use areas. In industrial/commercial areas where daytime surface heat island values are large, the observations here suggest directional variations of up to 6 K are possible (Table 1.4). The effect of anisotropic emissions on the determination of heat island magnitudes (assuming a consistent, regular surface structure throughout the urban area, and a flat isotropically emitting rural surface) can lead to either a reduction or enhancement of the heat island signal, depending upon the time of day and direction of view. This is potentially important for studies which use the maximum ΔT_{u-r} value in further analyses.

The relative magnitude of errors will be scale dependent. The scale dependence of anisotropy has already been noted. Emissivity differences are maximized at scales on the order of metres, and decreases with averaging across a ground resolution element (GRE) of the remote sensor. As GRE decreases the relative error in emissivity will increase as small, low emissivity areas become more important. Atmospheric variability is small and probably operates at scales on the order of hundreds of metres to a few kilometres.

Consideration of these effects from an operational perspective indicates that the effect of anisotropy is likely most important for aircraft-based sensors which combine a small IFOV and large range of off-nadir scanning angles to yield pixels for which anisotropy is likely to be high.

For the commonly used satellite-based thermal scanners employed in studies of the urban heat island (Table 1.6) only the NOAA series of satellites incorporates a large off-nadir scanning capability which can be affected by anisotropy. These polar-orbiting satellites have ground tracks of roughly NNE-SSW (descending node) or SSE-NNW (ascending node), and scan at right angles to the sub-orbital track. Under these conditions anisotropy for daytime, early afternoon passes is likely to be relatively minor in areas with a preferred N/S-E/W block structure, but may be large for areas where the block structure is rotated 45° (e.g., Flights 4–5 over Downtown Vancouver), although the effect of anisotropy is probably reduced due to the large GRE of these sensors at off-nadir angles. The morning passes made by NOAA-6,8,10 and 12 may be subject to the influence of anisotropy during the summer at higher latitudes, where east-facing facets are exposed to direct irradiance early in the morning. Results from the vehicle traverses indicate the development of significant temperature differences by 0730 LST between east and west facets during the study period which was almost 2 months from the summer solstice.

For satellite-based sensors which have restricted off-nadir capabilities, anisotropy will not be significant. However, the apparent surface temperature must still be reconciled

Table 4.6: Satellite parameters for satellites commonly used in thermal analysis of urban areas. Ascending and descending node times in LAT (Local Apparent (Solar) Time).

Satellite	Ascending Node	Descending Node	Scan Angle	IFOV (nadir)
TIROS-N	1500	0300	±57.	1.1 km
NOAA-6,8,10,12	1930	0730		
NOAA-7	1430	0230	"	"
NOAA-9	1420	0220	"	"
NOAA-11	1340	0140	"	"
Landsat (TM)	0945		±7.7	120 m
HCMM	1330	0200	±	600 m

with the fact that only a limited subset of the complete urban surface is viewed so that the observed temperature is not necessarily representative of the complete surface temperature. This effect is considered in Chapter 5.

Chapter 5

THE COMPLETE URBAN SURFACE TEMPERATURE

5.1 Definition of the Complete Urban Surface

Surfaces may be represented in meteorological applications by a variety of forms as discussed in Section 1.3. The actual surface which forms the boundary between the atmosphere and the substrate is often very complex. Surface representations simplify and approximate the actual surface, often using surfaces "seen" by a sensor, or planes of observation which coincide with the measurement level of a sensor (Figure 1.1). The surface representation adopted generally is scale dependent; details of the surface structure are increasingly simplified as the total area increases. The surface representation adopted in this thesis includes major surface structural features such as buildings and trees (including sizable shrubs), and horizontal surface categories such as roadways and grass. Component areas are defined in Figure 5.1 and Table 5.1.

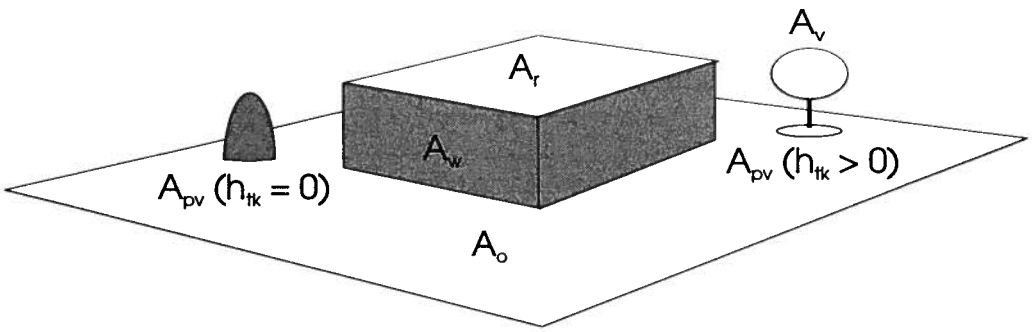

Figure 5.1: Illustration of component areas.

Table 5.1: Definition of area component symbols.

Symbol	Description
A_p	Plan (horizontal) area (obtained from map or air photo); also the area as seen by a nadir-pointing remote sensor
A_o	Horizontal ground-level area (grass, roads, gardens)
A_r	Roof area (actual)
A_{pr}	Plan or apparent roof area: for flat roofs $A_r = A_{pr}$; equivalent to building plan area
A_w	Wall area (total or with an additional subscript denoting facet direction)
A_b	Building area (Sum of roof and wall areas)
A_v	Vegetation area (three-dimensional tree representation)
A_{pv}	Plan or apparent vegetation area (horizontal projection) (Subdivided into trees with a trunk heights $(h_{tk}) = 0, > 0$
A_c	Complete surface area (Sum of A_o, A_b, A_v)

In general the surface representation does not include details at length scales less than that of a building or tree. Landform relief is ignored.

5.1.1 Estimating the Complete Surface Area

5.1.1.1 Buildings

The three-dimensional area of buildings (A_b), made up of roof area (A_r) and wall area (A_w) was calculated using building outlines digitized from high resolution (1:2500) aerial photography. Large roof-top structural elements such as elevator shaft housings were included but structural details with length dimensions less than one half the shortest facet were omitted. Roofs may be planar or consist of 2 or 4 angled surfaces.

The area A, of a polygon represented by a series of x_i, y_i points ($i = 1, N$) can be

determined from Stoke's theorem as

$$A = \frac{1}{2}(\sum_{i=1}^{N-1} x_i y_{i+1} - y_i x_{i+1}) + x_N y_1 - x_1 y_N \tag{5.1}$$

where the xy values are the digitized points for each building or surface object. Vertical facet areas were obtained by calculating the length of a vector (side of the polygon) and multiplying this by the assigned height of the building. Where adjacent buildings share a common wall, common vectors were identified. If the heights of the buildings differ, the area of the exposed wall was calculated. Wall orientation was derived from the sign of eq. 5.1 in combination with the slope (determined from the coordinates of the points relative to a reference point) of the line representing the wall segment (a slope near 0 indicates a north or south wall, a very large slope indicates an east or west wall).

5.1.1.2 Trees

Trees were digitized as points using air photo analysis and ground surveys. They were included only in the Residential study area; the Downtown and Industrial sites are largely devoid of trees. Trees were categorized into 5 types, based upon geometric form and relative abundance: B - bushes, C - evergreen (coniferous), D - broad-leaved (deciduous), E - evergreen (non-coniferous), F - flowering deciduous.

For surface area calculations, trees have been represented by cones (coniferous) (e.g., Li and Strahler, 1985), spheres or cylinders (deciduous), (Jupp, Walker and Penridge, 1986; Goel, 1988) or, more generally by ellipsoids (Campbell and Norman, 1989) for surface area calculations. A wide variety of tree forms may be represented by ellipse parameters, if the possibility of truncated ellipses is included (Charles-Edwards and Thornley, 1973; Goel, 1988). Comparison of surface areas calculated using ellipsoidal representations versus those based on cones, cylinders and spheres (assigned to representative tree types), yield total tree surface area estimates within approximately 4%. Ellipsoidal

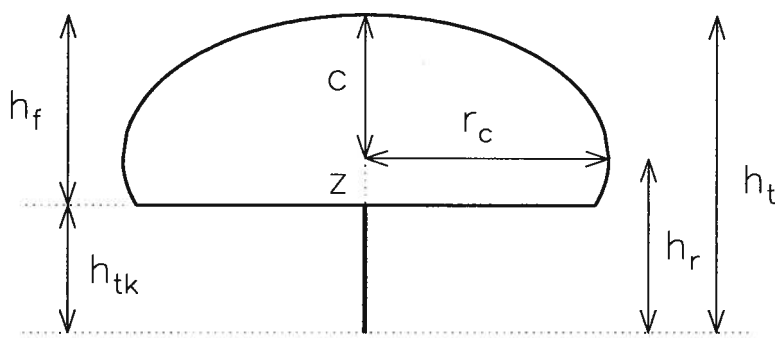

Figure 5.2: Definition of tree structural parameters.

representations are used for the estimates in this chapter.

Tree height (h_t), maximum crown radius (r_c) and height to the base of the foliage (equivalent to trunk height h_{tk}) were estimated from ground surveys for each of the trees in the study sub-area. The position of the ellipse centroid (height of maximum crown radius h_r) was estimated as a fraction (F_{hf}) of the total foliage height (h_f) where

$$h_f = h_t - h_{tk}. \tag{5.2}$$

F_{hf} was estimated to be 0.25, 0.1, 0.5, 0.25, 0.1 for types B,C,D,E, and F respectively.

Tree structural parameters are graphically portrayed in Figure 5.2. The ellipse semi-axes are represented by c and r_c (equivalent to a). When $z = c$ the tree canopy is represented by a complete ellipse; when $z < c$ the ellipse is truncated.

Calculated shapes for selected examples of each tree type in the Residential study sub-area are presented in Figure 5.3. Crown radius is assumed to be symmetrical (i.e., the crown circular) in the xy planes; the tree shapes are elliptical in the xz plane only, and may therefore be more precisely described as spheroids.

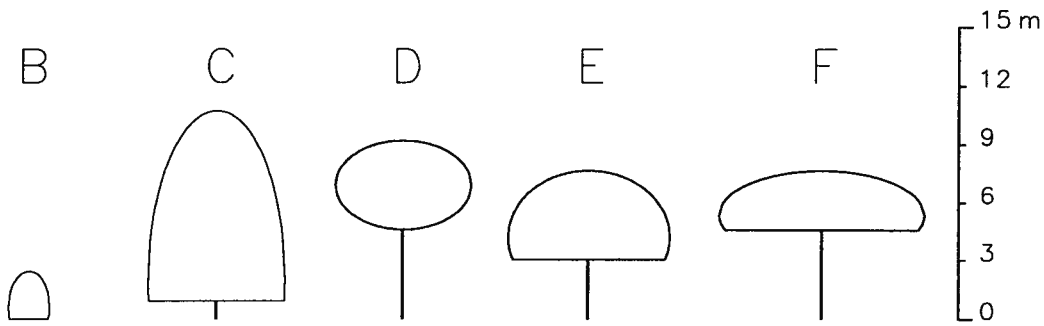

Figure 5.3: Modelled shapes for the tree types in the study area. B - Shrubs/Bushes, C - Coniferous, D - Deciduous, E - Evergreen (non-coniferous), F - Flowering (Cherry).

The representation of trees as simple geometric objects fails to account for gaps in the foliage which reduce the projected surface area. The actual "viewed" or apparent surface area directly emitting in a particular direction is theoretically defined as the projection of the total canopy foliage onto a plane orthogonal to the direction of view. Lang and McMurtrie (1992) describe the theoretical basis for the commonly required case of foliage projected onto a horizontal plane below the canopy. Chen *et al.* (1993) present projections based upon computer simulations.

The complete surface area of a tree canopy (A_v) may be defined as the area of foilage projected onto the bounding surface of the geometric shape representing the tree. This is the area of foilage which emits directly to the surroundings. The ratio (F_{gap}) between A_v and the area of the bounding geometric shape defines the reduction factor required to account for the gaps in the canopy foliage. Where available, F_{gap} allows the calculation of the complete canopy area from the simple geometric area, which can be estimated from basic structural parameters. Calculation of F_{gap} is theoretically difficult and requires details of the canopy foliage density, orientation and clumping beyond the scope of this study.

Observational alternatives exist (see e.g., Lang (1991) for a discussion), and those

employing photographic techniques appear to be most appropriate for this application. To obtain the projected area of the entire tree they need to be extended to side-views; plan and side views of some trees are hypothesized to show significant differences in F_{gap}. In this work, a very crude approximation is made for F_{gap}: based upon field observations, estimates of 0.15, 0.2, 0.3, 0.2, and 0.45 were made for tree types B–F, respectively. Where individual trees differed significantly from the average type value, an estimated field value replaced the default value.

Values of F_{gap} obtained from the literature often refer to canopies of tree types rather than single trees, and are generally based upon a cumulative projection of LAI onto the horizontal plane below the canopy. These values therefore do not account for the anticipated variations in F_{gap} for projections in the vertical plane. F_{gap} estimates for model poplar stands based upon downward cumulative leaf area index (Chen *et al.*, 1993) were in the range of 0.3 - 0.2 for a deciduous LAI of 4, the estimated maximum in the study area (Grimmond, 1988; Kramer and Kozlowksi, 1979). Gap estimates for lodgepole pine are also reported as 0.2-0.3, (Sampson and Smith, 1993), but these estimates are of gaps between individual tree canopies rather than gaps within any particular tree canopy.

5.1.1.3 Horizontal

The area of horizontal surfaces (A_o; grass, roads etc.) is determined as a residual from:

$$A_o = A_p - (A_{pr} + A_{pv(h_{tk}=0)}) \tag{5.3}$$

where A_p is the total plan area (calculated from a topographic map), A_{pr} is the plan area of roofs (equivalent to buildings), and $A_{pv(h_{tk}=0)}$ is the plan area of vegetation for which the canopy interesects the ground (most common for bushes but also occurs for some coniferous trees). A_o includes horizontal surfaces below tree canopies which have $h_{tk} > 0$ (Figure 5.1).

5.1.1.4 Top-of-Canopy Plan Area

The apparent plan area which is visible to a nadir-pointing remote sensor is the same as the map plan area, i.e., it is the horizontal projection of surface components onto a horizontal plane above the tallest structure. It is denoted by A_p and is the equivalent of the bird's eye view of the system (Figure 1.1d). In this projection, lower surfaces are obscured by parallel upper surfaces. The plan area generally includes the building plan area, the vegetation plan area, and that portion of the horizontal area not obscured by tree canopies (i.e., $A_o - A_{pv(h_{tk}>0)}$).

5.1.1.5 Complete Surface Area

The complete surface area A_c is estimated by adding the three-dimensional areas of vegetation (A_v) and buildings (A_b) to that of the horizontal area (A_o):

$$A_c = A_v + A_b + A_o. \tag{5.4}$$

5.1.2 Complete Surface Areas of the Study Sites

5.1.2.1 Industrial

Component surface areas calculated from the surface structural database (Figure 5.4) are presented in Table 5.2. Building heights were estimated in stories (to the nearest 0.25) with a story assigned as 3.66 m (12'). The building height frequency distribution is shown in Figure 5.5. A total of 733 buildings is included. However, many of these are adjoining buildings with common walls. Heights are distributed approximately normally, with only a few instances of tall (>4 story) buildings. The mean building height is estimated to be 7.3 m with a standard deviation of 3.2 m.

Combined wall areas constitute 29.4% of the complete surface area and horizontal surfaces (including roof tops) make up the remaining 70.6%. Greater areas of north- and

Table 5.2: Major surface component areas and percentages of the complete surface area for the Industrial area.

	A_p	A_o	A_r	$A_{w(N)}$	$A_{w(S)}$	$A_{w(E)}$	$A_{w(W)}$	$A_{w(M)}$	A_c	A_c/A_p
Area ($m^2 \times 10^3$)	617.5	380.2	237.3	68.76	69.77	55.38	54.46	8.68	874.5	1.42
% of A_c	70.6	43.5	27.1	7.9	8.0	6.3	6.2	1.0		

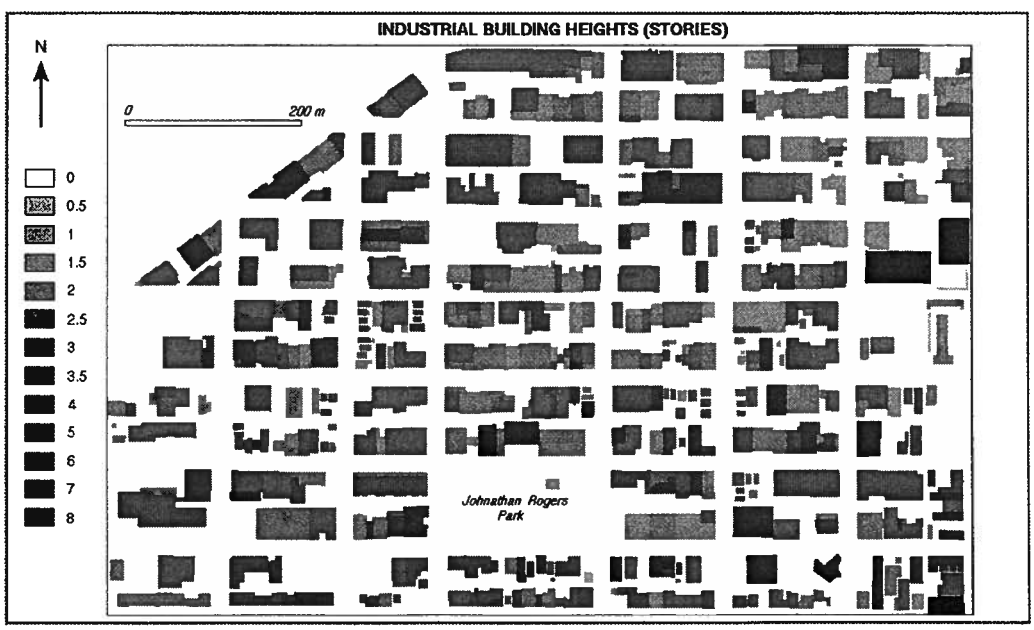

Figure 5.4: Building heights (stories); Industrial study area.

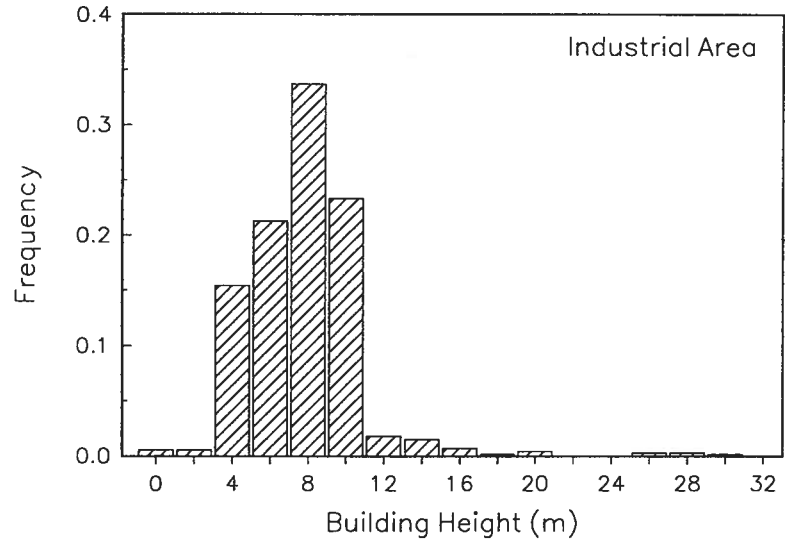

Figure 5.5: Frequency distribution of building heights in the Industrial study area.

south-facing facets are exposed compared to east- and west-facing ones because many of the buildings along the blocks share common east and west walls and therefore have no east or west exposure (Figure 5.4). There are relatively few trees in the study area; these are not included in the surface area calculations.

5.1.2.2 Downtown

The Downtown area represents the maximal extent of surface vertical structure in an urban area. Individual buildings may exceed 100 m in height (Figure 5.6). Heights for the 274 digitized buildings were obtained from City of Vancouver (1984) planning maps (in stories) updated by field observations of height estimated using Abney levels for buildings along the traverse route. Where heights in stories were used, conversion to metres assumed 3.66 m story^{-1}.

Table 5.3: Major surface component areas and percentages of the complete surface area for the Downtown area.

	A_p	A_o	A_r	$A_{w(NE)}$	$A_{w(SW)}$	$A_{w(NW)}$	$A_{w(SE)}$	A_c	A_c/A_p
Area ($m^2 \times 10^3$)	453.3	286.8	166.5	138.1	136.9	133.5	133.3	995.1	2.20
% of A_c	45.6	28.8	16.7	13.9	13.8	13.4	13.4		

The distribution of building heights (Figure 5.7) shows a strongly asymmetric distribution with greatest frequencies in classes centred between 5 and 15 m, and a long tail of frequencies extending towards greater building heights. The mean building height is 26.6 m, whilst the median height is 14.6 m.

Complete surface calculations have been restricted to areas of NW/SE and NE/SW street orientation (Figure 5.6) to conform to the traverse route and reduce the number of extracted facet temperature distributions required. Here, vertical facets combine to form 58.4% of the complete area, a value greater than the fraction of horizontal surfaces (41.6%) and much greater than the horizontal roof area (16.7%, Table 5.3). The variation of area with facet orientation is much less than for the Industrial area, but shows slightly greater values for the NE/SW facets. Trees are omitted from surface area calculations.

5.1.2.3 Residential

The Residential study area is characterized by one and two story single family houses generally arranged with the long axis of the building at right angles to the street (Figure 5.8). Garages and ancillary buildings are located at the back of the lot facing the alleyway. In the 8 block sub-area chosen for detailed analysis, 271 houses (an average of 34 block^{-1}), and 139 garages (approximately 17 block^{-1}) were digitized. The height (in

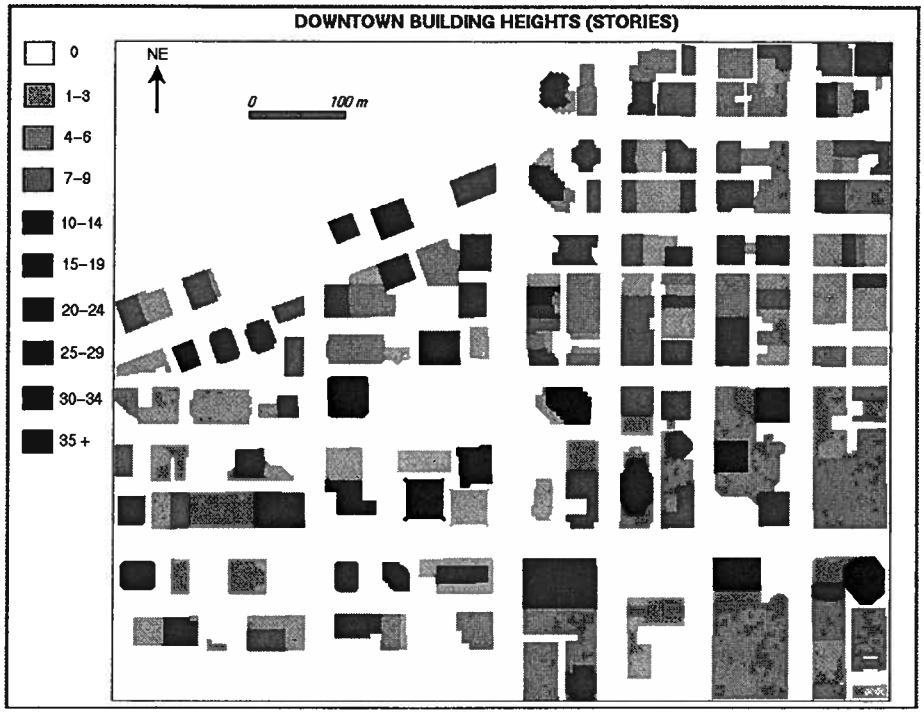

Figure 5.6: Building heights (stories); Downtown study area.

stories, to the nearest 0.25, using 3.05 m story^{-1}), roof type, and pitch were estimated for each building. Frequency distributions for the estimated building structural parameters are shown in Figure 5.9. Almost all garages are included in the 3 m height class (1 story) as might be expected. House wall heights are concentrated in the 5 and 6 m categories. Roof pitches for both building types are most frequently estimated to be between 10 and 20 degrees. The distribution is skewed, with substantial numbers of both houses and garages observed to have higher roof pitch angles. Roof types are fairly equally split among gabled and 4-sided types with only a minor proportion having flat roofs.

The mean building (house) height was 5.5 m, and the mean roof pitch was approximately 20°. This estimate is low in comparison to a previous estimate for the area (8.5 m, Steyn 1980), but note that the current estimate is actually the height of the vertical

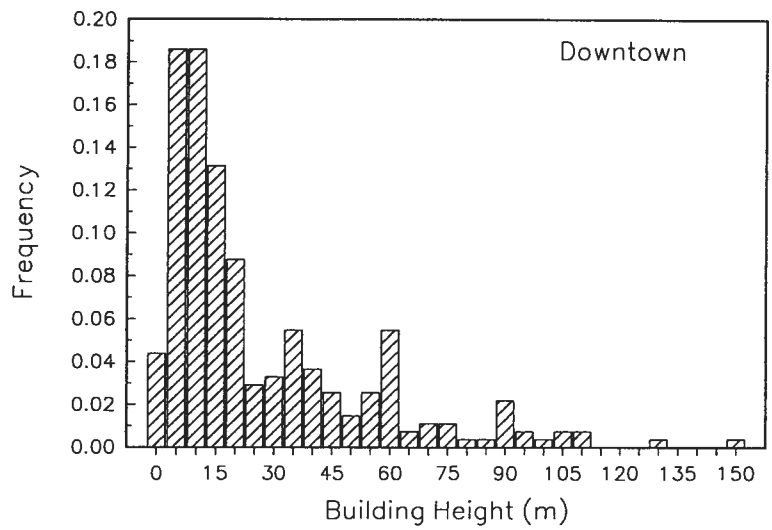

Figure 5.7: Frequency distribution of building heights in the Downtown study area.

walls, rather than the complete building height. For non-flat roofs the building height increases in relation to the tangent of the roof pitch. Using the average pitch angle and an estimated building width of 10 m, an additional 1.8 m may be added to obtain a building height estimate. Vertical facet surface area calculations for buildings with gabled roofs include the gables (triangular wall area above the level of the eaves on the end walls). Houses may be grouped into five major categories, (Table 5.4) according to their height, roof pitch and general layout. The most frequently occurring house type (37%) is the "Vancouver Special" a rectangular, 2 story building with a shallow ($< 25°$) roof pitch on a gabled (two-sided) roof (Type II).

Garages have a mean wall height of 3.1 m and a mean pitch angle of 20°; adding in a typical roof height yields a total height estimate of 4.0 m, which compares favorably to the 3.5 m estimate of Steyn (1980).

In contrast to the Industrial and Downtown sites, large numbers of trees are present.

Table 5.4: Building types in the Residential study area.

	House Type				
Parameter	I	II	III	IV	V
Height (stories)	1.5–2.5	1.5–2.5	1.5	2–3	misc.
Bldg Layout	rectangular	rectangular	square	rectangular	misc
Roof pitch (°)	15–25	15–25	15–25	> 25	misc.
Roof sides	4	2	4	2	misc.
Number	62	101	39	53	16
Frequency (%)	22.9	37.3	14.4	19.6	5.9

	Garage Type			
Parameter	I	II	III	IV
Height (stories)	1	1	1	1
Bldg Layout	rectangular	rectangular	rectangular	rectangular
Roof pitch (°)	0	0–25	> 25	> 0
Roof sides	0	2	2	4
Number	12	33	33	60
Frequency (%)	8.7	23.9	23.9	43.5

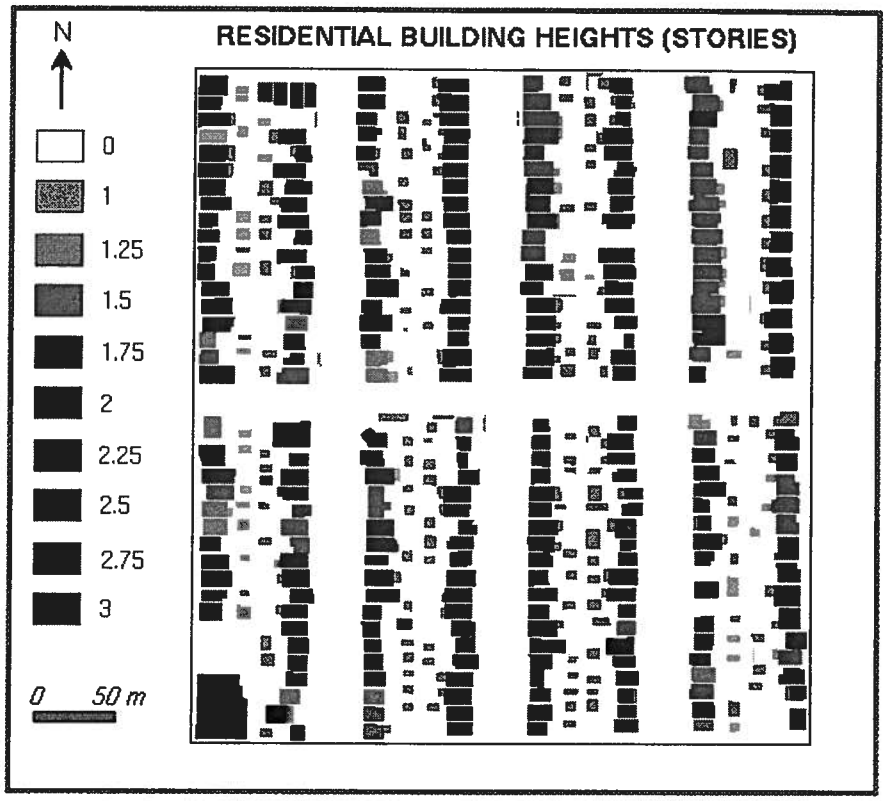

Figure 5.8: Building heights (stories); Residential study area.

Most streets have regularly spaced trees (street trees) along the roadway. Trees are also present in backyards and along alleyways, although less frequent and more randomly located. A count of the trees and large shrubs/bushes in the 8 block sub-study area yielded 385 trees and 41 shrubs. These were subdivided into shrubs/bushes (B), coniferous (C), deciduous (D), evergreen (non-coniferous) (E) or flowering deciduous (F) categories. Frequency distributions for the four most frequently occurring types (very few examples of type E are present) are presented in Figure 5.10. Descriptive statistics of the estimated tree dimensions are presented in Table 5.5 .

Deciduous trees are the most frequently occurring type, accounting for 59% of the

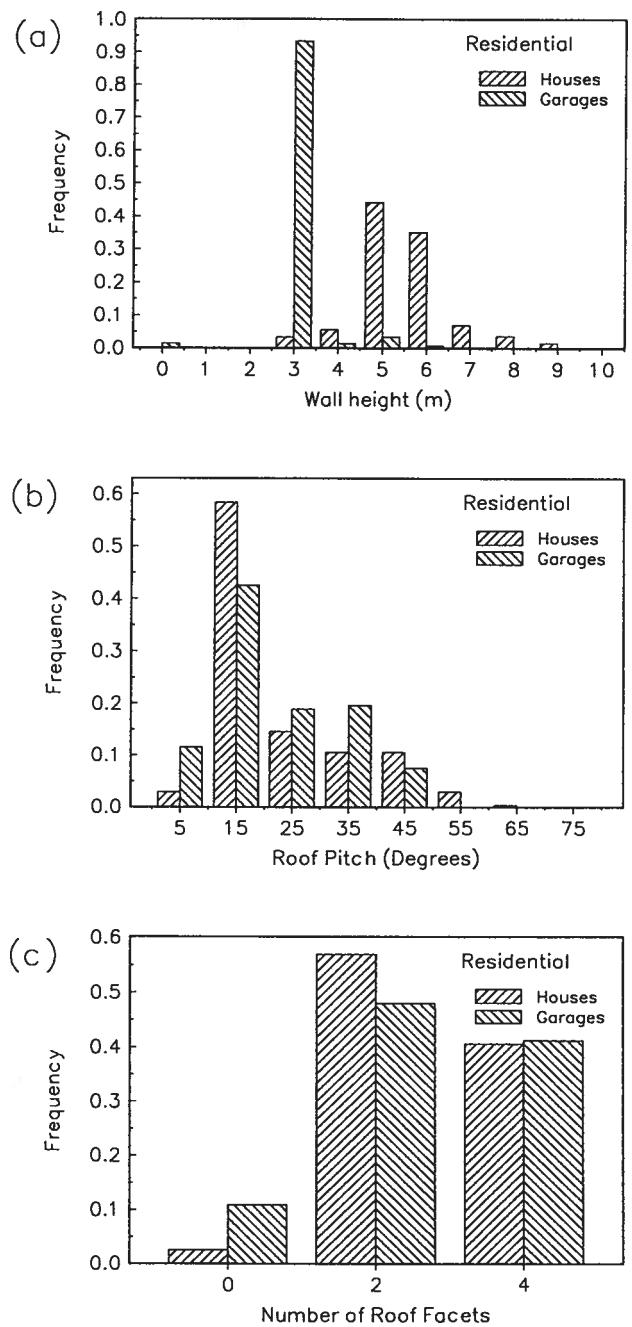

Figure 5.9: Frequency distributions of estimated building structural parameters (Residential area). (a) height, (b) roof pitch, (c) number of roof pitch azimuths; (0 = flat).

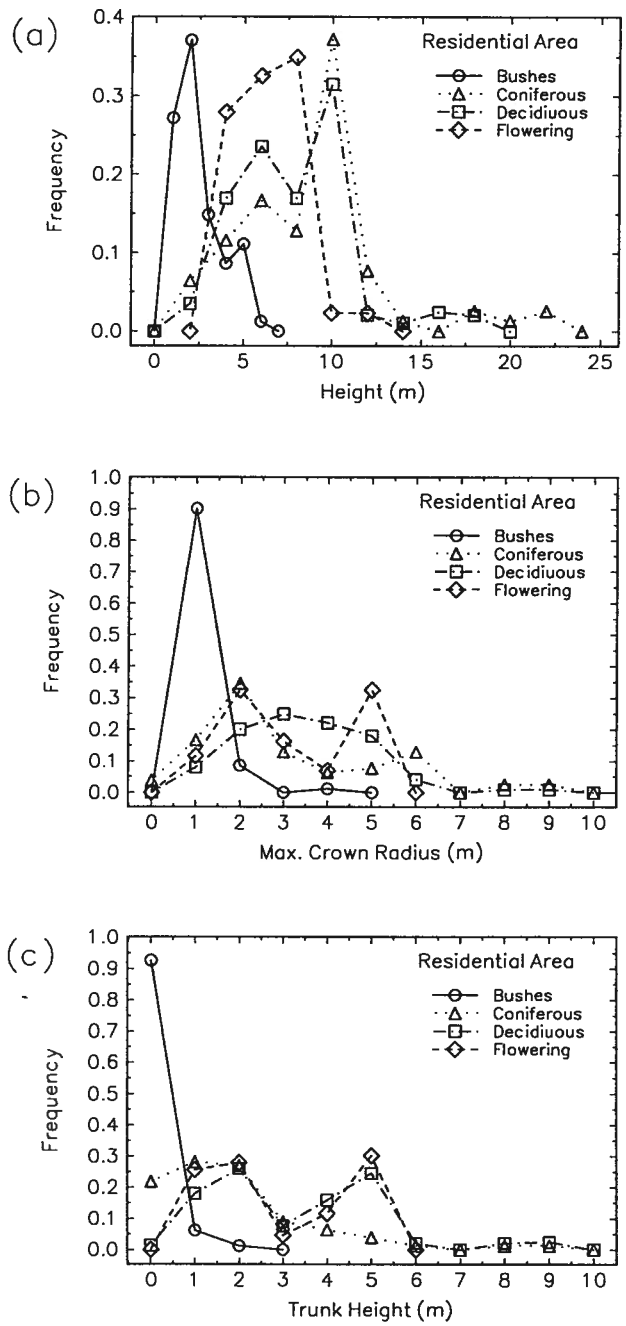

Figure 5.10: Frequency distributions for the estimated tree structural parameters (Residential area). (a) height, h_t; (b) maximum canopy radius, r_c; (c) trunk height, h_{tk} (height to base of canopy foliage).

Table 5.5: Statistical summary of estimated tree structural parameters.

Tree		h_t (m)			r_c (m)			h_{tk} (m)		
Type	n	mean	σ	med.	mean	σ	med.	mean	σ	med.
B	81	2.47	1.20	2.44	1.07	0.43	0.91	0.09	0.28	0.00
C	78	8.55	4.13	9.14	3.09	2.18	2.44	1.77	1.73	1.37
D	289	7.73	3.18	7.62	3.41	1.61	3.05	3.16	1.81	3.05
F	43	6.24	1.81	6.10	3.00	1.31	3.04	2.74	1.51	2.13

Table 5.6: Major surface component areas and percentages of the complete surface area for the Residential area.

	A_p	A_o	A_r	A_{pr}	A_v	A_{pv}	A_{pv} ($h_{tk} = 0$)
Area ($m^2 \times 10^3$)	170.0	121.3	52.73	48.23	51.75	13.02	22.90
% of A_c	55.5	39.6	17.2	15.8	16.9	4.3	0.2
	$A_{w(N)}$	$A_{w(S)}$	$A_{w(E)}$	$A_{w(W)}$	A_c	A_c/A_p	
	22.90	22.94	17.20	17.23	306.1	1.80	
	7.5	7.5	5.6	5.6			

total. The overall mean tree height (not including type B) is 7.73 m, which is approximately 50% of the height adopted by Schmid (1988). This difference is attributed to the small spatial domain and abundance of relatively small street trees which make up a large fraction of the total number of trees.

The component surface percentages are presented in Table 5.6. A two-dimensional projection of the canopy area, less the 2-D area of trees where foliage intersects the ground yields the obscured horizontal surface area (12547 m^2), 4.1% of the complete area).

5.2 A Complete Urban Surface Temperature

5.2.1 Definitions

The complete urban surface temperature (T_c) is an area-weighted temperature. The component surface temperatures are combined in proportion to their areal fraction of the complete surface. In the recently proposed terminology of Norman *et al.* (1995), the complete surface temperature is similar to the mean kinetic temperature, with the exception that the complete surface temperature used here is a brightness temperature uncorrected for surface emissivity, rather than a thermodynamic temperature.

In radiance form, the complete surface temperature, as defined above, is expressed as

$$L_c = \sum_{i=1}^{n} f_i \cdot L_i \tag{5.5}$$

for n component surfaces, where f_i are the fractional areas with emission L_i, and L_c is converted to an equivalent temperature (T_c), i.e., assuming blackbody emission. L_c requires the specification of surface classes, their representative temperatures and the fractional area of each surface class. T_c is not directly observable, although it may be possible to approximate it using hemispherical (or, preferrably, wide FOV) estimates of upwelling longwave radiation. These may provide a useful approximation because they reduce the directionality of the measurement and integrate both horizontal and vertical surfaces of all orientations. However, view factors for individual surfaces will be biased towards horizontal surfaces and those surfaces most directly beneath the sensor.

5.2.2 Estimating the Complete Surface Temperature

5.2.2.1 Nadir Airborne and Traverse Temperature Distributions

One method of estimating T_c is to combine the apparent surface temperature distributions obtained at nadir with the airborne scanner with the vertical facet distributions obtained from the vehicle traverse. This horizontal/vertical combination circumvents the need to subdivide the horizontal surface into component fractional areas and estimate mean temperatures or temperature distributions for each. The observed nadir temperature distribution is assumed to represent the various components in their correct proportions. The component frequency distributions (nadir and four vertical) are combined with weights according to their fraction of the complete surface area.

Figure 5.11a illustrates the component distributions for the morning flight over the Industrial area, where vertical facet distributions are from the vehicle traverse. The resultant composite distribution is presented in Figure 5.11b.

The mean temperature of the complete distribution is estimated using eq. 5.5, except f_i are the frequencies for each temperature class (rather than fractional areas of emission) and L_i is the radiance for that temperature class. A disadvantage of this approach is the need to truncate or otherwise modify the distribution of surface temperatures obtained from the vehicle traverse to remove mixed building and sky values and the likelihood that the resultant distribution slightly underestimates areas of high surface temperature. The method also assumes that the distribution of vertical facet temperatures is representative of all the vertical surfaces. The traverse methodology restricted observation to facets which may be viewed from positions along streets or alleyways and within the range of elevation angles of the EIRT. Facets orthogonal to the street are not sampled except on the ends of the block; the close inter-building spacing in the study areas means that these facets have a greater direct solar exposure on the ends of the blocks (where they

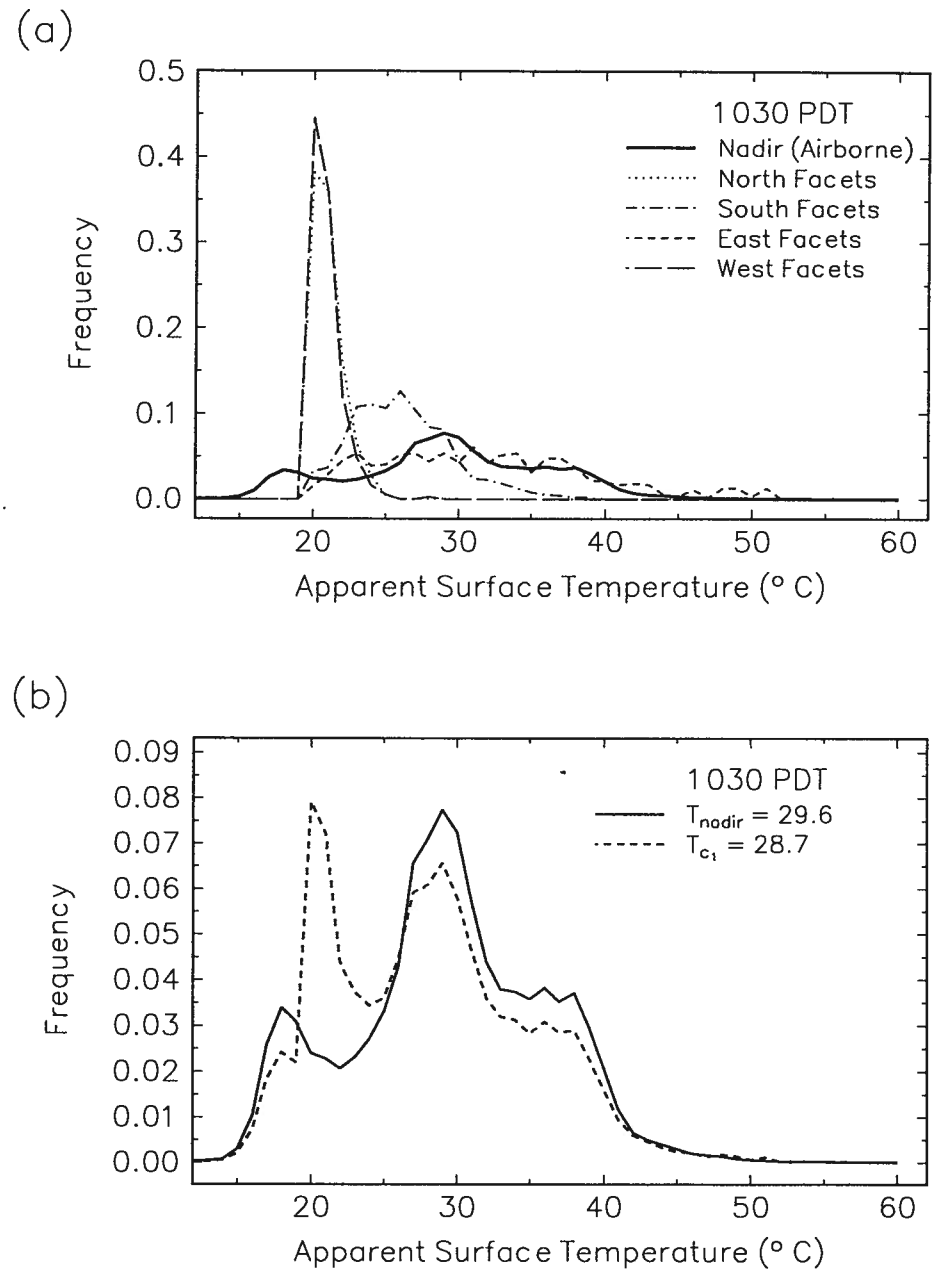

Figure 5.11: (a) Component surface temperature frequency distributions for the Industrial area, Flight 1 (1030 PDT). Vertical facet distributions are from the vehicle traverse. (b) Composite temperature distribution.

are sampled) than for similar facets within the block. Calculations for the Residential area indicate 57–80% of the area of inter-building walls are shaded during the morning and late afternoon flight, depending upon the building height and spacing. During the early afternoon flight, 35–55% are shaded.

5.2.2.2 Nadir and Off-nadir airborne

An alternative to the use of the vehicle traverse data is to use vertical facet surface temperature distributions extracted from the off-nadir airborne scanner imagery. These overcome some of the difficulties with the traverse vehicle data, but have their own limitations. When using the extracted data, results are dependent upon the sampling of the areas; recall that temperature patterns are the sole means of defining the spatial dimensions of the facets (c.f. Chapter 1). In the Residential and Downtown areas, temperatures of facets where inter-building spacing is small may be difficult to obtain due to the off-nadir angle used and the small area of these surfaces in the direction of view.

Figure 5.12 compares the vertical facet temperature distributions obtained from the two sources for the morning flight over the Industrial area. Note the underlying facet orientation convention: east facets face east. East facets are, however, viewed by a remote sensor with a west view azimuth (the convention used in the presentation of the remotely-sensed temperature frequency distributions). The vehicle traverse data combines EIRT observations at both 0 and 10° elevation angles, and has not been truncated. The agreement between the distributions is generally good except for the east facet (the directly irradiated facet) where the image-extracted temperatures are much warmer. This is probably due to sampling biases relative to the building geometry: east facets at mid-block have greater solar access earlier in the morning than do the end-of-canyon walls, which are more subject to shading by buildings on the opposite side of the street, and

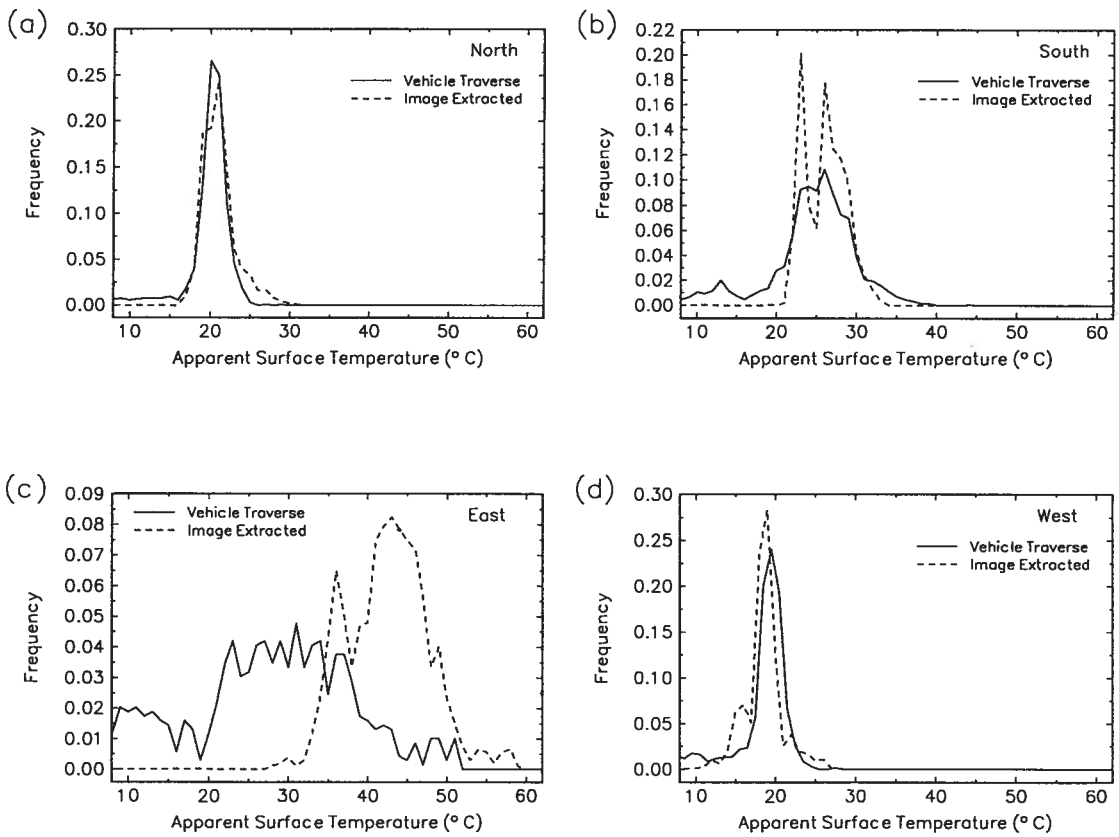

Figure 5.12: Traverse and image extracted vertical facet temperature distributions; Industrial area, Flight 1 (1030 PDT). Facet orientations are: (a) N, (b) S, (c) E, (d) W.

thus mid-block facets are warmer.

5.3 Comparison of Complete and Incomplete Surface Temperatures

5.3.1 Industrial Area

Complete surface temperature frequency distributions for the three flights made over the study area are presented in Figure 5.13. Two estimates of the complete surface temperature (T_c) distribution are made. In the first (T_{c_1}), the vertical facet temperatures are obtained from the traverse vehicle, and the second, (T_{c_2}), from off-nadir airborne thermal imagery. The T_{c_1} distributions exhibit a sharp break at 20°C due to truncation of the low temperature tail of the traverse temperature distributions. The two distributions differ primarily in the relative frequency of low temperatures; those obtained using the traverse vehicle enhance low temperature frequencies. Differences between the distribution means decrease from 0.6°C for the morning flight to 0.1° for the late afternoon flight. The decrease is due in part to better agreement between vehicle and image-extracted vertical facet temperature distributions of the most directly irradiated facets for the early and late afternoon flights (mostly westerly) (Figures 5.12, 5.14, 5.15).

North facets are equally well sampled by the two techniques, (except possibly in narrower alleyways where traverse data may be cooler) and so better agreement is expected. The anticipated bias in sampling east facets (traverse likely undersamples) yields smaller differences between the techniques than for the morning case with west facets, perhaps because relative solar access differences have not yet fully developed.

The most apparent difference between the complete and nadir temperature distributions is the enhancement of low temperature frequencies. This occurs because, except for the most directly irradiated facet, all vertical facets have temperature distributions which have greater frequencies of low temperatures compared to the horizontal (Figure 5.16).

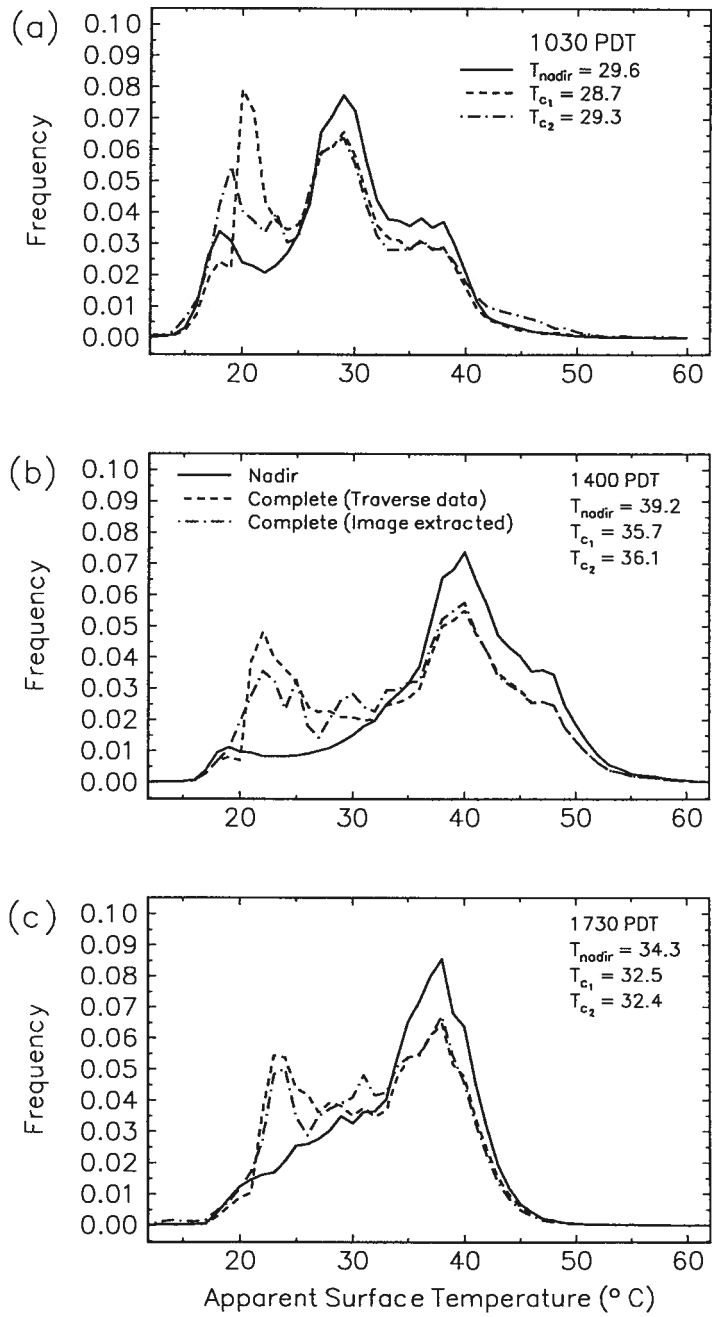

Figure 5.13: Estimated T_c distributions; Industrial area. (a) Flight 1 (1030 PDT), (b) Flight 2 (1400), (c) Flight 3 (1715).

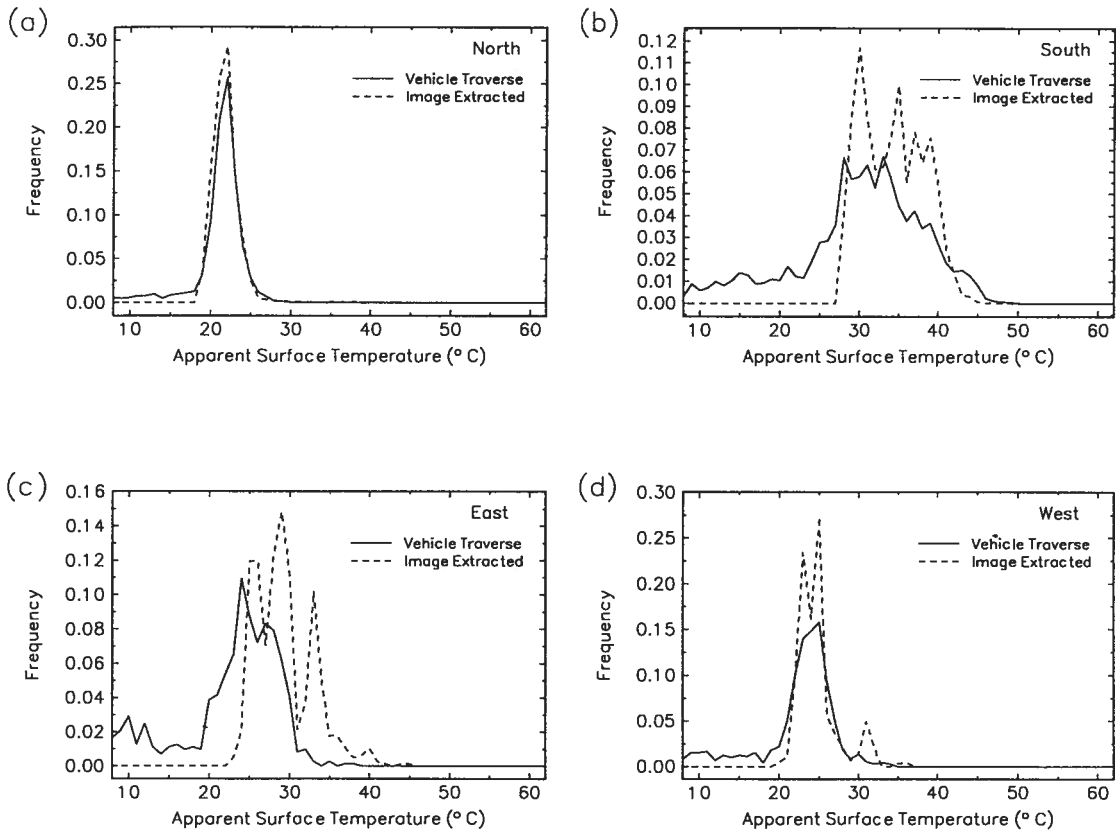

Figure 5.14: Traverse and image extracted vertical facet temperature distributions; Industrial area, Flight 2 (1400 PDT). Facet orientations are: (a) N, (b) S, (c) E, (d) W.

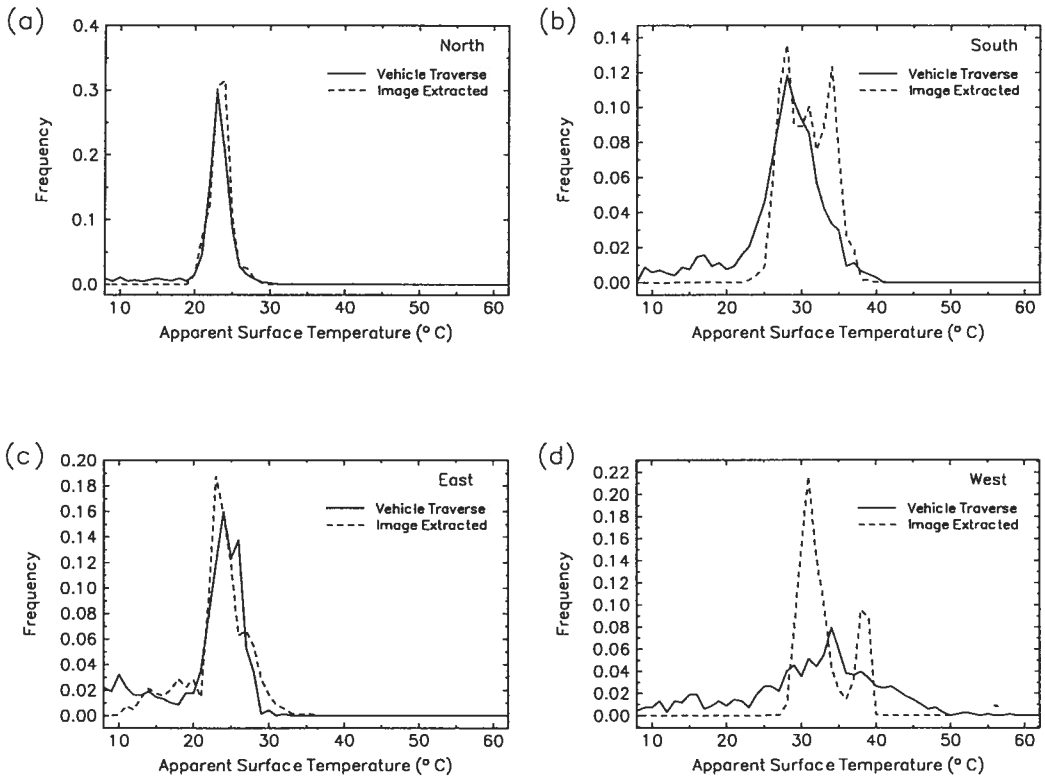

Figure 5.15: Traverse and image extracted vertical facet temperature distributions; Industrial area, Flight 3 (1730 PDT). Facet orientations are: (a) N, (b) S, (c) E, (d) W.

Temporally, the difference between the nadir and vertical distributions is strongest near solar noon. Then, because of the relatively small zenith angle, even the most directly irradiated facet is cooler than the horizontal (Figure 5.16b). At times earlier and later in the day, the most directly irradiated wall has a frequency distribution only slightly cooler than that of the horizontal, so T_c estimates are closer to T_r for nadir observations.

Comparison of the complete and off-nadir temperature distributions is presented in Figure 5.17. In each case, the complete distribution enhances the low temperature frequencies, resulting in a lower mean temperature. Agreement is best for off-nadir view angles in the direction of a shaded facet.

5.3.2 Downtown Area

Complete surface temperature distributions for the Downtown study area (Figure 5.18) show temperature decreases of 1-3°C compared with that of the nadir, depending upon the source of the vertical facet temperature distribution.

Large discrepancies are observed between extracted and traverse estimates of the temperature distribution for the most directly irradiated facet for both Flights 4 and 5 (Figures 5.19, 5.20) resulting in T_c differences of approximately 2°C for each flight.

Each platform suffers a bias due to viewing position: traverse temperature estimates include all viewing angles weighted in proportion to the number of "valid" (i.e., above the truncation level) observations for each EIRT angle, but are biased towards low temperatures for the most directly irradiated facet for the reasons discussed previously. Airborne observations preferentially view the top portion of walls, cannot "see" below the level of any awnings present, may have some of the lower wall obscured when H/W geometry is large, and the source of emission for specular reflections is the warm street.

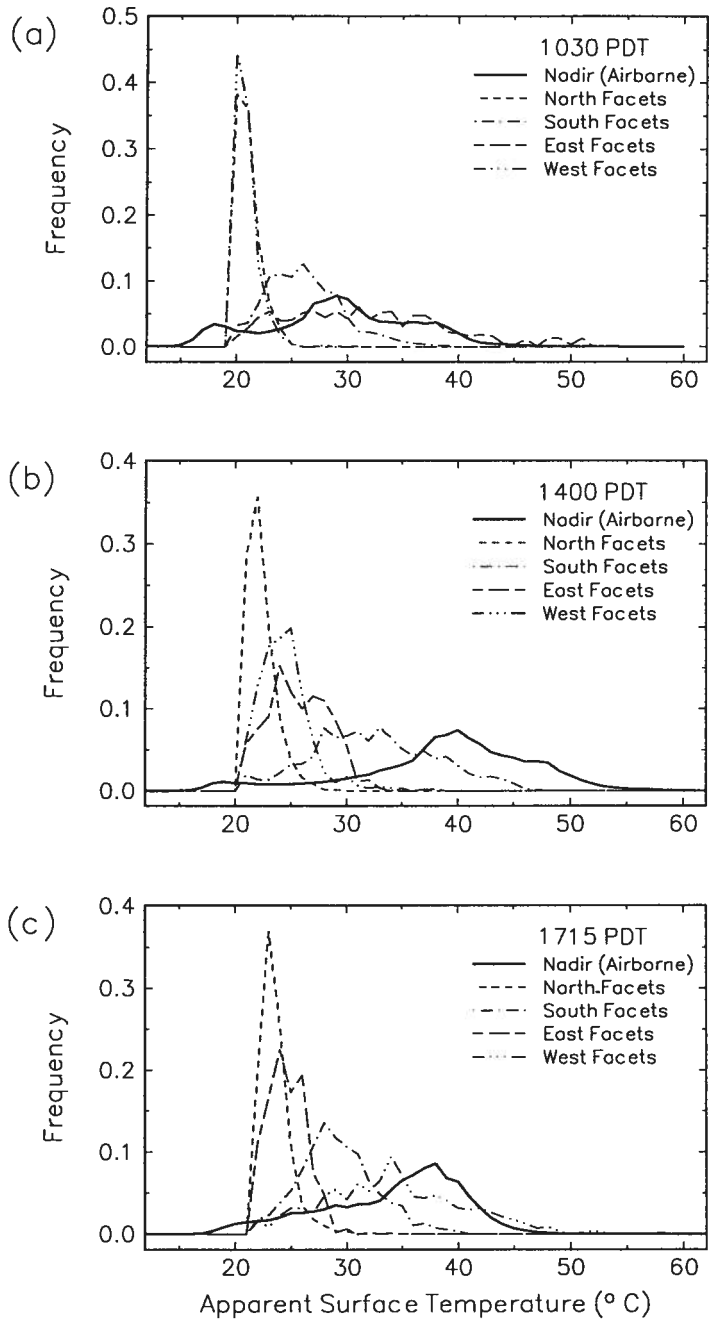

Figure 5.16: Component temperature distributions (from vehicle traverses); Industrial area. (a) Flight 1 (1030 PDT), (b) Flight 2 (1400 PDT), (c) Flight 3 (1715 PDT).

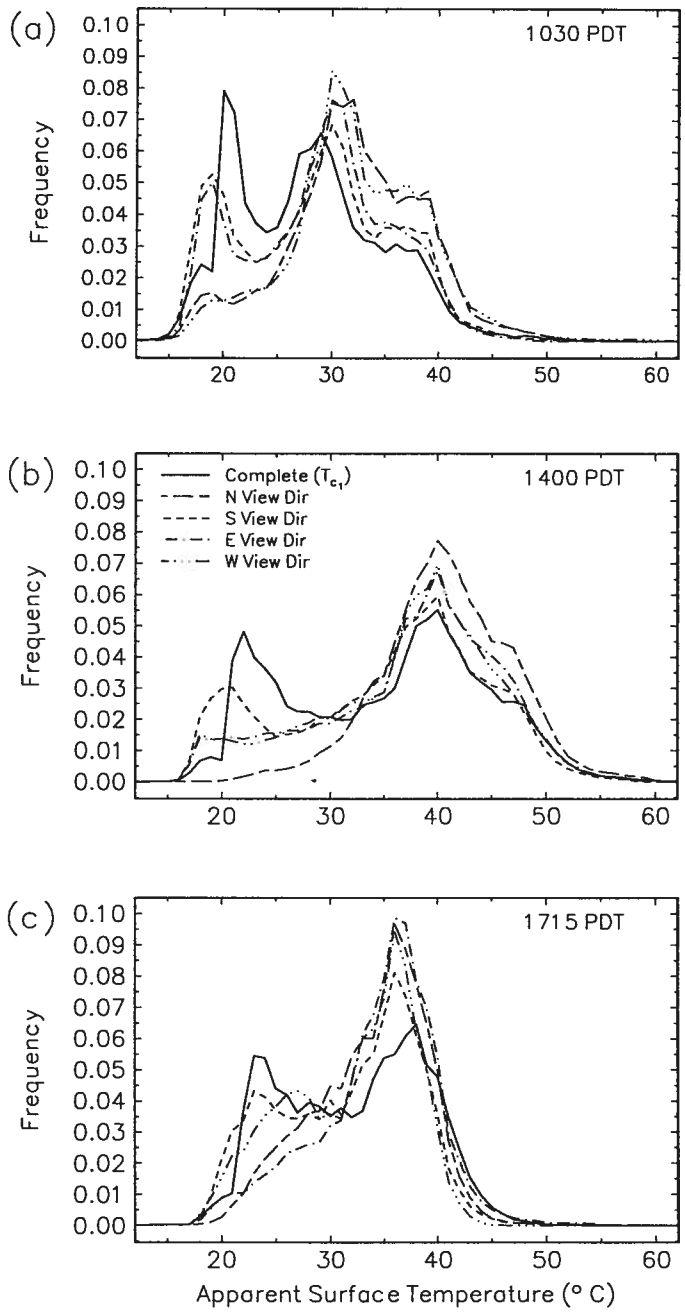

Figure 5.17: Complete and off-nadir apparent surface temperature distributions; Industrial area. (a) Flight 1 (1030 PDT), (b) Flight 2 (1400 PDT), (c) Flight 3 (1715 PDT).

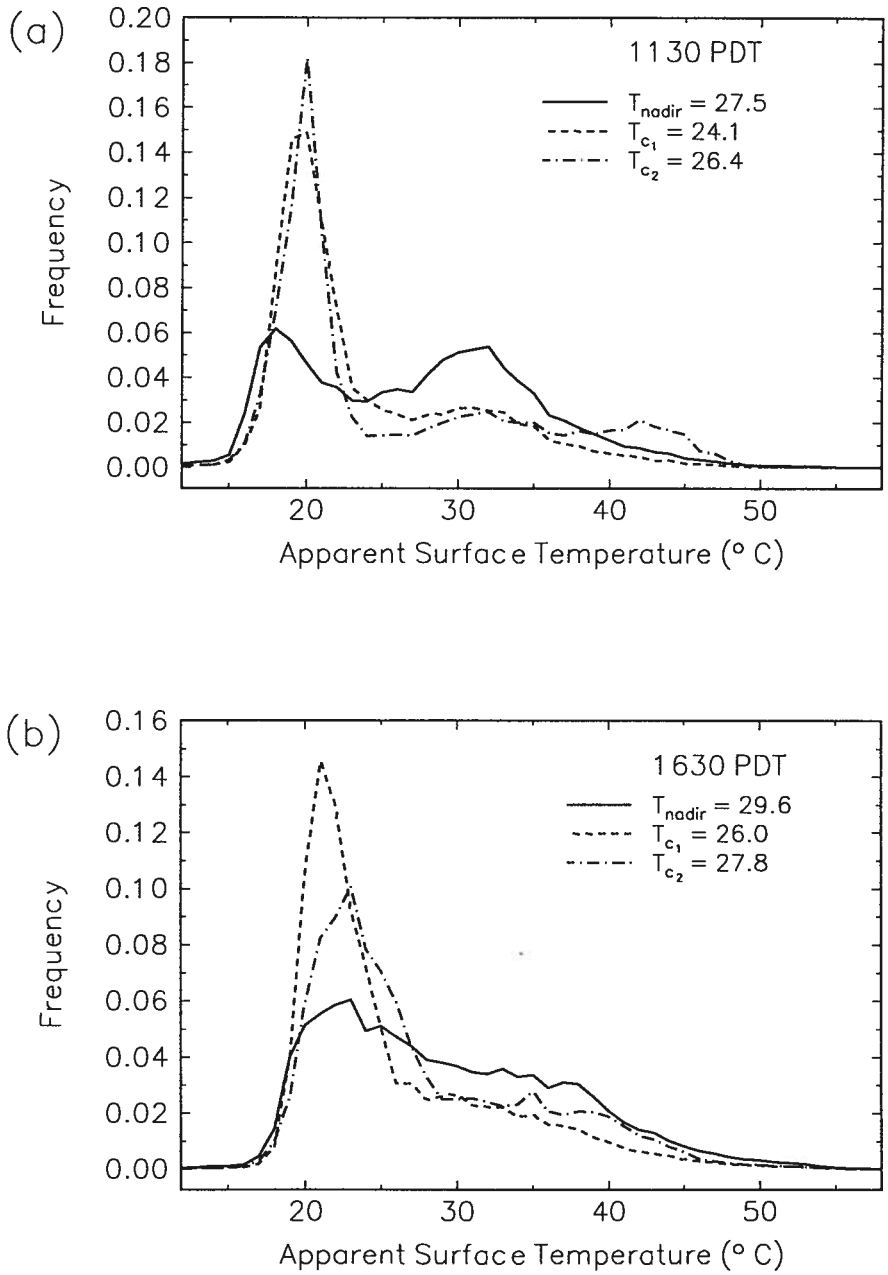

Figure 5.18: T_c distributions; Downtown study area. (a) Flight 4 (1130 PDT), (b) Flight 5 (1630 PDT).

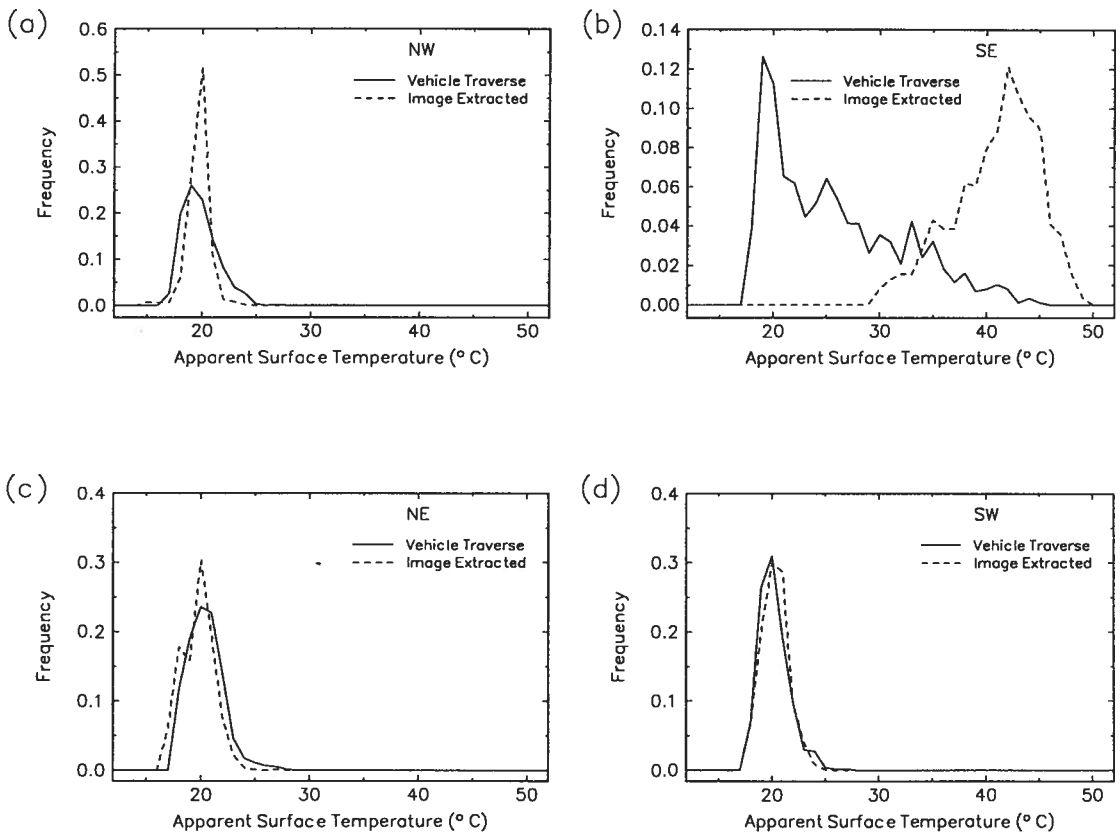

Figure 5.19: Traverse and image-extracted vertical facet temperature distributions; Downtown study area. Flight 4 (1130 PDT). Facet orientations are: (a) NW, (b) SE, (c) NE, (d) SW.

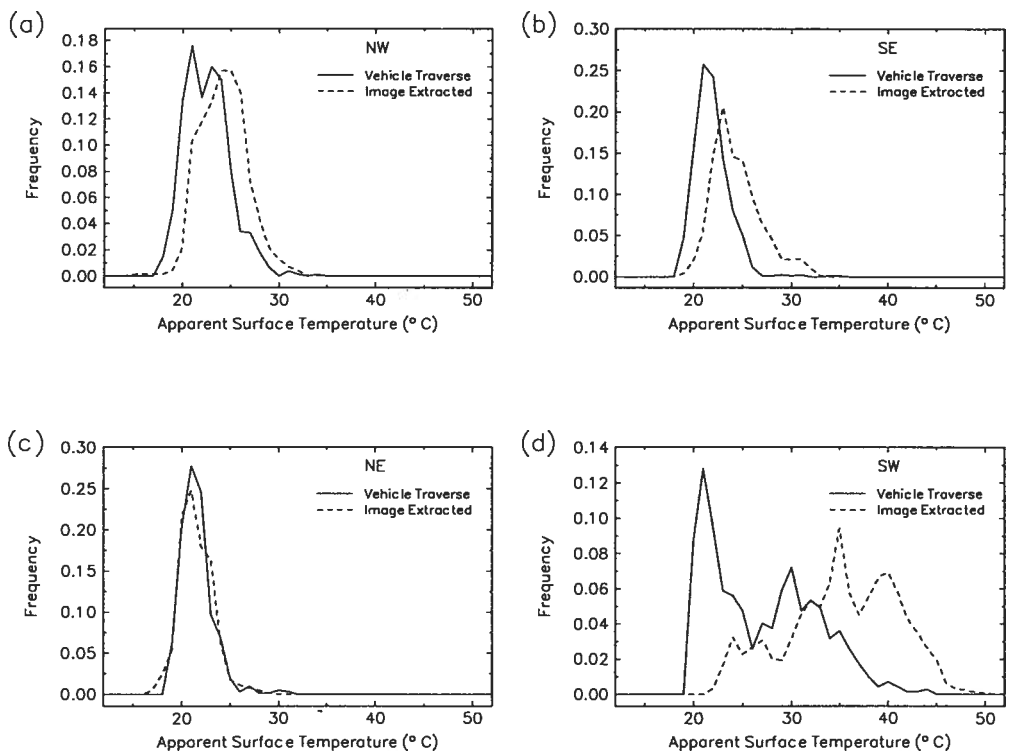

Figure 5.20: Traverse and image-extracted vertical facet temperature distributions; Downtown study area. Flight 5 (1630 PDT). Facet orientations are: (a) NW, (b) SE, (c) NE, (d) SW.

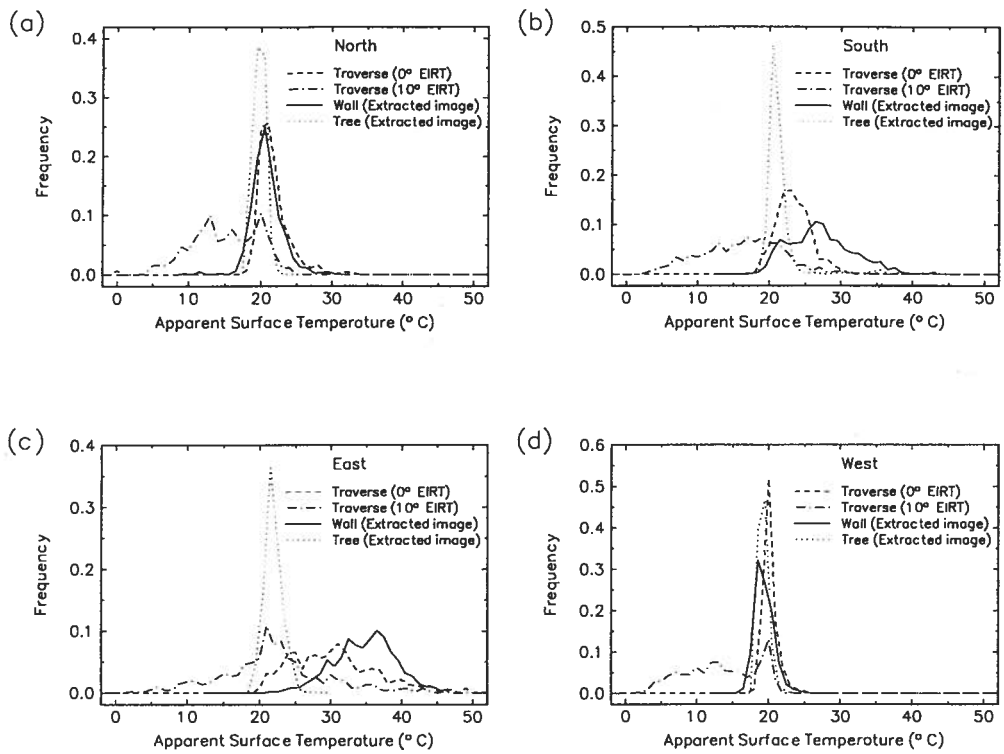

Figure 5.21: Apparent surface temperature distributions from traverse and image sources for building walls and trees; Residential area; Flight 6 (0945 PDT). Facet orientations are: (a) N, (b) S, (c) E, (d) W.

5.3.3 Residential Area

The first complete temperature estimate (T_{c_1}) uses, as previously, the temperature distributions obtained from the traverse vehicle. In this instance, the 0 and 10° EIRT are combined, and it is assumed that an adequate sampling of both the house and tree temperatures is obtained. Truncation of the traverse distribution is specified using a graphic analysis of the traverse and extracted temperature distributions (Figure 5.21) and looking for evidence of the tree canopy signal in the traverse (especially 10° EIRT) distribution.

This was related to a local minimum in the frequency distribution (Figure 5.21, east

and south facets).

The traverse data undersample the north and south facets and this may be important for the north facet case, as these are much more likely to be shaded at mid-block than at the ends of the block. Sampling by image extraction yields little improvement because of the very narrow inter-building spacing and pixel smearing. Comparison of image extracted and traverse distributions (Figure 5.21) show warmer temperatures for the extracted pixels, the opposite of that expected considering the inter-building spacing.

As in the case of the Industrial site, the complete surface temperature of the Residential area (Figure 5.22) is cooler than that obtained by nadir observations. Differences are greatest for the early afternoon flight when T_c is 4 - 5°C cooler than nadir T_r. The two estimates of T_c are similar, with T_{c_1} showing a slight enhancement at higher temperature frequencies. Sensitivity tests of the effect of F_{gap} upon T_c indicated increases in T_c of 0.5 - 0.7°C when F_{gap} was reduced from 1.0 for all tree types to the estimated values given in Section 5.1. Compared with the Industrial area, the effect of trees increases the difference between nadir and complete apparent surface temperatures.

Complete surface temperature estimates (T_{c_2}) combine extracted temperature distributions for vertical facets and tree canopies. Off-nadir tree canopy temperature distributions show variations in the mean of approximately 3°C between the most directly irradiated direction and the most shaded (Figure 5.23) for each flight over the Residential area.

Weighting the tree canopy temperatures by tree canopy area is accomplished by calculating the projected area in each of the north, south, east, west, and nadir-viewing directions and subdividing the complete tree canopy area by the relative projected area. Because trees are elliptical in the xz and yz plane, projected areas are greater for the vertical planes than the horizontal. A weighting is also calculated for the underside of the tree, for trees with $h_{tk} > 0$.

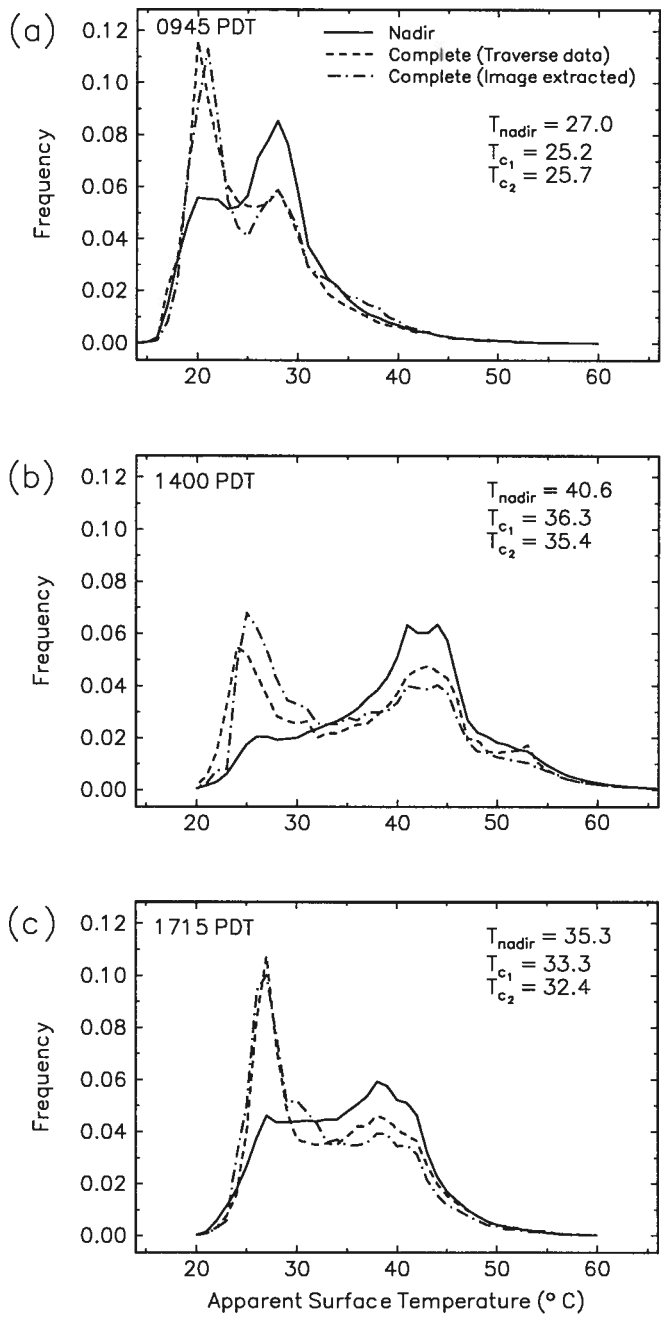

Figure 5.22: Estimated T_c distributions; Residential area. (a) Flight 6 (0945 PDT), (b) Flight 7 (1400 PDT), (c) Flight 8 (1715 PDT).

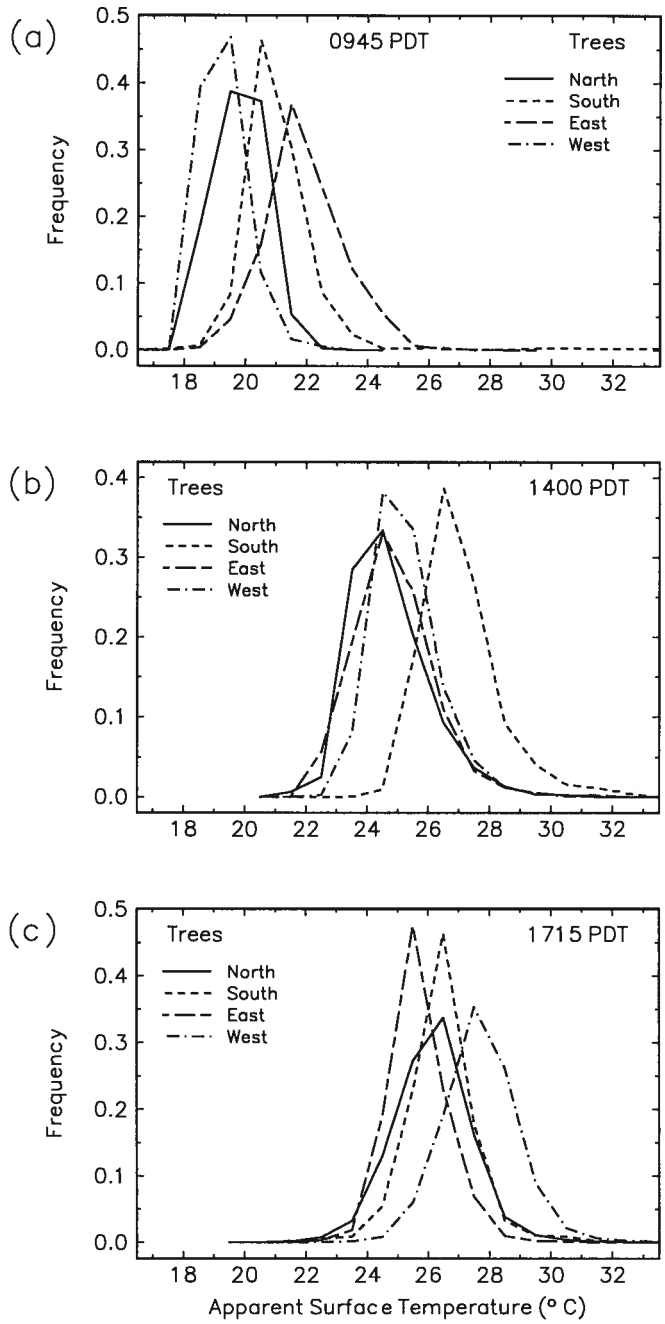

Figure 5.23: Apparent tree canopy temperatures extracted from off-nadir imagery; Residential area. (a) Flight 6 (0945 PDT), (b) Flight 7 (1400 PDT), (c) Flight 8 (1715 PDT).

5.4 Surface and Air Temperature Relations

Remote measurements of apparent surface temperature are often compared with surface-layer air temperature measurements (Lee, 1991; Stoll and Brazel, 1992; Dousset, 1989; Henry *et al.* 1989) with the goal of generating estimates of air temperature from thermal imagery. Results vary for the reasons discussed by Roth *et al.* (1989): remote sensors bias the surface observed; air and surface temperatures have a complex coupling through flux divergence of the lowest layers of the atmosphere; and there are mis-matches in the scales of observation used for remote and in-situ measurements. The estimation of complete surface temperatures addresses the problem of observational bias in the remote thermal measurements.

Complete mean apparent surface temperatures (T_{c_1}), and traverse air temperatures (T_{at}) have been added to Figure 4.32 to produce Figure 5.24. This figure summarizes the mean apparent temperatures of nadir and off-nadir viewed surfaces, the estimated complete surface temperature and canyon-level air temperature for each of the study areas.

Figure 5.24 demonstrates that the use of complete surface temperatures yields only a marginal improvement in the comparison of air and apparent surface temperatures. At the scale of the images used in this analysis, daytime mean apparent surface temperatures are substantially warmer than canyon-level air temperatures at all times, for all sites. The closest match occurs for Flight 6 (0945 PDT) in the Residential area where both off-nadir and complete surface temperatures are within 2°C degrees of the canyon-level air temperature. Much better agreement between air and surface temperatures is achieved by comparing the coolest modelled distribution obtained from the mixed distribution analysis of the surface temperature data (i.e., the results in Figure 1.27 derived from the distributions in Figure 1.5). Results are displayed by view direction (Figure 5.25) and as

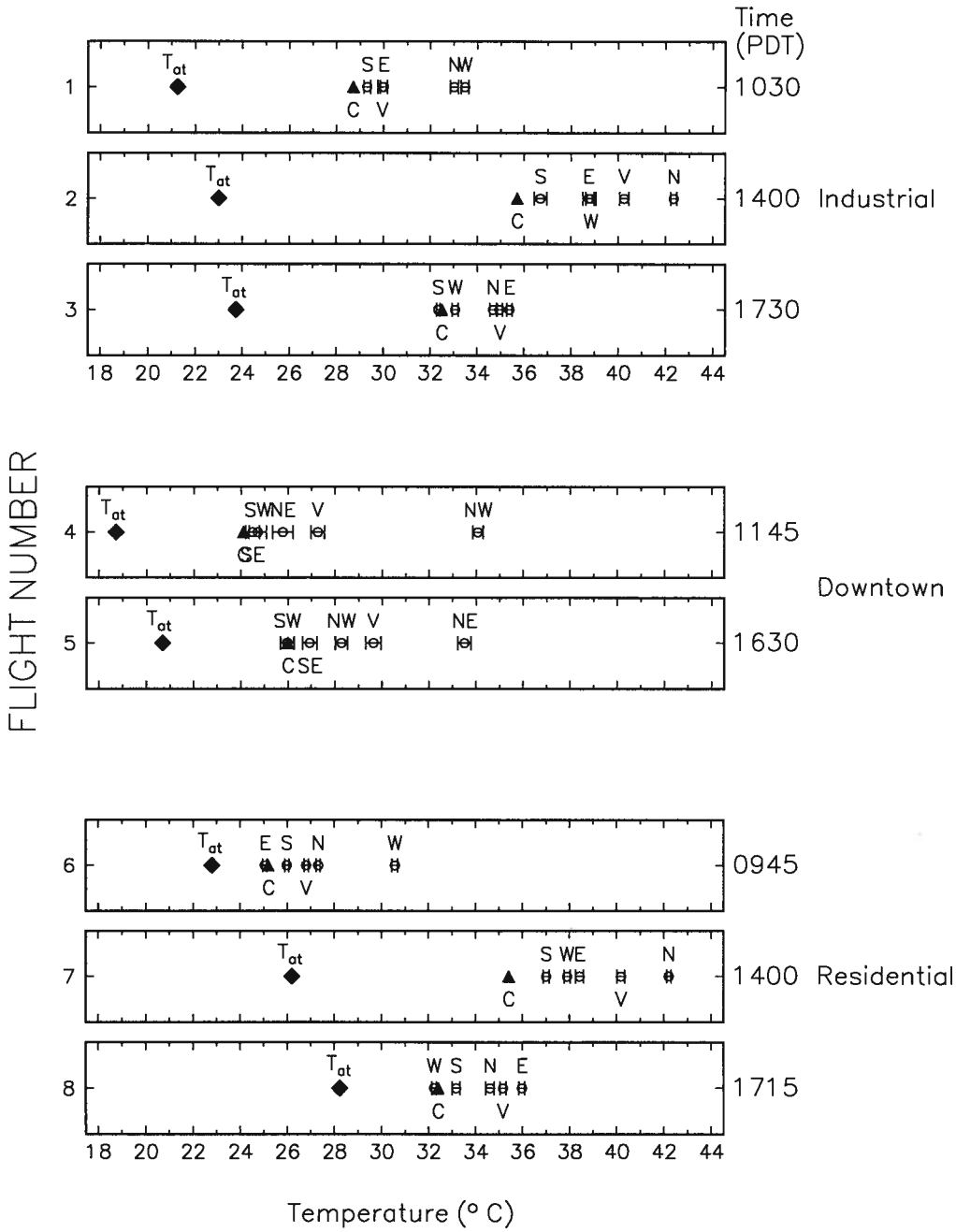

Figure 5.24: Comparison of mean image apparent surface temperatures by view direction, traverse air temperatures (T_{at}, denoted by solid diamonds), and complete apparent surface temperatures (T_{c_1}, solid triangles labelled C) for all study areas.

a composite for shaded and sunlit facets (Figure 5.26).

Very good agreement between T_{mod} and T_{at} is observed between the nadir and view directions towards shaded facets in the Downtown study area; the most directly irradiated facets (NW Flight 4 and NE Flight 5) substantially overestimate T_{at}. Winds were stronger on this day and the NW direction of the flow may have helped to equalize building and air temperatures on this day. The other Flights display a tendency for T_{mod} to underestimate T_{at}. The underestimate may be due in part to low emissivity surfaces (recall that in the downtown area, airborne observations of vertical facet surface temperatures influenced by spectral reflectivity lead to warmer apparent temperatures) while in the other areas, low emissivity surfaces are primarily confined to rooftops and would therefore lead to lower apparent temperatures. The Industrial area is characterized by greater numbers of low emissivity surfaces and also shows the largest difference between T_{mod} and T_{at}. Alternatively, the results may be a true indication of the temperature difference between the most shaded facets and air temperature.

The poorest observed agreement for shaded facets occurs in the Industrial area; especially during the morning and early afternoon flights (Flights 1, 2). T_{at} is substantially warmer than the coolest extracted distribution (Figures 5.25 and 5.26). Reasons for this are not obvious but it may be due in part to the ability for the remote imagery to view the bottoms of the street and alley-canyons along with lighter winds leading to greater temperature differentiation than for the Downtown study area. Comparison of these results with Figure 3.5 shows that T_{at} and T_{wt} (traverse air and building temperatures for North-facing walls) and the mean airborne apparent surface temperatures are closely related but T_{ramin} and T_{wt} are substantially cooler than T_{at}, confirming the presence of surfaces much cooler than air temperature.

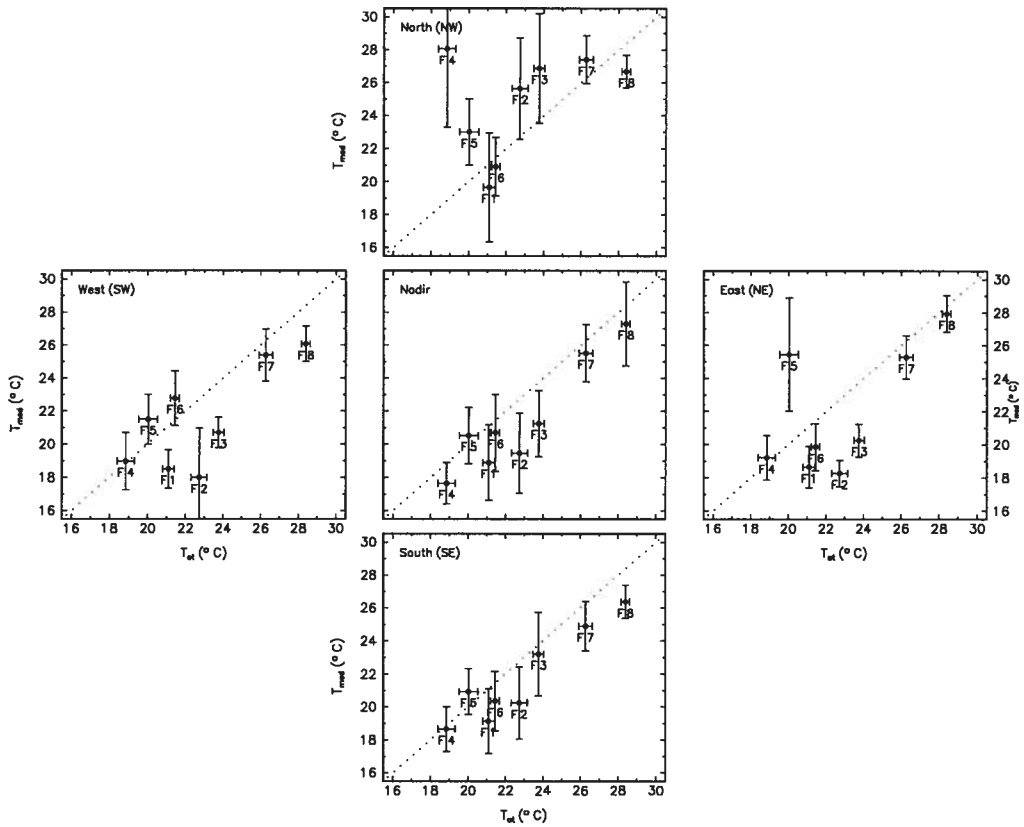

Figure 5.25: Traverse air temperature compared with the lowest modelled temperature distribution (T_{mod}) fitted to the composite frequency distribution. Plots separated by view direction for all flights. Error bars are $\pm 1\sigma$. Bracketed directions refer to Flights 4 and 5 (Downtown study area).

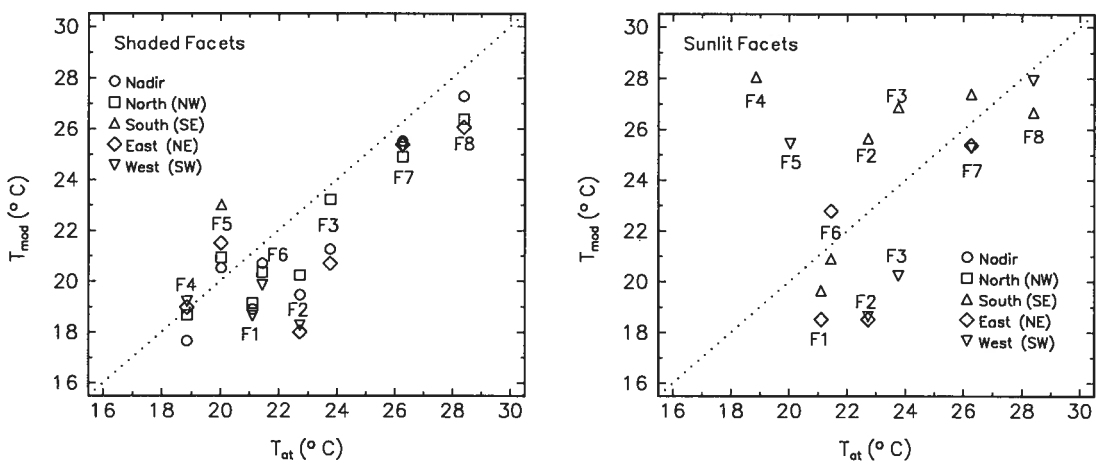

Figure 5.26: Same as Figure 5.25 except showing means only, and with data subdivided into shaded and sunlit facets. Bracketed directions refer to Flights 4 and 5 (Downtown study area).

5.5 Summary

It is apparent that, for the majority of cases, T_{c_1} is very close to the coolest observed off-nadir T_r. The two notable exceptions are the mid-day flights over the Industrial and Residential areas; these show T_{c_1} to be approximately 1° below the coolest off-nadir view direction (South). Differences between T_{c_1} and the warmest off-nadir direction are equal to, or greater than the range of off-nadir temperatures; differences of approximately 7°C are observed during the early afternoon flights over the Industrial and Residential area. These results suggest that, where available, off-nadir thermal imagery in the direction of the coolest (most shaded) facet yields the closest observable temperature to T_c. This approximation appears to be least valid at mid-day. The relation between air and surface temperatures shows the great majority of pixels have T_r values substantially warmer than air temperature. An approximate estimate of air temperature can be better derived by using the lowest fitted distribution to the composite frequency distributions from a view direction towards a shaded facet.

Chapter 6

MODELLING URBAN SURFACE THERMAL EMISSIONS

6.1 Introduction

In Section 1.6, a review of models for the prediction of thermal emissions over plant canopies concluded that a geometric projection modelling approach is appropriate when developing a model for urban surfaces because of the similarities between crop row structures and urban canyons. This chapter details the basis of the modelling approach, the modifications necessary to represent an urban surface, and a simple one-dimensional energy balance model to estimate component surface temperatures for use in the geometrical surface model.

6.2 Geometric Models to Estimate Longwave Surface Anisotropy

Geometrical models are one of a number of approaches to estimate longwave surface ansiotropy. Paw U (1992) presents a brief review of TIR model development and Goel (1988) provides a detailed review of geometric models used to calculate shortwave canopy reflectance. In the case of vegetation canopies, a geometric model consists of a ground surface plus geometrical objects placed to represent individual or combined canopy elements (e.g., single trees, or rows of closely-spaced plants; see Section 1.6.). The model used here is a slightly modified version of that first described by Sobrino *et al.* (1990) and Sobrino and Caselles (1990) for use under nighttime conditions over orange groves, and later modified to include daytime conditions (Caselles *et al.* 1992). It is referred to

here as the SC model.

6.2.1 Extension to Urban Surfaces

Row crops are often assumed to be sufficiently long to allow a two-dimensional surface representation using the row cross-section, thereby simplifying modelling. Urban street canyons are broken at regular intervals by intersecting streets. This creates a block structure which ideally requires three-dimensional surface representation. Similar modifications have been suggested by McGuire *et al.* (1989) for forest canopies and by Kimes and Kirchner (1982), and Cooper and Smith (1985) for short-wavelength surface reflection. Incorporation of a three-dimensional surface representation for the urban surface greatly increases the complexity of the sensor model and has been omitted from the present work. A slight modification to the form of the surface used by Sobrino *et al.* (1990) and Sobrino and Caselles (1990) is the addition of a second row spacing parameter to better represent the generally non-equal widths of street and alley canyons observed in the study areas (Figure 6.1).

6.3 Model Description

Sensor detected radiance is assumed to be a linear combination of surface component radiances weighted according to their fractional contribution (f) within the sensor IFOV:

$$L_s = \sum_{i=1}^{n} f_i \cdot L_i \tag{6.1}$$

where i represents a component surface within the sensor IFOV and L_i is a representative surface radiance for that component.

A geometrical model has been formulated to estimate f_i for simple two-dimensional urban surfaces given prescribed Sun-surface-sensor geometry. L_i may be estimated from

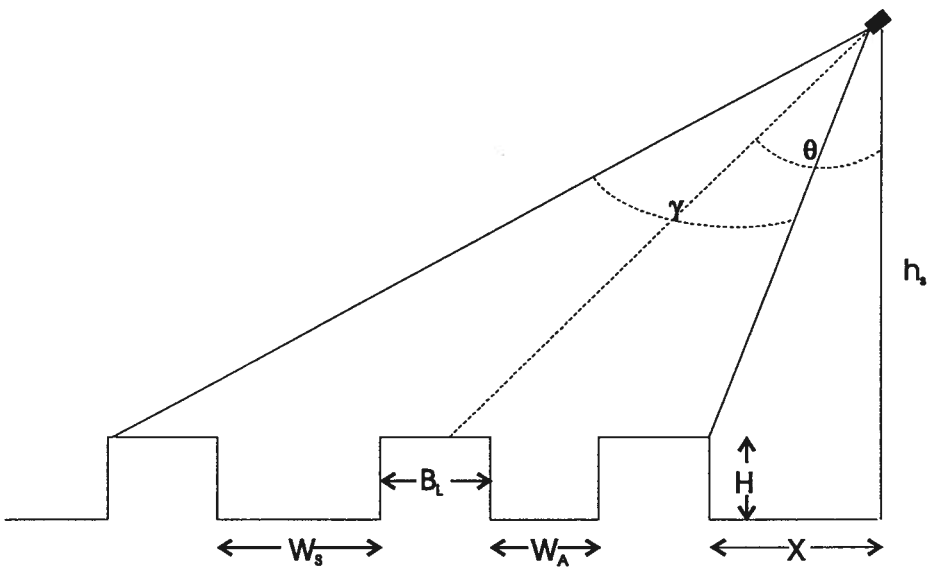

Figure 6.1: Two-dimensional model representation of an urban surface showing input dimensions. All buildings are of equal height H.

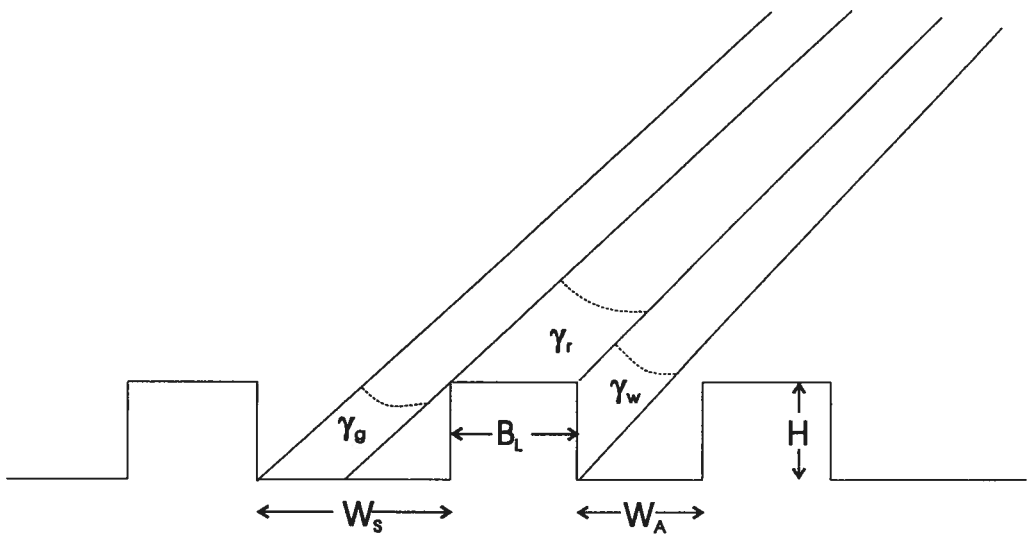

Figure 6.2: Detail of the component angles γ_r, γ_g, and γ_w calculated in the SC model.

observed data or a simple one-dimensional energy balance model (Section 6.4). The model has been developed using the concepts of Sobrino and Caselles (1990) but uses independently derived formulations for the angular portions of the IFOV occupied by roof, sunlit and shaded ground, and sunlit and shaded walls (γ_r, γ_g, and γ_w respectively). Tests of the model replicated the results presented by Sobrino and Caselles (1990) .

The γ components are determined using the general form:

$$\gamma_{x_i} = \gamma_{x_e} - \gamma_{x_s} \tag{6.2}$$

where x is replaced by r, g, or w and e and s refer to the start and end of the planar angle. The component angles (ignoring shading effects) are shown in Figure 6.2.

Specific formulae for roof, ground and wall are:

$$\gamma_{r_s} = \frac{X + (n-1)B_L + n_A W_A + n_S W_S}{h_s - H} \tag{6.3}$$

$$\gamma_{r_e} = \frac{X + nB_L + n_A W_A + n_S W_S}{h_s - H} \tag{6.4}$$

$$\gamma_{g_s} = \frac{X + (n-1)B_L + n_A W_A + n_S W_S}{h_s - H} \tag{6.5}$$

$$\gamma_{g_e} = \frac{X + nB_L + n_A W_A + n_S W_S}{h_s} \tag{6.6}$$

$$\gamma_{w_s} = \frac{X + nB_L + n_A W_A + n_S W_S}{h_s - H} \tag{6.7}$$

$$\gamma_{w_e} = \frac{X + nB_L + n_A W_A + n_S W_S}{h_s} \tag{6.8}$$

where X is defined as the distance from the sensor sub-point (directly below the sensor) to the beginning of the IFOV (assumed to be at the start of the first roof element) (Figure 6.1). The parameters n, n_A and n_S are counters which refer to the number of the element viewed; these differ for each γ and depend upon whether an alley or a street canyon is viewed.

The end of the IFOV is not pre-determined; the individual elemental angles are summed and a check is made following each addition to the sum, so that a slight over-estimate is always made because partial elements are not considered. The overestimate is minor when the elemental angles are small and this can be achieved by increasing the sensor height h_s.

The assumption of the IFOV beginning at the first roof has not been generalized. This is not considered to be restrictive for cases when the number of street-alley sequences on the ground are viewed. It does however, restrict exact comparison with observations which view only partial or a few series of street alley sequences.

Where surfaces are shaded and/or partially or fully obscured due to a large off-nadir viewing angle, additional expressions of γ are specified to account for these effects. Cases include viewing in both up- and down-Sun azimuth directions. The nadir case is similar except that the sensor subpoint is assumed to bisect a street canyon so that the IFOV is symmetrical about this point. Calculations are done separately in the up- and down-Sun azimuths to consider the different shading patterns.

Input required to specify the Sun-surface-sensor geometry is listed in Table 6.1.

Table 6.1: User input required for the SC model.

Parameter	Symbol	Units
Sensor description		
sensor view angle	θ	degrees
height of sensor	h_s	m
sensor IFOV	IFOV	planar degrees
sensor azimuth	ϕ_s	$\pm 90°$ relative to reference system
Solar Geometry		
zenith angle	Z	degrees
azimuth angle	ϕ	degrees
Surface Description		
Canyon azimuth	ϕ_c	degrees
Building dimensions		
height	H	m
length	B_L	m
building spacing (street)	W_S	m
building spacing (alley)	W_A	m

Model output consists of a tabulation of the sunlit and shaded fractional components of the major surface types (roof, wall, and ground) viewed. An example showing the variation in the proportions of these surfaces with view angle for north and south sensor azimuths at solar noon for YD 228 (August 15) over a model surface representing the Industrial area is presented in Figure 6.3.

The fractional components (f_i) are then used in eq. 6.1 in combination with observed or modelled estimates of L_i to estimate L_s for the given Sun-surface-sensor input geometry (Section 6.7).

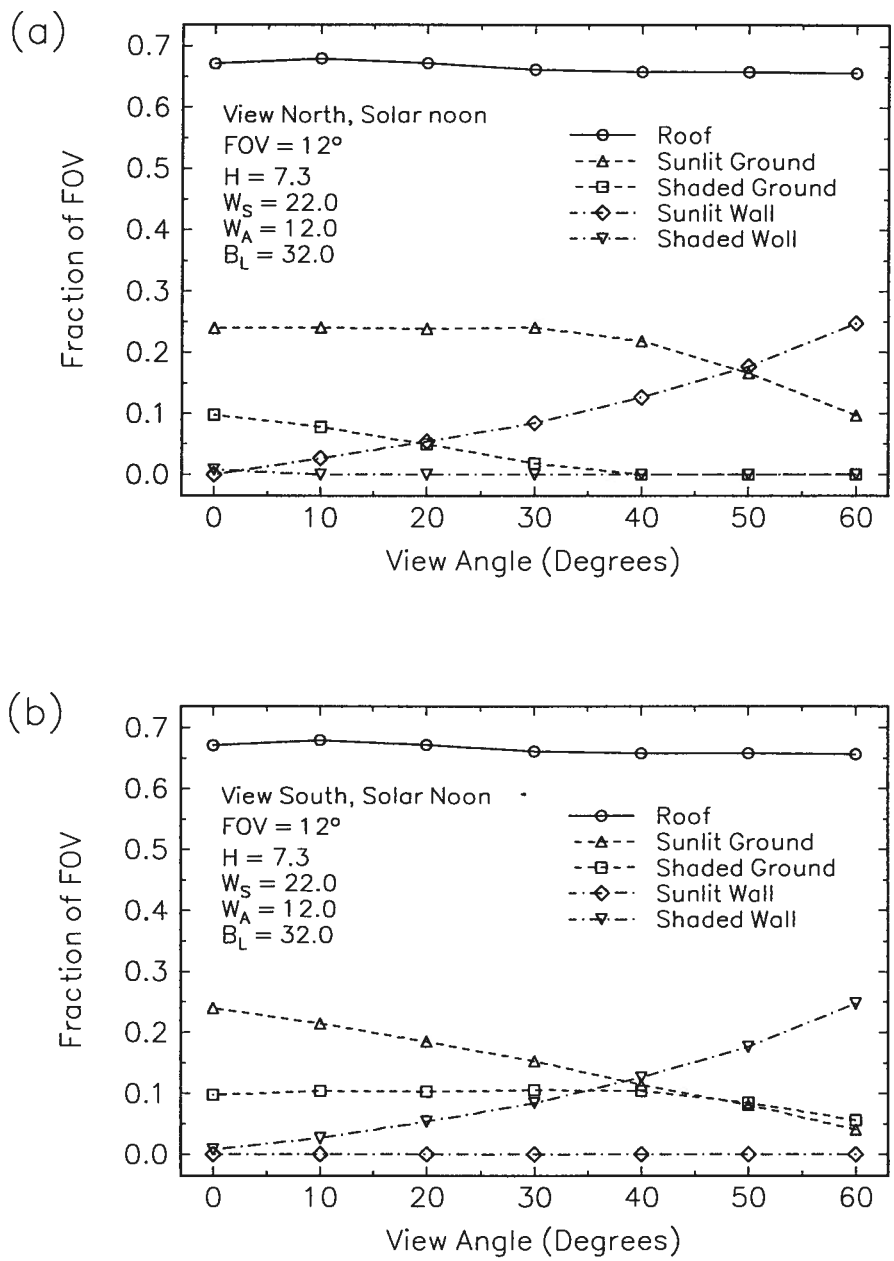

Figure 6.3: Proportions of roof, wall and ground surfaces calculated by the SC model for a 12° FOV sensor over a 2-D urban surface representing the Industrial study area. (a) View to the North; (b) view to the South. Solar geometry used is for YD 228 (August 15), solar noon.

6.4 An Energy Balance Model to Estimate Surface Temperatures

The SC model requires estimates of component surface emittance for use in eqn. 6.1. These can be obtained from observational data (e.g., traverse results, image extraction, or mixed distribution modelling), or surface emittance can be modelled. The ability to model component surface temperatures is important because it allows the model to be extended to a wide range of times and surface geometries and avoids the difficulty and expense of acquiring high resolution multi-temporal TIR coverage of various urban surfaces.

6.4.1 Urban Surface Temperature Models

Modelling the temperatures of surfaces which comprise the complex urban system is difficult. The microscale urban climate model of Sievers and Zdunkowski (1986) is designed to simulate air flow over rectangular obstacles but includes an energy budget to derive the surface temperature of canyon facets. Evaporative, advective and canyon radiative effects are included in the model. URBAN3 (Terjung and O'Rourke, 1980) combines information on urban morphology, building material, and building dimension to simulate energy budgets and temperatures for individual surfaces. The major model components are: view factor/obstructions, radiation interception by surfaces, and energy budget temperature calculations. However, since the ambient air is decoupled from the surface energy budget, feedbacks between air and surface temperatures are not included. The recent model of Mills (1993) combines a semi-empirical canyon windfield model with an urban canyon energy budget model. In the absence of evaporating surfaces, modelled surface temperatures agree well with observations. The canyon radiation calculations are handled in the manner of Arnfield (1982) which includes the ability to vary radiative properties in strips in the along-canyon direction. In all these models the structure and

code are extremely complex.

The present research requires a canopy layer model capable of rapidly providing temperature estimates for building facets with specified orientation and material properties for use with SC. The complexity of the urban energy balance models mentioned above renders them unsuitable. Model complexity can be reduced if it is assumed that component surface temperatures are largely controlled by the orientation and properties of the surface. A first order approximation to component surface temperatures can then be generated using a simple one-dimensional energy balance model. The goal is to correctly model the range and relative temperature difference among facets of different orientation and surface material.

6.4.2 The Myrup 1-D Surface Energy Balance Model

One-dimensional energy balance models use the equilibrium surface temperature concept. An equilibrium surface temperature is iteratively solved from the energy balance equation as the solution of a given set of boundary conditions and solar radiation forcing regime. Such models ignore heat and moisture advection.

The Myrup (1969) model with modifications by Outcalt (1971) was selected for use in this thesis. It was originally formulated to provide insight into genesis of the urban heat island but it has a deliberately simple structure which allows it to be adapted to a wide variety of problems (Myrup, 1969; Outcalt, 1971). It includes relatively simple parameterizations for the calculation of atmospheric diffusivity and incoming solar radiation when compared with other 1-D models (Loudon Ross and Oke, 1984), and therefore may be a less than ideal choice. Its merits were pragmatic: it is readily available, easily implemented, and most of its input can be satisfied by available data. Standard model inputs and outputs are listed in Tables 6.2 and 6.3. Further details of the model are provided in Myrup (1969) and Outcalt (1971).

Table 6.2: Myrup model input requirements.

Variable	Units
Label data	
Title	character string
Temporal data	
latitude	degrees
solar declination	degrees
solar radius vector	
start time	hours
Meteorological data	
station pressure	mb
mean daily air temperature	°C
mean daily vapour pressure	mb
mean daily wind velocity	m s^{-1}
precipitable water (w)	mm
dust particles (D)	cm^{-3}
anthropogenic heat	W m^{-2}
Geographical data	
subsurface volumetric heat capacity (C)	J m^{-3} K^{-1}
subsurface thermal diffusivity (κ)	m^2 s^{-1}
surface roughness (z_o)	m
albedo (α)	fraction
moisture availability factor	fraction
shadow ratio	fraction

Table 6.3: Myrup model output.

Parameter	Units
Computed boundary conditions	
soil damping depth	m
atmospheric damping depth	m
adiabatic heat transfer coefficient	$m^2\ s^{-1}$
Time-dependent output	(hourly)
Solar:	
Extraterrestrial, Incoming ($K\downarrow$), and reflected ($K\uparrow$)	$W\ m^{-2}$
Direct shortwave, diffuse shortwave	$W\ m^{-2}$
Energy balance terms Net radiation	$W\ m^{-2}$
sub-surface heat flux	$W\ m^{-2}$
turbulent sensible and latent heat fluxes	$W\ m^{-2}$
T_o	(°C)

The success of the Myrup model for estimating surface temperatures has been tested by Outcalt (1971) with respect to needle-ice events and more qualitatively by Loudon Ross and Oke (1984) against remotely sensed surface temperatures and air temperatures. Outcalt (1971) found the amplitude of T_o and the time dependent behaviour were correctly simulated, but considerable phase-shift discrepancies were noted because of heat-transfer processes not included in the model. Loudon Ross and Oke (1984) noted more serious discrepancies. Surface temperatures were considered unrealistic because their daily range was less than that observed for air temperatures and the peak at solar noon was too early when compared with observations. However, the authors note that improvements result when the model is run with hourly, rather than mean daily, meteorological input data. This provides some coupling between surface and air temperatures which is otherwise missing from the model (as evidenced by modelled maximum temperatures which occur at solar noon). Model comparisons against observed temperatures

from select component surfaces in this study are given in Section 6.5.

6.4.3 Modifications to the Myrup Model

Modifications to the basic Myrup model (which assumes an extensive horizontal surface) were made in order to incorporate the surface structure of urban areas. The modifications include:

- provision for radiation upon vertical (walls) and inclined (roof) surfaces through the calculation of $\hat{\theta}$, the angle of incidence between the normal to the slope and the solar beam for a given slope geometry (slope and azimuth) (see e.g., Oke (1987), Iqbal (1983));
- inclusion of an urban canyon structure with given canyon azimuth, H:W ratio, and wall and floor surface radiative properties (albedo and emissivity);
- incorporation of canyon radiative effects by either:
  - coupling to the canyon radiation model of Arnfield (1982), or;
  - addition of a simplified scheme for predicting radiation balance at the midpoint of the three canyon facets (floor and two walls), including multiple reflections;
- replacement of the mean daily boundary conditions with hourly updates.

The simplified radiation scheme calculates incident shortwave radiative fluxes for the midpoint of each facet. This is accomplished by calculating $\hat{\theta}$ for each surface and determining the horizon obstruction of the opposite wall in the direction of the sun. Diffuse radiation is assumed to be isotropic. The calculated irradiances are then input to the canyon multiple reflection routine of Arnfield (1982). View factors of each facet for the three facet midpoints are calculated using equations for plane and perpendicular

surfaces for a point derived using Nusselt Sphere techniques (Steyn and Lyons, 1985; Johnson and Watson, 1984). The sky view factor is determined as a residual. Incident longwave radiation at the facet midpoints is calculated as a weighted sum (using view factors) of the sky and facet longwave irradiances. Sky irradiance is determined using Idso (1981) or Idso and Jackson (1969). Facet emissions (except for the facet modelled) are calculated from air temperature. At night, this approximation holds well. During the daytime, air temperature underestimates surface temperature when the facet is directly irradiated. Multiple reflections are not incorporated.

A number of less substantive changes have also been made to faciliate model use including:

- replacement of the time of modelling (originally specified by means of the Earth's radius vector (or eccentricity) and the solar declination by equations from Spencer (1971) (as given by Iqbal (1983)) which require only year day (YD) as the base input;
- conversion between LAT (Local Apparent Time or solar time) and LST or LDT (Local Standard or Daylight time);
- addition of the Idso (1981) longwave radiation formulation to that of Idso and Jackson (1969); the former requires air temperature and humidity as input, the latter only air temperature.

The incoming solar radiation simulation of the Myrup model is derived from Gates (1962) and requires as input: extraterrestrial solar irradiance (W m^{-2}), surface pressure (mb), dust factor D, and precipitable water w (mm). Precipitable water is estimated by integrating the measured profiles obtained from the composite atmospheric soundings and dust content is estimated qualitatively from Gates (1962). The sensitivity to D and

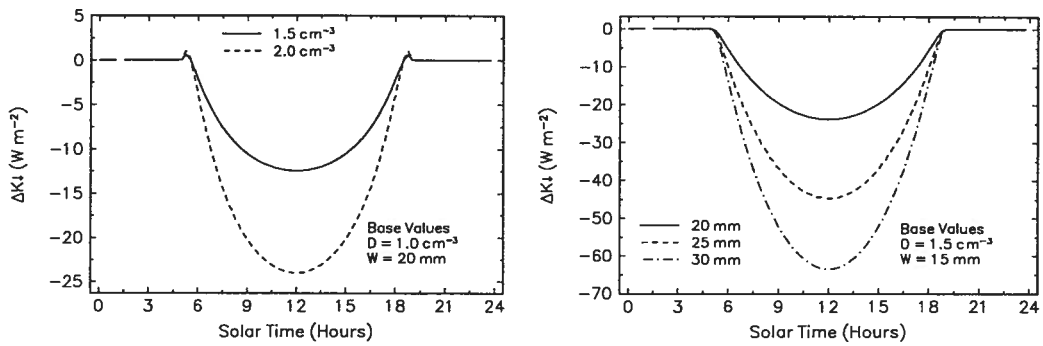

Figure 6.4: Sensitivity of K↓ to: (a) dust content D and (b) w.

w are shown in Figure 6.4. Increasing values of both parameters leads to lower modelled values of K↓. Substantial temporal variability exists in the estimates of w, and this is shown to qualitatively match with the temporal variations in K↓ (Figure 6.5).

Observed and modelled incoming global solar radiation for August 15/92 are plotted in Figure 6.6 for two values of D which cover the approximate range of values for polluted urban atmospheres (Gates, 1962). The model slightly overestimates but the difference is not large; percentage differences between the maximum modelled and observed values are less than 3% for $D = 1.5$ and less than 2% for D=2.0.

In-canyon radiation estimates obtained using the Arnfield (1982) routines and a more simple set of equations for the mid-point of each canyon facet, are almost identical (Figure 6.7). Comparison of the facet mid-point against the facet average (Figure 6.8) generated from the Arnfield model shows differences when the facet is partially shaded. However, this is not serious because it is not recommended to use average facet net shortwave radiation to estimate facet temperature. It is preferable to combine separate shaded and sunlit estimates. The difference between the facet mid-point and average facet irradiance is limited to a second order effect (in the simple model) associated with

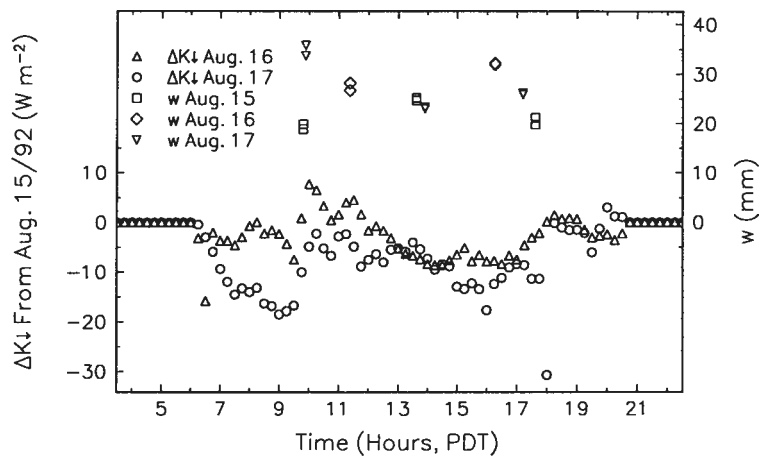

Figure 6.5: Difference of K↓ on August 16 and 17 from that of August 15, together with precipitable water calculated from the composite soundings made during each remote sensing flight.

substitution of the entire facet irradiance by the midpoint during the calculation of multiple reflections. The use of the simple mid-point scheme yields execution times almost two orders of magnitude faster than using the Arnfield routine (2.75 s versus 218 s).

6.5 Model Tests Against Observations

The traverse observations of the surface temperature of the road and canyon walls provide data with which model temperature estimates may be compared. This section presents comparisons of modelled and observed surface temperatures for both individual component surfaces and composite surfaces (e.g., all canyon facets of a given orientation) and investigates the model output sensitivity to various model input variables.

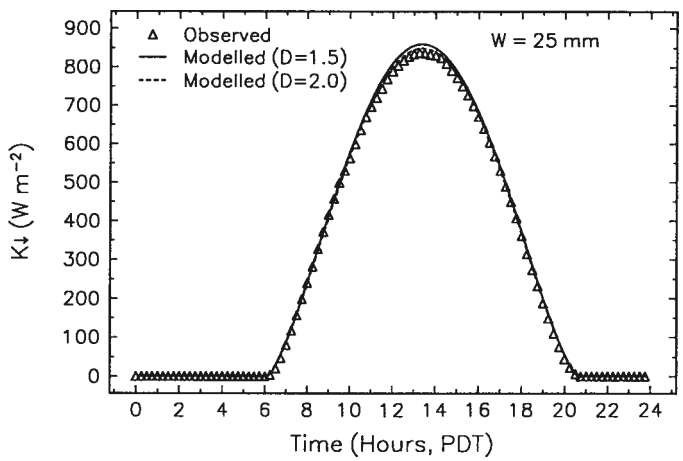

Figure 6.6: Observed (at the Sunset Tower site) and modelled incoming global solar irradiance for August 15, 1992.

6.5.1 Road surface temperatures

6.5.1.1 Sensitivity Analysis

Road surfaces are the most homogeneous surface type in the study area. Prior to a comparison of model results with observations, a sensitivity analysis to variations in the input values of: asphalt thermal, radiative and aerodynamic properties, hourly versus daily data, canyon H:W ratio, and surface slope and azimuth was conducted (Figure 6.9). Base model input values are presented in Table 6.4.

The specification of the air temperature is an important determinant of the magnitude and shape of the surface temperature curve. Using only the mean diurnal air temperature (recorded at Vancouver International Airport) yields maximum modelled T_o at solar noon (which is unrealistic) and the lowest diurnal temperature range of the tests. When the

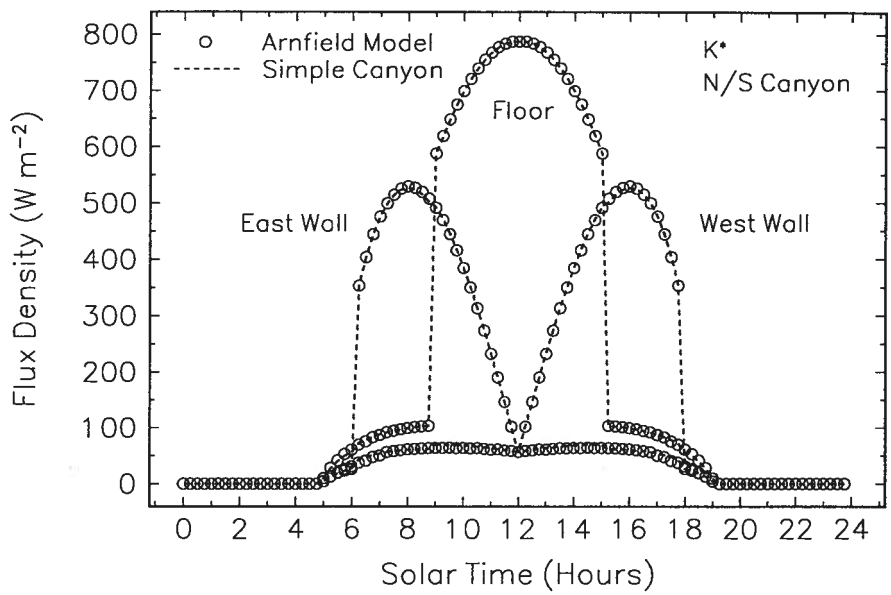

Figure 6.7: Comparison of mid-facet estimates of net shortwave radiation generated using the mid-point model and the Arnfield (1982) canyon radiation routines. Canyon is aligned N/S with H:W of 5:11, $\alpha_w = 0.2, \alpha_f = 0.05$.

mean daily air temperature is replaced by hourly values, the T_o peak is lagged relative to noon and the range is increased. A further increase in the surface temperature maximum is achieved when traverse air temperatures (T_{at}) are used in place of the airport data.

The sensitivity to asphalt thermal properties was tested using three separate reference values for thermal diffusivity (κ) and volumetric heat capacity (C) (Table 6.5.1.1).

The variation in modelled temperature is relatively small and large changes (an increase in C is most effective) are required to produce a change in phase.

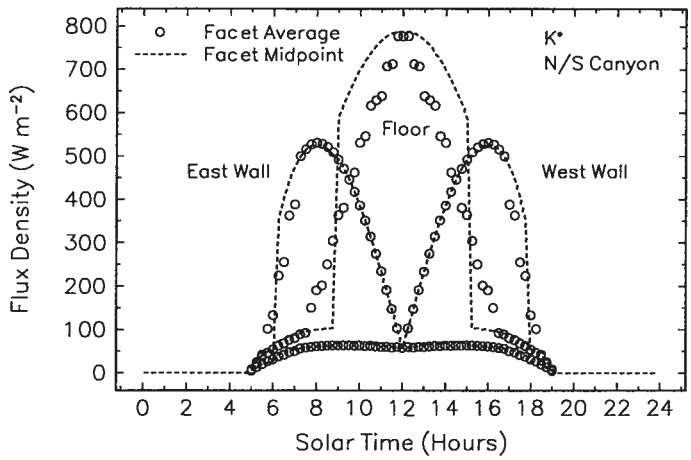

Figure 6.8: Comparison of mid-facet and facet average estimates of net shortwave radiation generated using the mid-point model and the Arnfield (1982) canyon radiation routines. Canyon is aligned N/S with: H:W of 5:11, $\alpha_w = 0.2, \alpha_f = 0.05$.

Table 6.4: Base input parameters: asphalt sensitivity tests.

Model Input	Value
ϵ	0.93
α	0.05
C	1.94×10^{6}
κ	0.38×10^{-6}
z_o	0.0001
Slope	0.0
Air temperature	hourly (T_{at} augmented with airport data
Longwave Radiation	Idso and Jackson (1969)

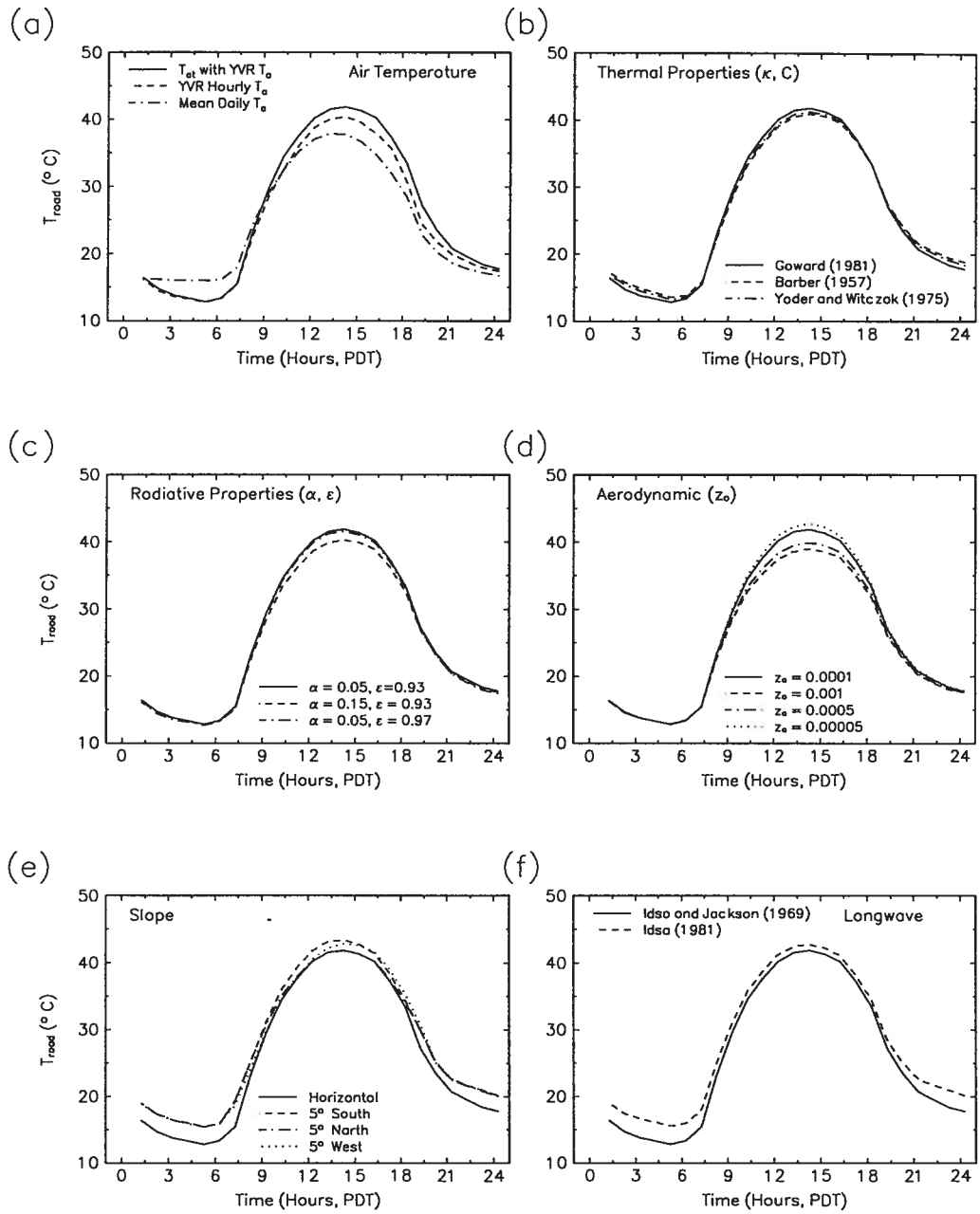

Figure 6.9: Sensitivity analysis of an asphalt road surface temperature to: (a) air temperature specification, (b) thermal properties (κ and C, (c) radiative properties (α, and ϵ), (d) surface roughness (z_o), (e) slope aspect, and (f) longwave radiation parameterization. Solid line represents the set of base input (See Table 6.4).

Table 6.5: Reference values of asphalt thermal properties used in the Myrup model.

Reference	C (J m^{-3}) K^{-1}	κ (m s^{-1})
Barber (1957)	2.07×10^{6}	0.59×10^{-6}
Yoder and Witczak (1975)	1.41×10^{6}	1.03×10^{-6}
Goward (1981)	1.94×10^{6}	0.38×10^{-6}

An increase in α (from 0.05-0.15) yields a decrease in the modelled surface temperature of approximately 1.5°C; increasing ϵ slightly reduces modelled surface temperature.

Specification of the surface roughness length, z_o can yield a large sensitivity in T_o. To achieve best agreement with observed data, low values of z_o were required (0.001 or less). These are somewhat arbitrarily specified considering the surface character of asphalt in isolation, rather than as a component of the urban surface (which has much larger values of z_o).

Slight changes in the slope of the road surface are possible due to: (a) road construction (the middle, or crown is higher than the sides), (b) topographic effects. A slope with westerly aspect shows a phase shift of T_o towards later times, and increases in the maximum modelled temperature. North and south aspect slopes show no phase shift but respectively reduce or enhance the maximum surface temperature.

To summarize, large sensitivities are observed with respect to the manner in which air temperatures are updated (if at all) within the model, and the aerodynamic roughness and slope of the surface.

6.5.1.2 Industrial

Modelled road surface temperatures (T_{road}) were generated using: $z_o = 1.0\times10^{-5}$, $\kappa = 0.86\times10^{6}$ m^2 s^{-1}, $C = 1.32\times10^{-5}$ J m^{-3} K^{-1}, $\epsilon = 0.94$, $\alpha = 0.05$. Traverse observations from two blocks were selected for a comparison of modelled and observed T_{road}. Results

are presented in Figure 6.10 for (a) E/W and (b) N/S-aligned blocks, each with H:W of approximately 6:22.

Observed results for the E/W block are the mean, and $\pm 1\sigma$ about the mean, from the traverse measurements along the block. Relatively constant canyon H:W along the block yields spatially consistent radiation conditions. The maximum road surface temperature is well approximated by the model, as is the afternoon cooling. The model over-predicts the rise of temperature in the morning, leading to an overall shift of the heating curve to times earlier in the day.

Individual temperature samples are plotted for the N/S block because of significant along-street variability due to shading by individual buildings, in contrast to the E/W canyon. Generally good agreement exists during the morning period. There is evidence of a period of shading not incorporated in the model around 1200 PDT. Peak and afternoon temperatures are underpredicted by the model, although the general trend of the observations is replicated.

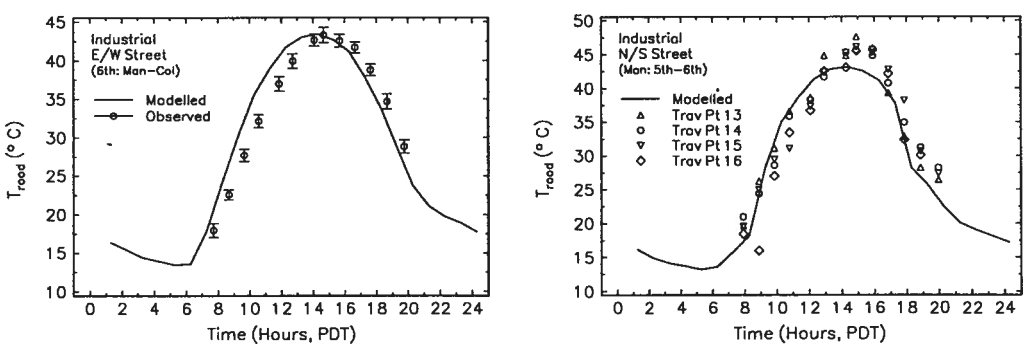

Figure 6.10: Modelled and observed road surface temperatures in the Industrial study area: (a) E/W street canyon, (b) N/S street canyon.

6.5.1.3 Residential

A composite two block comparison of an E/W street with few trees in the Residential area (Figure 6.11) exhibits results similar to those obtained in the Industrial area: the road surface warms too quickly and therefore T_{road} is overpredicted for the period prior to the peak. Afternoon temperatures and the timing of the maximum are generally well represented by the model. North/south Residential blocks have not been modelled because the shading by street trees cannot be accounted for in the model.

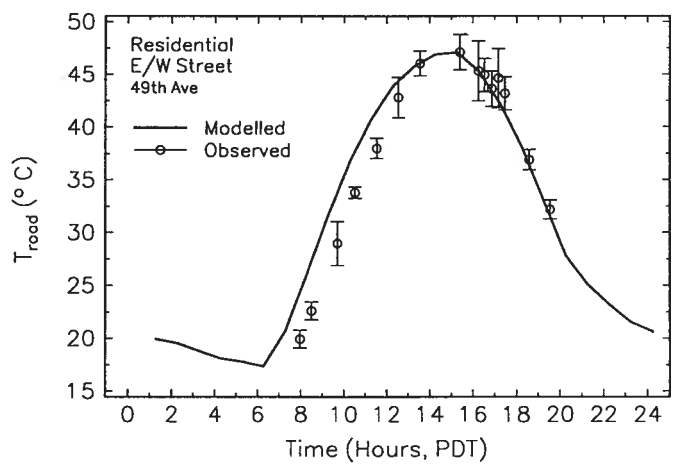

Figure 6.11: Modelled and observed road surface temperatures in the Residential study area: E/W street canyon.

6.5.1.4 Downtown

Modelling T_{road} is expected to be more difficult in the Downtown area because the model has a limited ability to handle the complex canyon geometry in this area (unequal canyon wall heights and large differences in building heights in the along canyon direction). Four

street canyons were tested, two for each of the street azimuths in the study area, where canyon geometries were relatively constant along the length of the block and wall heights were approximately equal. Model specifications relating to asphalt remain the same as previously. Canyon geometry was estimated from planning maps and field observations.

The NE/SW results (Figure 6.12a,b) show a range of agreement between modelled and observed temperatures. Very good agreement was obtained between the observed mean and the modelled surface temperature for the block on Howe St. between Hastings and Pender (H:W 29:23). The large error bars (representing $\pm 1\sigma$) arise because there are areas of both shaded and irradiated pavement along the block. The block on Hornby St. between Dunsmuir and Pender (Figure 6.12b) shows poorer agreement between observations and model output. The difference in model output between the two blocks is largely in the width of the main peak. The peak for the Hornby block is wider due to the more open canyon geometry (H:W 21:23). Observed road temperatures are generally cooler than the modelled values, particularly in the morning. This is similar to the differences noted in the Industrial and Residential areas. A further difficulty with comparing modelled and observed values in the Downtown area is the required bias of the traverse route to stay on one side of the canyon where the radiation conditions may differ from those in the centre of the canyon.

Results from the NW/SE street canyons (Figure 6.12c,d) show similar variation. In addition to the mean block road temperature, data are plotted for individual sampling points (labelled as Trav Pt) along the block to illustrate the large spatial variability of surface temperature along the street. Generally good agreement is obtained for the block on Hastings between Hornby and Howe, although large portions of the block receive direct radiation in the afternoon due to some lower buildings. Agreement for the block on Dunsmuir between Howe and Hornby is much poorer in the early afternoon when modelled temperatures are substantially lower than observed. Again, this is probably

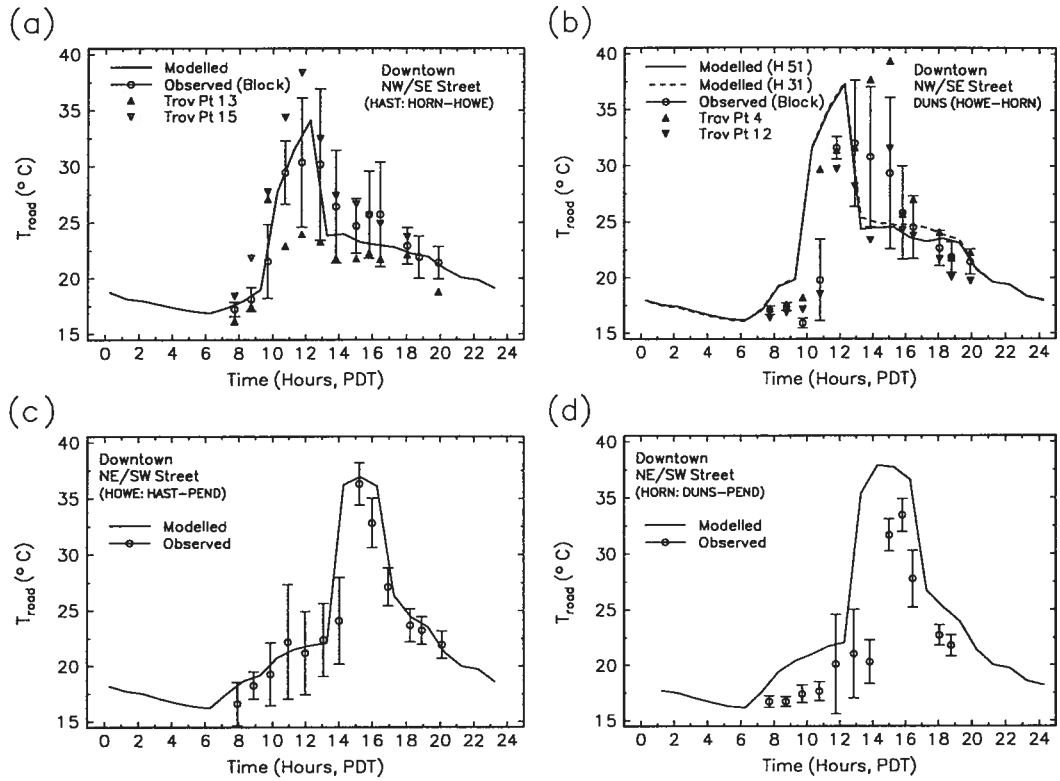

Figure 6.12: Modelled and observed road surface temperatures in the Downtown study area:(a),(b) NE/SW street canyons; (c),(d) NW/SE street canyons.

due to variations in the canyon geometry at scales too small to be resolved by the model.

6.5.2 Roof Temperatures

Roofs are an important component of the urban surface and form a relatively simple surface to model in that canyon effects can be neglected (at least in those areas where building heights are relatively constant). Roof surface temperatures are modelled and compared both to an individual building (Summer Equipment site) and for the Industrial area and Residential area as a whole (Figure 6.13).

As input a roof emissivity value of 0.92 was used based on the results of Artis and

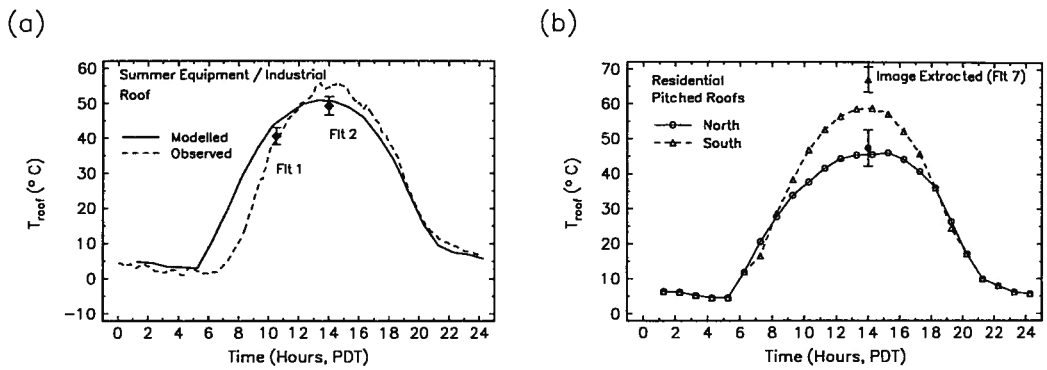

Figure 6.13: Roof surface temperatures for: (a) the Summer Equipment site and Industrial area, (b) north- and south-pitched roofs in the Residential area.

Carnahan (1982). Albedo was set at 0.10 and the thermal properties κ and C were set to 1.55×10^{-7} m^2 s^{-1} and 3.26×10^5 J m^{-3} K^{-1} respectively (based upon a roof construction using asphalt shingles overlaid upon a plywood base with polystyrene insulation (ASHRAE, 1989). It was necessary to modify the model to handle nighttime surface temperatures which were initially greatly overestimated. The modifications include:

- setting the latent heat flux to zero;
- reducing the nighttime sensible heat flux to 0.15 of the calculated value;
- replacing screen-level T_a in the atmospheric longwave emission formulation with a bulk atmospheric temperature of 10°C;
- reducing z_o to very low values.

Nighttime observed surface temperatures are significantly below air temperature, and it was desired to reduce the surface energy budget of the model to a balance between net radiative loss and heat conduction, however, tests showed that a solution could not be obtained when the sensible heat flux was reduced to values less than 15% of the

original for the z_o and thermal properties specified. Reducing the sensible heat flux and removing the latent heat flux (preventing dewfall) have the effect of reducing the modelled nighttime temperatures by approximately 5°C.

The observed temperature of the roof at the Summer Equipment building site shows a lag when compared with the modelled temperature in the morning heating curve, similar to that observed for road surfaces (Figure 6.13(a)). The afternoon and evening cooling period and night time temperatures are well replicated by the model. The image extracted roof temperature for Flight 2 (Industrial study area) agrees well with the maximum modelled value.

Tests of the model to shifts in the hourly input data, slight surface obstructions and using measured rather than modelled incoming shortwave radiation do not adequately account for the observed lag. The addition of a wet surface in the morning hours (i.e., following dewfall) was able to account for some of the lag, but resulted in surface warming before sunrise which was not present in the observations. The lag seems most likely to be related to the layering of materials with different thermal properties below the surface and/or the low effective thermal admittance of building surfaces.

In the Residential area, (Figure 6.13b), south-pitched roofs (a 25° pitch is assumed) are underestimated, although with the high surface temperature and low emissivity, large correction values are applied to the image temperatures (in excess of 8°C for the atmospheric correction and 5°C for the emissivity correction). Modelled north-pitched roof temperatures agree well with temperatures extracted from the early afternoon flight (Flight 7).

6.5.3 Grass Surfaces

Grass surfaces are an important surface component in urban areas, and may be included as a component of the horizontal surface of SC. Measured grass temperatures and net

radiation are available from a park study (Spronken-Smith, 1994). The site is in a large park so canyon effects are neglected. Input parameters are set to typical values for short grass: α=0.24, ϵ=0.95, $\kappa = 0.5\times10^{-6}$ m^2 s^{-1}, C=1.8$\times10^6$ J m^{-3} K^{-1}, z_o=0.001 (e.g., Oke, 1987). The fractional surface moisture parameter was set at 0.5, with the consideration that measured soil moisture was approximately 13%, the underlying soil had a high sand content, and the grass surface was not exhibiting visible signs of water stress (i.e., loss of green colouration).

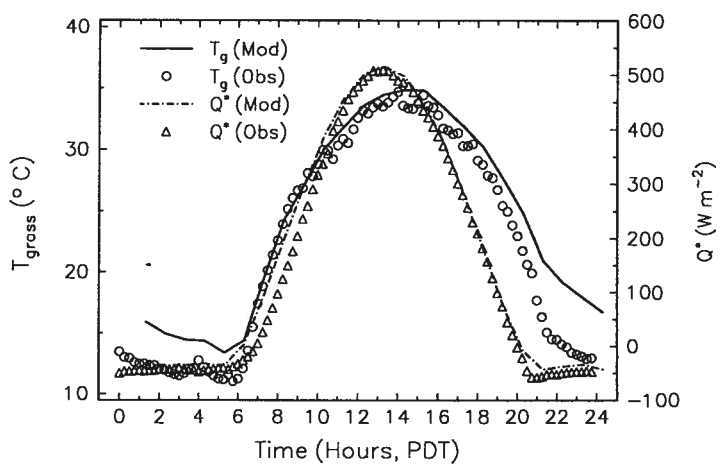

Figure 6.14: Modelled and measured surface temperatures and net radiation for a grass surface in Trafalgar Park.

Agreement between measured and modelled net radiation and surface temperature is very good during the daytime (Figure 6.14), although there is a slight overprediction of net radiation in the morning and an increasing difference (model overprediction) after the time of maximum surface temperature. Nighttime surface temperatures are (5–8°C colder than predicted, while the net radiation is slightly larger than observed. The

discrepancy between modelled and measured surface temperatures may be due to poor thermal coupling of the grass with the underlying soil at night: the tips of the grass (preferentially viewed by an off-nadir IRT) cool radiatively and are much colder than the base of the grass and soil surface.

6.5.4 Facet Temperatures

6.5.4.1 An Individual Building

As part of a parallel study, wall surface temperatures of a single building in the Industrial area (Summer Equipment site) were monitored and are available for comparison with the model. Input data are shown in Table 6.6 and the results are portrayed in Figure 6.15.

Table 6.6: Model input: Summer Equipment building facets. Facet azimuth refers to the direction in which the facet faces (i.e., North = North-facing). Subscripts w and f refer to walls and floor respectively.

Parameter	Units	North	South	East	West
α_f	fraction	0.05	0.10	0.20	0.20
α_w	fraction	0.20	0.20	0.20	0.20
ϵ_f	fraction	0.94	0.95	0.95	0.95
ϵ_w	fraction	0.98	0.98	0.98	0.98
κ	$m^2\ s^{-1}$	0.86×10^{-6}	0.86×10^{-6}	0.86×10^{-6}	0.86×10^{-6}
C	$J\ m^{-3}\ K^{-1}$	1.32×10^{6}	1.32×10^{6}	1.32×10^{6}	1.32×10^{6}
z_o	m	1.0×10^{-6}	1.0×10^{-6}	1.0×10^{-6}	1.0×10^{-6}
H	m	7	5	5	5
W	m	13	25	12	29
B_L	m	100	100	35	35

Canyon geometry was estimated from field observations. Surface thermal and radiative properties are estimates for yellow-painted hollow concrete blocks (ASHRAE, 1989) estimated in the manner of Hutcheon and Handegord (1983).

The general shape of the observed time series for each facet is replicated by the model,

with the exception of the west wall, which, perhaps due to local shading effects, shows much cooler surface temperatures in the morning. The peak modelled temperature in all cases precedes the observed data, similar to the results obtained for road surface temperatures.

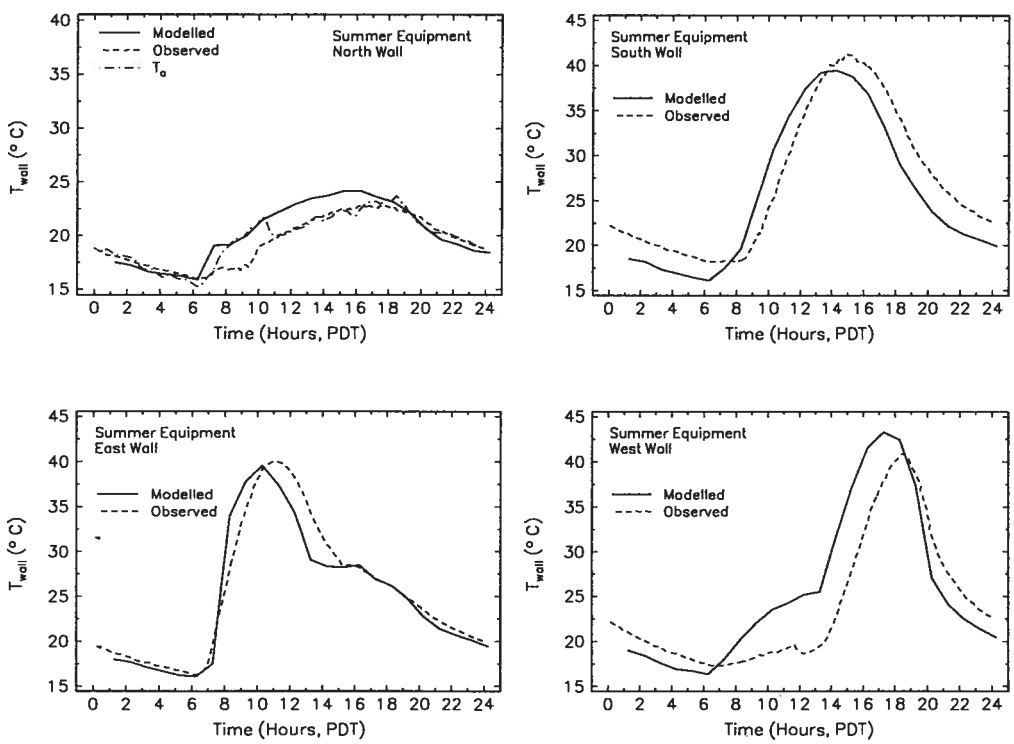

Figure 6.15: Modelled and observed surface temperatures for the Summer Equipment site (Industrial area).

North wall temperatures are consistently above those observed (which are very close to air temperature) during the day; this is a function of heating by diffuse shortwave radiation. Setting canyon albedo to zero results in better agreement between observed and modelled values but is not a realistic model value.

6.5.4.2 Canyon Facets in the Study Areas

The modified Myrup model was next compared with the average traverse results from the three study areas (Figures 6.16, 6.18, 6.20 and Table 6.7). The plotted error bars indicate $\pm 1\sigma$ from the mean of the traverse data. Where present, the solid symbols represent the values obtained from airborne thermal imagery.

Table 6.7: Model input: Industrial, Downtown and Residential Sites.

Parameter	Units	Industrial	Downtown	Residential
α_f	fraction	0.05	0.05	0.05
α_w	fraction	0.25	0.35	0.20
ϵ_f	fraction	0.94	0.93	0.93
ϵ_w	fraction	0.95	0.95	0.95
κ	$m^2\ s^{-1}$	0.86×10^{-6}	0.38×10^{-6}	0.37×10^{-6}
C	$J\ m^{-3}\ K^{-1}$	1.32×10^{6}	1.94×10^{6}	0.76×10^{6}
z_o	m	0.0001	0.0001	0.0005
H	m	8	35	9
W	m	22	30	33
B_L	m	100	88	80
Shadow Ratio	fraction	0	0	0.2-0.5
Wet Fraction	fraction	0	0	0.11

The simulated temperatures in the Industrial area are warmer than the mean traverse temperatures, particularly for the west and south canyon facets. Because of the mixed FOV problem and perhaps due to neglect of shading devices such as awnings, this finding is not too surprising. However, shaded facet temperatures are also warmer than observed. This leads to facet-pair differences which agree in magnitude with those observed. The earlier peak temperatures from the model are again evident in the difference plot.

Where hourly data are unavailable, the model must be run using mean daily input conditions for air temperature, vapour pressure and windspeed. The effect of using mean

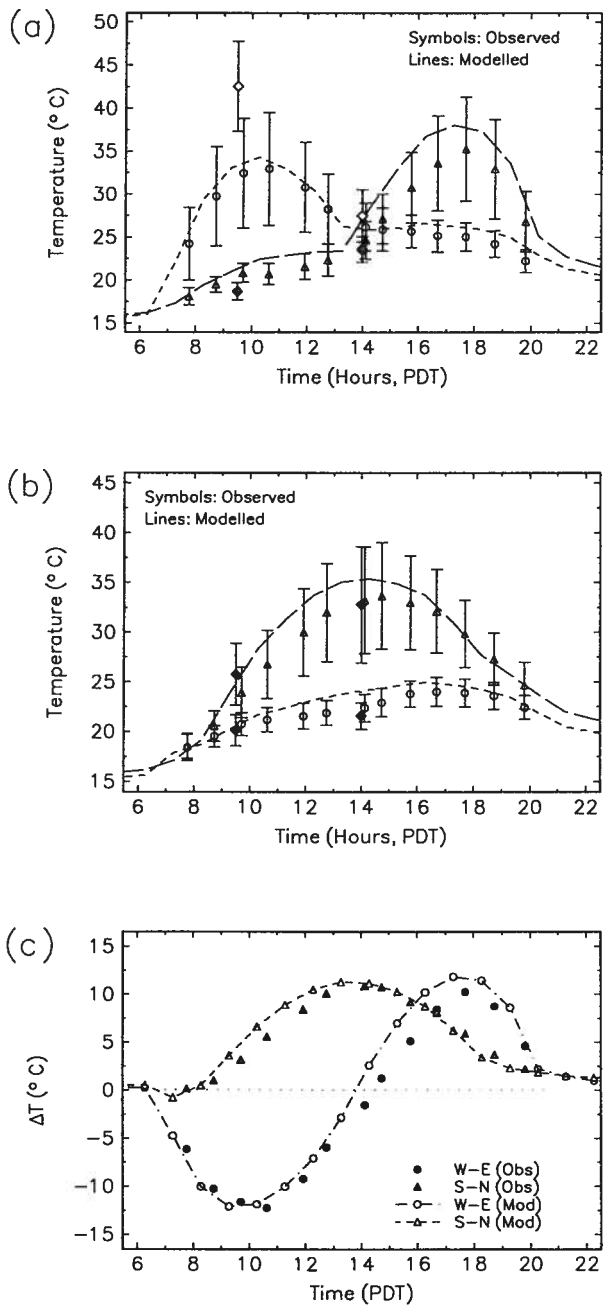

Figure 6.16: Comparison of modelled and traverse facet temperature for the Industrial study area. (a) east and west facets, (b) north and south facets, (c) facet pair differences.

daily input on modelled canyon facet temperatures and differences was examined for the Industrial study area (Figure 6.17). Differences between facets show an increase over those from the hourly modelled data, but it is not excessive, especially since the traverse data are probably biased on the low side for warm facets. Since the use of hourly air temperatures had a noticeable effect on the phase lag of the temperature curves, it was anticipated that the use of the mean daily data might also alter the temporal position of the maximum differences. The effect is relatively minor for the area tested. This improves confidence in the results when daily data are used.

Modelled temperatures for Downtown study areas replicate the observed pattern well but again modelled values are always higher (Figure 6.18). The observed temperatures are from the 30° EIRT, so as to obtain surface temperatures closer to the wall midpoint. A low bias in the traverse observations is more probable in this area because of the large H:W ratio and the shadows cast by tall buildings. Modelled facet-pair temperature differences agree well with those observed, although the morning peak occurs somewhat earlier in the model.

In the Residential area, comparison between modelled and observed temperatures is made more difficult by the presence of intervening vegetation which is not included in the canyon representation. The vegetation (in particular the street trees) shade the building walls and form a surface in themselves which is viewed by the EIRT. To accomodate this effect, the wet fraction and shaded fraction parameters of the Myrup model were employed. The wet fraction was set to 0.11 which is the fractional area of all vertical surfaces made up of trees (vertical plane projection of the model tree canopies). This assumes the trees were transpiring. Shadow fraction was calculated from a consideration of shading by street trees, roof overhangs and balconies. Simplistic representations were employed for the tree shading: a tree was considered to be a rectangle with a height

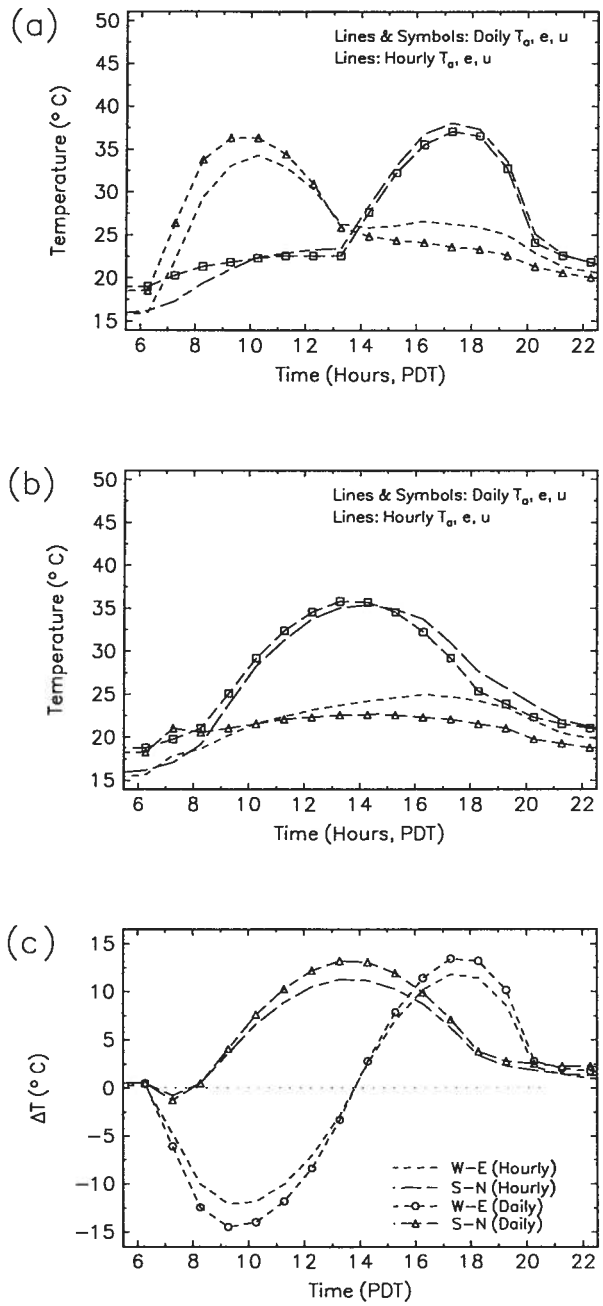

Figure 6.17: Comparison of modelled canyon facet temperatures obtained using hourly and daily input data (Industrial area).

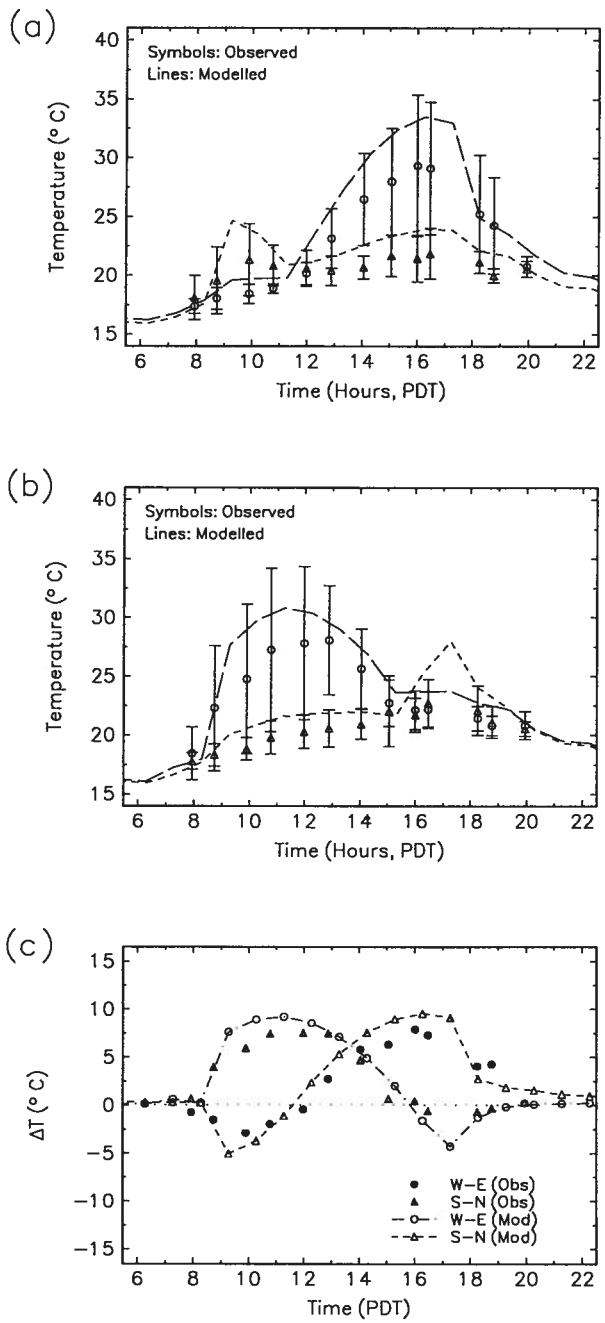

Figure 6.18: Comparison of modelled and traverse facet temperature for the Downtown study area. (a) northeast and southwest facets, (b) northwest and southeast facets, (c) facet pair differences.

equivalent to the mean tree height and an area equal to the mean projected tree (vertical plane) area, placed 10 m from the building. Shadow lengths and orientations were calculated for the daytime period. When shadows intersected the building wall plane the shaded area was calculated. These shadows are maximized at lower zenith angles (early and late in the day). Shading by roof overhangs (estimated as 0.45 m) and balconies (2.1 m; 37% of all buildings) is maximized at small zenith angles leading to an overall temporal shading fraction which exhibits a "W" shape (Figure 6.19).

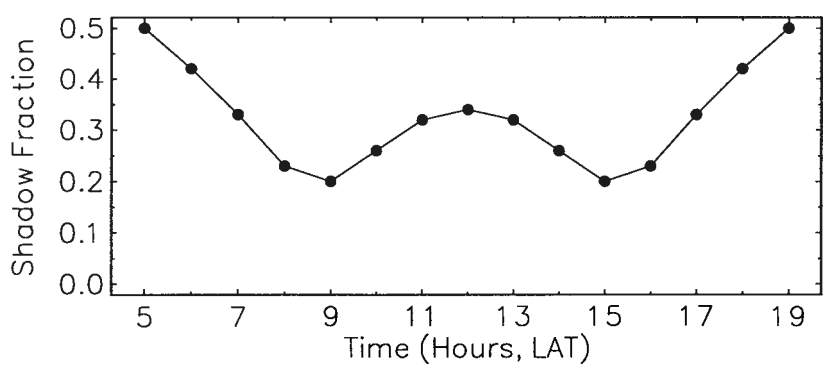

Figure 6.19: Estimated temporal variations of shadow ratio for vertical facets in the Residential area.

Model results for all facets show temperatures slightly above the mean observed traverse temperature (Figure 6.20). In most cases the differences between facet pairs cancel, yielding very good agreement between the observed and modelled temperature differences. An exception is the west-east difference in the afternoon when, because of warmer modelled west facet temperatures, the difference is greater than that observed. There are slight offsets in the timing of the maximum differences, with the modelled differences preceding the observed in each case.

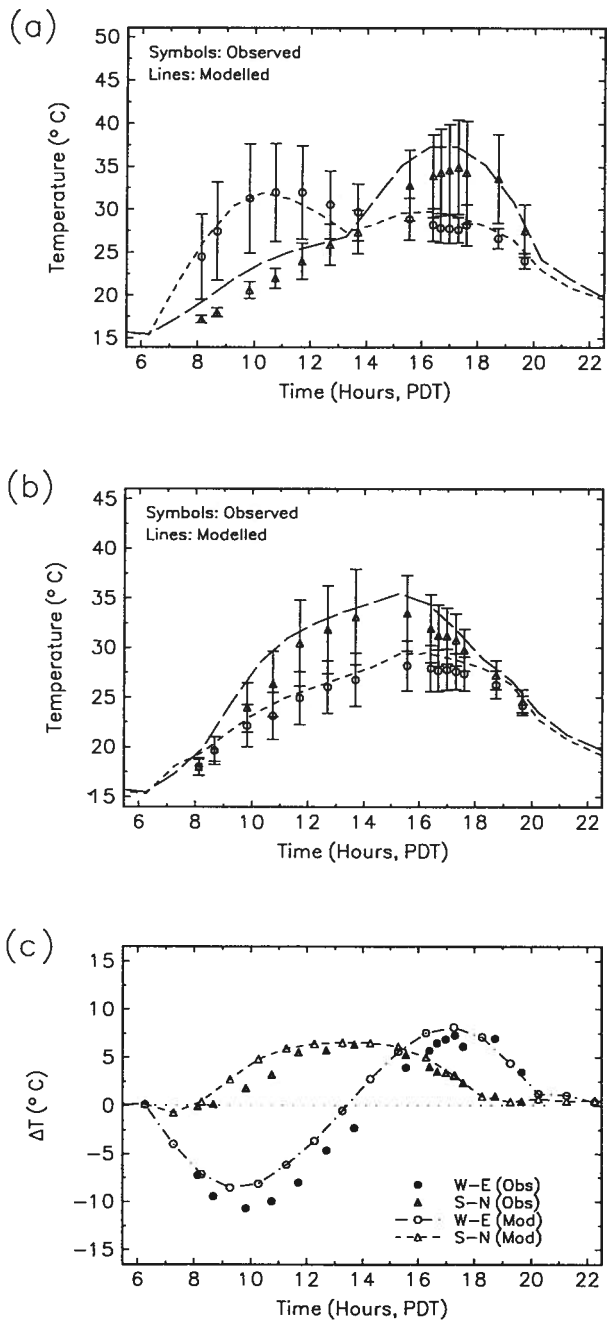

Figure 6.20: Comparison of modelled and traverse facet temperature for the Residential study area. (a) east and west facets, (b) north and south facets, (c) facet pair differences.

6.6 Summary

The modified Myrup model is able to correctly reproduce the form of surface temperature variations for canyon facet and road surface temperatures when local, hourly input data are available.

To achieve best results for surfaces exhibiting large diurnal temperature ranges, extremely low values of z_o are required, and, for roof surfaces, the magnitude of the night-time sensible heat flux has to be limited. Maximum surface temperature for many of the canyon surfaces (walls, roofs and roadways) was consistently modelled to occur before the time of the observed maximum. This effect was not present for the moist grass surface. The exact cause of this effect is not known but may be due to one or several of:

- layering effects in the substrate or wall materials (especially the low effective thermal admittance of hollow buildings, Goward (1981));
- a slight occurrence of surface moisture (e.g., from dewfall) in the morning;
- local shading effects.

Excellent agreement between measured and modelled K↓ would appear to preclude the third effect. Because the largest phase shifts were observed for a roof and building, and because dewfall is not commonly noted on vertical facets (Richards, *pers. comm.*) it is suspected that layering effects are the most probable cause for the phase shift.

Temperature differences derived from modelled surface temperatures between canyon facets agree very well with observed results; the phase shift evident in individual facets is reduced in the difference results. The use of mean daily input conditions overestimates the hourly modelled and observed results slightly, but given the low bias in the observed results, is not considered to be unduly large. In view of the simplistic nature of the Myrup

model and the limited canyon effects incorporated, the results obtained are considered to form a good basis for the surface temperature input requirements of SC.

6.7 Application of the SC Model

6.7.1 Application to the Study Areas: Overflight Days

This section presents results using the SC model with input data selected to represent the conditions present during the times of the remote sensing overflights. Surface structural parameters H, B_L, W_a, and W_s have been estimated from the surface structural database (Chapter 5). Surface parameters for the study areas are presented in Table 6.8. Example two-dimensional surface profiles derived from the surface structural database for each of the study areas as well as a graphic representation of the two-dimensional surface structure are presented in Figures in the subsequent subsections (Figures 6.24, 6.21, and 6.27).

Table 6.8: SC model surface parameters for the Study areas.

Parameter	Units	Industrial	Downtown	Residential
Canyon Azimuth	(°)	90	45/135	0
Sensor Azimuth	(°)	N,S	NW/SE, NE/SW	E/W
H	m	7.3	35	5.5
B_L	m	32.5	30	23.8
W_S	m	22.0	22	32.5
W_A	m	12.0	30	18.8
h_s	m	5000	5000	5000
IFOV	degrees	12	12	12
YD		228	229	230

Surface temperatures may be obtained using vehicle traverse data, remotely-sensed

imagery (image-extracted distributions), or modelled temperatures. In the results which follow, image-extracted temperatures were used when available, supplemented where required with vehicle traverse temperatures. When a wall or roadway is partially shaded, temperatures for the sunlit and shaded components may be estimated from the mixed-distribution modelling results of Chapter 3. Tests of the use of mean values versus frequency distributions yielded differences generally less than 0.2°.

6.7.1.1 Downtown

Surface structural parameters in the Downtown study area are difficult to estimate because of the wide range of building heights. In the NE portion of the study area, building heights are more nearly equal and a symmetrical block structure exists with generally two large buildings per block, separated by a narrow alleyway (Figure 6.21) which better matches the capabilities of the SC surface representation (Figure 6.21c).

The symmetry in the block structure allows all four view directions to be tested. Input conditions for the SC Model were set to match those observed during Flight 4. At this time both SE and SW facets were directly irradiated (although the SW facets were just beginning to warm following direct solar exposure).

Model estimates of proportions of the FOV occupied by the component surfaces are presented in Figure 6.22. As the off-nadir view angle increases, wall areas increase and ground area decreases; for angles greater than 40° the fraction of ground viewed is 0 for the input surface conditions. When viewing in the NW direction, there is a slight increase then decrease of shaded wall which is due to projected shadows on the viewed wall which are initially seen at small off-nadir angles and then become obscured as the view angle increases.

Modelled temperatures detected by the sensor for view angles from 0-60° (including the mean observed 45° off-nadir T_r) are shown in Figure 6.23. In the view direction

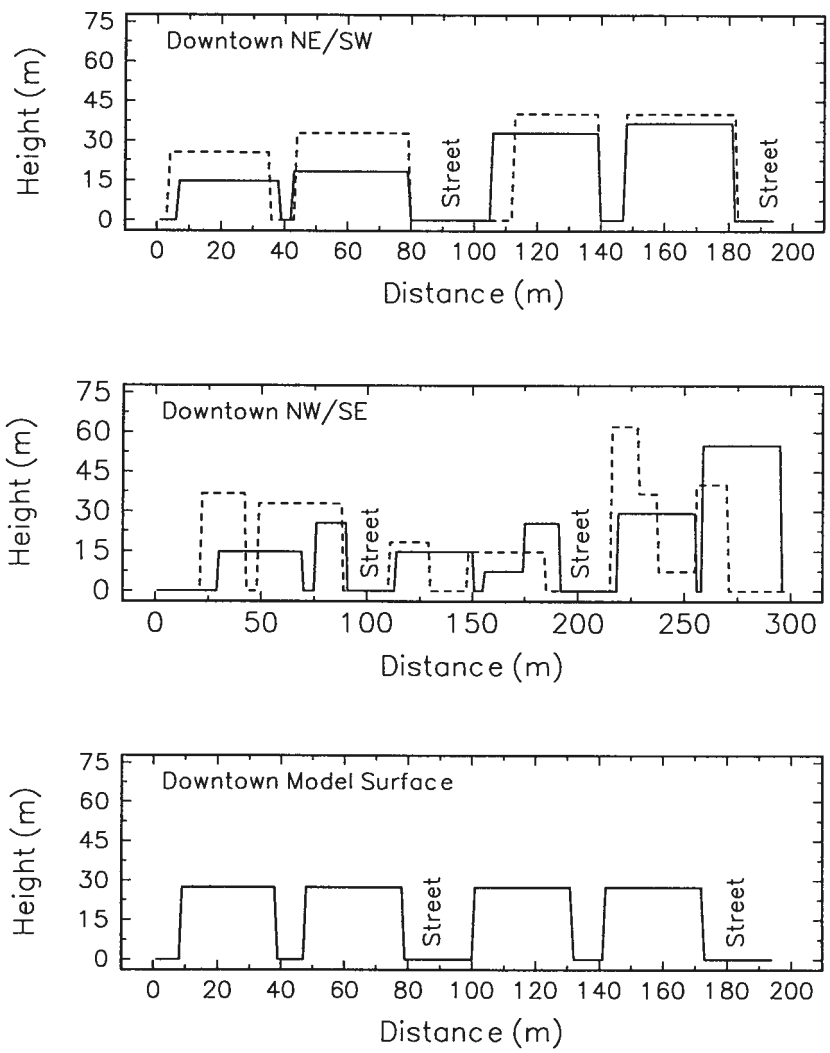

Figure 6.21: Surface profiles for the NE portion of the Downtown study area. (a) and (b) are example profiles extracted from the surface database in the NE/SW and NW/SE directions respectively. Solid and dashed lines represent two separate profiles. (c) is the surface profile defined by W_s=22, W_a=10, H=27.5, B_L=30 used in the SC model.

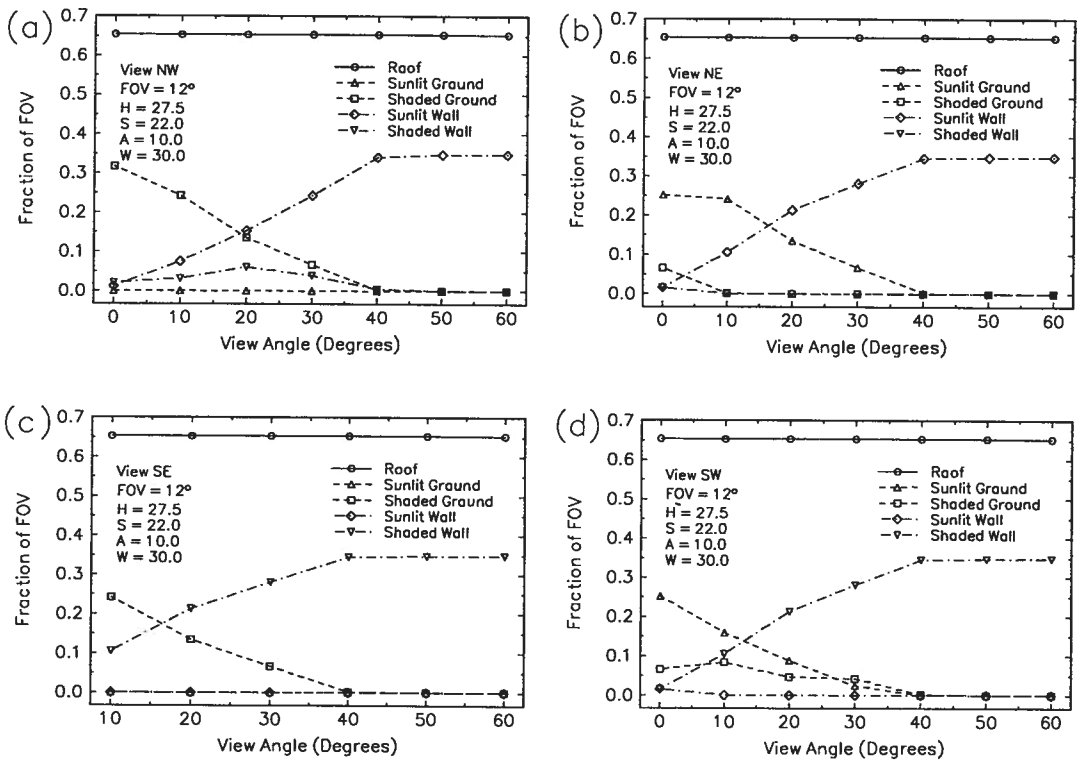

Figure 6.22: Surface proportions viewed: Downtown, Flight 4. View directions are: (a) NW, (b) NE, (c) SE, (d) SW.

(NW) of the most directly irradiated (and warmest) facet, increasing off-nadir view angles result in constantly increasing apparent temperature registered by the sensor up to approximately 40° after which the fractional FOV occupied by the wall changes only slightly. For the NE and SW view directions, the modelled sensor temperature decreases slightly with increasing view angle due to the replacement of sunlit ground surfaces with shaded wall surfaces. In the SE view direction, only minor changes in temperature with view angle are obtained. This arises because both the NW canyon facet and the entire canyon floor are shaded, and approximately equal in temperature.

The model overestimates the apparent surface temperature within the sensor FOV for all view directions. Differences are slightly greater for the shaded facets compared to the irradiated. Nadir temperatures differ between the two canyon orientations, an artifact of the two-dimensional surface representation. Modelled nadir temperature is significantly warmer than observed, particularly that associated with the NW and SE view directions (NE/SW street canyons). This occurs because these street canyons have relatively little shade at this time; the solar azimuth is very nearly aligned with the canyon axis, and the model does not take into consideration the cross-streets (completely shaded; Figure 6.22). Despite the large differences in observed and modelled temperature, the model does replicate the order of temperatures between the different view directions (i.e., NW view direction is warmest, followed by nadir, and the rest are very close in temperature; compare with Figure 1.34). The magnitude of the 45° off-nadir temperature differences with view direction are also fairly well represented.

6.7.1.2 Industrial

The Industrial study area was selected in part because of the relatively simple nature of the surface (box-like buildings, lack of vegetation). In several of the blocks, buildings, or sequences of buildings, extend the entire length of the block (Figure 5.4) which provides

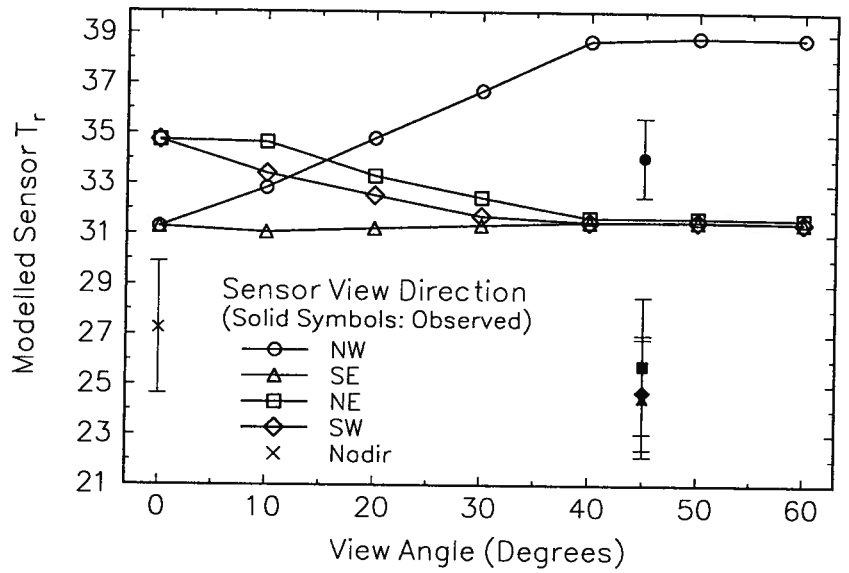

Figure 6.23: Variation of the modelled AGEMA scanner temperature for Flight 4 with view angle over the Downtown study area.

the long canyon structure assumed by the SC model. The surface structure across the building row direction (N/S) is well represented by the parameters H, B_L, W_s, and W_a (Figure 6.24).

In the E/W direction, along the building rows, the model is less able to replicate the combination of small, nonregularly occuring inter-building spacing and unequal building heights. The results which follow are restricted to the N/S view azimuths across the canyon structure.

Modelled apparent surface temperatures for the 12° FOV for north and south view directions over the model Industrial surface at 1030 PDT are presented in Figure 6.25. The mean apparent surface temperatures obtained from the nadir and 45° off-nadir flight lines over the study area are again included for comparison.

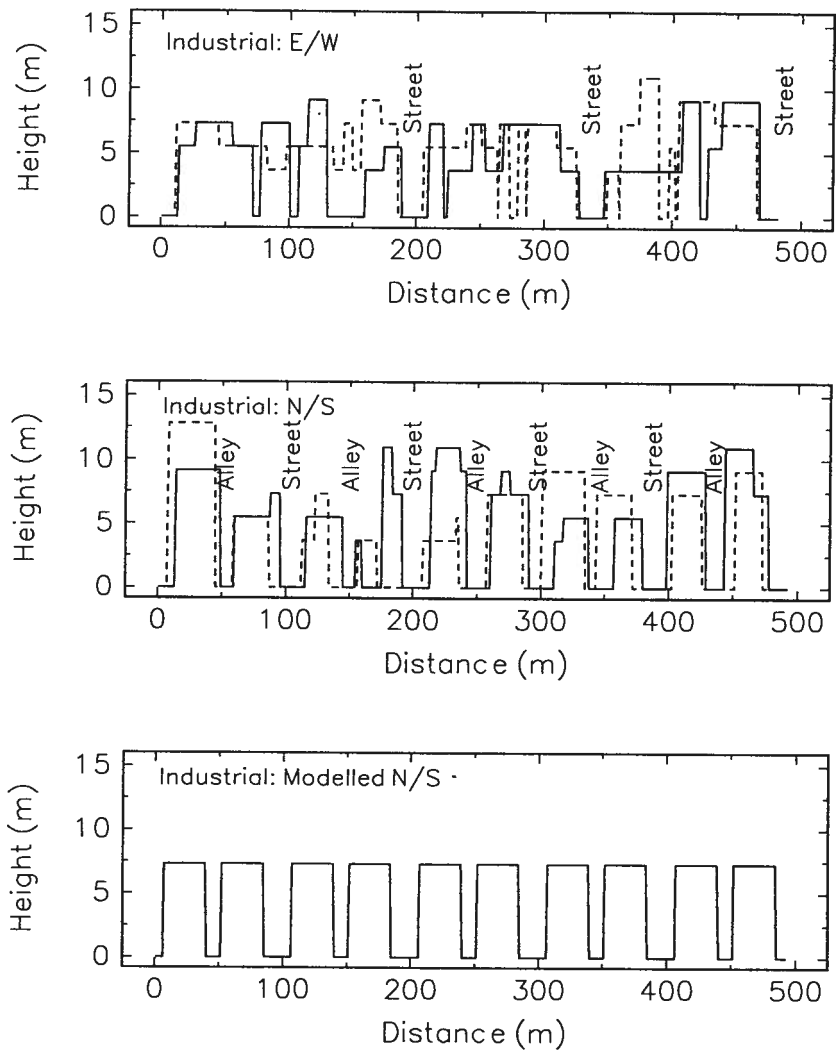

Figure 6.24: Surface profiles for the Industrial study area. (a) and (b) are example profiles extracted from the surface database in the E/W and N/S directions respectively. Solid and dashed lines represent two separate profiles. (c) is the surface profile defined by W_s=22, W_a=12, H=7.3, B_L=32.5 used in the SC model.

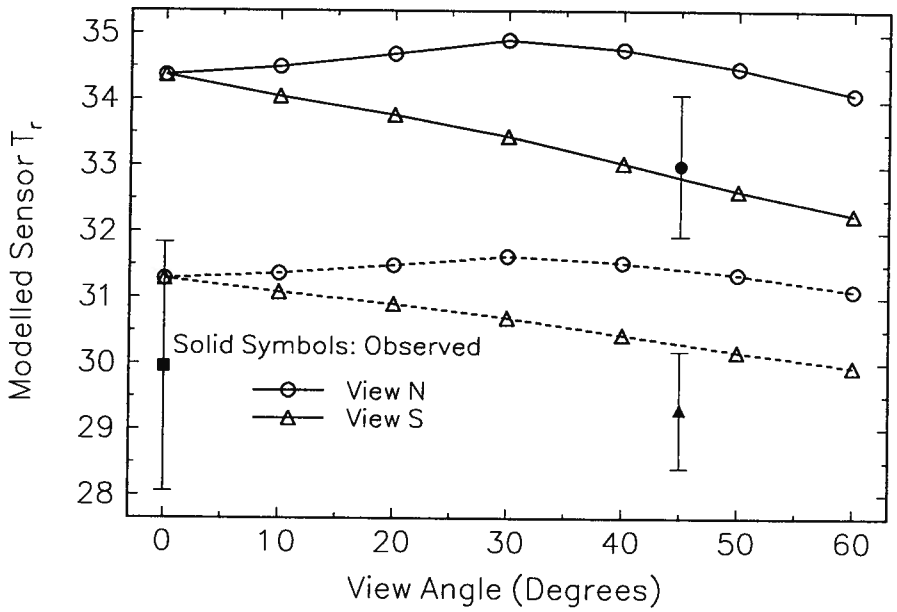

Figure 6.25: Variation of the modelled temperature seen by the AGEMA scanner with view angle in north and south view directions for Flight 1 over the Industrial study area for (solid line) original SC model output, (dashed line) including along-canyon interbuilding spacing and cross-streets (spacing between blocks).

In the morning, the temperature contrast between north and south facets is still developing and has yet to reach its maximum value. Off-nadir observations in the north view direction show a slight increase in apparent temperature as the shaded ground surfaces are obscured and replaced by sunlit road and wall surfaces. At angles greater than 30° the apparent temperature begins to decreases because the wall surface is cooler than the sunlit road. The south view direction shows an almost linear decrease in temperature as shaded surfaces occupy greater proportions of the FOV.

The dashed lines of Figure 6.25 test the effect of incorporating extra "ground" surfaces to represent cross-streets and inter-building spacing. These ground areas were estimated for the study area and divided into sunlit and shaded portions based upon projected shadows for the mean building height (58% sunlit, 42% shaded). The incorporation of

the extra ground surface has the overall effect of increasing the shaded area and reducing all temperatures. It also reduces the off-nadir differences with view angle and between view directions because there is a smaller proportion of wall area. Compared to the observed temperatures, the original model (which assigns all ground surfaces to road surface temperature), yields much warmer apparent surface temperature estimates. The differences are greater for the south view direction (which "sees" more shaded surfaces". The addition of the extra ground surface provides a better estimate of the nadir temperature and cooler off-nadir temperature, but now under predicts the warmest off-nadir temperature.

Model results for Flight 2 over the Industrial area (Figure 6.26 show a similar pattern to those described for Flight 1 with an enhancement of both the off-nadir and directional differences due to the greater wall temperature difference at this time. Agreement between observed and modelled values is improved over that of Flight 1 without modification of the model. At this time, shadows are largely confined to the E/W streets represented by the model, and open areas are approaching roof temperature so that the neglect of these surface components in the two-dimensional model is of less importance. The difference between observed and modelled temperatures is clearly greater when viewing shaded surfaces, and this may be an indication of the importance of small scale surface structure, not represented by the model. When viewing the "real" surface in the direction of the irradiated facet, microscale surface structure has no effect upon the sensor temperature because shadows are not viewed. However, when neglecting small scale surface structure (e.g., elevator shaft housings, balconies, roof vents in the up-Sun direction), all their shaded areas are neglected and lead to an overestimate of the modelled temperature.

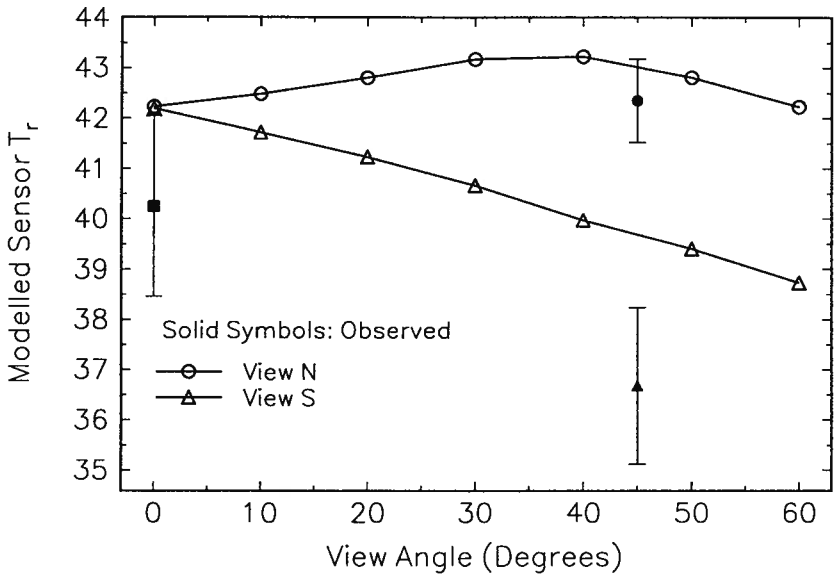

Figure 6.26: Variation of the modelled temperature seen by the AGEMA scanner with view angle in north and south view directions for Flight 2 over the Industrial study area.

6.7.1.3 Residential

The Residential study area is the most difficult surface structure to replicate in the SC model due to the inability of the model to handle trees or sloping roof surfaces. As with the Industrial area, the model has been applied only to view directions orthogonal to the block axis; in the study area subset, the block long axis is oriented N/S so only E/W view directions are considered here. Surface profiles extracted from the surface database and the modelled surface profile are presented in Figure 6.27.

Note that the presence of garages cannot be included in the model surface; in some cases these buildings form a second canyon bordering the alley, although their occurrence is more irregular than that of the buildings. The effective width of the building in the surface model has been increased slightly to account for the width (roof area) of the garages, but their wall area and the increase in ground shading due to their presence is

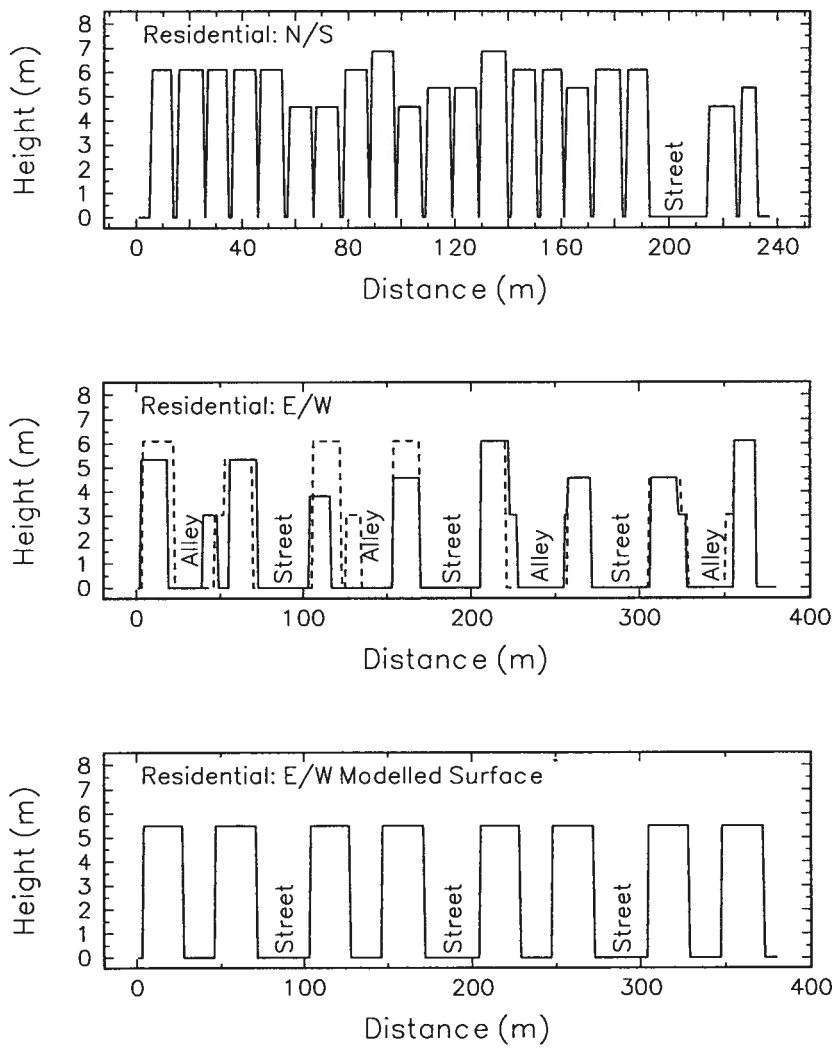

Figure 6.27: Surface profiles for the Residential study area. (a) and (b) are example profiles extracted from the surface database in the N/S and E/W directions respectively. Solid and dashed lines represent two separate profiles. (c) is the surface profile defined by W_s=32.5, W_a=18.8, H=5.5, B_L=23.8 used in the SC model.

not accounted for.

The SC model was run for conditions representative of Flights 6 (0945 PDT) and 7 (1400 PDT) (Figures 6.28 and 6.28). For each run, the canyons were considered to be both inifinitely long (solid lines in Figures 6.28 and 6.29) and to include additional ground surfaces representing the inter-building and street spacing along the block (dashed lines). Because of the extensive vegetated surface area in the residential area, the fractional FOV occupied by sunlit and shaded ground is further subdivided into paved and vegetated surfaces, each of which were assigned temperatures derived from the remotely sensed imagery.

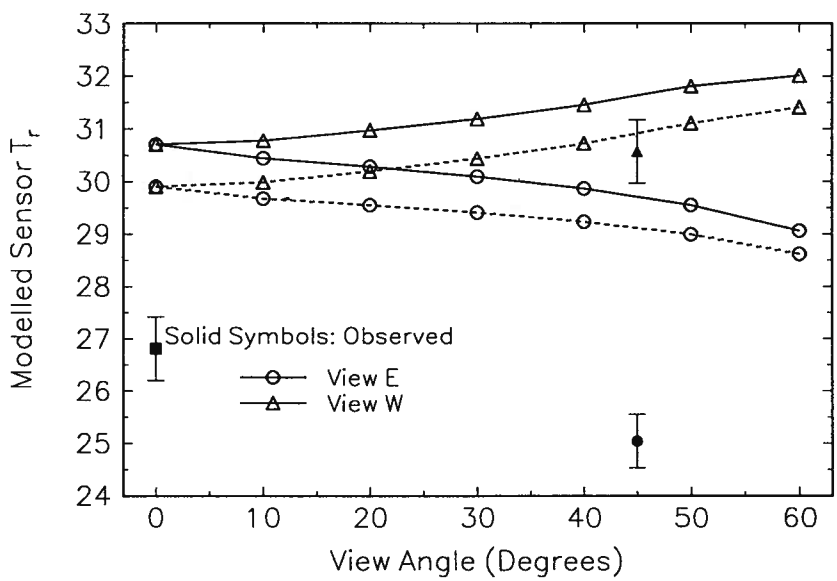

Figure 6.28: Variation of the modelled temperature seen by the AGEMA scanner with view angle in east and west view directions for Flight 6 over the Residential study area.

Results for conditions representing Flight 6 (Figure 6.28) show the apparent temperature seen by the sensor decreases with increasing view angle for the east view direction, and to increase by an approximately equal amount for the west view direction. Including

the extra open ground has the same effects as discussed for Flight 1. Nadir and east view direction temperatures are substantially warmer than observed, while the west view direction difference is much less.

A further difficulty in this area is the large number of trees which are not included in the surface representation. Shading by trees is one possible factor which can account for the much greater difference between observed and modelled temperatures in the direction of the shaded facet: in this direction both the cool side of the tree canopy as well as the shadow cast by the tree are visible and contrast with sunlit ground surfaces whereas,in the down-Sun direction, the shaded area can be wholly or partially obscured by the canopy, depending upon the particular Sun-surface-sensor geometry.

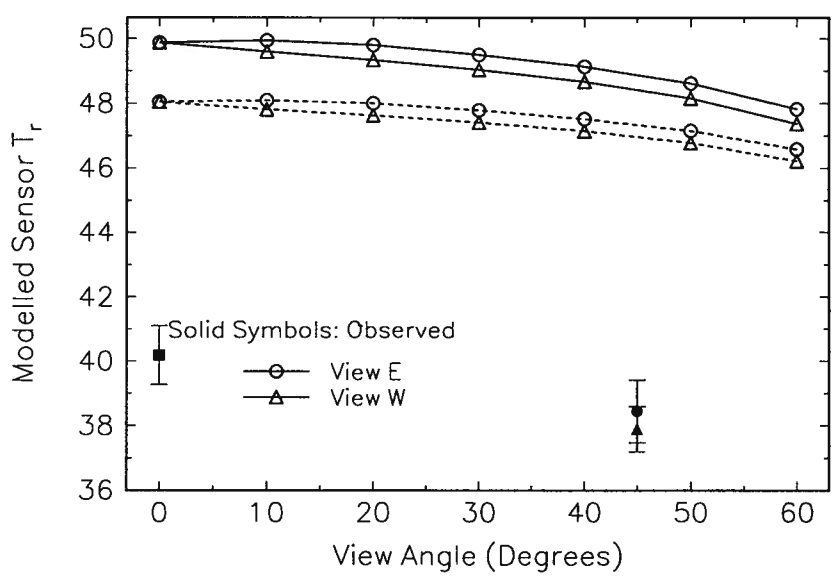

Figure 6.29: Variation of the modelled AGEMA scanner temperature with view angle in east and west view directions for Flight 7 over the Residential study area.

Off-nadir variations with view angle are only minor for the model results from Flight 7. Both view directions show a slight decrease of apparent temperature seen by the sensor

with off-nadir viewing angle. These are not unexpected given that the temperatures of the canyon walls are approximately equal at this time. The difference between observed and modelled temperatures are again large but the relative difference between view directions and between the nadir and 45° off-nadir viewing angles is reproduced well by the model.

6.7.2 Summary

A slightly modifed version of the Sobrino and Casselles (1990) model was run using input data representative of the across-block surface structure in the three study areas. Results were compared with the nadir and 45° off-nadir mean apparent surface temperatures obtained from the helicopter-mounted scanner. Large differences exist between observed and modelled results. These are attributed to the two-dimensional surface representation employed by the model, the simplistic representation of the surface structure (and omission of important elements such as trees from the surface model), and to biases in the image-extracted component temperatures. The model performs best when the solar azimuth is orthogonal to the canyon azimuth so that shadows are confined to the view direction of the sensor. Despite the large modelled-observed differences in temperature, the model does correctly portray the relative difference of facet temperatures with view direction and appears to replicate the pattern of temperature change with increasing off-nadir angle, although this conclusion is limited by the lack of other observed off-nadir angle data.

Chapter 7

CONCLUSIONS

The overall objective of this thesis was to investigate how the three-dimensional form of the urban surface affects observations of radiative surface temperature made by thermal infra-red remote sensors. The thesis is observationally based and employs a unique combination of sensor platforms in an effort to fully define the temperature of the complete urban surface. This approach has allowed the detailed examination of both the anisotropic emissions from selected urban land use areas, and the creation of a database from which estimates of the complete urban surface temperature can be made. These objectives would be difficult and/or prohibitively expensive to obtain using more conventional (i.e. satellite- or aircraft-based remote sensors).

7.1 Summary of Conclusions

Individual chapters provided detailed summaries of findings. In view of the overall objectives outlined in Chapter 1, the main conclusions of this thesis may be described as:

- Distributions of vertical facet apparent surface temperature obtained from vehicle traverses demonstrated large variations with facet orientation and strong temporal variation, particularly of the directly irradiated facets. The spatial variations are conditioned by variations in building properties at the land use scale, and are also influenced by the amount of vegetation "seen" by the sensor. Temperature differences between facet pairs are greater than 10°C in the Industrial area and

slightly less in the Residential, with the largest difference occurring mid-morning between east and west facets. Other times of maximal temperature differences between facet pairs occur within approximately 1 hour after solar noon between north and south facets and in the late afternoon between east and west facets. In the Downtown area, the different street orientation yields one time period with a large facet temperature difference and a second where the differences are minor, with results showing a fairly high degree of symmetry. These differences are an important factor in the establishment of anisotropic surface emissions from urban areas. Spectral reflection by low emissivity surfaces may pose a problem in some land-use areas; the effect of such reflections depends upon the sensor location relative to the observed surface.

- The analysis of distributions is complicated by the presence of "mixed-pixel" observations because the FOV of the sensor allows portions of both sky and building to be seen. Distribution truncation and distribution modelling were investigated as potential ways of separating facet temperatures from mixed building-sky or sky observations. Distribution modelling allows separate component populations of temperatures to be recovered. It is shown to successfully discriminate shaded and sunlit temperature distributions on road surfaces. Results for walls are dependent upon the surface materials and radiation regime: small scale temperature variations (at the building scale, or smaller) of directly irradiated facets within the sensor IFOV leads to a distribution with a long "tail" of warmer temperatures which is not easily separable into component Normal populations.

- A simple model of the apparent surface temperature distributions created by moving a sensor FOV across a sequence of model buildings with specified temperature

distributions which are separated by gaps emitting at a specified sky radiant temperature, was shown to give qualitative agreement with observed distributions. More precise agreement may result with improvements in the representation of the surface structure.

- Frequency distributions of apparent surface temperature in each of the study areas obtained from an airborne thermal scanner reveal a characteristic bimodal shape with the lower peak related to shaded surfaces and the upper peak coinciding with sunlit road surface temperatures. The distribution is most strongly defined in the morning when differential heating of surfaces yields the greatest variation in temperature between surface types. Distributions from land use areas characterized by more "simple" surfaces (regular, block-like buildings, and lack of vegetation) lead to more sharply defined temperature distributions.

- Mixed distribution modelling techniques were applied to the remotely-sensed apparent surface temperature distributions and frequency distribution differences with the objective of recovering component surface temperature information. The best results were obtained using morning temperature frequency distributions from the Industrial area, which has the most strongly defined composite temperature frequency distribution. Sunlit road, roof, and shaded surface components were the most successfully extracted components. Vertical facet temperatures, and particularly the most directly irradiated facet, were more difficult to extract. This is not surprising given the wide range of building materials which exist within the study areas. Significant differences between traverse and image-extracted estimates of the most directly irradiated facet were noted, and are attributed to the observation methodologies employed, and possible spectral emissivity effects.

- Strong directional variations (anisotropy) of apparent urban surface temperature were observed over each of the study areas. Differences were greatest over the Downtown study area (> 9°C) and coincide with the time of maximum surface temperature differentiation between opposing canyon facets. Anisotropy varies with time and view direction depending upon the orientation of the surface and the solar geometry for that time of the year. Temperature differences due to anisotropy over urban surfaces are shown to be equal to or greater in magnitude than those which result from surface emissivity and atmospheric absorption/emission (depending upon the Sun-sensor-surface geometry). This emphasizes the importance of including a consideration of anisotropy when using thermal remotely-sensed imagery over urban areas.

- Complete surface temperatures which attempt to combine temperatures of all the major surface orientations present in the study areas, have been estimated for the first time. Frequency distributions show an enhancement of low temperatures which yield mean values close to the coolest observed off-nadir apparent surface temperature. This suggests that, where available, off-nadir thermal imagery in the direction of the coolest (most shaded) facet may be the most representative remotely-sensed temperature to use where a temperature representative of the entire urban surface is desired. This approximation appears to be least valid at mid-day.

- Geometric projection models are advanced as a possible means of extending the observational results of anisotropic surface emissions to other times, locations and view angles. A simple two-dimensional model (based upon the work of Caselles *et al.* (1992) and Sobrino and Caselles (1990), and slightly modified to better represent the study area surface profiles in the across-block view direction), was applied to the study areas and compared with observed results. The model is able

to replicate the order of temperatures in different view-directions, but shows large differences from the airborne scanner results in the direction of shaded facets. The model performance is limited by the two-dimensional surface assumption which is not representative of most urban land use areas.

- A simple one-dimensional energy balance model was modified to incorporate canyon radiative effects and allow representation of vertical facets for the purpose of estimating temperatures of canyon surfaces in geometric projection models or to allow estimates of complete surface temperature in combination with the building databases for each of the study areas. The model performed reasonably well for a range of surface types, considering its simplicity. More recent models, incorporating a layered sub-surface, and better surface-air temperature feedback are advocated for future work.

7.2 Suggestions for Future Work

The results of this thesis have indicated the potential for further research in a number of areas.

The most important and direct extension of the current work is the development and application of a geometrical sensor-surface model which would incorporate a three-dimensional urban surface representation as well as solid angle sensor geometry. When coupled with a surface energy balance model, the extent of anisotropy over a range of surface geometries, locations and times could be investigated.

In conjunction with the development of a three-dimensional model, several other improvements are suggested including:

- Application of more recent and realistic canyon energy balance models (e.g., Mills, 1993) to better characterize the component surface temperatures.

- Addition of building material data at the same scale as the building height database. This would allow the identification of typical surface material combinations for use in temperature modelling, as well as providing a link between the observed temperatures and building properties.

- Incorporation of solar geometry/shading routines to the building database to define three-dimensional surficial shading patterns. When coupled with temperature estimates from energy balance models, this would allow complete surface temperature estimates to be modelled for the surface geometries characteristic of the study areas.

Complete surface temperatures have been estimated for urban surfaces for the first time. They form a new temperature which has not been directly confirmed observationally. Pyrgeometers or other wide FOV instruments capable of viewing vertical as well as horizontal surfaces should be tested over urban surfaces to determine if these provide a better representation of complete urban surface temperature than do narrow FOV remote sensors. It is also recommended that the feasibility of estimating the complete surface temperature using component surface temperatures from a few selected surfaces be investigated. Complete surface temperatures also need to be examined in relation to the surface energy balance.

Further work is also suggested on the utility of the mixed distribution modelling technique as applied to the identification of component surface temperatures at various scales. The simple model used to explore the form of surface temperature distributions measured by the traverse vehicle should be further investigated to determine if it can be inverted and used to separate building and mixed-building and sky temperatures.

The current work has clearly identified the presence of strong anisotropic emissions over urban areas at the land use scale. The extent to which it is present in current

and past operational remote sensors (primarily satellites) should be investigated and compared with the present observations. The extension of modelling will also aid in this analysis.

References

[1] AGEMA Infrared Systems 1991: *AGEMA Operator's Manual.* AGEMA Infrared Systems AB, Danderyd, Sweden.

[2] Arnfield, A.J. 1982: An approach to the estimation of the surface radiative properties and radiation budgets of cities. *Phys. Geog.* **3**, 97-122.

[3] Artis, D.A. and Carnahan, W.H. 1982: Survey of emissivity variability in thermography of urban areas. *Rem. Sens. Environ.* **12**, 313-329.

[4] Arya, P. 1988: *Introduction to Micrometeorology.* Academic Press: New York.

[5] ASHRAE 1989: *ASHRAE Handbook.* American Society of Heating, Refrigerating and Air-Conditioning Engineers Inc. Atlanta, Ga.

[6] Balick, L.K. and Wilson, S.K. 1980: Appearance of irregular tree canopies in night-time high-resolution thermal infrared imagery. *Rem. Sens. Environ.* **10**, 299-305.

[7] Balick, L.K. and Hutchison, B.A. 1986: Directional thermal infrared exitance distributions from a leafless deciduous forest. *IEEE Trans. Geosci. Rem. Sens.* **GE-24**, 693-698.

[8] Balick, L.K., Hutchison, B.A., Smith, J.A., and McGuire, M.J. 1987: Directional thermal infrared exitance distributions of a deciduous forest in summer. *IEEE Trans. Geosci. Rem. Sens.* **GE-25**, 410-412.

[9] Balling, R.C. Jr. and Brazel, S.W. 1988: High-resolution surface temperature patterns in a complex terrain. *Photogram. Eng. Rem. Sens.* **54**, 1289-1293.

[10] Barber, E.S. 1957: Calculation of maximum pavement temperature from weather reports *HRB Bull.* **168**, 1-8.

[11] Bärring, L., Mattsson, J.O., and Lindqvist, S. 1985: Canyon geometry, street temperatures and the urban heat island in Malmö, Sweden. *Journal of Climatology* **5**, 433-444.

[12] Becker, F. and Raffy, M. 1987: Problems related to the determination of land surface parameters and fluxes over heterogeneous media from satellite data. *Adv. Space Res.* **7**, 45-57.

[13] Becker, F. and Li, Z.-L. 1990: Towards a local split window method over land surfaces. *Int. J. Rem. Sens.* **11**, 369-393.

[14] Birnie, R.V., Ritchie, P.F.S., Stove, G.C. and Adams, M.J. 1984: Thermal infrared survey of Aberdeen City: data processing, analysis and interpretation. *Int. J. Rem. Sens.* **5**, 47-63.

[15] Boissard, P., Guyot, G., and Jackson, R.D. 1990: Factors affecting the radiative temperature of a vegetative canopy. In: *Applications of Remote Sensing in Agriculture*, Steven, M.D. and Clark, J.A. (eds.) Butterworths, London, 45-72.

[16] Byrnes, A.E. and Schott, J.R. 1986: Correction of thermal imagery for atmospheric effects using aircraft measurements and atmospheric modeling techniques. *Appl. Opt.* **25**, 2563-2570.

[17] Callison, R.D., Blake, P. and Anderson, J.M. 1987: The quantitative use of Airborne Thematic Mapper thermal infrared data. *Int. J. Rem. Sens.* **8**, 113-126.

[18] Campbell, G.S. and Norman, J.M. 1989: The description and measurement of plant canopy structure. In: *Plant Canopies: Their Growth, Form and Function*, Russell, G., Marshall, B., and Jarvis, P.G. (eds.) Cambridge University Press, pp.1-19.

[19] Carlson, T.N., Augustine, J.A. and Boland, F.E. 1977: Potential application of satellite temperature measurements in the analysis of land use over urban areas. *Bull. Amer. Meteorol. Soc.* **58**, 1301-1303.

[20] Carlson, T.N., Dodd, J.K., Benjamin, S.G. and Cooper, J.M. 1981: Satellite estimation of the surface energy balance, moisture availability and thermal inertia. *J. Appl. Meteorol.* **20**, 67-87.

[21] Caselles, V., Sobrino, J.A., and Becker, F. 1988: Determination of the effective emissivity and temperature under vertical observation of a citrus orchard. Application to frost nowcasting. *Int. J. Rem. Sens.* **9**, 715-727.

[22] Caselles, V. and Sobrino, J.A. 1989: Determination of frost in orange groves from NOAA-9 AVHRR data. *Rem. Sens. Environ.* **29**, 135-146.

[23] Caselles, V., Sobrino, J.A., and Coll, C. 1992: A physical model for interpreting the land surface temperature obtained by remote sensors over incomplete canopies. *Remote Sens. Environ.* **39**, 203-211.

[24] Charles-Edwards, D.A. and Thornley, J.H.M. 1973: Light-interception by an isolated plant: A simple model. *Ann. Bot.* **37**, 919-928.

[25] Chen, J.-M. and Zhang, R.-H. 1989: Studies on the measurements of crop emissivity and sky temperature. *Agric. Forest Meteorol.* **49**, 23-34.

[26] Chen, S.G. Impens, I., Ceulemans, R., and Kockelbergh, F. 1993: Measurement of gap fraction of fractal generated canopies using digitalized image analysis. *Agric. Forest Met.* **65**, 245-259.

[27] Choudhury, B.J. 1989: Estimating evaporation and carbon assimilation using infrared temperature data: vistas in modeling. In: *Theory and Applications of Optical Remote Sensing.* Asrar, G. (ed.), J. Wiley and Sons Ltd, New York. pp. 628-690.

[28] Cooper, K. and Smith, J.A. 1985: A Monte Carlo reflectance model for soil surfaces with three-dimensional structure. *IEEE Trans. Geosci. Remote Sens.* **GE-23**, 668-673.

[29] Cox, C. and Munk, W. 1954: Measurements of the roughness of the sea surface from photographs of the sun glitter. *J. Opt. Soc. Amer.* **44**, 838-850.

[30] Cracknell, A.P. 1993: A method for the correction of sea surface temperatures derived from satellite thermal infrared data in an area of sunglint. *Int. J. Rem. Sens.* **14**, 3-8.

[31] Crosby, D.S. and Glasser, K.S. 1978: Radiance estimates from truncated observations. *J. Appl. Met.* **27**, 1712-1715.

[32] Davies, J.A., Robinson, J., and Nunez, M. 1971: Field determinations of surface emissivity and temperature for Lake Ontario. *J. Appl. Met.* **10**, 811-819.

[33] Desjardins, R., Gray, J. and Bonn, F. 1990: Atmospheric corrections for remotely-sensed thermal data in a cool humid temperate zone. *Int. J. Rem. Sens.* **11**, 1369-1389.

[34] Dousset, B. 1989: AVHRR-derived cloudiness and surface temperature patterns over the Los Angeles area and their relationships to land use. Proceedings of IGARSS-89, 2132-2137.

[35] Dozier, J. 1981: A method of satellite identification of surface temperature fields of subpixel resolution. *Rem. Sens. Env.* **11**, 221-229.

[36] Duggin, M.J. and Saunders, R.W. 1984: Problems encountered in remote sensing of land and ocean surface features. In: *Satellite Sensing of a Cloudy Atmosphere.* Henderson-Sellers, A. (ed.). Taylor and Francis: London, pp. 241-287.

[37] Dutton, E.G. 1993: An extended comparison between LOWTRAN 7 computed and observed broadband thermal irradiances: Global extreme and intermediate surface conditions. *J. Atmos. Ocean. Tech.* **10**, 326-336.

[38] Eliasson, I. 1991: Urban geometry, surface temperature and air temperature. *Energy and Buildings* **15-16**, 141-145.

[39] Eliasson, I. 1992: Infrared thermography and urban temperature patterns. *Int. J. Rem. Sens.* **13**, 869-879.

[40] Elliott, W.P. and Gaffen, D.J. 1991: On the utility of radiosonde humidity archives for climate studies. *Bull. Amer. Met. Soc.* **72**, 1507-1520.

[41] Everest Interscience 1991: *Model 4000A Infrared Temperature Transducer Operating Manual.* Everest Interscience: Fullerton, CA.

[42] Forsythe, G.E., Malcom, M.A., and Moler, C.B. 1977: *Computer Methods for Mathematical Computation*, Prentice-Hall Inc., Englewood Cliffs, N.J.

[43] Foster, J.L., Ormsby, J.P., and Gurney, R.J. 1981: Satellite observations of England and North-Western Europe. *Weather* **36**, 252-259.

[44] Fuchs, M., Kanemasu, E.T., Kerr, J.P., and Tanner, C.B. 1967: Effect of viewing angle on canopy temperature measurements with infrared thermometers. *Agron. J.* **59**, 494-496.

[45] Gallo, K.P., McNab, A.L., Karl, T.R., Brown, J.F., Hood, J.J. and Tarpley, J.D. 1993: The use of a vegetation index for assessment of the urban heat island effect. *Int. J. Rem. Sens.* **14**, 2223-2230.

[46] Garand, L., Grassotti, C., Halé, J. and Klein, G.L. 1992: On differences in radiosonde humidity reporting practices and their implications for numerical weather prediction and remote sensing. *Bull. Amer. Met. Soc.* **73**, 1417-1423.

[47] Gates, D.M. 1962: *Energy Exchange in the Biosphere.* Harper and Row: New York.

[48] Goel, N.S. 1988: Models of vegetation canopy reflectance and their use in estimation of biophysical parameters from reflectance data. *Remote Sensing Rev.* **4**, 1-212.

[49] Goldreich, Y. 1985: The structure of the ground-level heat island in a central business district. *J. Clim. Appl. Met.* **24**, 1237-1244.

[50] Goward, S.N. 1981: Thermal behaviour of urban landscapes and the urban heat island. *Phys. Geog.* **2**, 19-33.

[51] Griggs, M. 1968: Emissivities of natural surfaces in the 8 to 14 micron spectral region. *J. Geophys. Res.* **73**, 7545-7551.

[52] Grimmond, C.S.B. 1988: An evaporation-interception model for urban areas. Unpubl. Ph.D. Thesis, The University of British Columbia, Vancouver, B.C.

[53] Gustavsson, T. and Bogren, J. 1991: Infrared thermography in applied road climatological studies. *Int. J. Rem. Sens.* **12**, 1811-1828.

[54] Henry, J.A., Dicks, S.E., Wetterqvist, O.F., and Roguski, S.J. 1989: Comparison of satellite, ground-based, and modeling techniques for analyzing the urban heat island. *Photogram. Eng. Rem. Sens.* **55**, 69-76.

[55] Holbo, H.R. and Luvall, J.C. 1989: Modelling surface temperature distributions in forest landscapes. *Rem. Sens. Environ.* **27**, 11-24.

[56] Hook, S.J., Gablell, A.R., Green, A.A., and Kealy, P.S. 1992: A comparison of techniques for extracting emissivity information from thermal infrared data for geologic studies. *Rem. Sens. Environ.* **42**, 123-135.

[57] Hoyano, A. 1984: Relationships between the type of residential area and the aspects of surface temperature and solar reflectance (based on digital image analysis using airborne multispectral scanner data). *Energy and Buildings* **7**, 159-173.

[58] Huband, N.D.S. 1985: An Infra-Red Radiometer for Measuring Surface Temperature in the Field. Part II. Calibration and Performance. *Agric. For. Meteorol.* **34**, 227-233.

[59] Huband, N.D.S. an Monteith, J.L. 1986a: Radiative surface temperature and energy balance of a wheat canopy. I. Comparison of radiative and aerodynamic temperatures. *Boundary-Layer Met.* **36**, 1-17.

[60] Huband, N.D.S. and Monteith, J.L. 1986b: Radiative surface temperature and energy balance of a wheat canopy. II. Estimating fluxes of sensible and latent heat. *Bounday-Layer Met.* **36**, 107-116.

[61] Hutcheon, N.B. and Handegord, G.O.P. 1983: *Building Science for a Cold Climate*, John Wiley and Sons, Toronto.

[62] Idso, S.B. 1981: A set of equations for full spectrum and 8-14 μm and 10.5-12.5 μm thermal radiation from cloudless skies. *Water Resources Res.* **17**, 295-304.

[63] Idso, S.B. and Jackson, R.D. 1969: Thermal radiation from the atmosphere. *J. Geophys. Res.* **74**, 5397-5403.

[64] Iqbal, M. 1983: *An Introduction to Solar Radiation*, Academic Press: Toronto.

[65] Jackson, R.D. 1988: Surface temperature and the surface energy balance. In: *Flow and Transport in the Natural Environment: Advances and Applications.* Steffen, W.L. and Denmead, O.T. (eds.). Springer-Verlag: Berlin, 133-153.

[66] Jackson, R.D., Reginato, R.J., Pinter P.J. Jr., and Idso, S.B. 1979: Plant canopy information extraction from composite scene reflectance of row crops. *Appl. Optics* **18**, 3775-3782.

[67] Johnson, R.B. and Branstetter, E.E. 1974: Integration of Planck's equation by the Laguerre-Gauss quadrature method. *Journal of the Optical Society of America* **64**, 1445-1449.

[68] Johnson, G.T. and Watson, I.D. 1984: The determination of view-factors in urban canyons. *J. Clim. Appl. Met.* **23**, 329-335.

[69] Jupp, D.L.B., Walker, J. and Penridge, L.K. 1986: Interpretation of vegetation structure in Landsat MSS imagery: A case study in disturbed semi-arid eucalypt woodland. Part 2. Model-based analysis. *J. Environ. Manag.* **23**, 35-57.

[70] Kahle, A.B. 1977: A simple model of the earths surface for geological mapping by remote sensing. *J. Geophys. Res.* **82**, 1673-1680.

[71] Kahle, A.B., Gillespie, A.R., and Goetz, A.F.H. 1976: Thermal inertia mapping: A new geologic mapping tool. *Geophys. Res. Lett.* **3**, 26-28.

[72] Khattak, S., Vaughan, R.A., and Cracknell, A.P. 1991: Sunglint and its observation in AVHRR data. *Rem. Sens. Environ.* **37**, 101-116.

[73] Kidder, S.Q. and Wu, H.-T. 1987: A multispectral study of the St. Louis area under snow-covered conditions using NOAA-7 AVHRR data. *Rem. Sens. Env.* **22**, 159-172.

[74] Kim, H.H. 1992: Urban heat island. *Int. J. Rem. Sens.* **13**, 2319-2336.

[75] Kimes, D.S. 1980: Effects of vegetation canopy structure on remotely sensed canopy temperatures. *Rem. Sens. Environ.* **10**, 165-174.

[76] Kimes, D.S. 1981: Remote sensing of temperature profiles in vegetation canopies using multiple view angles and inversion techniques. *IEEE Trans. Geosci. Remote Sens.* **GE-19**, 85-90.

[77] Kimes, D.S. 1983: Remote sensing of row crop structure and component temperatures using directional radiometric temperatures and inversion techniques. *Rem. Sens. Environ.* **13**, 33-55.

[78] Kimes, D.S., Idso, S.B. Pinter, P.J. Jr., Jackson, R.D., and Reginato, R.J. 1980a: Complexities of nadir-looking radiometric temperature measurements of plant canopies. *Appl. Optics* **19**, 2162-2168.

[79] Kimes, D.S., Idso, S.B., Pinter, P.J. Jr., Reginato, R.J., and Jackson, R.D. 1980b: View angle effects in the radiometric measurement of plant canopy temperatures. *Rem. Sens. Environ.* **10**, 273-284.

[80] Kimes, D.S., Smith, J.A., and Link, L.E. 1981: Thermal IR exitance model of a plant canopy. *Appl. Optics* **20**, 623-632.

[81] Kimes, D.S. and Kirchner, J.A. 1982: Radiative transfer model for heterogeneous 3-D scenes. *Appl. Opt.* **21**, 4119-4129.

[82] Kimes, D.S. and Kirchner, J.A. 1983: Directional radiometric measurements of row-crop temperatures. *Int. J. Rem. Sens.* **4**, 299-311.

[83] Kimes, D.S., Holben, B.N., Tucker, C.J., and Newcomb, W.W. 1984: Optimal directional view angles for remote-sensing missions. *Int. J. Rem. Sens.* **5**, 887-908.

[84] Kneizys, F.X., Shettle, E.P., Abreu, L.W., Chetwynd, Jr. J.H., Anderson, G.P., Gallery, W.O., Selby J.E.A., and Clough, S.A. 1988: *User's Guide to LOWTRAN 7*, Air Force Geophysics Laboratory Report No. AFGL-TR-88-0177, Hanscom AFB, MA 01731. 137 pp.

[85] Kramer, P.J. and Kozlowski, T.T. 1979: *Physiology of Woody Plants*, Academic Press: New York.

[86] Kustas, W.P., Jackson, R.D. and Asrar, G. 1989: Estimating surface energy-balance components from remotely sensed data. In: Asrar, G. (ed.) *Theory and Applications of Optical Remote Sensing.* J. Wiley and Sons Ltd.: New York. 604-627.

[87] Kustas, W.P., Choudhury, B.J., Inoue, Y., Pinter, P.J., Moran, M.S., Jackson, R.D., and Reginato, R.J. 1990: Ground and aircraft infrared observations over a partially-vegetated area. *Int. J. Rem. Sens.* **11**, 409-427.

[88] Labed, J. and Stoll, M.P. 1991: Spatial variability of land surface emissivity in the thermal infrared band: spectral signature and effective surface temperature. *Remote Sens. Environ.* **38**, 1-17.

[89] Lacis, A.A. and Oinas, V. 1991: A description of the correlated k distribution method for modeling nongray gaseous absorption, thermal emission, and multiple scattering in vertically inhomogeneous atmospheres. *J. Geophys. Res.* **96**, 9027-9063.

[90] Lang, A.R.G. 1991: Application of some of Cauchy's theorems to estimation of surface areas of leaves, needles and branches of plants, and light transmittance. *Agric. Forest Met.* **55**, 191-212.

[91] Lang, A.R.G. and McMurtrie, R.E. 1992: Total leaf areas of single trees of *Eucalyptus grandis* estimated from transmittances of the sun's beam. *Agric. Forest Met.* **58**, 79-92.

[92] Leak, S.M. and Venugopal, G. 1990: Thematic mapper thermal infrared data in discriminating selected urban features. *Int. J. Rem. Sens.* **11**, 841-857.

[93] Lee, H.-Y. 1993: An application of NOAA AVHRR thermal data to the study of urban heat islands. *Atmos. Environ.* **27B**, 1-13.

[94] Lewis, J.E. and Carlson, T.N. 1989: Spatial variations in regional surface energy exchange patterns for Montreal, Quebec. *The Canadian Geographer* **33**, 194-203.

[95] Li, X. and Strahler, A.H. 1985: Geometrical-optical modelling of a conifer forest canopy. *IEEE Trans. Geosci. Remote Sens.* **GE-23**, 705-721.

[96] Liption, A.E. 1992: Effects of slope and aspect variations on satellite surface temperature retrievals and mesoscale analysis in mountainous terrain. *J. Appl. Met.* **31**, 255-264.

[97] Lorenz, D. 1966: The effect of the long-wave reflectivity of natural surfaces on surface temperature measurements using radiometers. *J. Appl. Met.* **5**, 421-430.

[98] Loudon Ross, S. and Oke, T.R. 1988: Tests of three urban energy balance models. *Boundary-Layer Meteor.*, **44**, 73-96.

[99] Matson, M., McClain, E.P., McGinnis, D.F. Jr., and Pritchard, J.A. 1978: Satellite detection of urban heat islands. *Month. Weather Rev.* **106**, 1725-1734.

[100] Matson, M. and Legeckis, R.V. 1980: Urban heat island detected by satellite. *Bull. Amer. Meteorol. Soc.* **61**, 212.

[101] McGuire, M.J., Balick, L.K., Smith, J.A. and Hutchison, B.A. 1989: Modeling directional thermal radiance from a forest canopy. *Rem. Sens. Environ.* **27**, 169-186.

[102] Mills, G.M. 1993: Simulation of the energy budget of an urban canyon - 1. Model structure and sensitivity test. *Atmos. Environ.* **27B**, 157-170.

[103] Monteith, J.L. and Szeicz, G. 1962: Radiative temperature in the heat balance of natural surfaces. *Quart. J.R. Met. Soc.* **88**, 496-507.

[104] Myrup, L.O. 1969: A numerical model of the urban heat island. *J. of Applied Met.* **8**, 908-918.

[105] Nakamura, Y. and Oke, T.R. 1988: Wind, temperature and stability conditions in an east-west oriented urban canyon. *Atmos. Environ.* **22**, 2691-2700.

[106] Nichol, J.E. 1994: A GIS-Based approach to microclimate monitoring in Singapore's high-rise housing estates. *Photogramm. Eng. and Rem. Sens.* **60**, 1225-1232.

[107] Nielsen, D.C., Clawson, K.L., and Blad, B.L. 1984: Effect of solar azimuth and infrared thermometer view direction on measured canopy temperature. *Agron. J.* **76**, 607-610.

[108] Norman, J.M. 1975: Radiative transfer in vegetation. In: *Heat and Mass Transfer in the Biosphere.* deVries, D.A. and Afgan, N.H. (eds.). Scripta Book Company: Washington D.C.

[109] Norman, J.M. and Welles, J.M. 1983: Radiative transfer in an array of canopies. *Agron. J.* **75**, 481-488.

[110] Norman, J.M., Divakarla, M., and Goel, N.S. 1995: Algorithms for extracting information from remote thermal-IR observations of the Earth's surface. *Remote Sens. Environ.* **51**, 157-168.

[111] Oke, T.R. 1984: Towards a prescrpition for the greater use of climatic principles in settlement planning. *Energy and Build.* **7**, 1-10.

[112] Oke, T.R. 1987: *Boundary Layer Climates.* Methuen: London.

[113] Otterman, J., Brakke, T.W., and Susskind, J. 1992: A model for inferring canopy and underlying soil temperatures from multi- directional measurements. *Boundary-Layer Meteorol.* **61**, 81-97.

[114] Outcalt, S.I. 1971: A numerical surface climate simulator. *Geographical Analysis* **3**, 379-393.

[115] Parsons, A.J. 1985: Directionality in emitted infrared radiation from grassy surfaces. *Int. J. Rem. Sens.* **6**, 903-910.

[116] Paw U, K.T. 1992: Development of models for thermal infrared radiation above and within plant canopies.*ISPRS. J. Photogramm. Rem. Sens.* **47**, 189-203.

[117] Paw U, K.T., Shaw, R.H., and Myers, T.P. 1985: Evapotranspiration as modelled by a higher-order closure scheme. *Proc. Nat. Conf. on Advances in Evapotranspiration.* Am. Soc. Agric. Eng., Chicago, IL 43-50.

[118] Paw U, K.T., Ustin, S.L., and Zhang, C. 1989: Anisotropy of thermal infrared exitance in sunflower canopies. *Agric. For. Meteorol.* **48**, 45-58.

[119] Pease, R.W., Lewis, J.E., and Outcalt, S.I. 1976: Urban terrain climatology and remote sensing. *Ann. Assoc. Amer. Geog.* **66**, 557-569.

[120] Press, W.H., Flannery, B.P., Teukolsky, S.A. and Vetterling, W.T. 1986: *Numerical Recipes*, Cambridge University Press, Cambridge.

[121] Price, J.C. 1979: Assessment of the urban heat island effect through the use of satellite data. *Month. Weather Rev.* **107**, 1554-1557.

[122] Price, J.C. 1982: On the use of satellite data to infer fluxes at meteorological scales. *J. Appl. Met.* **21**, 1111-1122.

[123] Price, J.C. 1989. Quantitative aspects of remote sensing in the thermal infrared. In: *Theory and Applications of Optical Remote Sensing.* Asrar, G. (ed.) John Wiley: New York, 578-603.

[124] Quattrochi, D.A. and Ridd, M.K. 1994: Measurement and analysis of thermal energy responses from discrete urban surfaces using remote sensing data. *Int. J. Rem. Sens.* **15**, 1991-2022.

[125] Rao, P.K. 1972. Remote sensing or urban heat islands from an environmental satellite. *Bull. Amer. Met. Soc.* **53**, 647-648.

[126] Rees, W.G. and James, S.P. 1992: Angular variation of the infrared emissivitiy of ice and water surfaces. *Int. J. Rem. Sens.* **13**, 2873-2886.

[127] Roth, M. 1991: Turbulent transfer characteristics on a suburban surface. Unpubl. Ph.D. Thesis, The University of British Columbia, Vancouver, B.C.

[128] Roth, M., Oke, T.R., and Emery, W.J. 1989: Satellite-derived urban heat islands from three coastal cities and the utilization of such data in urban climatology. *Int. J. Rem. Sens.* **10**, 1699-1720.

[129] Sader, S.A. 1986: Analysis of effective radiant temperatures in a Pacific Northwest forest using Thermal Infrared Multispectral Scanner data. *Rem. Sens. Environ.* **19**, 105-115.

[130] Salisbury, J.W. and D'Aria, D.M. 1992: Emissivity of terrestrial materials in the 8-14μm atmospheric window. *Rem. Sens. Environ.* **42**, 83-106.

[131] Sampson, D.A. and Smith, F.W. 1993: Influence of canopy architecture on light penetration in lodgepole pine (*Pinus contorta* var. *latifolia*) forests. *Agric. and Forest Met.* **64**, 63-79.

[132] Schmid, H.-P. 1988: Spatial Scales of Sensible Heat Flux Variability Representativeness of Flux Measurements and Surface Layer Structure over Suburban Terrain. Unpubl. Ph.D. Thesis, The University of British Columbia, Vancouver, B.C.

[133] Schmugge, T.J., Becker, F., and Li, Z.-L. 1991: Spectral emissivity variations observed in airborne surface temperature measurements. *Rem. Sens. Environ.* **35**, 95-104.

[134] Sheahen, T.P. 1983: Effects of atmospheric attenuation on temperature measurements made using IR scanning systems. *Appl. Optics* **22**, 1070-1077.

[135] Shoshany, M., Aminov, R. and Goldreich, Y. 1994: The extraction of roof tops from thermal imagery for analyzing the urban heat island structure. *Geocarto International* **4**, 61-69.

[136] Sievers, U. and Zdunkowski, W.G. 1986: A microscale urban climate model. *Beitr. Phys. Atmosp.* **59**, 13-40.

[137] Sinclair, A.J. 1976: Applications of Probability Graphs in Mineral Exploration. The Association of Exploration Geochemists, Special Vol. 4.

[138] Smith, J.A., Ranson, K.J., Nguyen, D., Balick, L., Link, L.E., Fritschen, L., and Hutchison, B.A. 1981: Thermal vegetation canopy model studies. *Rem. Sens. Environ.* **11**, 311-326.

[139] Smith, R.C.G., Prathapar, S.A., Barrs, H.D. and Slavich, P. 1989: Use of a thermal scanner image of a water stressed crop to study soil spatial variability. *Rem. Sens. Environ.* **29**, 111-120.

[140] Smith, W.L. 1985: Satellites. In: *Handbook of Applied Meteorology.* Houghton, D.D. (Ed.). John Wiley and Sons: New York, pp. 380-472.

[141] Sobrino, J.A., Caselles, V., and Becker, F. 1990: Significance of the remotely sensed thermal infrared measurements obtained over a citrus orchard. *ISPRS Journ. of Photogramm. and Rem. Sens.* **44**, 343-354.

[142] Sobrino, J.A., and Caselles, V. 1990: Thermal infrared radiance model for interpreting the directional radiometric temperature of a vegetative surface. *Remote Sens. Environ.* **33**, 193-199.

[143] Spencer, J.W. 1971: Fourier series representation of the position of the Sun. *Search* **2**, 172.

[144] Spronken-Smith, R.A. 1994: Energetics and Cooling in Urban Parks. Unpubl. Ph.D. Thesis, The University of British Columbia, Vancouver, B.C.

[145] Stanley, C.R. 1987: Instruction Manual for PROBPLOT, Association of Exploration Geochemists, Special Volume #14.

[146] Steyn, D.G. 1980: Turbulence, Diffusion and the Daytime Mixed Layer Depth over a Coastal City. Unpubl. Ph.D. Thesis, The University of British Columbia, Vancouver, B.C.

[147] Steyn, D.G. and Lyons, T.J. 1985: Comments on "The determination of view-factors in urban canyons". *J. Clim. Appl. Met.* **24**, 383-385.

[148] Stoll, M.J. and Brazel, A.J. 1992: Surface-air temperature relationships in the urban environment of Phoenix, Arizona. *Phys. Geog.* **13**, 160-179.

[149] Sutherland, R.A. 1986: Broadband and spectral emissivities (2-18μm) of some natural soils and vegetation. *J. Atmos. and Oceanic Tech.* **3**, 199-202.

[150] Sutherland, R.A. and Bartholic, J.F. 1977: Significance of vegetation in interpreting thermal radiation from a terrestrial surface. *J. Appl. Met.* **16**, 759-763.

[151] Taconet, O., Bernard, R., and Vidal-Madjar, D. 1986: Evapotranspiration over an agricultural region using a surface flux/temperature model based on NOAA-AVHRR data. *J. Appl. Clim. Met.* **25**, 284-307.

[152] Terjung, W.H. and O'Rourke, P.A. 1980a: Simulating the causal elements of urban heat islands. *Boundary-Layer Meteorol.* **19**, 93-118.

[153] Terjung, W.H. and O'Rourke, P.A. 1980b: Influences of physical structures on urban energy budgets. *Boundary-Layer Meteorol.* **23**, 415-424.

[154] Van de Griend, A.A., Owe, M., Groen, M., and Stoll, M.P. 1991: Measurement and spatial variation of thermal infrared surface emissivity in a savanna environment. *Water Resour. Res.* **27**, 371-379.

[155] Verseghy, D.L. and Munro, D.S. 1989: Sensitivity studies on the calculation of the radiation balance of urban surfaces: II. Longwave radiation. *Boundary-Layer Met.* **48**, 1-18.

[156] Voogt, J.A. 1989: Validation of an Urban Canyon Radiation Model for Nocturnal Long-Wave Radiative Fluxes and the Effect of Surface Geometry on Cooling in Urban Canyons. Unpubl. M.Sc. Thesis, University of British Columbia, Vancouver, B.C.

[157] Vukovich, F.M. 1983: An analysis of the ground temperature and reflectivity pattern about St. Louis, Missouri, using HCMM satellite data. *J. Appl. Meteorol.* **22**, 560-571.

[158] Vukovich, F.M. 1984: A comparison of surface temperature derived from HCMM infrared measurements with field data. *Rem. Sen. Env.* **15**, 63-76.

[159] Willmott, C.J. 1981: On the Validation of Models. *Phys. Geogr.* **2**, 184-194.

[160] Wilson, S.B. and Anderson, J.M. 1986: The applicability of LOWTRAN 5 computer code to aerial thermographic correction. *Int. J. Rem. Sens.* **7**, 379-388.

[161] Woodcock, C.E. and Strahler, A.H. 1987: The factor of scale in remote sensing. *Rem. Sens. Environ.* **21**, 311-332.

[162] Wright, I.R. 1990: A laboratory calibration of infrared thermometers, *Int. J. Rem. Sens.* **11**, 181-186.

[163] Yoder, E.J. and Witczak, M.W. 1975: *Principles of Pavement Design.* John Wiley: New York.

Appendix A

AGEMA 880 LWB INFRARED SCANNER

A.1 Instrument Description

The thermal infrared imager used in this study is the AGEMA Thermovision 800 BRUT System equipped with a Model 880 LWB scanner. The system is owned by the Ontario Laser and Lightwave Research Corporation (OLLRC) and was loaned for the study period. The complete system consists of a scanner, system controller (essentially a specially configured computer), monitor and keyboard. The system is designed for real-time thermography in industrial and research applications. There are no special system features which adapt or preclude it from use on airborne platforms, although direct DC power-in is an available option which could be used to draw power from aircraft power systems. AGEMA systems have been successfully employed from helicopters in other studies of urban and roadway climate (Eliasson, 1992; Gustavsson and Borgen, 1991). Airworthiness regulations prohibit modification of any aircraft structure without inspection and re-certification, so the AGEMA system was installed independent of all helicopter systems including a DC power supply and inverter.

The scanner uses a cryogenically-cooled (LN) Mercury Cadmium Telluride detector which is sensitive primarily in the 8–12 μm waveband (typical spectral response curves are shown in Figure A.1).

A 12° lens with a stated geometric resolution of 1.2 mrad (measured as slit response at 50% contrast) was used with the scanner. Table A.1 presents a summary of the technical

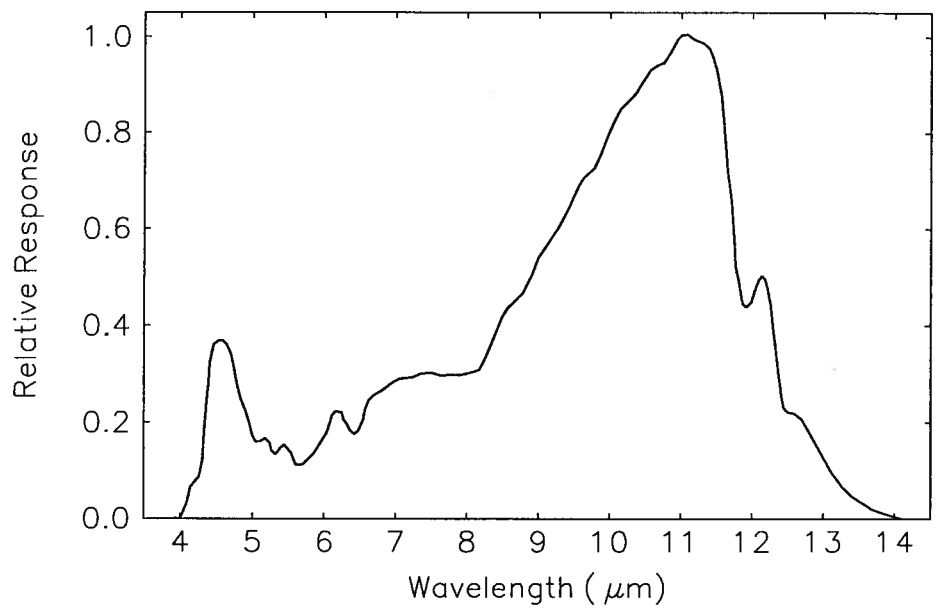

Figure A.1: AGEMA 880 LWB system response. Data supplied by Linnander (*pers. comm.*).

specifications of the AGEMA 880 LWB system used.

Incident radiation is directed by a set of rotating mirrors though a scalable aperature unit, a filter unit, and finally onto a point detector. Detector output is converted into a 12 bit digital signal by the processor. The instrument gain is software selectable; a gain of 2 allows the resolution to be doubled but limits the maximum signal from the scanner to 0.5 of the FSR. This is not a limitation for the range of surface temperatures present in urban areas, therefore most images were recorded using a gain of 2.

Images are built up from a set of scanned lines with 140 pixels per line. A number of scanner modes are available (Table A.1). These vary the number and order (interlaced or non-interlaced) of scanned lines. Images with fewer lines are scanned more quickly; this allows a greater frame rate to be sustained. Modes which scan less than 140 lines per frame may consist of non-overlapping adjacent lines and were not used. In this study,

Table A.1: Technical specifications: AGEMA 880 LWB TIR system.

Range	-30°C to 1300°C	
Sensitivity	0.05°C at 30°C	
Accuracy	±2% or ±2°C	
Digitization	12 bit (4096 levels) full scale range (FSR)	
	12 bit (4096 levels) half FSR (GAIN = 2)	
Scanning Modes	0 - 280 lines @ 6.25 Hz	4:1 interlace
	1 - 140 lines @ 6.25 Hz	2:1 interlace
	2 - 70 lines @ 25 Hz	non-interlaced
	3 - 140 lines @ 12.5 Hz	non-interlaced
	4 - 280 lines @ 6.25 Hz	non-interlaced
	5 - Line scanning mode	

mode 4 (280 lines × 140 pixels) was most commonly used. In turbulent flight conditions, the slower frame rate of mode 4 resulted in some blurring of the images. Under these conditions scanner mode 3 (140 lines × 140 pixels) was selected at operator discretion.

A.2 Instrument Theory

The AGEMA system uses two special units in the measurement and storage of the thermal images. Sample values (SV) are the digital output from the 12 bit A/D converter (0 to 4095). Thermal values (TV), which use "isotherm units (IU)", are described as a "... practical arbitrary unit of measurement" (AGEMA Operators Manual, 1991 p 8.1). They are a measure of the amount of infrared radiation received and detected by the scanner. Thermal values are used for level and range settings (which control the greyscale of the displayed image) and in the calibration curves of the scanner. The following equations present relationships between scanner output voltage, sample value, thermal value, incident photon flux, and object temperature.

$$TV = 100 \cdot V_{scan} \tag{A.1}$$

where V_{scan} is the scanner voltage and

$$SV = \frac{TV}{iups} \tag{A.2}$$

where *iups* is an internal constant which varies only with the gain. Because the AGEMA utilizes a photon detector rather than an energy detector, the relationship between the thermal value (represented by IU) and received photon radiation (P) is given by

$$TV = C \cdot P \tag{A.3}$$

Spectral photon emission at wavelength λ and temperature T, $P(\lambda, T)$ is obtained by dividing the Planck function

$$L(\lambda, T) = \frac{hc^2}{\lambda^5(\exp(\frac{hc}{\lambda kT}) - 1)} \tag{A.4}$$

by the energy of a photon

$$Q = \frac{hc}{\lambda} \tag{A.5}$$

where h is Planck's constant (6.6262×10^{-34} J s), k is Boltzmann's constant (1.281×10^{-23} J K^{-1}), and c is the speed of light (2.998×10^8 m s^{-1}). Scanner detected photon emissions may be obtained using

$$P(T) = \frac{\frac{1}{\pi}\int_{\lambda_1}^{\lambda_2} \epsilon_\lambda \cdot P(\lambda, T) \cdot \Phi(\lambda) d\lambda}{\int_{\lambda_1}^{\lambda_2} \Phi(\lambda) d\lambda} \tag{A.6}$$

where $\Phi(\lambda)$ is the relative spectral response of the instrument as a function of wavelength (Figure A.1), and ϵ_λ is the wavelength dependent value of the surface emissivity. In narrow wavebands the wavelength dependence of ϵ is often ignored (greybody assumption) and ϵ is removed outside the integral. The calibration function used to relate temperature (T) and thermal value (as measured in IU units) is

$$TV = \frac{R}{\exp(B/T) - F} \tag{A.7}$$

where R, B, and F are the response, spectral, and shape factors respectively. These factors are obtained from a least squares fit of eq. A.7 over a wide temperature range (-30°C – 1300°C) during factory calibration. The factors are instrument, filter and aperture specific and are fixed in the system memory. Table A.2 presents the scanner constants for the system configuration used.

Table A.2: Scanner constants: AGEMA THV880 LWB (AGEMA, 1991)

Filter	NOF	no filter
Aperature	0	fully open
Lens	12	FOV = 11.55° exact
R	16930	response factor
B	1470	spectral factor
F	7.08	shape factor
α	0.008	atmospheric constant
β	0	atmospheric constant
iups	0.1257545	gain = 1

The atmospheric constants α and β are used in a model to determine atmospheric transmission τ, based upon a user-entered air temperature and object distance. The constants are calculated for standard atmospheric conditions and incorporate the instrument spectral response (including the effects of any filter selected). This correction method is not used here, because it applies to a fixed relative humidity (50%) and is designed for applications in which the path between sensor and object is near-horizontal, with no variation in atmospheric properties. This study uses independent atmospheric corrections determined for measured atmospheric profiles at the time of image acquistion using the LOWTRAN 7 model B. Sample calculations show the internal AGEMA corrections can differ by more than 2 degrees from those estimated using the LOWTRAN 7 model.

A.3 Instrument Calibration

Calibration of the full-scale instrument range uses a factory-set reference voltage and is carried out each time the instrument is turned on and each time a sequence of images is to be viewed in real time and/or recorded. The AGEMA technical specifications (Table A.1) state a temperature accuracy of ±2°C or ±2% (no indication of when to apply either specification) over a wide temperature range (-30°C to 1300°C). An independent check of the accuracy of AGEMA temperature measurements was made using the blackbody calibration facility of the UBC Soil Science Department. This facility consists of a cylindrical blackbody cavity heated or cooled by a stirred water bath (Figure A.2).

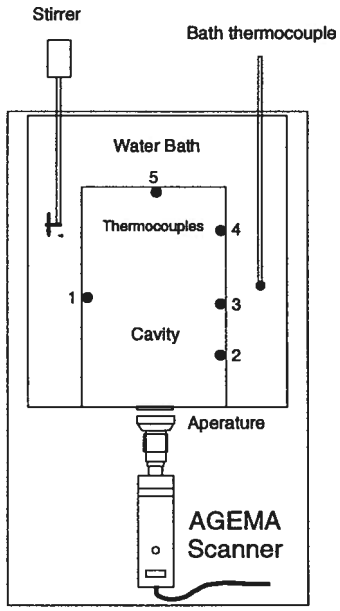

Figure A.2: UBC Soil Science blackbody calibration facility.

Cavity temperatures between -20°C and 70°C may be obtained using a precooled water-glycol mixture and a small immersion heater. Cavity temperature is measured by fine-wire (0.003″) welded chromel-constantan thermocouples affixed to the inside of the

chamber by specially designed mylar/aluminum "sandwiches" which electrically insulate the thermocouples from the chamber walls and provide good thermal contact with the cavity. The thermocouples are accurate to within 0.01°C; total error, including datalogger limitations, is ±0.05°C (R. Adams, *pers. comm.*). The maximum spatial variation in cavity temperature among the four (of five) operating thermocouples was 0.11°C at -15°C, but on average was ≈ 0.02°C.

The AGEMA scanner was mounted vertically below the cavity port (Figure A.2). This position is less than ideal because the scanner dewar containing the liquid nitrogen (LN) has a reduced holding time when used at angles close to 90°. To avoid loss of detector sensitivity, the dewar was refilled with LN at short intervals.

The configuration of the scanner lens assembly, and the design of the calibration cavity, prevent the scanner lens from being mounted flush with the bottom of the cavity. The scanner lens is large with respect to the size of the cavity port, so the scanned image was averaged over a subset (140 × 70) of the complete frame (280 × 140) to reduce possible edge-effects from non-cavity emissions. The presence of non-cavity emissions may be evidenced by a non-symmetrical distribution of temperatures, where the mode is skewed towards the cavity temperature and a tail of higher (lower) temperatures exists for low (high) cavity temperatures; the "tail" corresponding to the ambient room temperature. Figure A.3 shows that such a distribution does exist for the complete image but that the effects are substantially reduced over the image subset.

Visual inspection of the images revealed that temperature patterns associated with the image subset tended to be organized into vertical bands and lines, rather than as radial patterns about the image centre. Patterns were similar for different cavity temperatures. They do not appear to be related to the cavity and are thought to be associated with internal system variations. Variations of temperature within these patterns were a maximum of about 0.8 degrees at AGEMA apparent temperatures of 339 K and 260 K.

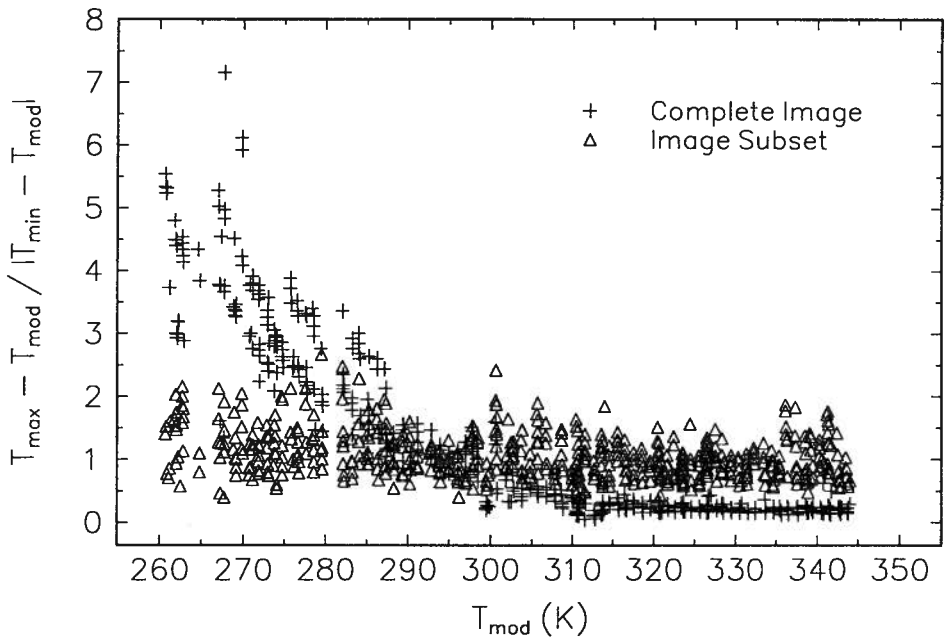

Figure A.3: Relative position of the image mode for complete and subset areas of the calibration images.

However, the majority of pixels scanned showed relatively little variation; 75% of the most frequently occurring classes from a histogram analysis yielded a temperature range of between 0.2 and 0.4 degrees.

Results of the calibration test are presented in Figure A.4. The temperature plotted is the image modal temperature based upon a histogram analysis employing 15 classes. There is a consistent overestimation by the AGEMA with respect to the cavity temperature which is especially evident at low temperatures. Differences exceed 2°C below 0°C, decreasing to 0.2–0.5 degrees above 50°C. These results have been reported previously (Isbrucker, *pers. comm.*) and are accepted as accurate. When atmospheric corrections are not required, image temperatures may be corrected using

$$T = -1.08217 + 1.0137 \cdot T_{ag} \tag{A.8}$$

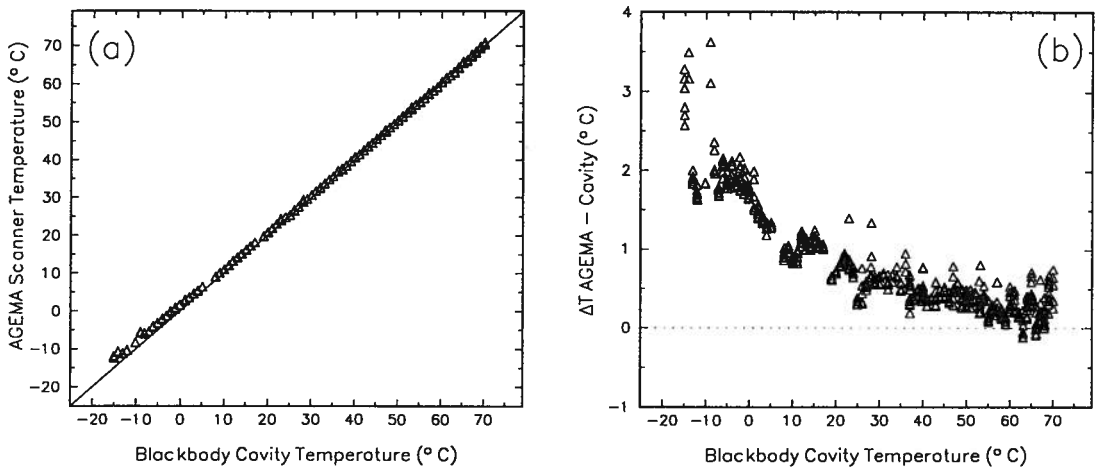

Figure A.4: Comparison of AGEMA scanner temperature with average blackbody cavity temperature. (a) Calibration plot, (b) Temperature differences.

for the range $8 \leq T \leq 70°C$.

A.4 Radiance-Photon-Temperature Relations

Conversion between radiance, photon emission, and TV is required because the atmospheric radiation model used to estimate atmospheric emission and transmission produces radiance values. Blackbody cavity temperatures were converted to photon emissions using eq. A.4 and eq. A.5, and integrated over the spectral band pass of the AGEMA, weighted by the relative sensor response (using the curve supplied by Linnander (*pers. comm.*) (Figure A.1)). The integral is then normalized by the total integrated sensor response. Integrations were performed using an adaptive quadrature method (Forsythe *et al.*, 1977). Results are compared to the AGEMA thermal values where apparent AGEMA modal temperature is used as T. This implicitly accounts for the temperature difference between the cavity and AGEMA (Figure A.3). A plot of the results (Figure A.5) shows a slight deviation from linear.

A better approximation over the calibration temperature range is obtained using a power law model. Parameters for the two empirical models are included in Figure A.5.

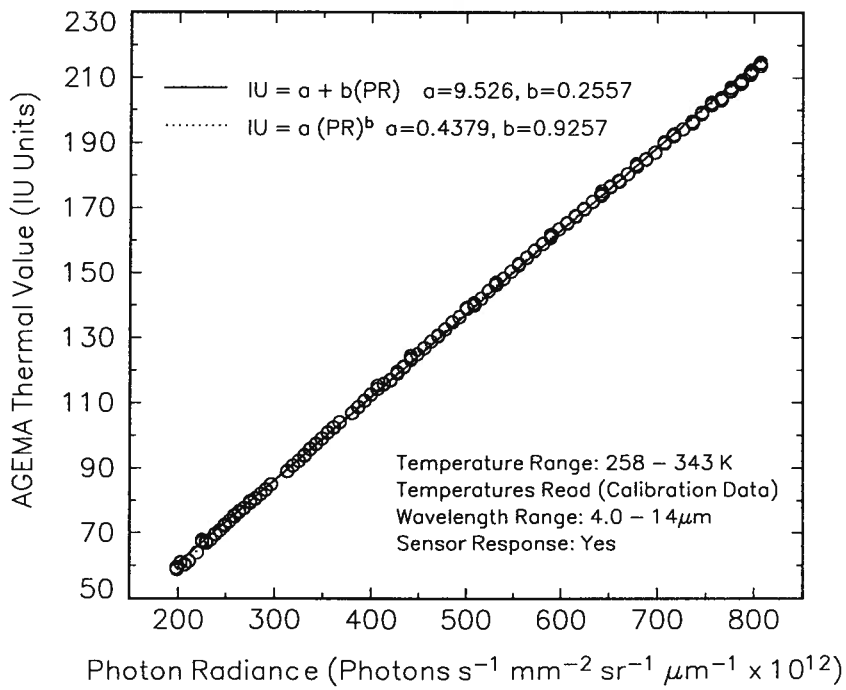

Figure A.5: Relation between AGEMA Thermal Value and photon emission over the calibration range.

The power law model yields an average deviation from the mean of $-0.01°C$ with a median value of $0.0962°C$. Over the range of temperatures most commonly observed in the field, ($5°C - 50°C$) equivalent temperature differences are on the order of $0.3°C$ with most differences less than ± 0.2 degrees. Larger differences (up to $0.7°C$) exist at very low (below $-10°C$) or high (above $55°C$) temperatures. No improvement is gained from linear or power-law models fit to subset ranges of observed temperatures, therefore the power-law model fit to the entire range of data was selected for operational use.

A.5 Spectral Response Considerations

A.5.1 Introduction

The spectral response diagram for the AGEMA scanner (Figure A.1) indicates some system response is present at wavelengths in the shortwave infrared. The inclusion of solar radiation, via surface reflection or atmospheric scattering, into the scanner field of view increases the total radiance incident upon the detector (by the amount P_{solar} and results in an overestimation of the apparent surface radiative temperature (T_r). Because of Wien's law and the respective radiating temperatures of the Earth and Sun, the ratio of reflected solar radiation to the infrared radiation emitted by Earth increases rapidly at shorter wavelengths (Figure A.6) leading to significant errors in T_r. This section investigates the degree to which system response to solar radiation affects the temperature measurements made by the AGEMA scanner. The analysis is conducted with the aid of the LOWTRAN 7 model in order to estimate the solar and thermal radiances, including the processes of atmospheric absorption and scattering, at typical observation altitudes.

A.5.2 LOWTRAN 7 Parameters

The LOWTRAN 7 model was run using the parameters listed in Table A.3. The surface emissivities considered were: a blackbody; a greybody ($\epsilon = 0.3$), representative of highly reflective urban surfaces, such as uncoated aluminum roofs; a greybody ($\epsilon = 0.9$), typical of many urban building materials; and, as a limiting case, a surface with $\epsilon = 0.0$.

The reflective character of the surfaces is assumed to be diffuse; while spectral reflections are possible from smooth surfaces such as glass, observations of this effect are confined to very limited Sun-target-sensor geometries when the reflecting surface is smooth (Duggin and Saunders, 1984). When spectral reflection does occur, errors may be significant, even for thermal infrared wavelengths. Errors in remotely sensed sea surface

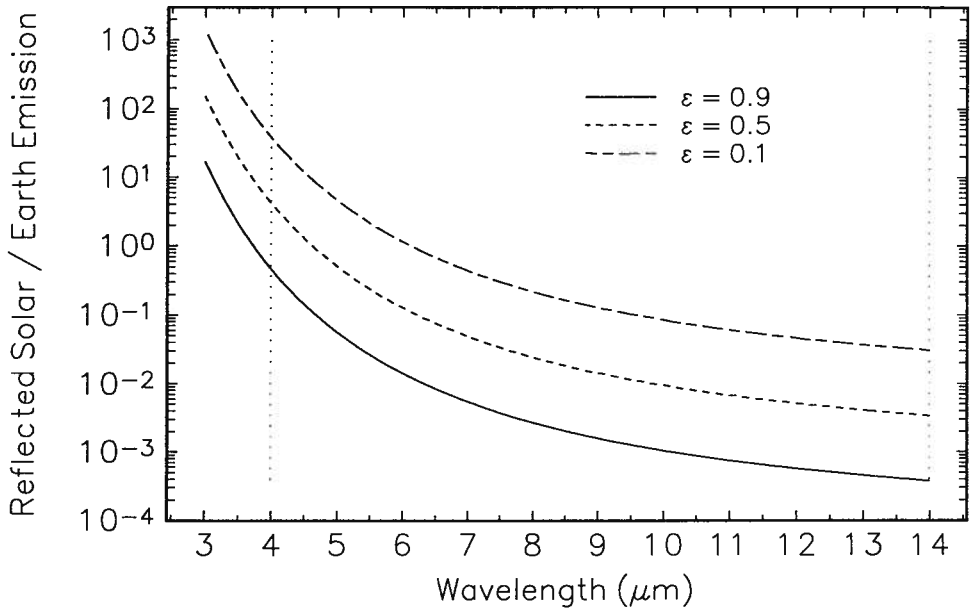

Figure A.6: Ratio of reflected solar radiance to Earth-emitted radiance for three surface emissivities. Solar radiance is approximated as the blackbody radiance at $T = 6000K$(appropriately reduced by the inverse square law for the Earth-Sun distance). Earth emissions are calculated assuming a surface temperature of 300 K. Emissions and reflections are related as $\rho_\lambda = 1 - \epsilon_\lambda$.

temperatures of 2 K have been attributed to sunglint from waves on the ocean surface (Khattak *et al.*, 1991) using the thermal channels of the AVHRR (band 4 10.3 μm – 11.3 μm, band 5 11.5 μm – 12.5 μm).

LOWTRAN 7 model runs produce estimates of:

- atmospheric radiance which includes:
  - surface emission
  - atmospheric emission
  - atmospheric scattered thermal emission
  - surface reflected thermal emission

Table A.3: LOWTRAN 7 input parameter summary.

Model Parameter	Setting
atmospheric profile	mid-latitude summer
execution mode	solar radiance
scattering	multiple scattering
T_o	294.2 K (from profile)
ϵ_s	0.9, 0.3, 0.0
boundary layer aerosol	rural, visibility 23 km
stratospheric aerosol	background stratospheric
clouds	none
sensor altitude	647 m
ground altitude	0 m
sensor angle	0° (nadir angle)
zenith angle	37° (solar noon, August 15)
latitude	49° 15′ N

- path scattered radiance (solar radiation)
- ground reflected radiance including:
  - reflected direct solar
  - reflected scattered solar
- total radiance (sum of the above components)

Sensor normalized photon emissions were then calculated from the LOWTRAN radiance results using eq. A.6. These were converted to thermal values using the results of section A.3 and finally to apparent temperature differences using the internal AGEMA functions.

A.5.3 Results

The results (Table A.4) show that the equivalent temperature error, due to inclusion of P_{solar} in the total normalized photon emission reaching the scanner, is small, except over very low emissivity surfaces. Because the reflected solar component is constant, while surface emission increases non-linearly with temperature, the relative error decreases as temperature increases. The surface temperature used in this analysis (294.2 K) is low with respect to the observed daytime temperature of many urban surfaces, thus providing a relatively conservative estimate of expected temperature errors. The AGEMA technical specifications list a sensitivity of 0.05°C at 30° C but an accuracy of only ±2% or ±2°. This suggests that while P_{solar} may be detectable, it is small with respect to the stated accuracy of the system and is comparable to, or smaller than the temperature differences attributed to system noise in the calibration tests.

Table A.4: Sensor normalized photon emissions calculated from LOWTRAN 7 radiance estimates with multiple scattering for $\lambda_{3.9-13}$.

ϵ	${P_{atm}}^a$	${P_{solar}}^b$	${P_{scan}}^c$	${T_r}^d$	$\partial {T_r}^e$
	Photons $s^{-2}cm^{-2}sr^{-1} \times 10^{16}$			(K)	(K)
0.0	2.2739	1.4051E-2	2.2878	267.08	0.28
0.3	2.7645	9.8388E-3	2.7742	276.31	0.18
0.9	3.7441	1.4069E-3	3.7452	292.16	0.02
1.0	3.9051	3.4871E-6	3.9051	294.53	≈ 0

[a]sensor normalized atmospheric photon emission (including surface emission)
[b]sensor normalized sum of ground reflected and path scattered solar emission
[c]total sensor normalized emission at sensor altitude
[d]apparent temperature from P_{scan} (from relations in A.3)
[e]change in T_r due to presence of P_{solar}

A.6 Conclusions

The calibration measurements show a substantial systematic error (an overestimation) between the cavity temperature and apparent AGEMA temperature over the range of cavity temperatures tested. The differences decrease with increasing cavity temperature; over the range 10°C–50°C AGEMA temperatures are 0.1–1.0°C warmer than those measured by the cavity. Confidence in the AGEMA temperatures is restricted by evidence of non-cavity emissions within the scanner FOV, and by structurally consistent apparent temperature variations within the images attributed to system noise. The form of the relation between thermal value and photon emission was found to be slightly better modelled by a power law model rather than the linear model suggested by eq. A.3. This model agrees to within 0.3°C of the observed cavity temperature for temperatures above 0°C. The analysis assumes that the sensor spectral response function includes all system components and is representative of the instrument used. Errors due to inclusion of reflected solar radiation are shown to be small based upon an analysis using the LOWTRAN 7 model coupled with specified instrument spectral response.

Appendix B

ATMOSPHERIC CORRECTIONS OF THERMAL IMAGERY

B.1 Introduction

Remotely-sensed surface temperatures require correction for atmospheric absorption and re-emission which takes place along the path length of atmosphere between the sensor and surface. For the short path-lengths viewed using airborne thermal imagery the primary influence of the atmosphere is absorption and re-emission of thermal radiation by water vapour, with absorption and re-emission by ozone, and the uniformly mixed gases of carbon dioxide, nitric oxide, carbon monoxide and methane also having an effect (Desjardins *et al.*; 1990; Wilson and Anderson, 1986). Atmospheric absorption and re-emission serves to reduce the range of apparent surface temperatures measured by a thermal remote sensor, because surface emissions are replaced by atmospheric emissions.

The atmospheric correction technique adopted in this study is the single infrared channel method (Becker and Li, 1990). This method uses an atmospheric radiation transfer model to estimate atmospheric emission and transmission using a description of the atmosphere obtained from vertical remote soundings, radiosonde ascents or climatological data, and a model of the sensor-detected radiance which combines the atmospheric, surface, and reflected sky radiance components.

B.2 Methodology

The radiance L observed by a sensor at altitude h_s and pointing at an angle θ to the normal may be represented as (Byrnes and Schott, 1986)

$$L(h,\theta) = \tau(h,\theta) \cdot \epsilon \cdot L_o + \tau(h,\theta) \cdot (1-\epsilon) \cdot L_{sky} + L_a \tag{B.1}$$

where τ(h,θ) is the atmospheric-path transmission to the sensor, ϵ is the surface emissivity, L_o is the surface blackbody radiance at temperature T, L_{sky} is the hemispheric incoming sky radiance at the ground surface, and L_a is the atmospheric emission in the path between the sensor and the ground surface. Note that all the quantities in eq. B.1 are spectral quantities.

The actual radiance received by the sensor is an integration over the sensor bandpass weighted by the sensor response

$$L_s = \frac{\int L(\lambda,h,\theta) \cdot \Phi(\lambda) d\lambda}{\int \Phi(\lambda) d\lambda} \tag{B.2}$$

(see Section A.2). As in Section A.2, the wavelength dependence of ϵ is ignored, thereby invoking the assumption that surface materials behave as greybodies. Because the AGEMA thermal scanner used has a detector with a linear response to photon radiation rather than radiance, the above equations are converted to photon emittances by dividing the spectral quantities by the energy per photon (eq. A.5).

Using the relations determined between AGEMA *IU* units and photon emission, and the internal AGEMA calibration function, model estimates of photon emission at sensor height and view angle can be converted to apparent temperature estimates. Results are expressed by way of look-up tables for specified surface apparent temperature and sensor apparent temperature from which a low degree polynomial can be used to speed the application to image data. The accuracy of the polynomial approximation is generally

within ±0.03°C for the temperature range 0–55°C, and to within ±0.06°C outside this range.

No additional correction due to angle within the sensor FOV is incorporated. For nadir imagery, the ±6° swath across the image yields temperature differences of less than 0.02°C compared with the 0° look-up table. When scanning at the 45° off-nadir angle, the differences are greater, ranging from −0.4–0.3°C for the 51° upper limit of the FOV, and −0.2–0.3°C for the 39° FOV limit. However, actual differences may be larger, due to uncertainties in the absolute angle of the scanner (likely ±10° from the specified 45° angle); apparent temperature differences calculated between a 40° and 50° off-nadir angle range from −0.4°C at 270 K to 0.6°C at 330 K.

B.3 LOWTRAN 7 Atmospheric Radiation Model

The atmospheric radiation transfer model used is the LOWTRAN 7 Atmospheric Transmittance/Radiance model (Kneizys *et al.*, 1988). This is a narrow-band radiation model which has been used extensively in other studies employing aircraft-mounted thermal scanners (Hook *et al.*, 1992; Schmugge *et al.*, 1991; Desjardins *et al.*, 1990; Byrnes and Schott,1986; Callison *et al.*, 1987; Wilson and Anderson, 1986; Sheahen, 1983).

The LOWTRAN model is used with a composite atmospheric profile (Section B.4) consisting of measured and climatological values of pressure, temperature and humidity. The concentrations of ozone, methane, nitrous oxide and carbon monoxide are obtained from the mid-latitude summer atmosphere model (as supplied by LOWTRAN) and other atmospheric trace gas concentrations are given by the U.S. Standard Atmosphere (Kneizys *et al.*, 1988). The model produces estimates of τ and L_a tabulated at 5 cm^{-1} intervals for use in (eqs. B.1, B.2, A.5). Emitted surface radiance, L_o, is calculated using the Planck function. The hemispheric incoming sky radiance L_{sky} is estimated following

Dutton (1993) using the quadrature method of Lacis and Oinas (1991) whereby L_{sky} is approximated by a weighted sum of the radiances obtained at zenith angles of 0, 60, and 84.26°.

B.4 Composite Atmospheric Profiles

The use of temporally and spatially relevant profiles has been found to be important for successful modelling of the atmospheric radiative fluxes using LOWTRAN and therefore the accurate retrieval of surface radiative temperature (Desjardins *et al.*, 1990; Wilson and Anderson, 1986).

In order to meet this requirement, three sources of data are used: local radiosonde launches coincident with the time of the over-flight to characterize the lower atmosphere, climatological soundings from the nearest upper-air station to supplement local soundings, and standard climatological values for the highest levels of the atmosphere, above the range of radiosondes. Two composite atmospheric profiles were constructed for each local sounding. The composite profiles are used to estimate incident sky radiance at the surface, and for path emission and transmission for satellite data. The components of the composite profile are described in the following subsections.

B.4.1 Local Radiosonde Profiles

Profiles of pressure, dry and wet-bulb temperature in the lower atmosphere were obtained from radiosondes launched (using an AIRSONDE^{TM} system) near the study site during the time of helicopter over-flights. Altitudes and dewpoint temperature T_d required for LOWTRAN were derived from measured variables using the online-software of the AIRSONDE^{TM} system (Tetens saturation vapour pressure formula) with the modification that saturation vapour pressure with respect to the ice phase was not used until

evidence of wet bulb freezing was obtained. The height of ascent varied between launches, some launches ended prematurely due to instrument failure and/or data transmission or reception problems (Table B.1).

Table B.1: Local radiosonde (Airsonde) launch times and maximum altitude. *est.* indicates maximum altitude was estimated based upon assumed ascent rate and comparison of temperature and humidity profiles with other flights.

Flight	Date	Launch Time (PDT)	z_{max} (m)
1	15/08/92	0949	2298
2	15/08/92	1337	6613
3	15/08/92	1738	3271
4	16/08/92	1123	4142
5	16/08/92	1616	5491
6	17/08/92	0953	1768(*est.*)
7	17/08/92	1354	3811
8	17/08/92	1712	3538(*est.*)
9a	24/08/92	1544	failed
9b	24/08/92	1646	5710(*est.*)
10	24/08/92	2029	4151
11	24/08/92	2357	failed
12	25/08/92	0530	6725

Of the 13 launches, 2 failed completely (Flights 9 and 11), and 3 suffered problems thought to be associated with the pressure sensor (Flights 6, 8, and 9b). For those flights with suspect pressure data, heights were estimated using assumed ascent rates, and by comparing the structure of the temperature and humidity profiles with those of "good" flights on the same day, or from a similar launch time on another day. Pressures

were then calculated using the height and temperature data. Of the failed launches, Flight 9a was replaced by a second launch (Flight 9b), and Flight 11 was estimated by temporal interpolation using Flights 10 and 12. Plots of the finalized atmospheric profiles (which include upper atmospheric data from climatological soundings (Section B.4.2)) are provided in Figure B.1.

B.4.2 Climatological Radiosonde Profiles

Temperature and humidity at altitudes above those measured by the local radiosonde profiles were obtained from reported pressure, temperature and dewpoint depressions (DPD) at significant and mandatory levels at one of the 2 nearest 12 hour radiosonde launch sites (Figure B.2): Port Hardy, B.C., (station YZT) or Quillayute WA, (station UIL). Table B.2 summarizes the radiosonde data collected.

No temporal interpolation of the data is attempted because, for the most part, it is used only for altitudes well above the boundary layer, where most of the diurnal variation takes place. The soundings are plotted in Figure B.1 which allows comparison between the two stations and the local sounding.

Humidity data are much sparser for station UIL due in part to differences in radiosonde reporting practices between the U.S. and Canada (Table B.4.2 and Garand *et al.*, 1992; Elliott and Gaffen, 1991). Reported DPD for the uppermost levels at station YZT are subject to a 1% relative humidity limit; this practice sets all layers with a humidity $\leq 1\%$ as 1% and calculates the DPD based upon reported air temperature. This introduces a moist bias into the profile. The US practice of replacing low RH values with a fixed DPD of 30 K results in a dry bias for those levels so assigned. For thermal imagery obtained from the helicopter, these biases will have a minor effect, because it affects only the estimation of L_o, which is reflected to the sensor in only small amounts from most surfaces. For satellite data, the effects are more important, since the layers

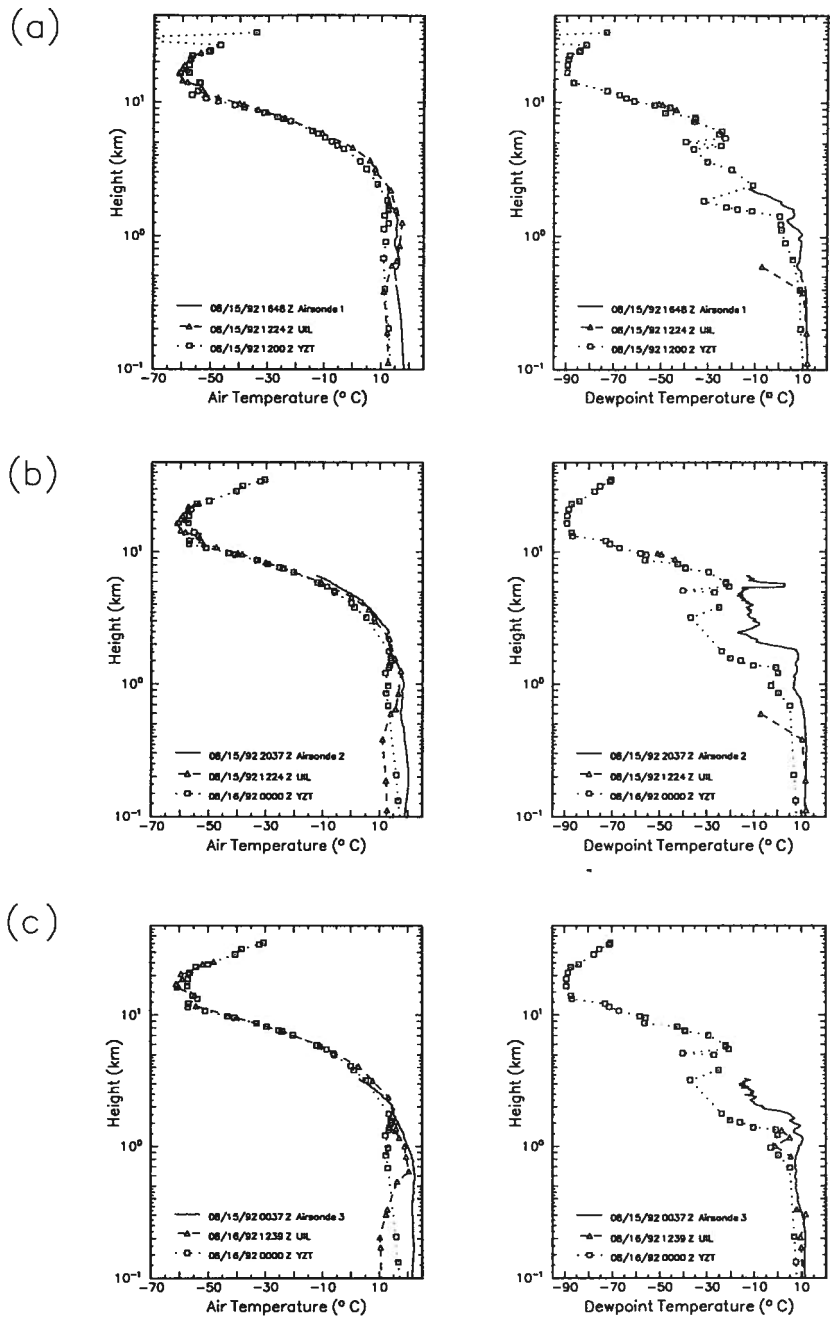

Figure B.1: Atmospheric profiles of temperature and humidity as measured by local AIRSONDE launches, and the closest (temporally) profile obtained from the upper air reporting stations Port Hardy B.C. (YZT) and Quillayute WA (UIL) for each flight conducted: (a-c) Flights 1–3 respectively.

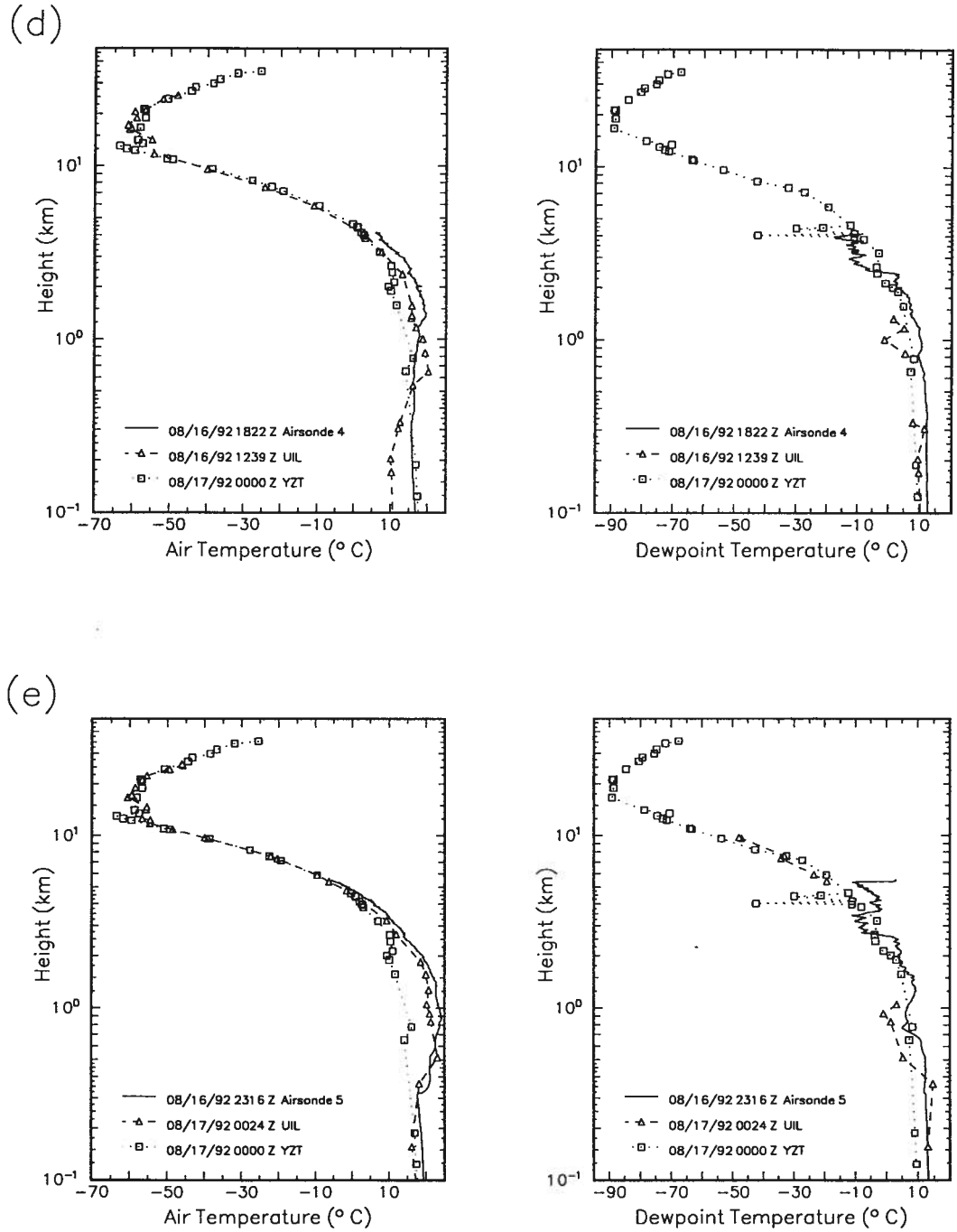

Figure B.1 (*Continued*). Atmospheric profiles for: (d) Flight 4, (e) Flight 5.

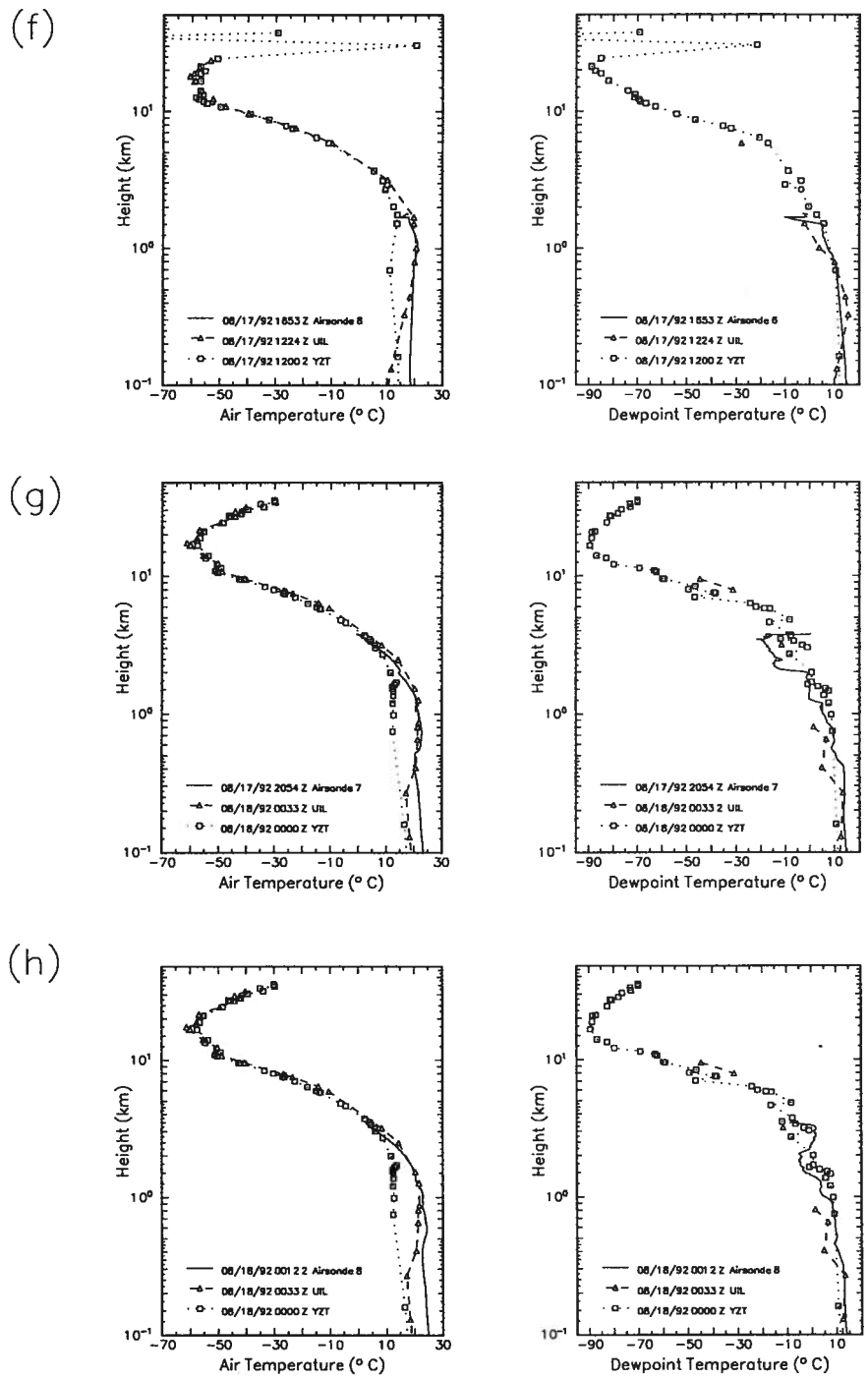

Figure B.1 (*Continued*). Atmospheric profiles for: (f) Flight 6, (g) Flight 7, (h) Flight 8.

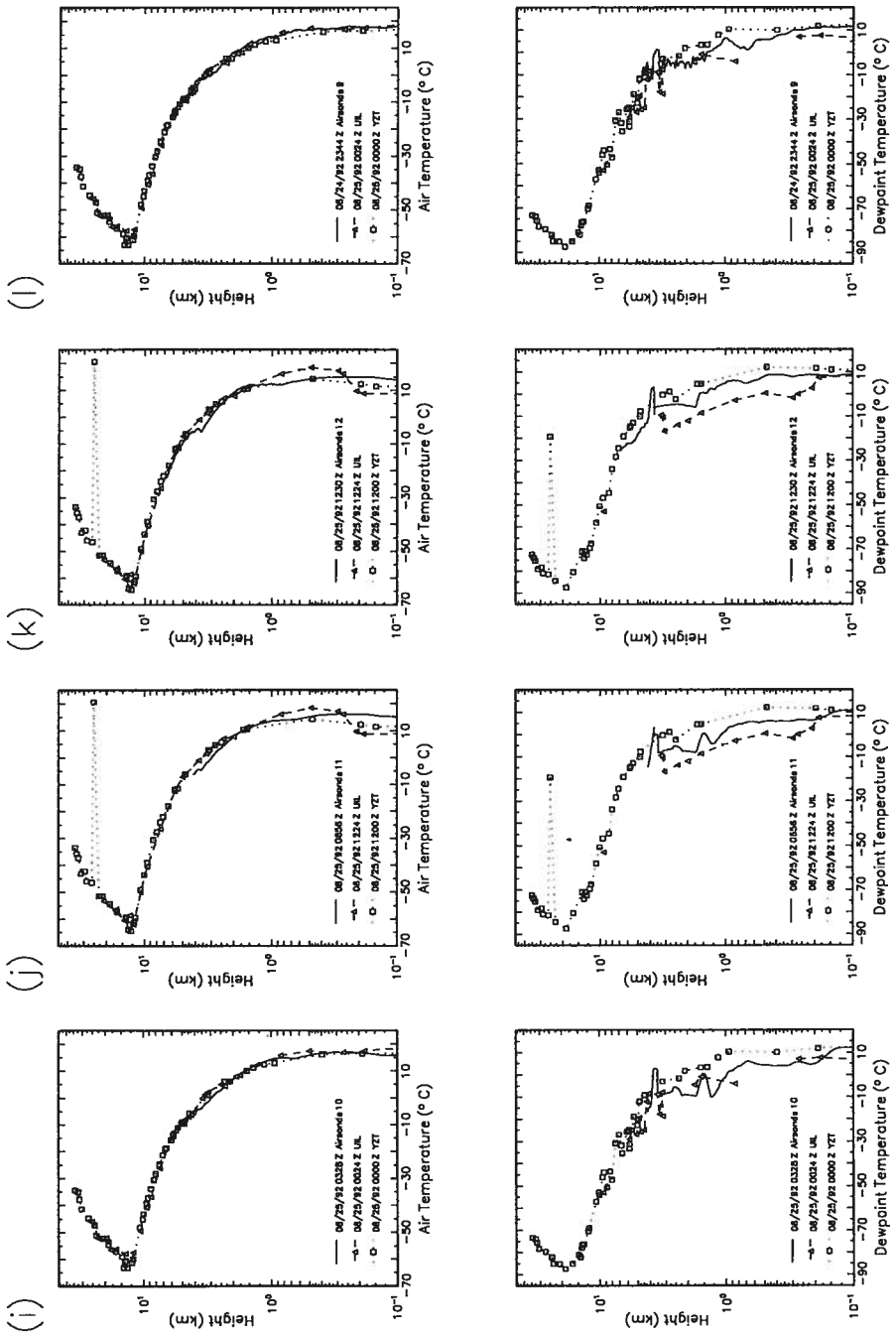

Figure B.1 (*Continued*). Atmospheric profiles for: (i-l) Flights 9–12.

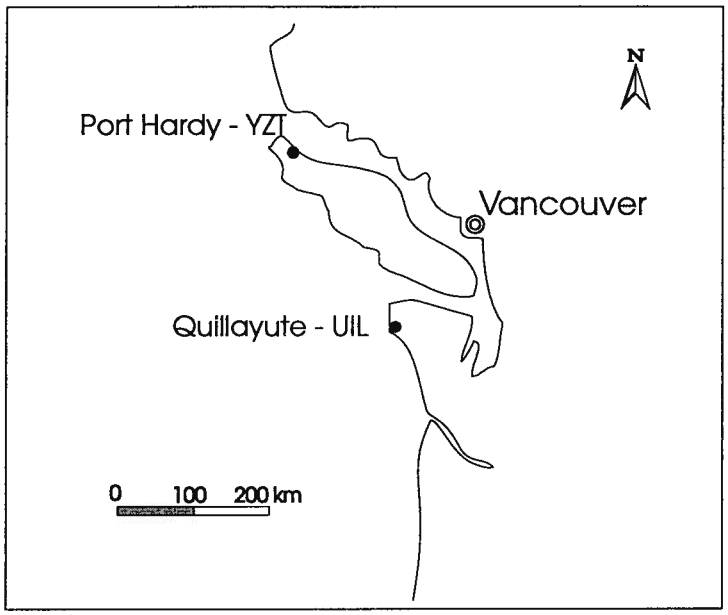

Figure B.2: Location of the Vancouver study area and upper air reporting stations Port Hardy, B.C. (YZT) and Quillayute, WA (UIL).

are now part of the atmospheric path between the surface and sensor. In the absence of raw sounding data (which are accurate down to a *RH* of 1% (Garand *et al.*, 1992)) the recovery of the actual humidity is not possible. This leaves only the possibilities of layer omission, replacement or interpolation. In this study, humidity data from the mid-latitude summer atmosphere are used to replace missing data, or data below the 1% *RH* limit.

B.4.3 Climatological Data

When atmospheric data are required for levels above the maximum altitude of the radiosondes, pressure and temperature data are taken from the mid-latitude summer atmosphere as specified in the LOWTRAN 7 model. This climatological profile matches observed

Table B.2: Summary of radiosonde data collected.

Flt	Airsonde		YZT		UIL		Reported Levels[a] / z_{max}[b]		
	Date	Time[c]	Date	Time	Date	Time	YZT	UIL(T_a)	UIL(T_d)
1	15	1648	15	1200	15	1224	43/33.3	35/23.3	20/9.7
2	15	2037	16	0000	15	1224	42/35.2	35/23.3	20/9.7
3	16	0037	16	0000	16	1239	42/35.2	29/25.4	19/9.6
4	16	1822	17	0000	16	1239	42/35.3	29/25.4	19/9.6
5	16	2316	17	0000	17	0024	42/35.3	34/26.1	19/9.7
6	17	1653	17	1200	17	1224	33/37.2	23/22.5	13/9.6
7	17	2054	18	0000	18	0033	50/35.3	36/31.7	18/9.3
8	17	0012	18	0000	18	0033	50/35.3	36/31.7	18/9.3
9	24	2346	25	0000	25	0024	51/34.1	42/26.6	27/9.3
10	24	0328	25	0000	25	0024	51/34.1	42/26.6	27/9.3
11	24	0656	25	1200	25	1224	40/35.1	32/22.5	18/9.4
12	24	1230	25	1200	25	1224	40/35.1	32/22.5	18/9.4

[a]number
[b]km
[c]UT time

profiles of air temperature well (Figure B.3a). The local soundings are shown to be somewhat drier than the mid-latitude summer profile, especially at mid-levels (Figure B.3b), but there is some variation between soundings. Generally good agreement exists at upper levels when relative humidities are greater than 1%. The 1% *RH* limitation for station YZT is clearly evident (Figure B.3c).

B.5 Airborne Imagery vs. Surface-Based Measurements

Coincident with the time of the over-flights, ground-based observations of the temperature of selected surfaces were conducted at a nearby site. The surfaces sampled were

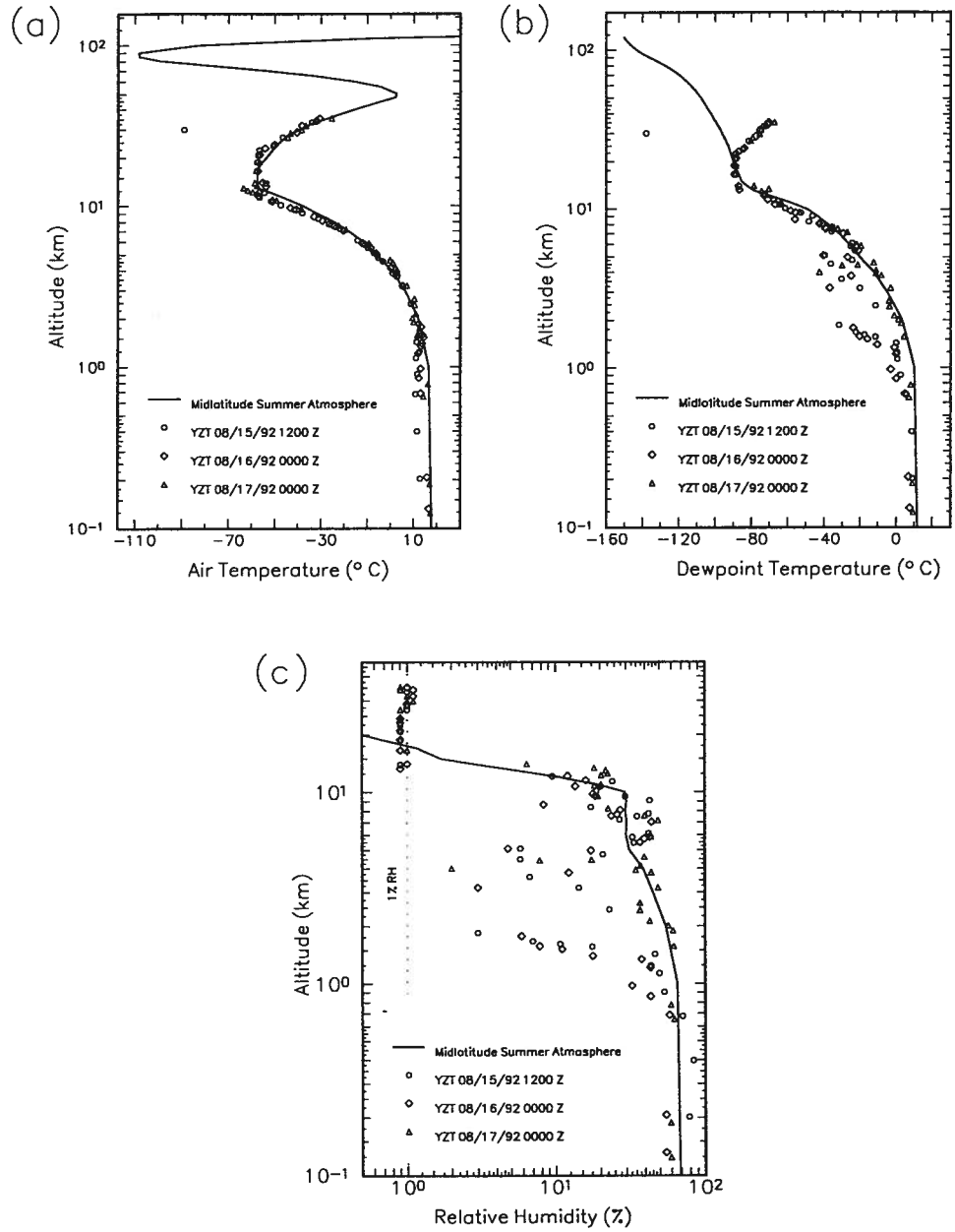

Figure B.3: Comparison of the LOWTRAN 7 Midlatitude summer atmosphere model with measured profiles from station YZT; (a) air temperature, (b) dewpoint temperature, (c) relative humidity.

Table B.3: Summary of reporting differences for radiosonde measurements. Compiled from Garand *et al.* (1992) and Elliot and Gaffen (1991).

U.S. Practice	(1)	when $RH < 20\%$, DPD set to 30 K
	(2)	when $T_a < -40°C$, no humidity reported
	(3)	when $RH > 90\%$, use old sensor algorithm for signal to RH conversion
Canadian Practice	(1)	when $RH < 9\%$, set $RH = 9\%$ and convert to DPD
	(2)	when $T_a < -65°C$, no humidity reported
	(3)	when $RH > 90\%$, use new sensor algorithm for signal to RH conversion

chosen to give as wide a temperature range as possible (Table B.4).

Ground-based sampling was carried out using a 60° FOV Everest IRT (sensitive to radiation in the 8–14 μm waveband) held approximately 0.5–0.75 m above the target surface, and at an off-nadir angle of approximately 30–45°, to avoid viewing the operator.

Calculated surface areas viewed for these sensor positions range from approximately 0.5 m to 3.1 m. The large FOV of the Everest allows better spatial sampling and matching with the IFOV of the AGEMA scanner at higher flight altitudes. However, the off-nadir sampling is not ideal for rough surfaces such as grass, which may be susceptible to variations in emission with view angle and direction (Parsons, 1985) and the large viewed area may encompass several AGEMA pixels, at the lower scanning altitudes used for Flights 1–8. Samples were made at 1 s intervals for 6 s per surface and recorded on a CS 21X datalogger. The fast sampling rate and relatively few samples per site allow all surfaces to be sampled within 5–10 min of the time of the overpass. Comparisons are made using apparent surface temperatures uncorrected for emissivity. This requires that the surface emissivities be constant over the spectral range of both instruments (surfaces are

Table B.4: Ground calibration sites and surface types sampled

Flights	Calibration Site	Surface Types	Samples
1 – 3	Johnathan Rogers Park	grass	(3)
		concrete	(3)
		asphalt	(3)
4 – 5	Portside Park	grass	(3)
		sand	(3)
		asphalt	(3)
		water	(1)
6 – 8	Memorial Park	grass	(3)
		asphalt a	(3)
		asphalt b	(3)
		water	(3)
9 – 1	Trafalgar Park	grass	(3)
		concrete	(3)

greybodies), and for sky radiance to be considered as blackbody emission. If radiance received by the Everest IRT on the ground is represented by

$$L_{ev} = \epsilon \cdot L_o + (1 - \epsilon) \cdot L_{sky} \tag{B.3}$$

then the radiance at the AGEMA scanner at a given flight altitude can be written

$$L_{ag} = \tau \cdot L_{ev} + L_a. \tag{B.4}$$

Look-up tables (LUT) for AGEMA apparent temperature were constructed at 1°C intervals of surface (Everest IRT) apparent temperature using eq. B.4 (converted to photon emissions), with L_{ev} given by an integration of Planck's law for the surface apparent temperature, and τ and L_a modelled using LOWTRAN 7. Plots of the LUT are presented

in Figure B.4.

The temperature corrections are equivalent to the temperature difference which must be added to, or subtracted from, the apparent AGEMA surface temperature in order to obtain the true surface apparent temperature. Note the large range of correction required across the range of temperatures possible in urban areas. Cool, irrigated lawns may require a reduction in temperature while very hot surfaces such as roads or rooftops require a large positive correction.

The calibration site is located on an AGEMA image and a subset of pixels centred on this point is extracted. The pixel apparent temperatures are converted to surface apparent temperatures (corrected for atmospheric emission and transmission) via the LUT. A window of pixels is used because the Everest FOV may cover several pixels and precise location of the ground calibration point on the image is difficult in some cases. This is important for those surfaces which show significant spatial variation in surface temperature but are devoid of highly contrasting thermal features which could be used to more precisely fix the ground measurement site. This is often the case with the grass surfaces which show local spatial variations of uncorrected apparent temperature exceeding 2 degrees. The use of the low emissivity target as a control point helps to overcome this problem but is not completely satisfactory; image blurring due to platform and operator motion results in a smearing of the relatively cool target temperature into the nearby surfaces which makes comparison of grass temperatures difficult for high altitude flights.

A check was made to compare the results of this method with that of using eq. B.1. Measured values of ϵ were obtained for the sites (Table B.5). Generally good agreement exists between the measured ϵ values and those reported in the literature (Table B.6), keeping in mind expected variations in ϵ of sand (due to quartz content) and grass (due to moisture content, species and surface structure). Sky radiance in the 8–14 μm waveband

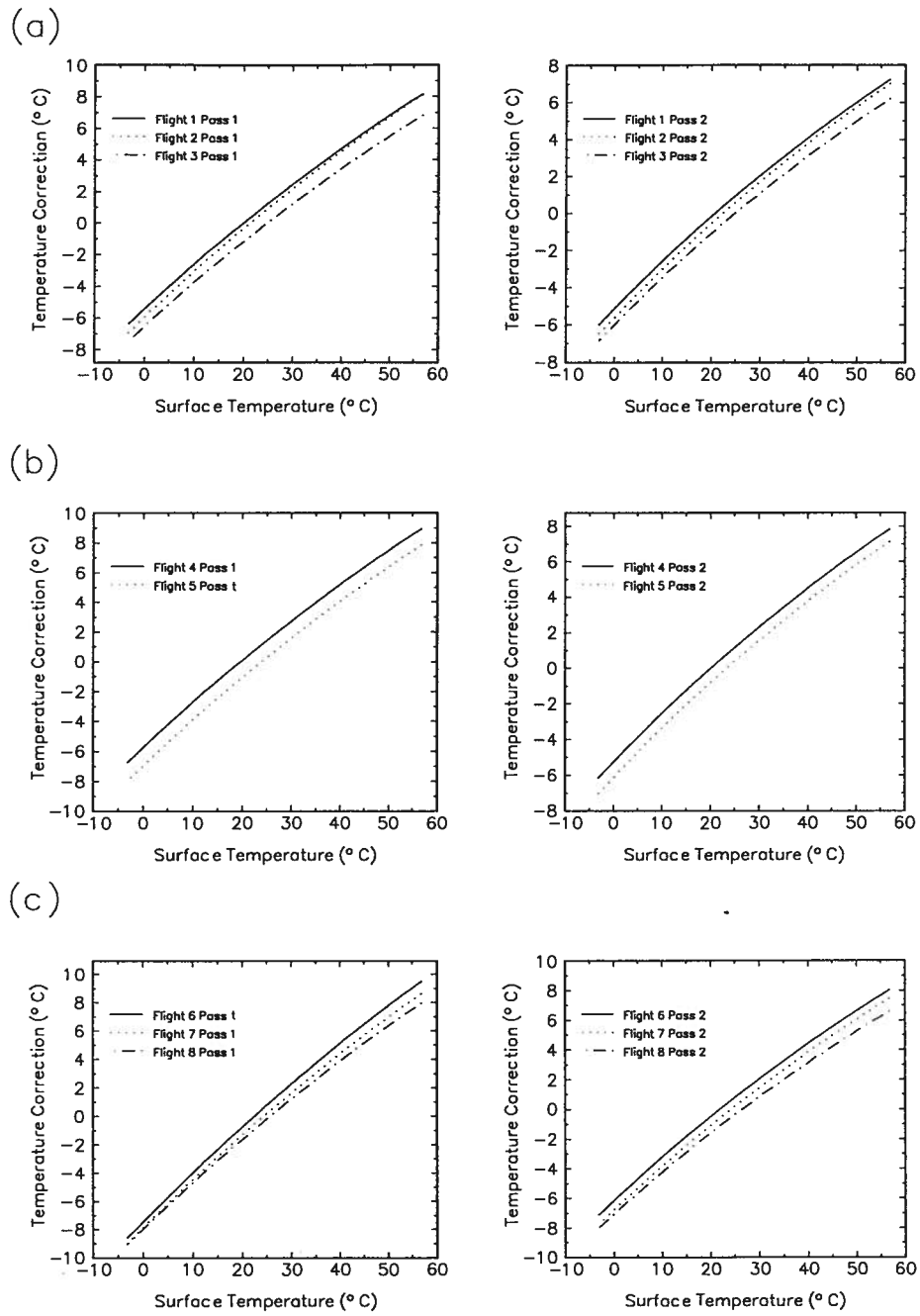

Figure B.4: Look-up table plots of the atmospheric correction required to account for atmospheric absorption and transmission (but not surface reflection) on each day flights were conducted: (a) Flights 1–3, (b) Flights 4–5, (c) Flights 6–8.

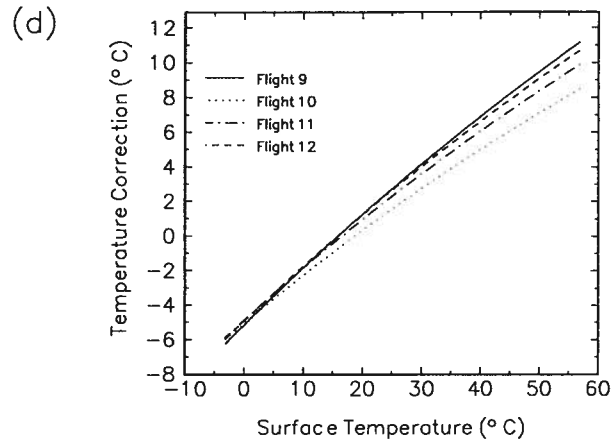

Figure B.4 (*Continued*). (d) Flights 9–12.

was modelled using LOWTRAN 7 using the composite atmospheric profiles. Ground-sampled apparent temperatures were converted to L_{ev}, and L_o was obtained from (B.3) using measured surface emissivities and modelled L_{sky}.

Differences between the methods are generally less than 0.1°C. For Flights 1–8, two sets of ground calibration checks were made: one at the start of the mission, at the altitude used for nadir image acquisition (referred to as pass 1), and a second, upon completion of the lower, 45° off-nadir flightlines, (pass 2). Both calibration checks are done at nadir, or near-nadir, sensor angles. Flights 9–12 have a single calibration set and use a limited set of surface types. Results are presented in Figure B.5 where the following plotting conventions have been used:

- vertical solid lines represent the temperature range in the small pixel subset extracted about the estimated location of the sampling point;
- vertical dashed lines represent the range of temperatures viewed over a much larger pixel subset containing the sampling point to indicate the temperature variations possible for that surface type;

- horizontal error bars represent $\pm 1\sigma$ of the ground sampled surface apparent temperature (T_r).

B.5.1 Discussion

Several consistent observations arise from inspection of Figure B.5:

1. agreement between corrected scanner temperature and ground-sampled temperature is better for the second pass of Flights 1–8; the lower scanning altitude results in a shorter path length with a slightly reduced atmospheric correction and also allows more precise location of ground sample points on the image;

2. sea surface temperatures obtained for Flights 1–5 do not agree well. The Everest IRT values are consistently lower and show substantially more variation than the corrected AGEMA temperatures;

3. grass (and to some extent sand) surfaces exhibit a large range of temperatures around the calibration sites, both in the image data and from ground-sampled data;

4. flights conducted after sunset (10–12) show significantly less variation in apparent grass temperature by both Everest IRT and AGEMA (the extension towards cooler temperatures of the AGEMA temperatures is more a function of smearing of the low emissivity target into the pixel subset extracted for the ground sample point, and not indicative of true temperature variation of the grass surface;

5. asphalt and road surfaces exhibit a relatively narrow range of temperature (except the shaded portion of the asphalt surface in Flights 6–8) and generally show good agreement despite the large correction applied, and a relatively low surface emissivity.

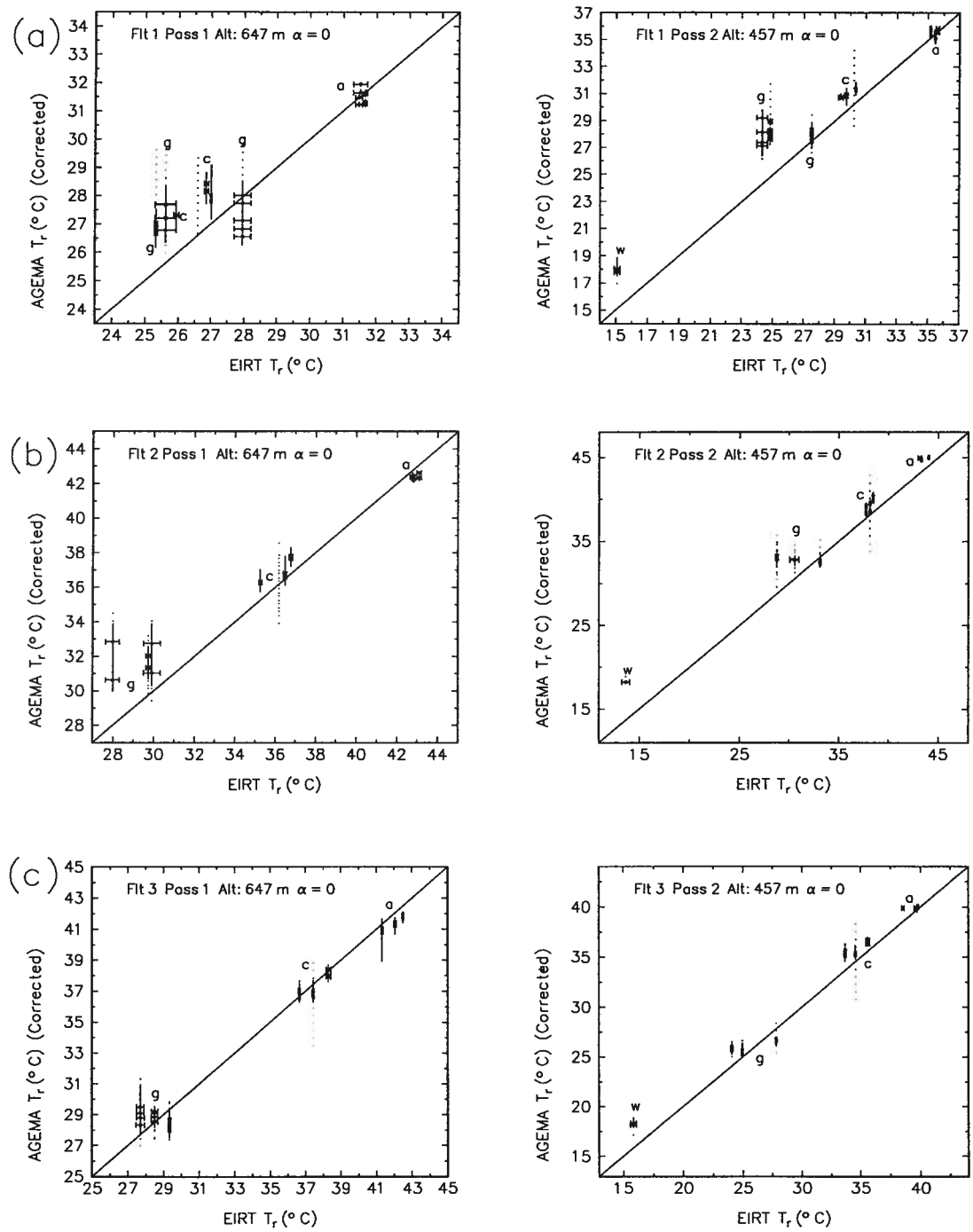

Figure B.5: Comparison of ground-sampled T_r with corrected AGEMA scanner T_r. See text for plotting conventions. Surface types sampled are: a - asphalt (road surface for all but Flights 6–8), c - concrete, g - grass, s - sand, r - road surface (asphalt) (Flights 6–8 only), w - water. Figures (a - c) are Flights 1–3 respectively.

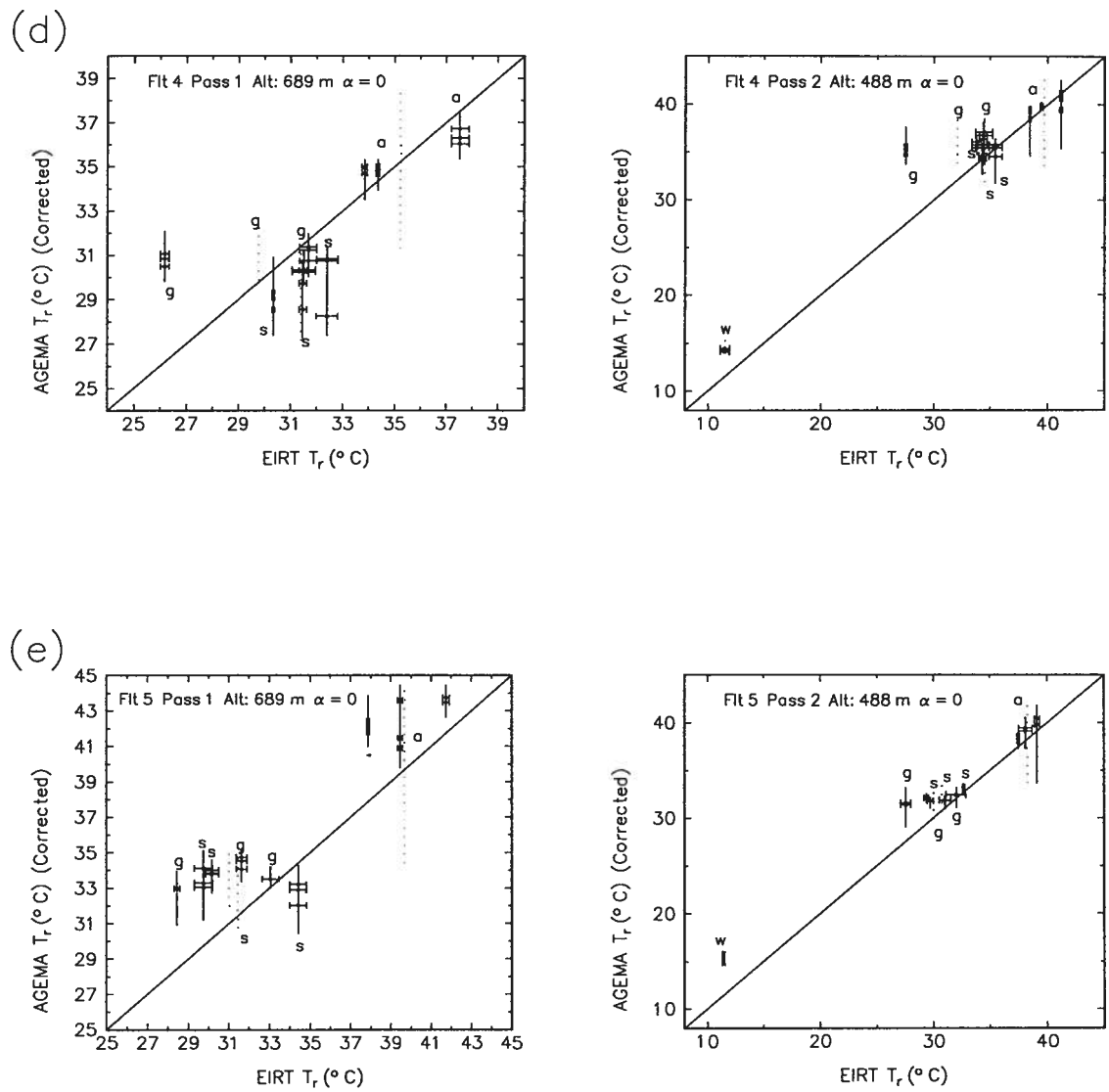

Figure B.5 (*Continued*). (d) Flight 4, (e) Flight 5.

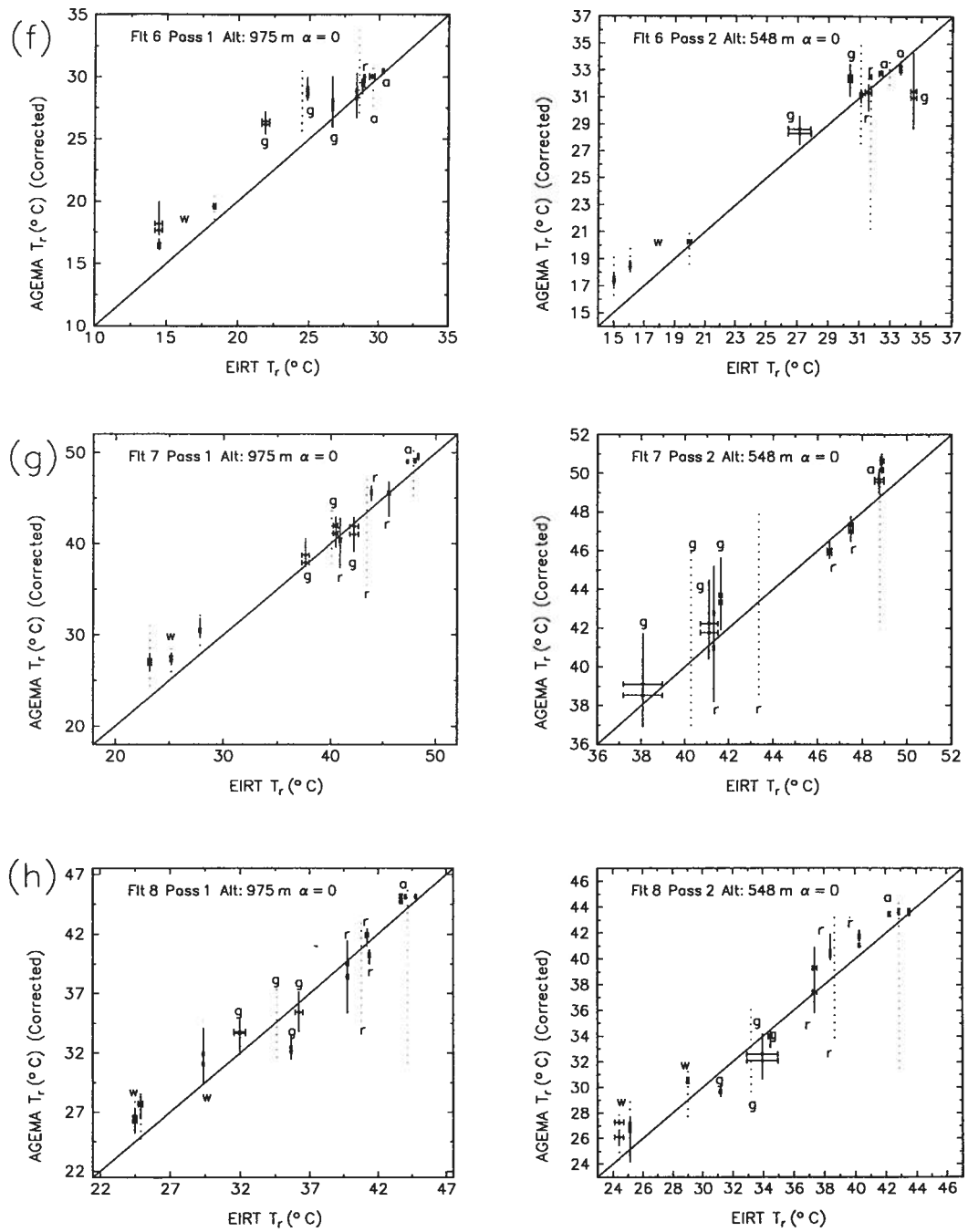

Figure B.5 (*Continued*). (f-h) Flights 6–8.

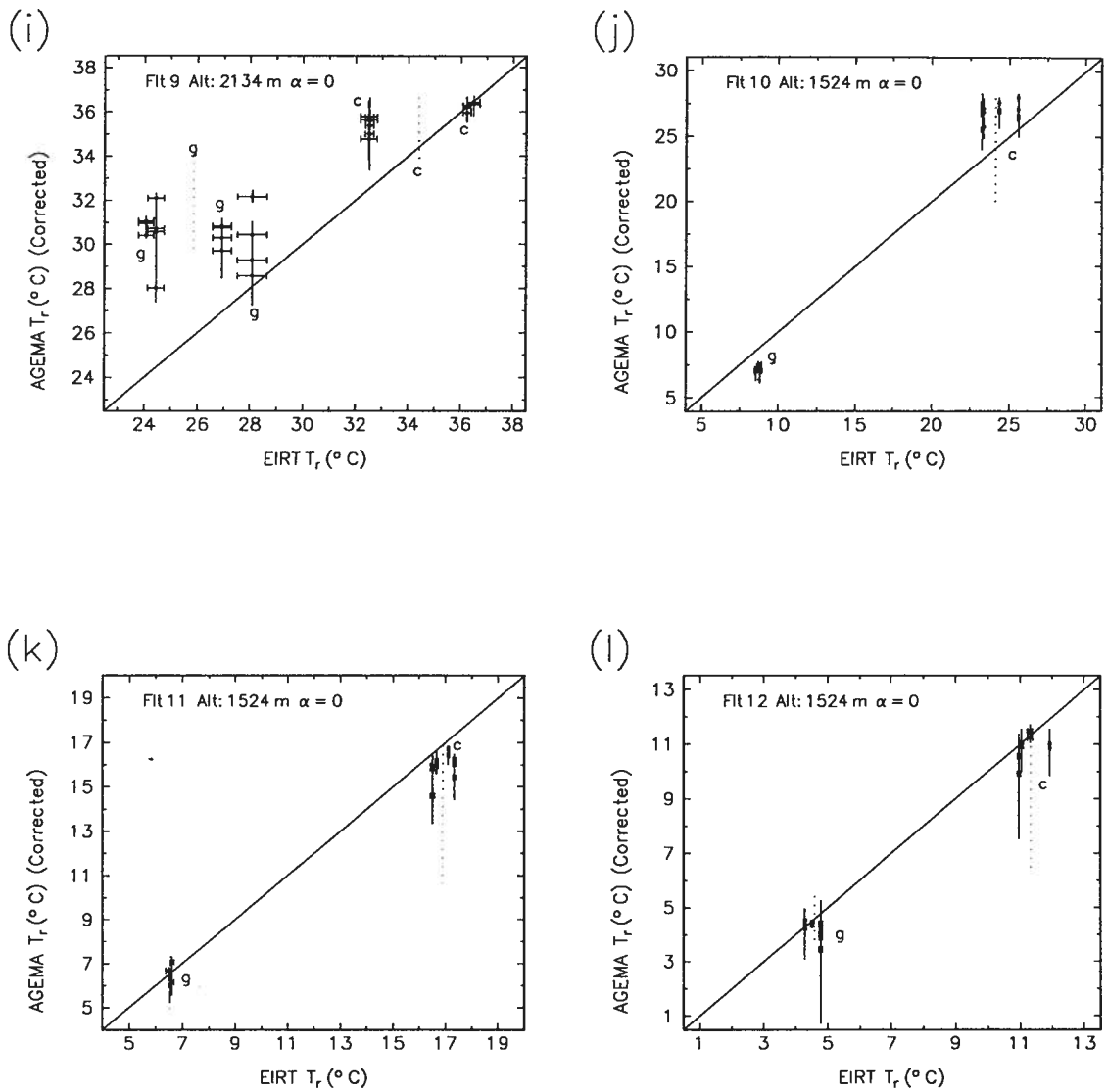

Figure B.5 (*Continued*). (i-l) Flights 9–12.

Table B.5: Surface emissivities for ground calibration surfaces.

Location	Surface	$\bar{\epsilon}$	σ_ϵ	n	Date	Method
Jonathan Rogers park	grass	0.973	0.009	9	08/30/92	1[a]
		0.988	0.004	12	08/03/93	1
		0.993	0.004	12	08/03/93	2[b]
	concrete	0.956	0.008	8	08/30/92	1
		0.960	0.003	19	08/03/93	1
		0.956	0.003	19	08/03/93	2
	asphalt (road)	0.932	0.004	7	08/30/92	1
		0.932	0.005	19	08/03/93	1
		0.926	0.006	19	08/03/93	2
Portside Park	sand	0.957	0.004	20	08/30/93	1
		0.961	0.005	20	08/30/93	2
	asphalt	0.959	0.004	19	08/30/93	1
		0.956	0.005	19	08/30/93	2
	grass (dry)	0.972	0.008	20	08/30/93	1
		0.980	0.007	20	08/30/93	2
	grass (green)	0.988	0.003	18	08/30/93	1
		0.992	0.005	18	08/30/93	2
Memorial Park	grass	0.979	0.007	8	08/30/92	1
		0.985	0.004	24	08/04/93	1
		0.992	0.004	24	08/04/93	2
	asphalt (road)	0.944	0.004	7	08/30/92	1
		0.937	0.003	23	08/04/93	1
		0.928	0.006	23	08/04/93	2
	asphalt (playing sfc)	0.956	0.004	24	08/04/93	1
		0.953	0.005	24	08/04/93	2

[a]Method 1: Davies *et al.* (1971).
[b]Method 2: Chen and Zhang (1989)

Table B.6: Reported values of ϵ for surface types tested. Except where noted spectral range is 8–14 μm.

Surface	ϵ	Reference
grass (dead)	0.966	Sutherland (1986)
grass (live)	0.990	"
very short grass	0.979	Labed and Stoll (1991)
tufts of grass	0.981	"
grass (almost complete cover)	0.958	Van de Griend *et al.* (1991)
lawn: dense and well kept	0.973	Lorenz (1966); 7–15 μm
Big blue stem	0.972	Salisbury and D'Aria (1992); 11.3–11.6 μm
Indian grass	0.971	"
Switch grass	0.969	"
Rye grass (senescent)	0.903	"
sand	0.893–0.915	Sutherland (1986)
	0.938	Lorenz (1966); 7–15 μm
sand (dry)	0.84–0.90	Arya (1988)
concrete	0.942	Lorenz (1966); 7–15 μm
	0.71-0.90	Oke (1987)
asphalt	0.955	Lorenz (1966); 7–15 μm
(old road surface)	0.95	Oke (1987)
water	0.972	Davies *et al.*(1971)
	0.990	Salisbury and D'Aria (1992); 11.3–11.6 μm
	0.925–0.969	Rees and James (1992); ϵ decreases as observing angle (relative to normal) increases

B.5.1.1 Sea Surface Temperatures

Perhaps the most troubling of these observations is the disagreement between AGEMA and Everest apparent sea surface temperatures for Flights 1–5. Presuming the correction method, atmospheric profile, and scanner calibrations to be correct, there are two possible explanations for the disagreement.

Firstly, the off-nadir sampling by the surface-based Everest IRT with it's large FOV may lead to a contribution of direct atmospheric radiance within the FOV. The total FOV of the Everest IRT is actually larger than 60°, with the 60° being defined as the FOV which contributes 80% of the total power distribution (Everest Interscience, 1991). Figure B.6 illustrates the potential for a reduction in T_r for off-nadir instrument angles, due to atmospheric radiance in the Everest FOV. This diagram was constructed as follows. Surface emissions are predicted for given SSTs using the Planck function with a constant emissivity of 0.98. Atmospheric radiance is calculated for a range of angles using LOWTRAN 7 with the composite atmospheric profile constructed for Flight 1. Radiance at the sensor is tabulated at 2° intervals with the source of radiance determined as either the sky or sea surface. Surface emissions are reduced by the prescribed ϵ and a reflected component of atmospheric radiance added. The radiance is weighted with the sensor FOV response, and the total radiance is then converted to an apparent temperature. The results in Figure B.6 indicate that for off-nadir angles greater than 30°, sharp decreases in apparent surface temperature are possible. The slight warming trend evident at 35° for lower SSTs is due to the relatively high atmospheric emission for angles close to the horizontal (i.e., close to blackbody emission at air temperature).

The importance of these effects is enhanced if the angular emissivity variations of Rees and James (1992) are considered. These authors found a decrease in emissivity of 0.05 with depression angles between 30 and 60°, for shallower angles further decreases

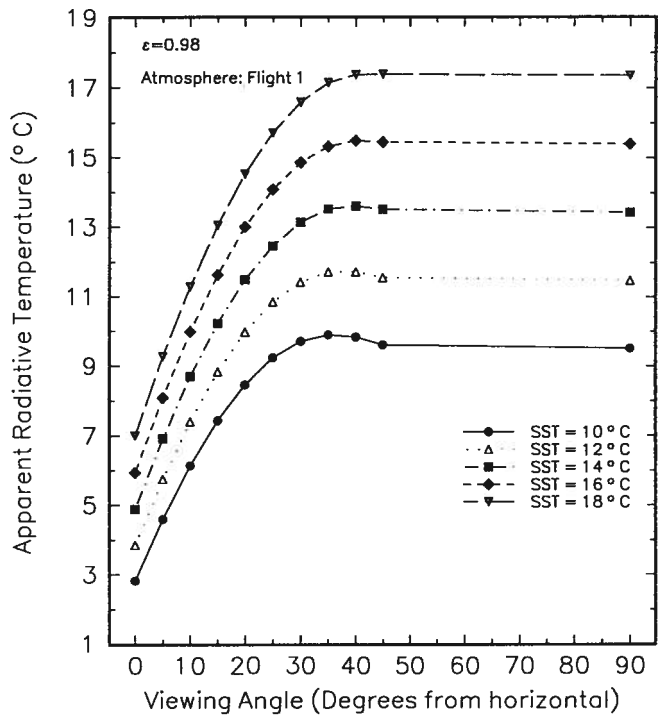

Figure B.6: Modelled variations in apparent radiative surface temperature for a 60° FOV Everest IRT viewing a water surface.

were observed (down to 0.4) but confidence in these results was limited. These results were for calm water conditions and so are not directly applicable here, however, the general trend, leads to the type of disagreement found here. The relatively large standard deviation obtained from the Everest IRT water samples may be a result of variations in the angle at which the instrument is held between samples. Secondly, the apparent discrepancy between AGEMA and Everest IRT SSTs might be due to specular reflection of solar radiance into the sensor FOV. This is commonly known as sunglint. If the sensor is pointing towards the specular point of the Sun, specular reflection of solar radiance into the sensor FOV will result in increased apparent surface temperatures. When the sea surface is calm, the range of angles at which this is possible is low, but as wind speeds increase and surface roughness increases, the range of observation angles affected

Table B.7: Solar position and AGEMA scanner and Everest azimuth angle direction: Flights 1–5. Image azimuths approximate only. Scanner angle is nominally 0° (nadir) but may be up to 20° off-nadir. Z - solar zenith angle, ϕ - solar azimuth angle. Time is local time (PDT).

Flight	Time	Z	ϕ	Image Azimuths	Everst Az	Time
1	1103	44.9	131.2	203	292.5	1114
2	1424	38.4	207.5	180	"	1438
3	1744	65.0	261.5	180 - 225	"	1758
4	1208	38.6	153.2	225 - 248	337.5	1217
5	1608	50.5	239.7	315	"	1634

increases up to 30° from the specular point (Duggin and Saunders, 1984).

Recent observations of sunglint in NOAA polar orbiting satellites indicate SST differences of up to 2 K in the thermal infrared channels 4 and 5 (Khattak *et al.*, 1991). Greater errors may be anticipated for the AGEMA sensor which also responds to some shorter wavelength infrared radiation. In lieu of attempting to model the degree to which specularly reflected solar radiation may be present in the AGEMA (see e.g., Cox and Munk (1954), Khattak *et al.* (1991), Eitner (1992), Cracknell (1993)) which requires knowledge of slope distribution functions of waves, or a second visible channel, Table B.7 is presented to determine the extent to which the view angles are aligned with the solar specular point.

Table B.7 indicates there is potential for several of the flights to be affected when considering the spread of sunglint about the specular point with waves on the sea surface, but there is no consistent pattern of alignment for all flights. The Everest alignment also shows some potential for sunglint observation in Flights 3 and 5, however, significant differences between it and the AGEMA apparent temperature remain (Figure B.5).

Inspection of the AGEMA images taken over False Creek (Flights 1–3), and Burrard Inlet (Flights 4–5), fail to show evidence of sunglint in terms of areas of increased surface apparent temperature or increased local variation of temperature. Unfortunately, no ground-based observations of water temperature were made during the flights after sunset; the available remotely-sensed images taken over Lost Lagoon, (a small freshwater lake) and English Bay (tidal, saltwater) do not indicate an increase in the range, or variation of surface apparent temperatures, taken during the afternoon flight, when compared to the post-sunset flights.

In conclusion, the available evidence appears to indicate a discrepancy in the Everest IRT value rather than the AGEMA temperature.

B.5.1.2 Grass Temperatures

The apparent scatter between airborne- and surface-sampled grass temperatures may arise as the result of a number of factors. The relatively large range of temperatures obtained for both the surface and airborne measurements indicate there is significant spatial variation over the grassy surfaces which makes the correct identification of the ground sampling point critical. These variations may be a function of microscale differences in moisture content, slope, emissivity and surface structure. Differences in the look angle and IFOV of the two instruments used may also contribute, especially considering grass, as with other vegetation canopies (see e.g., Paw U, 1992), has been observed to be a non-Lambertian emmitter (Parsons, 1985). This behaviour occurs due to the combination of vertical (grass blades) and horizontal (turf layer) components which are seen in differing proportions by sensors at different viewing positions.

Although the agreement in the mean between the points is not good, the ranges spanned by the two instruments tend to be similar for most flights, and decreases significantly for the night time flights. This suggests local differences in sensor position and

orientation, coupled with the relatively large, true variation in surface temperatures, are responsible for the apparent scatter.

Appendix C

EVEREST INTERSCIENCE MODEL 4000A IRT

C.1 Instrument Description.

The EIRT is a small, light, self-contained, micro-computer based infrared temperature transducer incorporating a mechanical chopper. Instrument specifications are listed in Table C.1.

Table C.1: Everest Interscience Model 4000A Infrared Transducer Specifications. (Everest Interscience, 1991)

FOV:	15° (80% of total signal)
Spectral response:	8 - 14 μm
Scale Range:	-30°C–100°C
Precision:	± 0.1°C
Accuracy:	± 0.5°C
Resolution:	0.1°C
Emissivity:	0.1–0.999 software selectable (normally 0.98)

C.2 Instrument Operation

The EIRT optics collect incident radiation and focus it on a detector. The stated FOV is for 80% of the total signal; the radiant power distribution received from a surface is shown in Figure C.1.

The detector produces an electrical signal proportional to the radiation received. This is conditioned, using internal circuitry, to produce a linear voltage-temperature

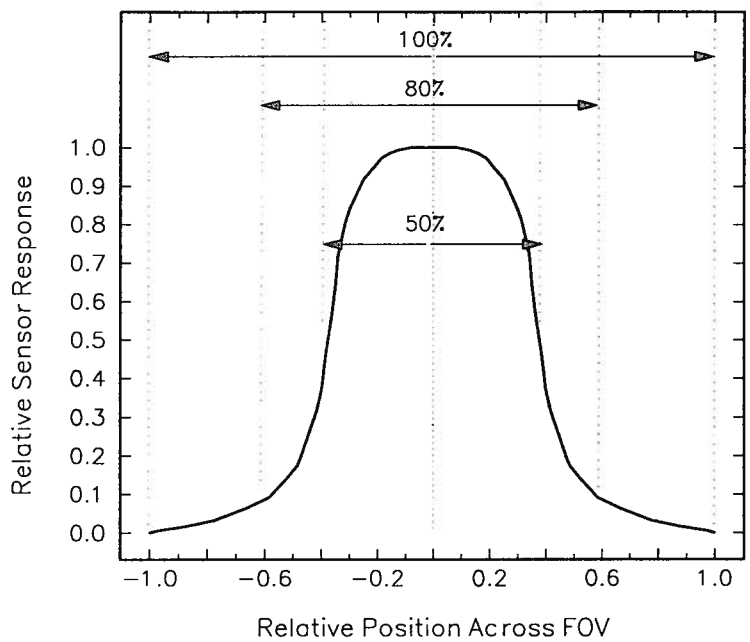

Figure C.1: Radiant power distribution received by EIRT from a surface. (Everest Interscience, 1991).

relation. The output analog voltage signal was recorded using a Campbell Scientific CS 21X datalogger. A block diagram of the EIRT components is presented in Figure C.2.

The Model 4000A EIRT uses a mechanical chopper of known temperature to self-calibrate during instrument operation. The chopper operates on a 500 ms period. For the first 250 ms of the period the chopper obscures the optical aperature. During the remaining 250 ms, the aperature is open and the temperature value is updated, based upon the last 50 ms of the time during which the aperature is open (C. Everest *pers. comm.*). The use of the mechanical chopper significantly improves the performance of the EIRT under conditions of changing ambient temperature, removing the need to monitor instrument body temperature (Wright, 1990). During operation, the instruments were shielded and insulated to minimize heating and cooling gradients imposed by alternate sun and shade while traversing, and to reduce the effects of diurnal temperature changes.

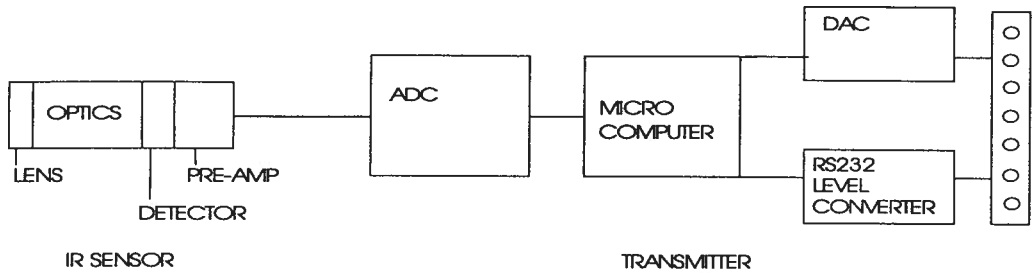

Figure C.2: Block diagram of EIRT. (Everest Interscience, 1991).

The software selectable emissivity is used to amplify the detector output signal (by a factor of $\frac{1}{\epsilon}$) so that the output is analogous to that of a blackbody at the same temperature; ϵ was set at 0.98 on the EIRTs used in this study. Conversion to blackbody apparent temperature is possible using eqs. C.1- C.4, supplied by the manufacturer:

$$T_{r_1} = T_{r_1} - T_{det} \tag{C.1}$$

$$\begin{aligned} E_1 &= -4.022402 \cdot 10^{-3} + 1.47937473 \cdot 10^{-2} \cdot T_{r_1} + 9.84784552 \cdot 10^{-5} \cdot T_{r_1}^2 \\ &- 1.16050526 \cdot 10^{-7} \cdot T_{r_1}^3 - 1.08464168 \cdot 10^{-8} \cdot T_{r_1}^4 \\ &+ 4.39174381 \cdot 10^{-11} \cdot T_{r_1}^5 \end{aligned} \tag{C.2}$$

$$E_2 = \frac{\epsilon_1}{\epsilon_2} \cdot E_1 \tag{C.3}$$

$$\begin{aligned} T_{r_2} &= -0.3794 + 68.1983 \cdot E_2 - 21.9711 \cdot E_2^2 + 15.1732 \cdot E_2^3 \\ &- 11.8715 \cdot E_2^4 + 5.2213 \cdot E_2^5 \end{aligned} \tag{C.4}$$

$$T_{t_2} = T_{det} + T_{r_2} \tag{C.5}$$

where T_{rn} is the relative temperature at emissivity setting ϵ_n, T_{t_n} is the target temperature recorded with ϵ_n, E_n is the adjusted voltage, and T_{det} is the detector temperature.

Figure C.3 illustrates the sensitivity of recorded target temperature to a change in ϵ from 0.98 to 1.0 for two detector temperatures, and the difference in temperature incurred by errors in estimating a detector temperature. The results suggest that if equivalent blackbody temperature is desired, the accuracy in estimating the detector temperature is less important than not including the emissivity setting at all, except for surfaces much colder than the detector.

C.3 Instrument Calibration

The EIRT are delivered having undergone factory calibration checks for two surface temperatures (26 and 76°C) at an air temperature of approximately 25°C. Checks on the instrument calibrations were conducted using the calibration facilities of the University of California (Davis) (1991) and the UBC Soil Science Department (1992, 1993). Differences in the calibration procedures lead to differences in the derived relations between cavity temperature (T_{cav}) and EIRT temperature (T_{ev}) (Table C.2). The 1991 and 1993 calibrations utilized short exposure to a blackbody cavity of relatively constant temperature, whereas the second calibration used a long term exposure to a slowly changing blackbody cavity temperature. Greater differences between the cavity and EIRT temperatures were obtained for the 1992 calibration, especially at low cavity temperatures, which may be due to thermal coupling between the cavity and EIRT creating temperature gradients within the EIRT. These are known to cause errors in EIRT output temperature (Wright, 1990) on the order of 0.5°C for a body temperature gradient of -2°C/10 min. Measurement of external EIRT surface temperature changes (probably larger than internal temperature gradients) during some parts of the 1992 calibration, yielded surface cooling gradients at the start of the calibration between -1.5–2.5°C over 10 minute periods. Some instances exceeded 4°C/10 min at the beginning of the calibration (calibrations began

at the low temperature end of the EIRT scale). During traverse operations, instrument temperature is assumed to be near air temperature and the results of the 1991 and 1993 calibrations are probably most relevant, because instrument temperature is more constant in those calibrations. Calibration equations are based upon an emissivity setting of 0.98. Conversion of EIRT recorded temperature to apparent blackbody temperature requires estimation of T_{det}. This can be accomplished by using air temperature (available for the 1992 and 1993 calibrations) although this introduces an error if $T_{det} \neq T_a$ (see Figure C.3). Regression relations between T_{cav} and T_{ev} ($\epsilon = 0.98$) and T_{cav} and T_{ev} ($\epsilon = 1.0$) yield results generally to within ± 0.1°C.

Table C.2: EIRT calibration results using $T_{ev} = a + bT_{cav}$; $\epsilon_{ev} = 0.98$.

Instrument	a	b	Temp. range (°C)
2094-1	0.203	1.001	10-54
2094-2	0.124	0.996	12-50
2094-3	1.632	0.988	12-54
2094-4	0.571	0.993	11-54
2094-5	5.051	0.937	15-55
2094-6	1.835	0.941	12-52

Results of the most recent calibration indicate that one EIRT (SN 2094-5) incorporates a substantial offset (Table C.2). The remaining EIRT show some differences from a perfect fit, although only 2 were best fit by models which lie outside the expected accuracy range of the EIRT (± 0.5°C). In this study, instruments are corrected using the most recent calibration results to obtain equivalent blackbody temperature, with an instrument emissivity setting of 0.98.

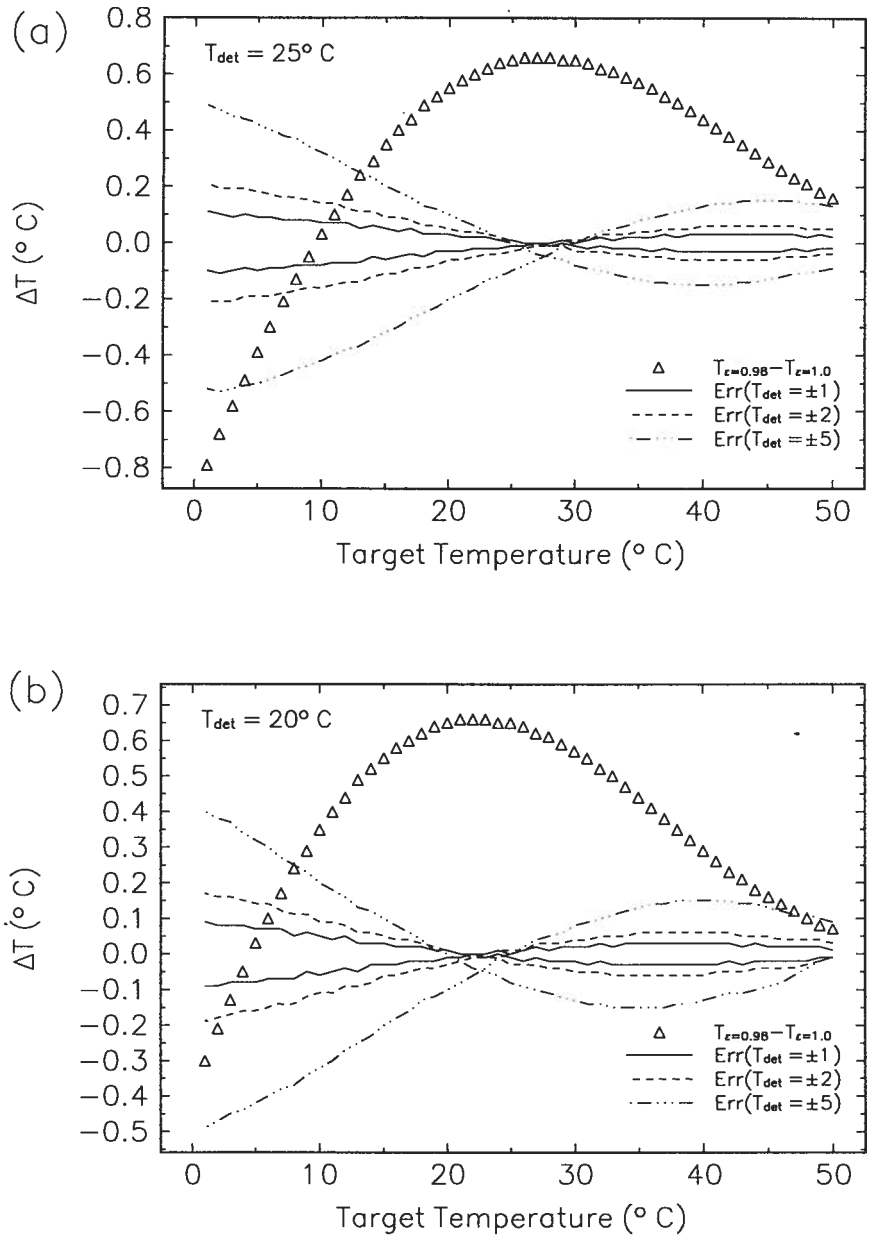

Figure C.3: Temperature differences due to conversion of T_{ev} from $\epsilon_{ev} = 0.98$ to 1.00 (symbols) and differences due to using T_{det} ±1,2,5°C in place of T_{det} (lines).

Appendix D

TIR REMOTE SENSING COVERAGE OF THE STUDY AREAS

This appendix presents maps illustrating the location of the study sites within the Vancouver area (Figure D.1) and the approximate bounds of coverage obtained for each scanner orientation on each flight (Figures D.2 – D.9). The figures include composite coverage maps for orthogonal scanner azimuths (North-South, East-West), a complete composite for all four scanner azimuths, and a total composite which includes the nadir coverage.

Gaps in the coverage of some flights are a result of difficulties by the scanner operator in maintaining the required scanner orientation due to motion of the helicopter and difficulties in locating the correct target on the ground. The area of coverage for Flights 6-8 (Residential study area) was restricted by air traffic control because of noise concerns of residents.

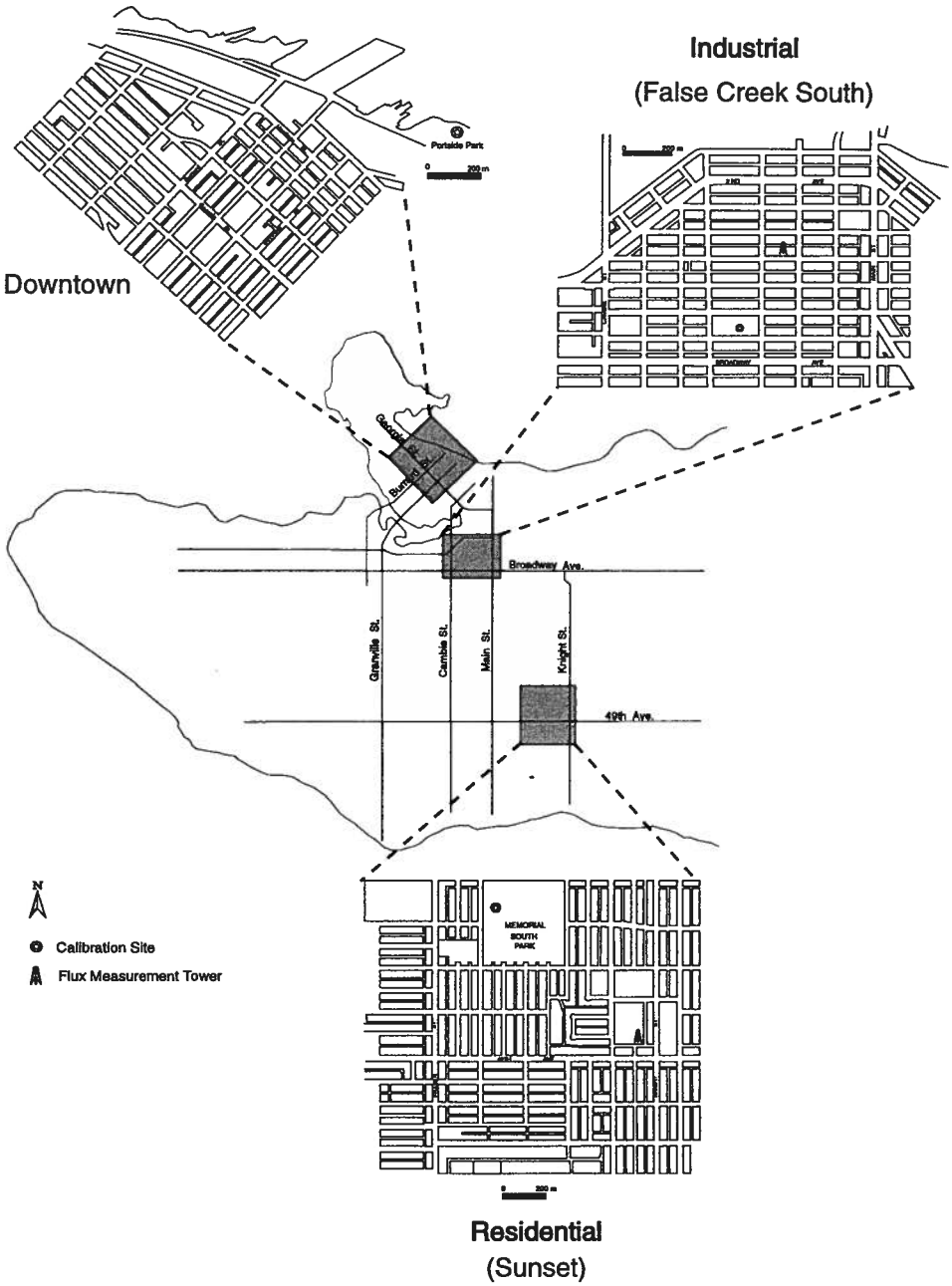

Figure D.1: Study areas in Vancouver, B.C. Clockwise, from top right: Industrial (False Creek South) Flights 1–3, Residential (Sunset) Flights 6–8, Downtown Flights 4–5.

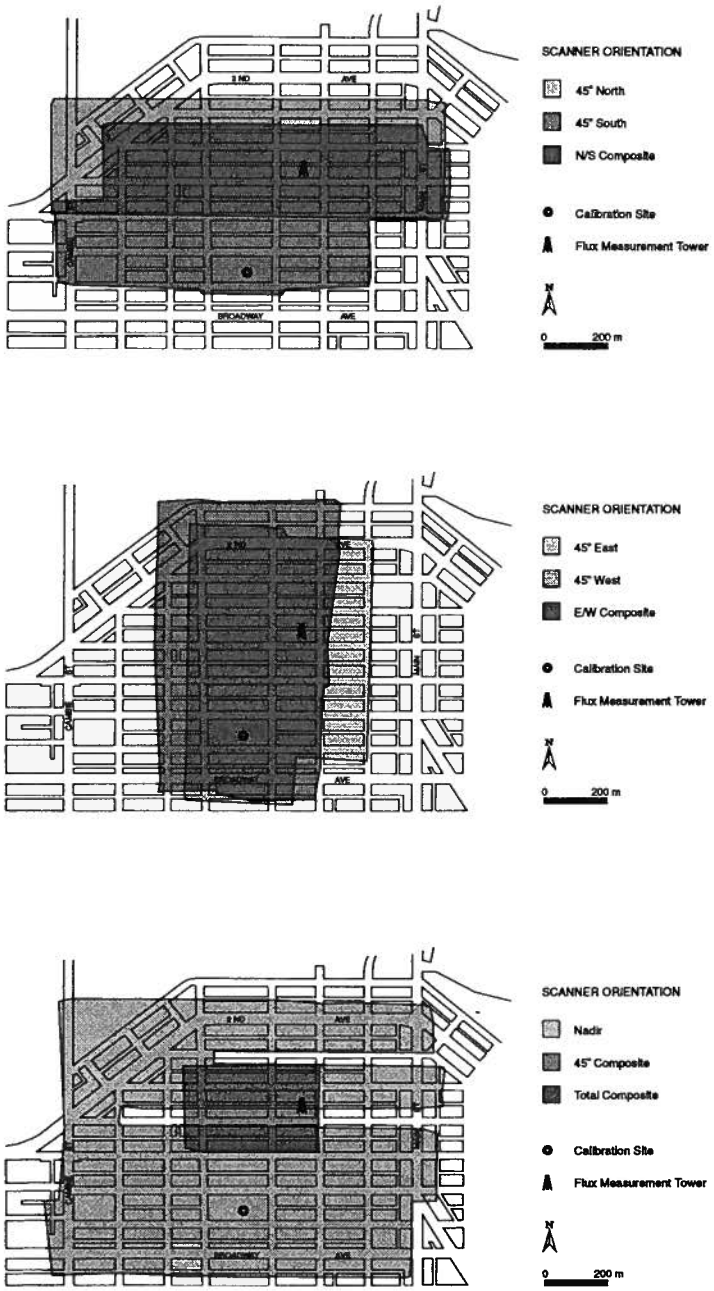

Figure D.2: Scanned areas (by direction) and composites for Flight 1 (Industrial area: August 15, 1992; 1030 PDT). (a) North and south scanner azimuths, (b) east and west scanner azimuths, (c) nadir and total composites. Scanner angle is approximately 45° off-nadir for each azimuth.

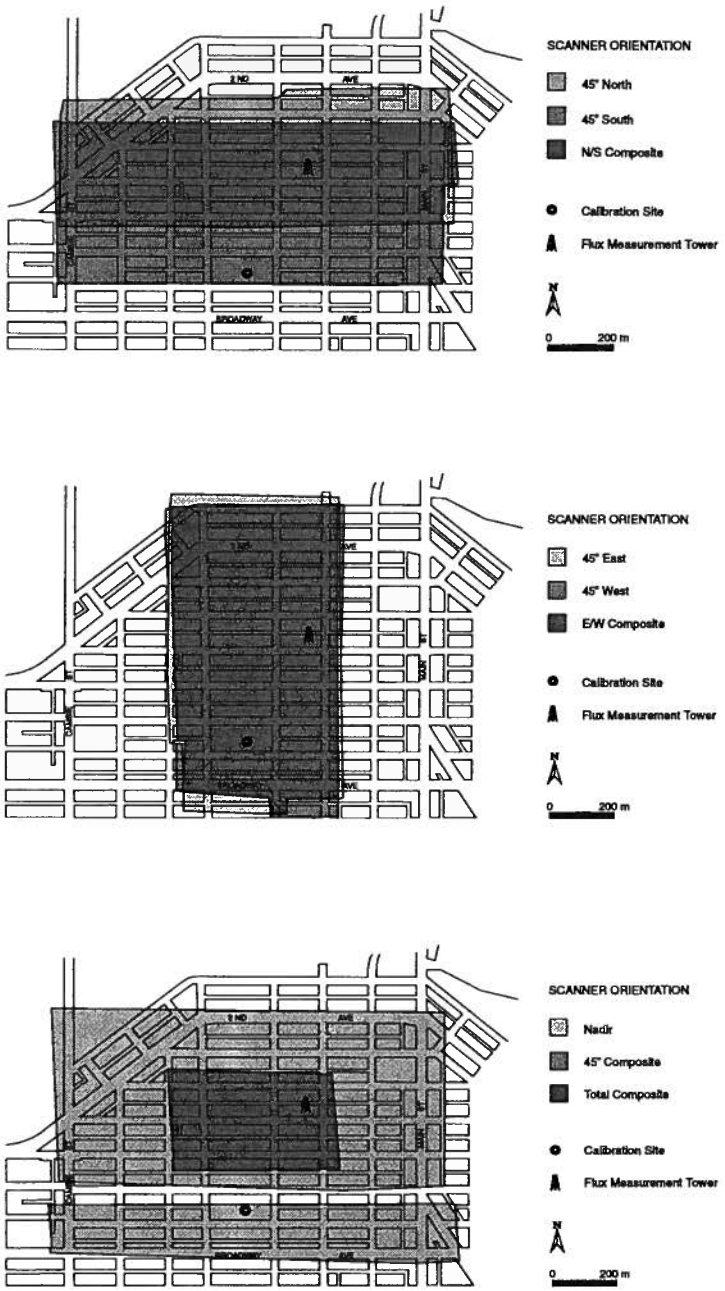

Figure D.3: Scanned areas (by direction) and composites for Flight 2 (Industrial area: August 15, 1992; 1400 PDT).

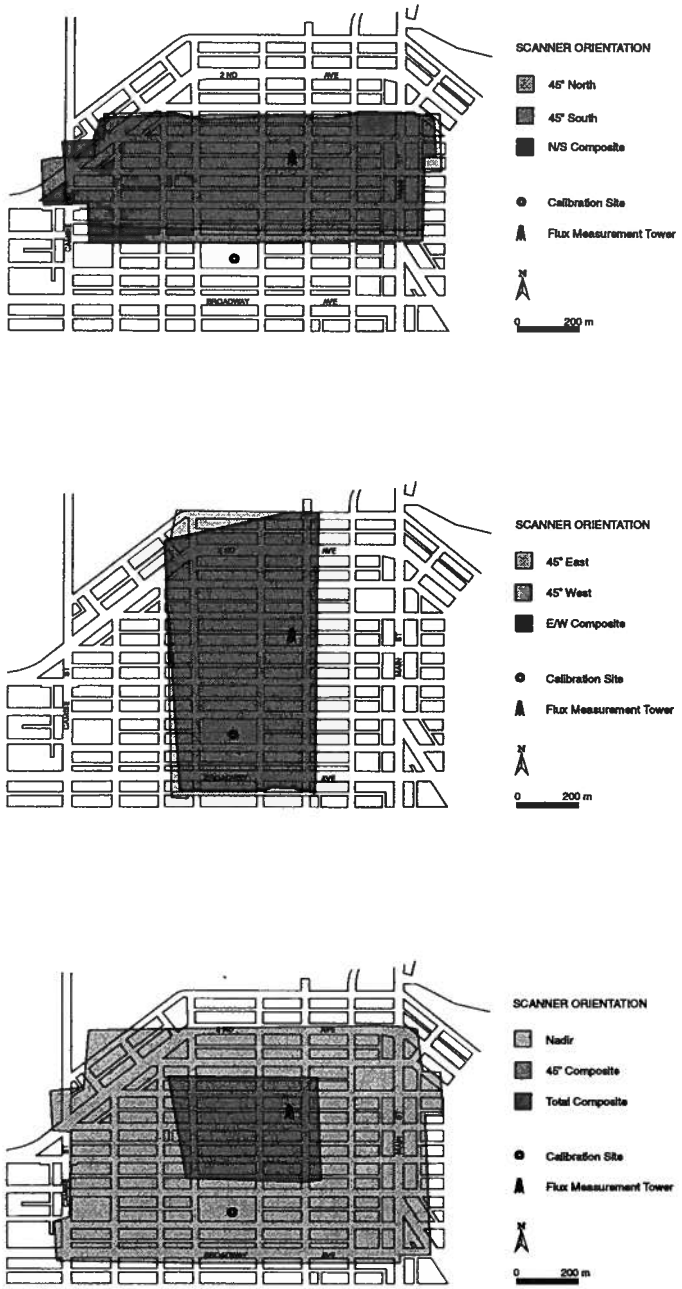

Figure D.4: Scanned areas (by direction) and composites for Flight 3 (Industrial area: August 15, 1992; 1730 PDT).

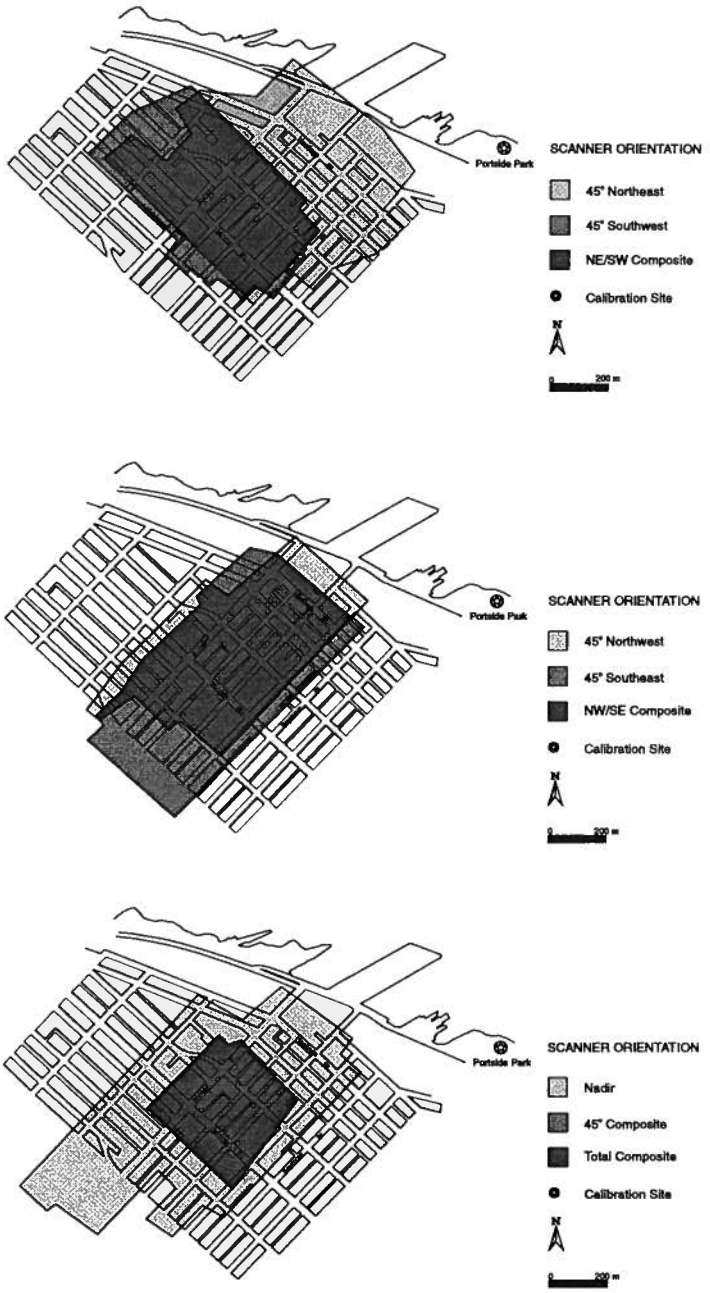

Figure D.5: Scanned areas (by direction) and composites for Flight 4 (Downtown area: August 16, 1992; 1130 PDT).

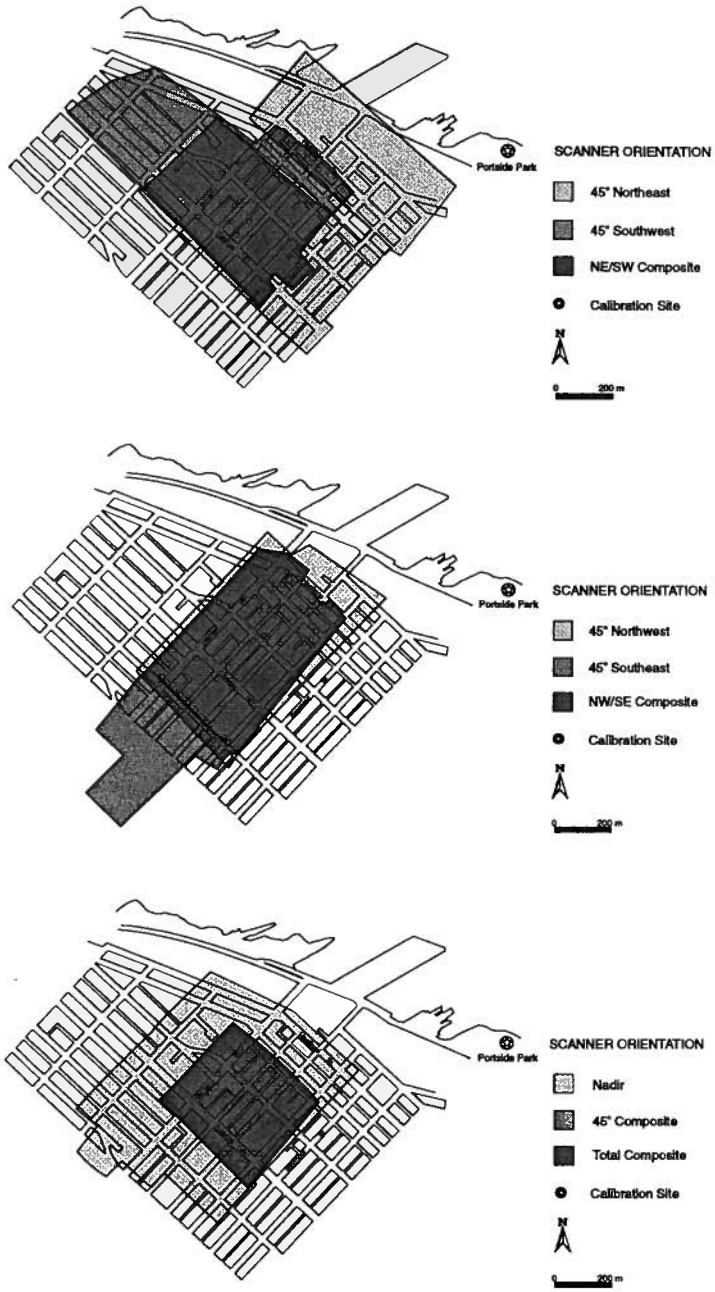

Figure D.6: Scanned areas (by direction) and composites for Flight 5 (Downtown area: August 16, 1992; 1630 PDT).

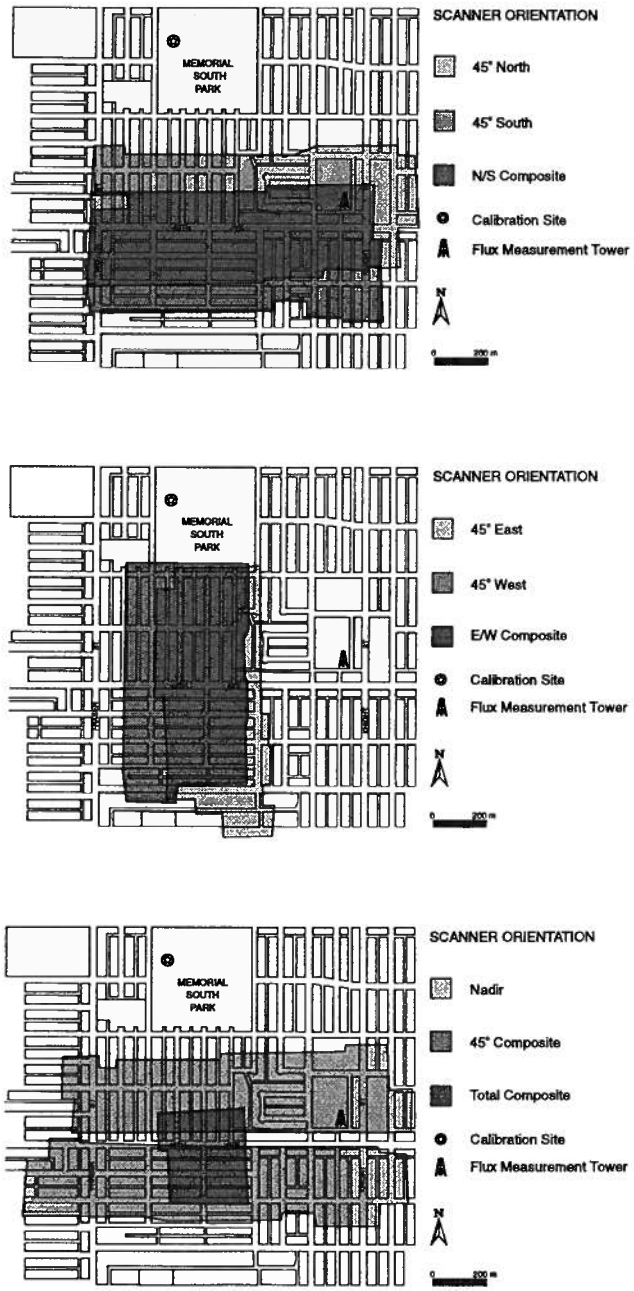

Figure D.7: Scanned areas (by direction) and composites for Flight 6 (Residential area: August 17, 1992; 0945 PDT).

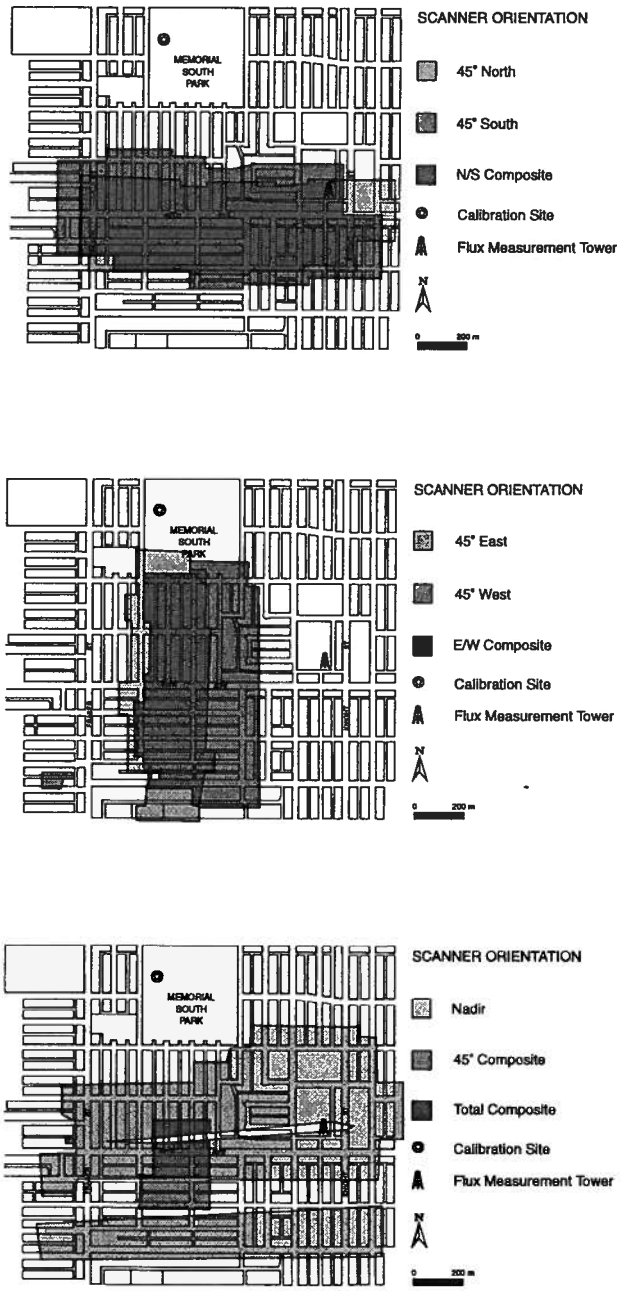

Figure D.8: Scanned areas (by direction) and composites for Flight 7 (Residential area: August 17, 1992; 1400 PDT).

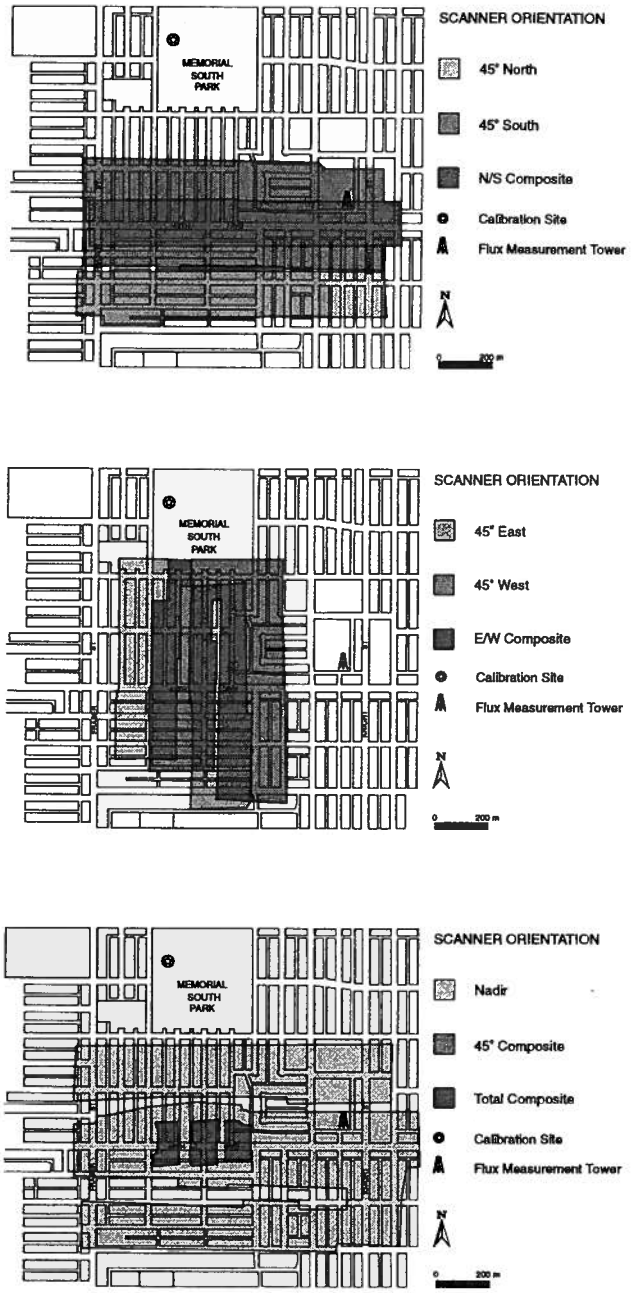

Figure D.9: Scanned areas (by direction) and composites for Flight 8 (Residential area: August 17, 1992; 1715 PDT).